DEPARTMENT OF

SURGERY, DENTISTRY, PAEDIATRICS AND GYNAECOLOGY

PHD SCHOOL

LIFE AND HEALTH SCIENCES

PHD IN

CARDIOVASCULAR SCIENCE

With funding by

UNIVERSITY OF VERONA

CYCLE / YEAR of initial enrolment XXXII (2016)

PHD THESIS TITLE

Structural and functional differences between cardiomyocytes from right and left ventricles in health and disease

S.S.D. (Disciplinary Sector) MED/11

Coordinator: Prof. GIOVANNI BATTISTA LUCIANI

Signature _____

Tutor: Prof. GIUSEPPE FAGGIAN

Signature _____

Tutor: Prof. JULIA GORELIK

Signature _____

Tutor: Prof. MICHELE MIRAGOLI

Signature _____

PhD candidate: ROMAN MEDVEDEV

Signature _____

STRUCTURAL AND FUNCTIONAL DIFFERENCES BETWEEN CARDIOMYOCYTES FROM RIGHT AND LEFT VENTRICLES IN HEALTH AND DISEASE

Roman Medvedev
PhD thesis
Verona,
ISBN 12324-5678-910

Abstract

Several disorders including pulmonary hypertension (PH) and heart failure (HF) could lead to right ventricle (RV) hypertrophy and failure. RV failure is one of the most important prognostic factors for morbidity and mortality in these disorders. However, there is still no therapy to prevent the RV hypertrophy in PH. Treatments developed for the left ventricle (LV) failure do not improve the survival in patients with RV failure probably due to the significant differences in the chambers physiology and hemodynamic function. A better understanding of the cellular and molecular mechanisms of RV hypertrophy is needed. Our focus lies into the alterations of cellular microarchitecture that promotes functional changes in Ca^{2+} handling. Recently our group showed that reorganisation of the transverse-axial tubular system (TATS) in HF are of particular importance for Ca^{2+} mishandling and contractile impairment of failing cells.

Rationale: This study aims to establish the differences in membrane organisation of Ca^{2+} handling between healthy RV and LV myocytes, and to investigate the remodelling of RV during disease.

Specifically, the objectives are: (1) To study the membrane organisation of RV and LV myocytes by revealing the surface topography using Scanning Ion Conductance Microscopy and by studying the TATS using confocal microscopy. (2) To assess the contraction and Ca^{2+} transients in RV and LV myocytes. (3) To determine the spatial distribution and properties of single L-type Ca^{2+} channels (LTCC) in RV myocytes using "smart patch clamp" technique. (4) To describe the changes occurring in the RV and LV in the two disease rat models: PH induced by monocrotaline injection and HF induced by chronic myocardial infarction (MI).

This thesis showed that in healthy samples the TATS of RV myocytes has a different organization as compared to LV. Two main Ca^{2+} channels for the excitation-contraction coupling: LTCC and ryanodine receptors (RyR) were studied by immunofluorescence staining. The density of LTCC was lower in RV than in LV myocytes. However, the density of RyR was similar between the chambers. Contraction duration was longer in RV than in LV myocytes. The distribution of

functional LTCCs in RV myocytes was uniform along the cell surface, in contrast to LV myocytes, where LTCCs were primarily located in the T-tubules.

Secondly, PH rats showed a reduction of the conduction velocity anisotropy throughout the RV as well as prolongation of the refractoriness of the tissue. The hypertrophy of RV myocytes in PH was accompanied by the reduction of the TATS organisation. The amplitude of contraction of RV PH myocytes was higher, the activation of Ca^{2+} transients was more desynchronised than in controls, and the rate of spontaneous Ca^{2+} activity was significantly elevated. Functionally, in PH the open probability (Po) of LTCC located in the T-tubules was significantly higher. On the other hand, PH LV myocytes had preserved TATS but still showed prolonged Ca^{2+} transients that could influence increased refractoriness of LV tissue.

Thirdly, by studying RV myocytes from the MI model, a significant hypertrophy was found, accompanied by a reduction of TATS organisation. The study reports a prolongation of Ca^{2+} transients with more frequent local Ca^{2+} waves in MI versus control RV myocytes. Higher Po of LTCCs was shown in MI RV myocytes could be associated with the PKA-mediated phosphorylation.

In summary, RV myocytes have a lower TATS organisation than LV myocytes probably related to the lower workload of the RV chamber. Consequently, RV myocytes present several differences with LV myocytes, including changes in the Ca^{2+} handling or a more uniform distribution of LTCC on the membrane. Diseases induce reduction of TATS and Ca^{2+} mishandling in both chambers. Due to the intrinsic differences of RV versus LV myocytes, the RV could be more prone to pathological events in early stages of the diseases, which should be investigated further.

Publications (submitted or expected from this work)

Medvedev RY, Sanchez-Alonso J.L., Alvarez-Laviada A., Rossi S., Dries E., Abdul-Salam V.B., Wojciak-Stothard D., Miragoli M., Faggian G., Gorelik J. Nanoscale study of calcium handling remodelling in right ventricular cardiomyocytes following pulmonary hypertension. (In preparation, to be submitted to Hypertension).

Medvedev RY, Sanchez-Alonso J.L., Pagiatakis C, Miragoli M, Faggian G. Gorelik J. Local hyperactivation of L-type Ca^{2+} channels and spontaneous Ca^{2+} sparks in the right ventricle after membrane disorganisation in heart failure. (In preparation, to be submitted to Scientific Reports.)

Medvedev RY, Sanchez-Alonso JL, Alvarez A., Miragoli M, Faggian G. Gorelik J. Right ventricular myocytes have less organized membrane structures and different localization of L-type Ca^{2+} channels compared to myocytes from left ventricle. Journal of molecular and cellular cardiology, Issue 120 (Supplement 1) 2018.

Presentations

1. "Differences in localisation of calcium channels and membrane structures in right and left ventricular myocytes" Poster and Oral presentation, International Society for Heart Research, Amsterdam, 2018
2. "Structural and functional differences between cardiomyocytes from right and left ventricles in health and disease." Departmental presentation in Imperial College London, 30 January 2019.

Declaration:
This thesis resents my own work unless otherwise indicated within the text. This work has not been submitted at any other academic institution.
Roman Medvedev, Verona, September 2019

Acknowledgments

I want to thank my supervisor Prof. Giuseppe Faggian for providing me the possibility to make this work and for his great interest and supervising of all my studies.

I want to thank my second supervisor, Prof. Julia Gorelik, for encouraging me to microdomain world and providing the possibility to make this work, whose enormous energy and patience helped a lot during all my studies.

I am very grateful to Dr. Michele Miragoli who was my co-supervisor at Humanitas University and University of Parma for providing me the possibility to learn a lot about different methodologies and helpful conversations regarding my project.

I want to say many thanks to Dr. Sanchez-Alonso who introduced me to the world of electrophysiology and who provided me great discussions and help in building up the story of the work. His support and enormous energy helped to finish this work.

I want to thank all the members of Prof. Gorelik's group at Imperial College. Dr. Ivan Diakonov, Dr. Anita Alvarez-Laviada, Dr. Peter Wright, and all the Ph.D. students. Thank you for helping me to settle down when I first visited London and started to work in the laboratory. I am very thankful Mr. Peter O'Gara for his technical support in cell isolations. I want to thank my colleagues from the Humanitas Research institute: Dr. Marta Mazzola, Dr. Silvia Crasto, Mr. Fernando Hall, Dr. Cristina Pagiatakis, and Dr. Veronica Larcher for a great company in Milan and your nice support for me. I want to thank Dr. Tilo Schorn from Imaging Unit in Humanitas Research Institute for his big help with super-resolution STED microscopy.

I am very grateful for my colleagues: Mr. Francesco Lo Muzio, Mr. Giacomo Rozzi, Dr. Cristina Caffara, Ms. Amparo Guerrero, and other members of Dr. Michele Miragoli group in Parma for great scientific discussions during the work and funny meeting after it.

Lastly, I want to thank my family and friends who supported me all the time and taught me never to give up.

List of acronyms

AC	Adenylyl cyclase
AF	Atrial fibrillation
AKAP79	A-kinase anchoring protein
ALC1	Atrial myosin light chain 1
ANOVA	Analysis of variance
AP	Action potential
APD	Action potential duration
A-tubule	Axial tubule
AV	Atrioventricular node
AVN	Atrioventricular node
BayK	BayK8644
CaM	Calmodulin
CaMKII	Ca2+/calmodulin-dependent protein kinase II
cAMP	Cyclic AMP
Cav3	Caveolin3
Cavα1C, Cav1.2	α subunit of L-type Ca^{2+} channels
Cavα2/δ	α2/δ subunit of L-type Ca^{2+} channels
Cavβ	β subunit of L-type Ca^{2+} channels
Cavγ	γ subunit of L-type Ca^{2+} channels
CCBs	Ca^{2+} channels blockers
CDF	Ca^{2+} dependent facilitation
CDI	Ca^{2+} dependent inactivation
CICR	Ca^{2+} induced Ca^{2+} release
CON	Control
CPVT	Catecholaminergic polymorphic ventricular tachycardia
Crest	Surface sarcolemma membrane
CSQ	Calcequestrin

CV	Conduction velocity
CV-l	CV was computed longitudinally
CV-t	CV was computed transversally
DADs	Delayed afterdepolarizations
DHPs	Dihydropyridines
DMSO	Dimethylsulfoxide
EADs	Early afterdepolarizations
ECC	Excitation - contraction coupling
ECG	Electrocardiogram
Enz	Enzyme buffer
ERP	Effective refractory period
EVG	Elastic van Gieson
F50	Fluorescence at 50 % of the Ca^{2+} transient amplitude
FDHM	Duration at half-maximum of amplitude
FKBPs	FK506-binding proteins
FWHM	Width at half-maximum of amplitude
HBSS	Hank balanced buffer solution
HF	Heart failure
HVA	High voltage activated channels
ICaL	Voltage gated Ca^{2+} current
IK1	Inward-rectifier K^+ current
IKr	Rapid delayed-rectifier K^+ efflux
IKs	Slow delayed-rectifier K^+ efflux
INa	Voltage gated Na^+ current
IP3Rs	Inositol-1,4,5-triphosphate receptors
ISO	Isoprenaline
Ito,f	Voltage gated outward current
IV	Current-Voltage

JPH2	Junctophilin-2
KH	Krebbs-Henseleit
LowCa	Low Ca^{2+} buffer
LTCC	L-type Ca^{2+} channels
LV	Left ventricle
LVA	Low voltage activated channels
LWR	Length to width ratio
MCT	Monocrotaline
MHC	Myosin heavy chain
MI	Myocardial infarction
MβCD	Methyl-β-cyclodextrin
NCX	Na+- Ca2+ exchanger
OM	Optical mapping
PAH	Pulmonary arterial hypertension
PDE4D3	Phosphodiesterase 4D3
PH	Pulmonary hypertension
PKA	Protein kinase A
PKC	Protein kinase C
PLB	Phospholamban
Po	Open probability
PV	Pressure-volume
RV	Right ventricle
RVF	Right ventricle failure
RVSP	Right ventricle systolic pressure
RyR	Ryanodine receptor
SA	Sinoatrial node
SERCA2A	Sarcoendoplasmic reticulum Ca2+-ATPase
SICM	Scanning ion conductance microscopy

SR	Sarcoplasmic reticulum
TAT	Transverse axial tubules
TBS	Tris buffer saline
T-Cap	Telethonin
TTF50	Time to F50 of Ca2+ transient
T-tubule	Transverse tubule
VGCCs	Voltage regulated Ca2+ channels
VT	Ventricular fibrillation
WLL	White light laser
α-SKA	Alpha-skeletal actin
α-SMA	Alpha-smooth muscle actin
βAR	β-adrenoreceptors

List of figures

List of tables

Table of Contents

1. General introduction

For the many years, more attention was given to study the left ventricle (LV) disorders, overshadowing the investigation of the right ventricle (RV) physiology and pathologies (Greyson, 2010). Recently, RV pathological changes was not considered as primary ones and not as critical for heart functioning and ejection fraction maintenance as the LV, and that's why less attention was paid to the RV. Now growing body of clinical and experimental data indicates the participation and importance of RV in many severe disorders. RV is suffering in the settings of respiratory disorders, which leads to pulmonary vasoconstriction and pulmonary hypertension (Greyson, 2010; Thenappan et al., 2010; Zapol and Snider, 1977). In case of primary pulmonary hypertension, in average 1 in 2000 of the 10–15 million pulmonary hypertensive people will develop RV failure (Naeije, 2005). Pulmonary embolism induced causes more than 50,000 deaths annually, mostly due to acute RV failure (Hirsh and Hoak, 1996). Several disorders like sepsis and coronary ischemia, can directly induce RV dysfunction (Goldstein, 2002; Lambermont et al., 2003). Idiopathic dilated cardiomyopathy can lead to pulmonary hypertension and RV failure. (La Vecchia et al., 2001). Moreover, in patients with left heart failure, RV failure was shown to be an independent risk factor for morbidity and mortality (Ghio and Tavazzi, 2005). RV failure is still a leading cause of death early after cardiac transplant (Stobierska-Dzierzek et al., 2001) and following several other cardiothoracic procedures (Kaul, 2000). Altogether this indicates a high clinical importance of RV function in heart pathophysiology.

Interventricular differences could be important for understanding the RV physiology and pathophysiology. RV differs stridently from LV in terms of working conditions and responses to high pressure and load (Greyson, 2008). Inter-ventricular differences in organisation of excitation- contraction coupling were observed on cellular level (Molina et al., 2014; Sathish et al., 2006). These findings indicate that the mechanisms of RV progression in disease can differ from those observed in LV.

This chapter will review the recent findings of RV and LV behaviour, especially cell organisation and excitation- contraction coupling.

1.1 Mechanics of the right and left ventricle contraction

1.1.1 General heart function

The heart is a muscular organ located in the chest immediately posterior to the sternum. The heart is connected to the vascular system which delivers blood through the body. The main function of cardiovascular system is to transport oxygen and nutrients to the cells of the body and remove carbon dioxide and other metabolic waste products. The heart consists of two thin walled atria and two more thicker muscular ventricles (Figure 1.1; (Bettex et al., 2014)). The right and left sides of the heart have different functions. The right heart pump the blood in the lungs for oxygenation and the left heart pumps the oxygenated blood to the body.

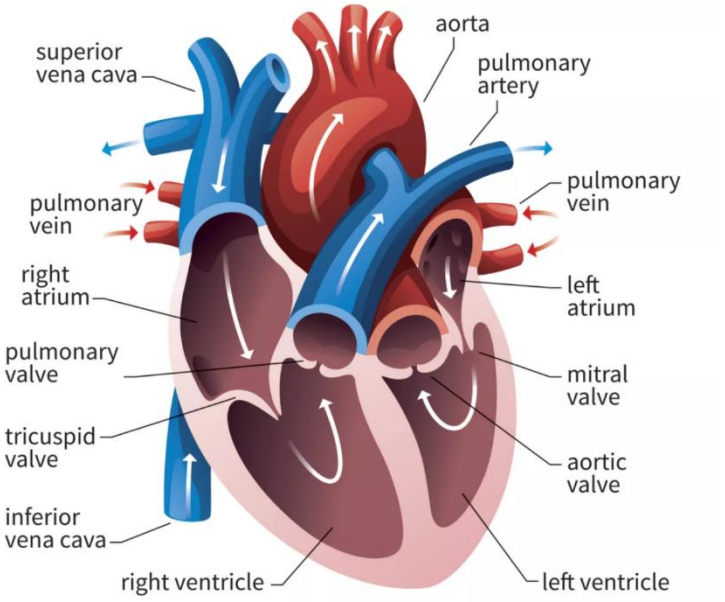

Figure 1.1 General heart organisation. From thoughtco.com

Atria main function is to receive the blood from the veins and to pump it to the ventricles. Their thin-walled organisation allows atria to cope with sudden changes in venous return. The right atrium gets the deoxygenated blood from systemic circulation and delivers it to the RV which pumps it out to the pulmonary vein. The left atrium takes the oxygenated blood from pulmonary circulation and brings it to the LV which pumps it in the systemic circulation. The ventricles have a more muscular body than the atria to pump the blood out of the heart. Each cardiac cycle consists of two phases, namely diastole and systole. In diastole, atria are contracting

and ventricles are filling with blood. In systole, the ventricles are contracting and atria are relaxing (Sonnenblick et al., 1967).

1.1.2 Pulmonary and systemic circulation cycles

The structure and the function of ventricles cannot be described without taking in consideration a circulation cycle. RV pumps blood into pulmonary circulation and LV pumps blood into systemic circulation. Pulmonary circulation has several remarkable differences from the systemic circulation. Anatomically, the systemic circulation presents a big circuit that consists of one large main artery with small brunches. On the contrary, the pulmonary circulation has a wide network of short vessels which repeatedly branches in three daughter vessels (Horsfield, 1978).

Besides structural differences between pulmonary and systemic circulations they markedly differ in function. Systemic circulation has a much higher pressure and resistance than pulmonary system (Table 1). Also, these circuits act differently under external stimuli. For example, hypoxia causes the dilation of systemic circulation but constricts pulmonary circulation constricts.

Table 1. Average values of systemic and pulmonary circulation resistance and pressure. Adapted from (Greyson, 2008).

	Pulmonary/ RV/RA	Systemic/ LV/LA
Vascular resistance (dyne*s*sm^{-5}M^{2})	123±54	2130±450
Pressure (mmHg)		
Atrial mean	2-7	2-12
Ventricular systolic	15-28	90-140
Ventricular diastolic	0-8	4-12
Vascular mean	10-16	65-105

1.1.3 Left ventricle

Properties of the circulation system are among main factors that determine the ventricular properties. The LV presents an ellipsoidal thick walled chamber (Figure 1.1. Two thick papillary muscles anchor the *chordae tendinae* to the two flaps of

the mitral valve which prevents backflow of blood into the atrium during systole (Sengupta et al., 2008).

When the heart contracts during systole, the apex of the heart is pulled towards the base while simultaneously sheets of fibres slide past each other in a "wringing" motion due to muscle fibre orientation. It then thickens the ventricle wall reducing the chamber lumen further and efficiently ejecting blood (Figure1.2, Hales et al., 2012).

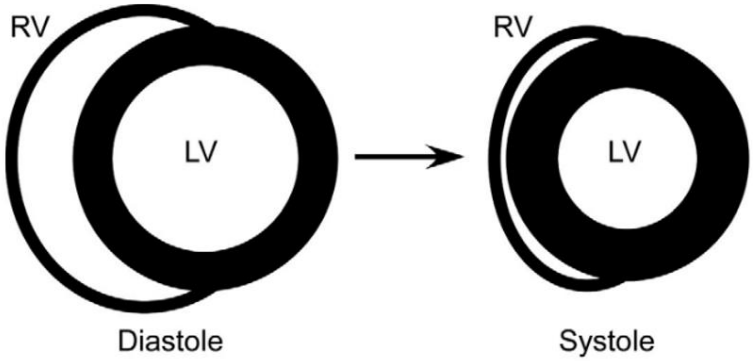

Figure 1.2. Schematic of the RV and LV contractions. From (Greyson, 2008).

1.1.4 Right ventricle

The RV pumps blood out into a highly compliant and low resistance pulmonary circulation, which requires around one sixth of the work of the LV (Greyson, 2008). The amount of blood injected in one contraction cycle is similar between the RV and LV. In LV a relatively large portion of stroke goes to pressure generation whereas in RV most part of the stroke generates the blood steam momentum. Moreover, there is a small blood ejection from the RV even during diastole (Pouleur et al., 1980).

In cross-section, the RV has a crescent shape (Figure 1.2). The normal RV seldom exceeds 2–3 mm wall thickness at end-diastole, compared with 8–11 mm for the LV (Portman et al., 1987). The contraction pattern of the RV is drastically different from the LV. The RV has a peristaltic like contraction through longitudinal shortening that begins at the apex and moves to the outflow tract (Dell'Italia et al., 1995; Greyson, 2008). Ejection is further assisted by the LV pulling on the RV at

the points of attachment to the interventricular septum. The differences between the RV and LV result in a higher ratio between the RV volume change to RV free wall surface area change and let the RV eject a large volume of blood with a less amount of RV stretch (Greyson, 2008). This type of contraction allows the RV to move large and varying volumes of blood but it is not well adapted to generate a high pressure. In addition, at end-systole, LV free wall radius of curvature decreases, which facilitates further development of pressure by decreasing the wall stress. Whereas the free wall of the RV increases the radius of curvature at the end of systole that produces a higher stress at peak pressure and prevents high pressure development (Greyson, 2008).

The dynamics of contracting hearts is usually analysed by using pressure-volume (PV) loops. The typical examples of PV loops for the LV and RV are shown in Figure 1.3. LV contraction produces a square shape of PV loop with clear points of end-systole and aortic valve closure. The function of the LV is usually described in terms of time varying elastance. This parameter can be determined from the slope of the PV relation at specific ("isochronal") times in the cardiac cycle (Suga, 2003). In contrast, RV ejects blood even during the ventricular relaxation, that produces a triangular shape of the PV loop (Shaver et al., 1974). This leads to a problematic determination of the "end-systole" and difficulties in interpretation of RV dynamics.

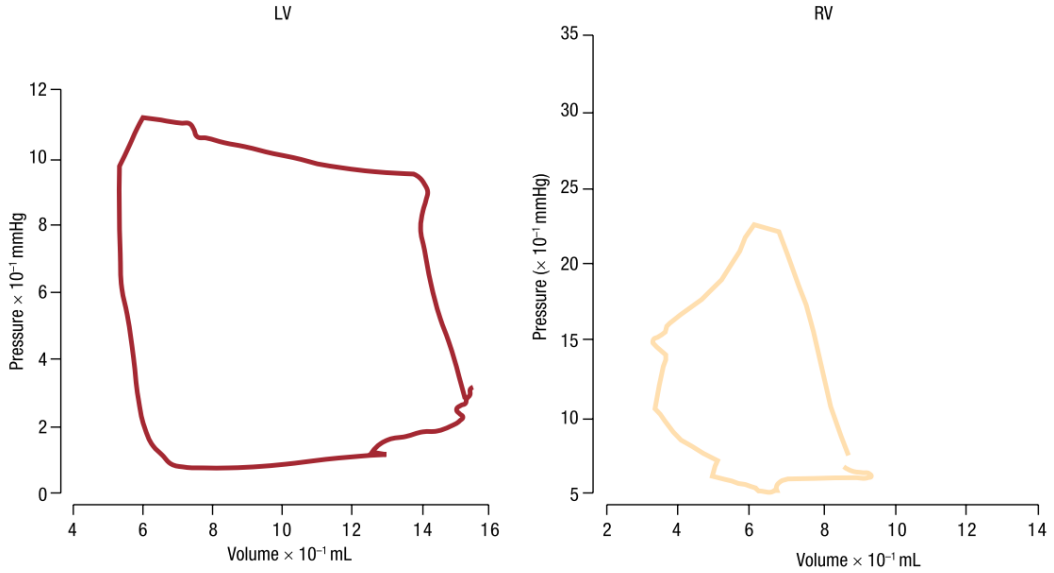

Figure 1.3. Pressure-volume relationships for the LV (left) and RV (right). From (Greyson, 2010).

1.2 Electrical properties of cardiac tissue

Synchronous contraction of all the parts of the heart is led by electrical waves. Cardiac tissue represents a striated muscle that is structurally similar to the skeletal one. However, the physiology of the cardiac tissue is distinct from that of the skeletal one (Hopkins, 2006). The skeletal muscle generates a very short action potential which is controlled by the nervous system. The heart can autonomously generate the action potentials at the specialized areas called nodes. Neurons can only modulate the rate of spontaneous electrical activity of the heart. The duration of the cardiac action potential is quite long (200-400 ms), which results in the generation of a full force during one action potential, but not a from a sequence of stimulations. Moreover, the force of contraction can be modified according to a load or modulated by the cardiac nerves.

The heart walls can be divided into three different cell layers: the pericardium, the myocardium and the endocardium (Sanchez-Quintana et al., 1990). The myocardium is a main layer that is responsible for contraction. It represents a special tissue, consisting of individual cells joined by electrical gap junctions. This communication allows the spread of electrical wave from one cardiac cell to another throughout the whole heart (Carmeliet and Vereecke, 2002). The depolarization wave causes a contraction, which also spreads like a wave throughout the heat from atria to ventricles.

There are two main types of muscle cells in the heart: contractile cells and conductive cells. The main difference between them is the generation of spontaneous action potential (Woodcock and Matkovich, 2005). Conductive (pacemaker) cells are able to spontaneously generate the depolarization waves (action potentials (APs)), whereas contractile cells contracts following these APs. Furthermore, an AP in one cardiac muscle cell will stimulate its neighbouring cells to undergo the depolarization (Hill, 2016). The waveform of AP depends on the tissue type, the typical waveforms of APs in different parts of the heart are shown in Figure 1.4.

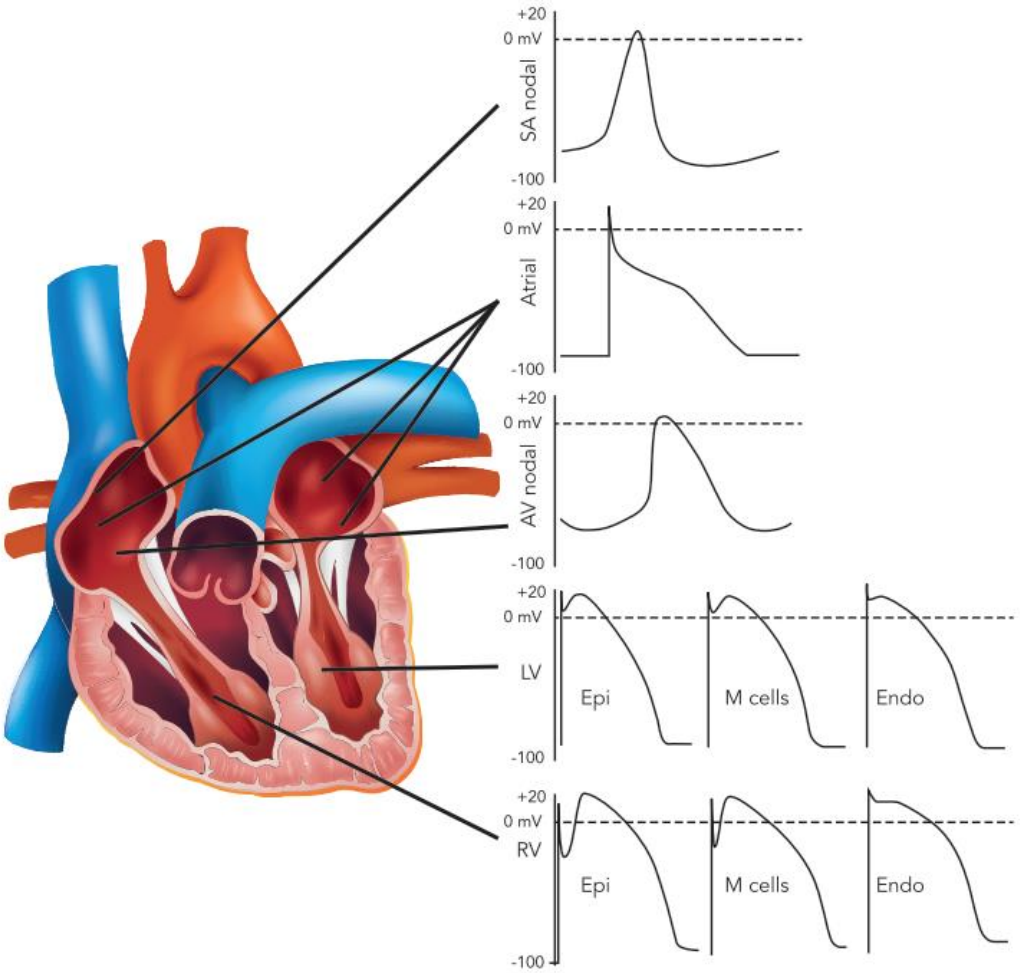

Figure 1.4. Representative action potential waveforms from different regions of the heart. AV = atrioventricular node; Endo = myocytes from endocardium; Epi = myocytes from epicardium; LV = left ventricle; M Cells = myocytes from midmyocardium; RV = right ventricle; SA = sinoatrial node. From (Molina et al., 2016)**.**

The propagation of depolarization waves starts in the sinoatrial (SA) node. This is a specialized tissue located in the right atrium, which can trigger a normal pacemaker activity of the heart (Hill, 2016). The impulse then travels from the SA node into the atrial syncytium, and the atria begin to contract. After that the impulse reaches the atrioventricular (AV) node. AV node has two main functions: to transfer depolarization from the atria to the ventricles and to induce a delay in the propagation of excitation from the atria to the ventricles (Kléber and Rudy, 2004). This time delay is important to allow the atria to eject blood into ventricles in prior of ventricular contraction. Then the depolarization wave reaches the specialized

conducting cells, called Purkinje fibres (Hill, 2016). This special cells can rapidly transmit electrical signals down to the apex of the heart so that all the contractile cells in the apex can contract nearly simultaneously (Silverthorn, 2009).

1.2.1 Action potential in myocytes

The excitation and repolarization of cardiomyocytes during each cycle of contraction are produced by the work of multiple ion channels and pumps which regulate disequilibrium of the electrical potential between inner and outer sides of the cellular plasma membrane. Ion channels and pumps modulate membrane potential through the entry or extrusion of selected ions.

The shape of cardiac AP shows large variations depending on the cell type (Figure 1.4), but generally it can be subdivided into five phases presented in Figure 1.7 (Carmeliet and Vereecke, 2002). Phase 0 starts when a negative resting membrane potential (-90 mV) reaches the threshold value (-70 mV) that necessary to open the fast voltage gated Na^+ channels. Influx of Na^+ ions depolarises the membrane, and the transmembrane potential reaches +20 mV. Phase 1 starts when Na^+ current inactivates. The openings of voltage gated outward K^+ ($I_{to,f}$) channels produce increased K^+ efflux out of the cytosol. This step leads to a slight repolarization of the cardiomyocytes (back to +5 mV). Phase 2 characterized by the opening of voltage gated Ca^{2+} ion channels. For a short time the rapid and slow delayed-rectifier K^+ efflux (I_{Kr} and I_{Ks}, respectively) and the Ca^{2+} influx counterbalance each other and keep the membrane potential at a relative plateau. Later, the Ca^{2+} current declines due to voltage and Ca^{2+} dependent inactivation of the voltage-gated Ca^{2+} channels which finishes the phase 2. However, the K^+ efflux continues during the phase 3. The inward-rectifier K^+ current (I_{K1}) activates late during the AP and controls final repolarization and resting membrane potential stability. At the end of phase 3, the membrane potential is turned back to its resting state (at -90mV) (Nerbonne and Kass, 2005). In working myocardium, phase 4 is determined by a stable membrane potential at -80 mV (Bers and Perez-Reyes, 1999; Fabiato and Fabiato, 1978).

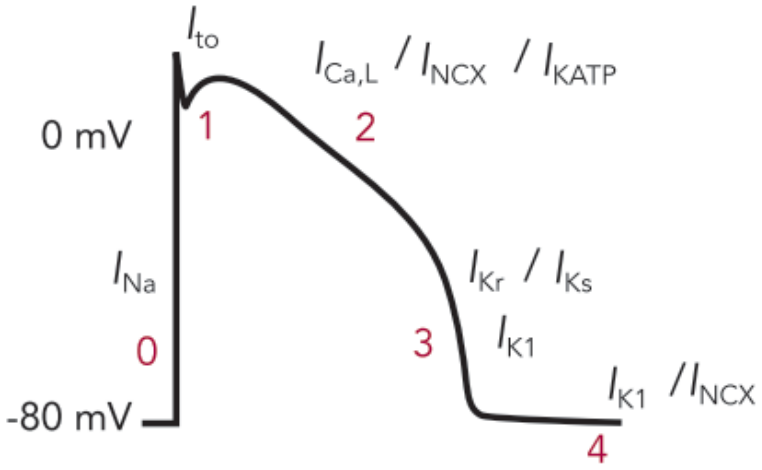

Figure 1.5. Shape of ventricular AP. Phases: resting (4), upstroke (0), early repolarization (1), plateau (2), and final repolarization (3). I_{Na} = Na^+ current; I_{to} = transient outward K^+ current; I_{CaL} = L-type Ca^{2+} current; I_{NCX} = Na^+-Ca^{2+} exchange current; $I_{K,ATP}$ = ATP-sensitive K^+ current; I_{Kr} = rapid component of delayed-rectifier K^+ current (I_K); I_{Ks} = slow component of I_K; I_{K1} = inward-rectifier K^+ current. Schematic from (Molina et al., 2016).

It is important to mention the differences between the heart rate and AP properties from different species (Figure 1.6 and Table 2). There is a big difference of the heart rate between rodents and large animals such as rabbit, dog and human (Table 2). These differences are responsible for a much shorter AP duration measured in rat and mouse compared to a human. Moreover, APs in rodents lack the plateau phase (2 phase of AP) (Figure 1.6). All these differences account for the limitations of the usage of small rodents as a models of human disease.

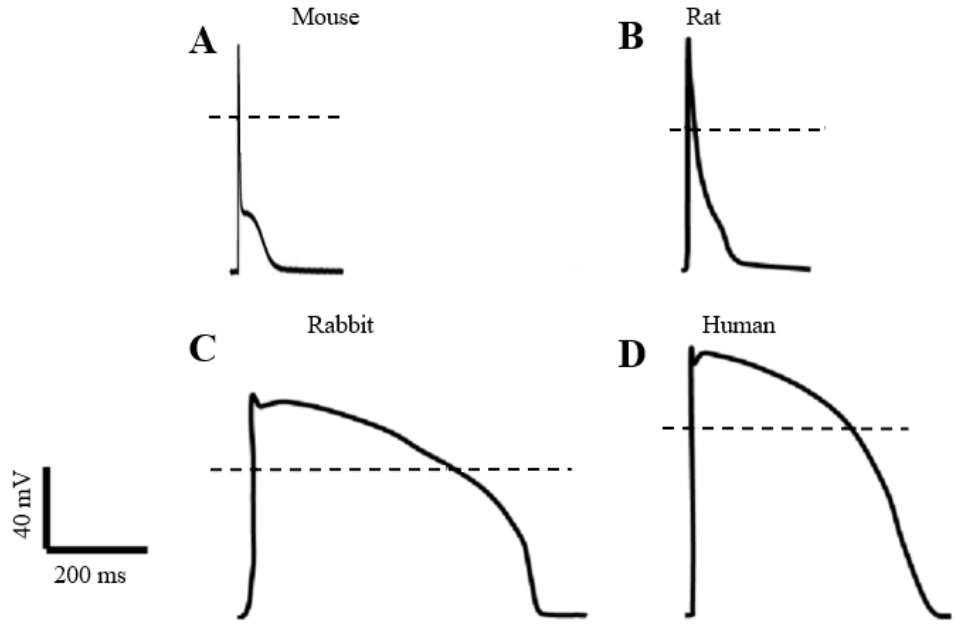

Figure 1.6. Representative shapes of ventricular APs, recorded from mouse, rat, rabbit and human ventricular myocytes. All action potentials were stimulated in 0.5 Hz and recorded in room temperature, from isolated ventricular myocyte. Figures were adapted from (Varro' et al., 1993).

Table 2. Species related properties of APs

Properties	Specie				
	Mouse	Rat	Rabbit	Dog	Human
Heart rate, bpm	500-724	330-480	120-150	60-140	56-101
Resting membrane potential, mV	-73±1	−75±4	-76±3	−82±2	−82 ± 2
Maximum upstroke velocity, V/s	114±12	148±12	158±18	275 ±58	
AP amplitude, mV	125.6±2.7	98.5±2.3	125.8±3.9	120-145	120-130
AP duration at 50%, ms	4.5±0.3	13±1	193±25	189+34	314 ± 23
AP duration at 90%, ms	64.0±2.7	62±3	225±6	295±34	434 ± 39
	(Knollmann et al., 2007)	(Pandit et al., 2001; Sanchez-Alonso et al., 2016)	(Giles and Imaizumi, 1988; Mcintosh et al., 2000; Tsuji et al., 2000)	(Kääb et al., 1996; Lue and Boyden, 1992)	(Bayer et al., 2010; Feng, 1998)

The data presented from AP recorded from isolated cardiomyocytes at stimulation frequency 1Hz.

1.2.2 Interventricular differences in action potential

Workload and electrophysiological specialisation of different regions of the heart have resulted in characteristic patterns of AP (Nerbonne and Kass, 2005). These patterns are determined by the specific properties of the ion channels, which have been shown at mRNA, protein, and functional levels (Molina et al., 2016). This specificity is species- dependent, but there are some similarities which are presented in Figure 1.9 and Table 3.

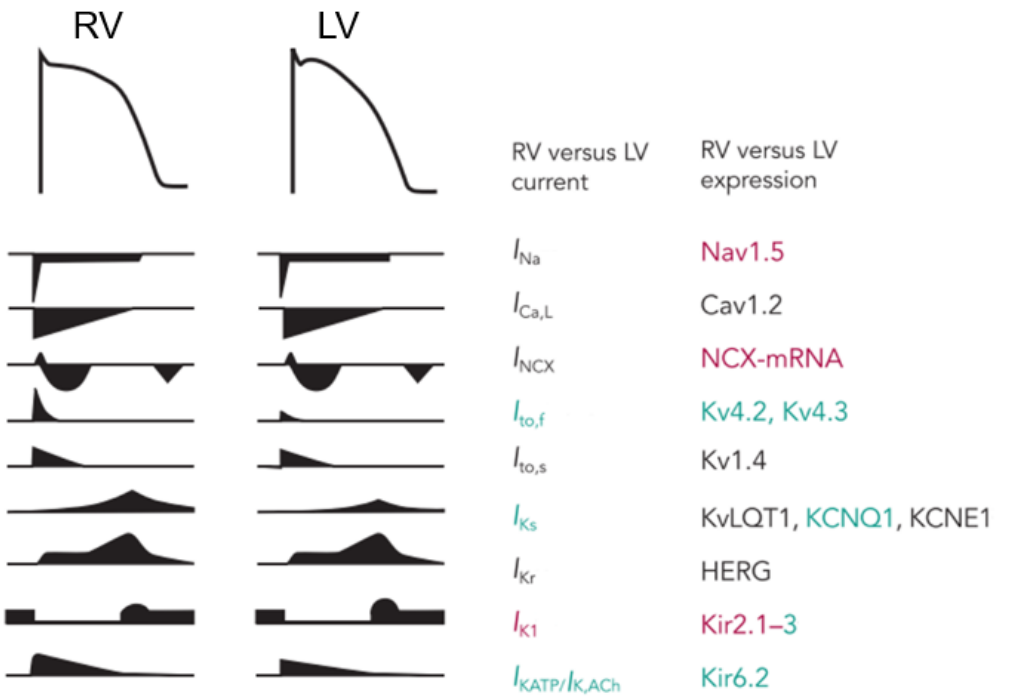

Figure 1.7. Representative shape of action potential waveforms from the RV and LV. Ionic currents involved in the initiation and maintenance of an action potential (AP) and their chamber-specific differences. Green means up-regulation and red down-regulation in the RV versus the LV and black indicates no change between chambers. Schematic is taken from (Molina et al., 2016).

Table 3. Differences in mRNA, protein expression and current density between RV and LV myocytes for the major ion currents participating in the AP formation.

Current	Species	Differences in RV versus LV myocytes			References
		mRNA	Protein levels	Current density	

$I_{Na,}$	Mouse	ND	ND	ND	(Martin et al., 2012)
I_{to}	Mouse Dog	↑ (50%) ND	↑ (50%)	↑ (40%) ↑ (60-70%)	(Martin et al., 2012) (Volders et al., 1999)
I_{CaL}	Mouse Cat Dog	ND	ND	ND ND ND	(Kondo et al., 2006) (Kleiman and Houser, 1988) (Ramakers et al., 2003)
I_{K1}	Mouse Dog Guinea pig	ND ↓ (30 %)	ND ↓ (10 %)	ND ND ↓ (40 %)	(Kondo et al., 2006; Martin et al., 2012) (Volders et al., 1999) (Warren et al., 2003)
I_{Kr}	Dog	↑ (75%)		ND	(Volders et al., 1999)
I_{Ks}	Dog	↑ (20-80%)	↑ (20%)	↑ (37-50%)	(Molina et al., 2014; Volders et al., 1999)

↑, ↓ or ND – is upregulated, downregulated or not different levels of the mRNA, protein expression or whole cell current density, respectively; I_{Na} = Na^+ current; I_{to} = transient outward K^+ current; $I_{Ca,L}$ = LTCC; I_{Kr} = rapid component of delayed-rectifier K^+ current (I_K); I_{Ks} = slow component of I_K; I_{K1} = inward-rectifier K^+ current.

In most of the species, the RV myocardium shows a slight overexpression of $K_v4.2$ and $K_v4.3$ as compared to the LV (Martin et al., 2012; Ramakers et al., 2005). These channels are the molecular components of I_{to}. KCNQ1 which shows a greater expression in the RV versus the LV (Ramakers et al., 2003; Sathish et al., 2006). Functional studies showed that the RV has a larger I_{Ks} and I_{to} as compared with the LV. Finally, some studies have suggested that I_{Na} is similarly expressed in the RV than the LV (Martin et al 2012).

The regional differences of the ion channel expression lead to a deeper notches and shorter AP durations (APD) at 50 % and 95 % of repolarization in the RV vs. the LV in canine myocardium (Di Diego et al., 1996; Ramakers et al., 2005). Also in rats the APD at 90% of repolarisation was significantly shorter in RV than in LV myocytes (Benoist et al., 2011). Similarly, the duration of monophasic APs *in vivo* in dogs was shown to be shorter in the RV than in the LV (Ramakers et al., 2003). Despite such variation of the AP duration between ventricles, the resting membrane potential and AP upstroke velocity was found to be similar in LV and RV (Di Diego et al., 1996; Volders et al., 1999).

1.2.3 Electrocardiography

Electrocardiography is the one of the gold-standard methodologies, which allow investigation of the electrical activity in the heart. Electrocardiogram (ECG) represents a temporal recording of the changes in electrical charge of all four chambers of the heart during each beat (Figure 1.8; Farraj et al., 2011). ECG consists of two major components: waves and segments. All the deflections of the signal above or below baseline are called waves, whereas sections between two waves are named segments. The first wave is P wave which represents the depolarization of atria. The depolarization of the right atrium produces first half of P wave and the left atrium produces the second half of it (Carmeliet and Vereecke, 2002). PQ segment represents the contraction of the atria. The next complex of waves (QRS complex) appears due to the ventricular activation. This activation is followed by a period of contraction, ST interval. The last component is T wave which indicates ventricular repolarization. The peak of T wave correlates in time with the full repolarization of myocardium. The average duration of the QT interval reflects the ventricular APD. Since QT interval depends on the heart rate, for a proper APD evaluation QT should be corrected for the duration of RR interval. In order to evaluate the duration, it needs to be corrected for frequency. Interval between T wave and next P wave represents the time of ventricular relaxation and filling it by blood. Described sequence of all waves and complexes repeats with each heartbeat at 60 bpm (in human heart). ECG is a common tool for the characterization of the electrical activity in the heart.

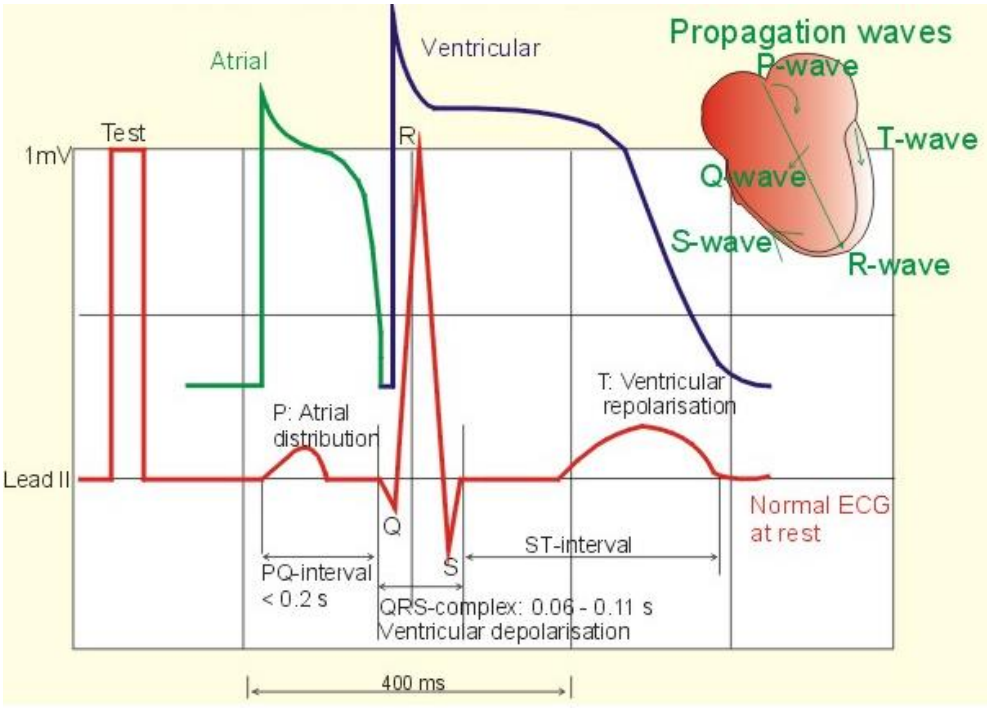

Figure 1.8. Electrocardiogram and related action potentials. ECG signal is present in red, the atrial action potential in green and ventricular action potential in blue. The right top panel shows the direction of wave propagation (Zubieta and Paulev, 2004).

The traces described above presents a typical example of a human ECG. Rats have some specific differences. Examples of a human and rat ECG are shown in Figure 1.9. Rat heats have a much higher contraction rate than a human, ~400 bpm vs. 60 bpm in human that produces some alterations in the shape of ECG. The traces of rat heart ECG sometimes lacks a pronounced Q wave and have very short QT segment (Figure 1.9; Konopelski and Ufnal, 2016). Nevertheless, essential similarities between rat and human ECG allow wide usage of rat studies for heart physiology (Sambi and White, 1960).

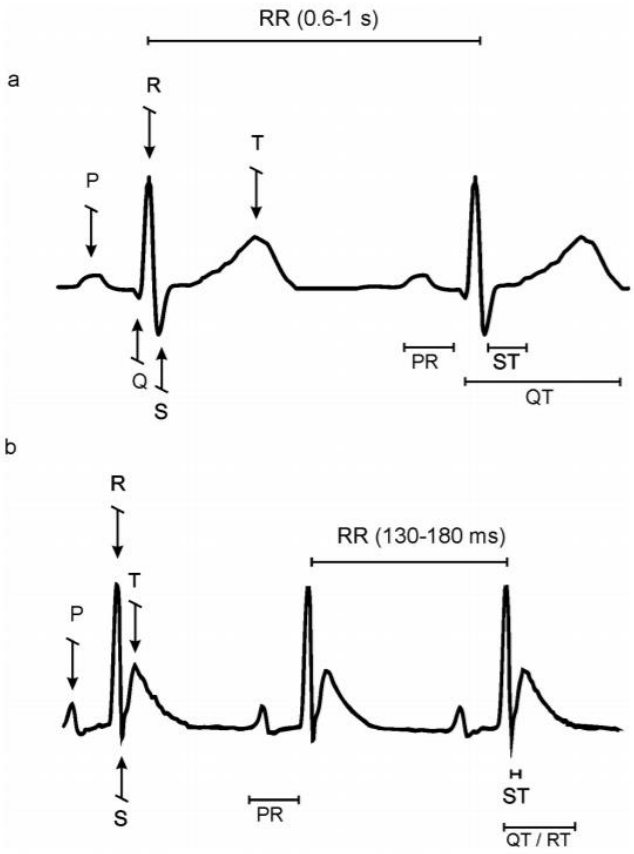

Figure 1.9. Relative time lapse of the human (a) and rat (b) ECG. In rat ECG Q waves and ST segments in rats are difficult to detect. Schematic from (Konopelski and Ufnal, 2016)

1.3 Excitation-contraction coupling

When the impulse reaches the myocyte it causes a contraction through the cascade of processes known as excitation-contraction coupling (ECC) (Bers and Perez-Reyes, 1999). Schematic representation of ECC is shown in Figure 1.10. Briefly, the AP -induced depolarization of the cell membrane causes activation of the voltage-gated Ca^{2+} channels also named as L-type calcium channels (LTCCs) located at the surface membrane and invaginations called transverse tubules (T-tubules). Ca^{2+} influx via LTCCs triggers Ca^{2+} release from the sarcoplasmic reticulum (SR) stores through ryanodine receptors (RyRs) (Saucerman and Bers, 2008). This amplifying process is called Ca^{2+}-induced Ca^{2+} release (CICR) (Fabiato and Fabiato, 1978). The result of CICR is a rapid increase of the intracellular Ca^{2+} concentration up to ~1 μM that binds troponin C. Activation of troponin C by Ca^{2+}

causes a release of the myosin heads from the tropomyosin complex and a subsequent hydrolysis ATP to ADP to generate energy. The myosin filaments use this energy to change their conformation and move along the actin filaments that leads to cell contraction (Carafoli et al., 2001).

After contraction, cardiac myocytes need to remove Ca^{2+} from cytosol to relax again. There are several ion pumps and transporters that are responsible for Ca^{2+} removal from the cytosol. First, Ca^{2+} ions are sequestrated back to SR stores by sarcoendoplasmic reticulum Ca^{2+}-ATPase (SERCA2). Second, Ca^{2+} is extruded out of the cell via the NCX and plasma membrane Ca^{2+} ATPase (PMSA) (Bers, 2008). A small amount of Ca^{2+} can be uptake into the mitochondria via the Ca^{2+} uniporter (Nerbonne and Kass, 2005).

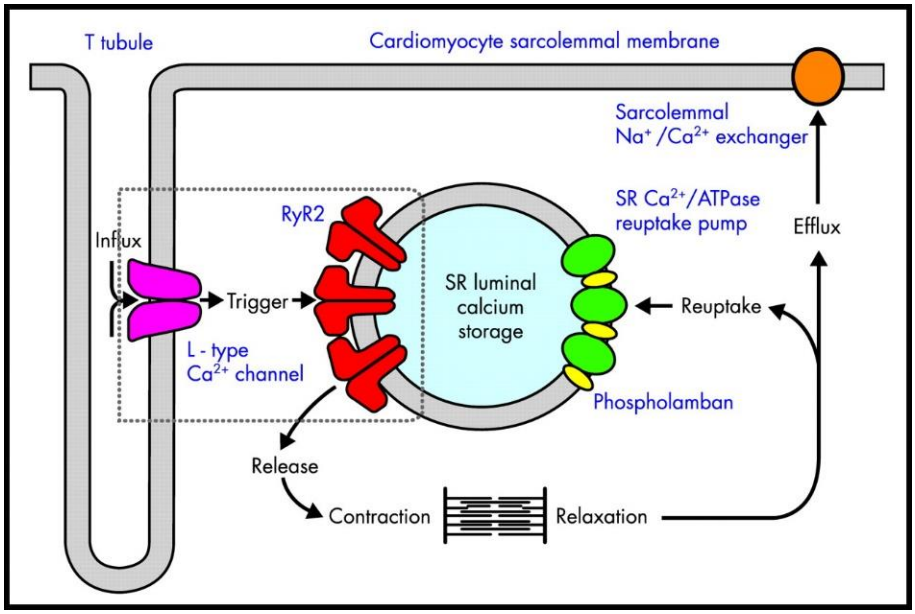

Figure 1.10. Cardiac E-C coupling. The action potential (AP) induces membrane depolarization, which activates L-type Ca^{2+} channels openings. Ca^{2+} influx through LTCC triggers RyR2 openings and release a large amount of Ca^{2+} from the sarcoplasmic reticulum, a mechanism called "calcium induced calcium release" (CICR). This high intracellular [Ca^{2+}] binds to the myofilaments through troponin C and activates contraction through release of myosin heads. During diastole phase Ca^{2+} is removed from the cytosol mainly by the SR Ca^{2+} ATPase (SERCA) and the NCX in its "forward" mode. (Schematic taken from (Scoote et al., 2003)).

1.3.1 Interventricular features of Ca^{2+} handling and contractility

Analysis of interventricular differences regarding ECC in the RV and the LV is very limited and depends on species. Literature summary of interventricular differences in ECC are shown in Table 4, focusing in the cardiac contraction and expression of related proteins. Kondo et al. showed much lower cell shortening and Ca^{2+} transients in RV myocytes as compared to LV myocytes in murine myocytes (Kondo et al., 2006). Whereas in rats, Sathish and colleagues found as well longer Ca^{2+} transients but the same amplitude of contraction (Sathish et al., 2006). On the other hand, a study performed in rats by Sabourin et al. showed a lower amplitude and a longer decay time of Ca^{2+} transients in RV myocytes compared to LV myocytes (Sabourin et al., 2018). In larger species such as dogs and cats, similar contraction properties of RV and LV myocytes were reported at baseline, but the contraction became significantly different under β-adrenergic stimulation (Kleiman and Houser, 1988; Molina et al., 2014). Diversity of the data indicates the complexity of the differences between contraction of RV and LV myocytes.

Table 4. Interventricular differences in contraction, Ca^{2+} transients and Ca^{2+} handling proteins.

Property	Species	RV versus LV myocytes	References
Cell shortening	Mouse	↓ (30%)	(Kondo et al., 2006)
	Rat	↓ (35%)	(Sathish et al., 2006)
	Rat	ND	(Sabourin et al., 2018)
	Dog	ND	(Molina et al., 2014)
Contraction duration	Mouse	↑ (20%)	(Kondo et al., 2006)
	Dog	ND	(Molina et al., 2014)
Diastolic Ca concentration	Mouse	ND	(Kondo et al., 2006)
	Rat	ND	(Sathish et al., 2006)
	Dog	ND	(Molina et al., 2014)
Ca transient amplitude	Mouse	↓ (40%)	(Kondo et al., 2006)
	Rat	ND	(Sathish et al., 2006)
	Rat	↓ (35%)	(Sabourin et al., 2018)

	Dog	ND	(Molina et al., 2014)
Ca transient duration	Rat Rat Dog	↑ (40%) ↑ (30%) ND	(Sathish et al., 2006) (Sabourin et al., 2018) (Molina et al., 2014)
RyR (mRNA)	Mouse Rat Dog	ND ND ↓ (32%)	(Kondo et al., 2006) (Sabourin et al., 2018) (Molina et al., 2014)
RyR (protein)	Rat Dog	ND ↓ (55%)	(Sabourin et al., 2018) (Molina et al., 2014)
NCX (mRNA SLC8A1)	Mouse Rat Dog	ND ↓ (50%) ↑ (50%)	(Kondo et al., 2006) 33 (Ramakers et al., 2005)
SERCA2 (mRNA)	mouse	ND	(Kondo et al., 2006)
SERCA2 (protein)	Rat	↓ (14%)	(Sathish et al., 2006)
SERCA2 (current)	Mouse Rat Dog	ND ↓ (80%) ↓ (27%)	(Kondo et al., 2006) (Sathish et al., 2006) (Gupta et al., 1997)
Phospholamban (mRNA)	Mouse	ND	(Kondo et al., 2006)
Phospholamban (protein)	Rat	↓ (17%)	(Sathish et al., 2006)

↑, ↓ or ND – increase, reduction or not different cell property, mRNA, protein expression or whole cell current density in RV myocytes versus LV myocytes, respectively.

Why RV myocytes have different ECC is not so clear. Different embryonic origins of the RV and LV or differences in loading conditions were proposed as the main reasons for such alterations. Another possible reason for such alterations could be a different force of contraction produced by the RV and LV. It was shown that contractile strength of myocytes depends on a balance between Ca^{2+} influx and Ca^{2+} removal from cytosol (Watanabe et al., 1983). Duration of AP significantly determines the duration of LTCC openings (Watanabe et al., 1983). In adult mice and rats, the APD at a fixed heart rate is shorter in the RV vs. the LV (Clark et al.,

1993; Knollmann et al., 2001). In larger mammals RV and LV have similar duration of AP but the notch during phase 1 of the AP is deeper in the RV than in the LV (Di Diego et al., 1996). Voltage-clamp study of (Bouchard et al., 1995) showed that prolongation of APD increased a total amount of Ca^{2+} entry per AP waveform and also increased maximal myocyte shortening. Similar total density of LTCCs in RV and LV myocytes (Kleiman and Houser, 1988) suggests that a larger SR Ca^{2+} load or faster SR Ca^{2+} uptake in LV vs. RV myocytes could be responsible for larger Ca^{2+} transients. Proteomics study of SERCA2a and RyR2 showed similar expression levels in the RV and the LV myocytes of pigs and rabbits (Phillips et al., 2011). Alteration could occur on the regulation of the proteins, for example, Sathish et al. found a smaller fraction of SR SERCA2 units available in the RV compared to LV in rats that leads to reduced effectivity of Ca^{2+} sequestration in the RV myocytes and prolonged Ca^{2+} transients (Sathish et al., 2006).

It is important to mention that in rodent myocytes more than 90% of total Ca^{2+} flux during each beat originates from the SR Ca^{2+} release and subsequent SR Ca^{2+} reuptake (Luss et al., 1999). In contrast, in larger mammals there is a much larger role for Ca^{2+} entry via $I_{Ca,L}$ and NCX-mediated Ca^{2+} extrusion, which accounts for ~30 % of the total Ca^{2+} flux (O'Rourke, 2008). Thus, a direct extrapolation of the data on LV/RV differences in Ca^{2+} handling from rodents to humans is difficult.

1.4 Arrhythmogenic activity in the heart

In pathological conditions, disruptions of the normal propagation of AP can lead to arrhythmias. These alterations of the normal impulse generation and propagation induce atrial (AF) or ventricular fibrillation (VF) that are the most common causes of sudden cardiac death (Rubart and Zipes, 2005). The arrhythmogenic activity could be classified in several groups, such as non-re-entrant and re-entrant activity or activity occurred at cellular and tissue levels (Anumonwo and Pandit, 2015; Tse, 2016). At the cellular level, arrhythmias could originate from abnormal oscillations (automaticity) of pacemaker cells or early and delayed depolarizations, i.e., EADs and DADs, respectively (Anumonwo and Pandit, 2015). At the tissue level, different types of re-entry in the form of spiral waves or rotors is now thought to

play an important role in sustaining arrhythmias, including AF and VF (Pandit and Jalife, 2013).

1.4.1 Arrhythmogenesis at cellular level

Cellular arrhythmogenesis could originate from the enhanced automaticity of pacemaker cells located in sinoatrial node (SAN) and atrioventricular node (AVN). This can be physiological, due to increased sympathetic tone during exercise, or pathophysiological, due to hypovolemia, ischemia, or electrolyte disturbances (Tse, 2016). Enhanced automaticity can also occur in the AVN, under conditions of acute myocardial infarction, digitalis toxicity, isoprenaline administration, and recent cardiac surgery (De Azevedo et al., 1973). When the discharge rate of the AVN is higher than the sinus rate, it can lead to abnormal rhythms called accelerated junctional rhythms (De Azevedo et al., 1973). Extra beats could happen when a latent pacemaker is protected from the dominant pacemaker by entrance block and becomes ectopic, discharging APs independently. A region of entrance block can occur when the dominant pacemaker is surrounded by ischemic, infarcted, or otherwise compromised tissues that prevent conduction of APs to the latent pacemaker (Gussak and Antzelevitch, 2003).

Abnormal impulses that originate outside of the SA could occur during or after APs. EADs and DADs are able to trigger, if of sufficient magnitude, self-sustaining APs, resulting in cardiac arrhythmias (Rosen and Schwartz, 1991). Generally, EADs are promoted by APD prolongation when the loss of repolarizing K^+ currents occurs. Prolonged APs could reactivate the LTCC that further depolarizes the membrane (Cranefield and Aronson, 1989; Michael et al., 2009). This sets up a positive feedback loop, triggering an AP. EADs have also been associated with shortening in APDs, occurring late in phase 3 of the AP (Patterson et al., 2006)]. This could happen if the intracellular Ca^{2+} concentration remains elevated when the membrane potential is lower than the equilibrium potential for NCX. So I_{NCX} can be activated, causing membrane depolarization. These late EADs are clinically relevant, as they can occur immediately after termination of other types of tachycardia, such as atrial flutter, AF and VF (Burashnikov and Antzelevitch, 2006).

In contrary, DADs happen after APs under conditions of intracellular Ca^{2+} overload, which can result from exposure to digitalis, catecholamines, hypokalaemia, hypercalcemia, and in hypertrophy and HF (Tse, 2016). SR Ca^{2+} overload leads to increased Ca^{2+} leak that in turn activates NCX and the calcium-activated chloride current, I_{Cl}. Together, these currents could depolarise the membrane and trigger additional APs (Cranefield and Aronson, 1989; Llach et al., 2011).

DADs and late EADs are somewhat similar, as they occur under conditions of intracellular Ca^{2+} overload and involve spontaneous SR Ca^{2+} release. The difference appears to be the timing of this release which occurs during the repolarizing phase of the AP in the case of late EADs, and at the resting membrane potential for DADs (Fink and Noble, 2010).

1.4.2 Re-entry

Re-entry occurs when an AP fails to extinguish itself and reactivates a region that has recovered from refractoriness (Janse and Wit, 1989). It can be divided into two types: (i) circus type re-entry occurred with an obstacle; and (ii) re-entry that occurs without an obstacle (reflection or phase 2).

Circus type of wave occurs when an AP moves around an anatomical or functional obstacle and reexcites the site of origin (Mines, 1913). This type of re-entry was proposed by Mayer and it happens when a slower conduction and a shorter duration of excitation wave would permit the tissue ahead of the excitation wave to recover from refractoriness. In contrary, when the excitation wave has a high propagation rate and a long duration, the whole circuit would be excited at the same time, causing the excitation to die out (Mines, 1913). Three criteria for this type of re-entry were proposed: (a) occurrence of the area with unidirectional block; (b) the excitation wave propagates along a distinct pathway, returns to its point of origin, and starts again; and (c) interruption of the circuit at any point would terminate this circus movement (Mines, 1913). Thus, for these events, both the conduction velocity (CV) and the refractory period determine whether re-entrant arrhythmogenesis occurs. Propagating waves in the myocardium have a wave front that represents AP depolarization, and a tail that represents repolarization (Weiss et

al., 2000). The length of this excitation wave is given by the product of its CV and refractory period (Wiener and Rosenblueth, 1946), and must be smaller than the length of the circuit in order for re-entry to be successful (APD).

Circular re-entry could happen with a functional obstacle, which could be a part of the tissue held above the threshold by the electrotonic influences of the depolarization wavefront that is going around it (Allessie et al., 1976). Here, the circuit is defined entirely by the electrophysiological properties of the tissue. The smallest circuit permitting successful re-entry, which was called the leading circle, is the one in which the circulating wave front can just excite again the tissue ahead that is still in the relative refractory period (Allessie et al., 1977).

The occurrence of this re-entry depends on the AP wave curvature (Cabo et al., 1994). For a planar wave, each cell activates one cell downstream. If a wave has front curving inwards (concave), each cell will be activating less than one cell downstream. This will induce a source–sink mismatch that will increase the depolarizing current available for each downstream cell. All this results in a greater rate of voltage rise, and therefore, a higher CV compared to that of a planar wave. The opposite is true for a wave front curving outwards (convex). This is situation when each cell will be activating more than one cell downstream, and thus the CV will be smaller than that of a planar wave. If the curvature is sufficiently convex, conduction block can result (Cabo et al., 1994). The point where the activation and repolarization wave fronts meet is called the phase singularity (Winfree, 1989). The latter corresponds to the functional obstacle because all phases of the wave meet here.

This model was later modified for a moving obstacle called spiral wave re-entry (Ikeda et al., 1996). A spiral wave is a two-dimensional wave of excitation emitted by a self-organizing source of functional re-entrant activity, termed a rotor (Ikeda et al., 1996). Spiral waves have been subsequently observed in the chemical reaction of Belousov–Zhabotinsky and in the thin slices of epicardial muscle using a potentiometric dye (Tse, 2016). The phase singularity is excitable part of myocardium but remains nonexcited, and therefore acts as a functional obstacle around which the spiral wave can circulate (Ikeda et al., 1996). The sites in front of

the wave are excited faster than those behind the wave. This may be the underlying mechanism of torsade de pointes (Dessertenne, 1966), in which the periodic torsion of the QRS axis has been attributed to two widely separated foci discharging at different frequencies.

1.4.3 Reflection

The arrhythmogenic events occur also without an obstacle and reflection is one of them. It was originally observed in canine Purkinje fibers (Wit et al., 1972). It these preparations AP traveling in the forward direction was sometimes followed by a return potential that travelled in the backward direction. These events happen when the initiating impulse reached an area of depressed excitability. To illustrate this type of re-entrant arrhythmias a sucrose gap model was developed (Figure 1.11; (Antzelevitch et al., 1980)). It included canine Purkinje fibres where a central unexcitable gap was produced by an ion-free isotonic sucrose solution. Electrical stimulation at the proximal segment elicits an AP. This excitation is transmitted across the gap to the distal segment after a delay. However, AP cannot be activated in the middle part of the tissue because the extracellular space is ion-free. The excitation induces a passive spread of the local current (electrotonic current) across the low-resistance intracellular pathway. When depolarization reaches threshold, an AP is initiated in the distal segment. This, in turn, generates electrotonic currents in the retrograde direction. With a further delay, the proximal region can be excited again when it has recovered from refractoriness. This results in a return extrasystole, completing reflection (Antzelevitch et al., 1980). Successful segment-type reflection requires a balance between the conduction delay and the cellular membrane excitability (Tung, 2011). Segment-type reflection has been demonstrated in isolated atrial (Lukas and Antzelevitch, 1989) and ventricular (Rozanski et al., 1984) tissues.

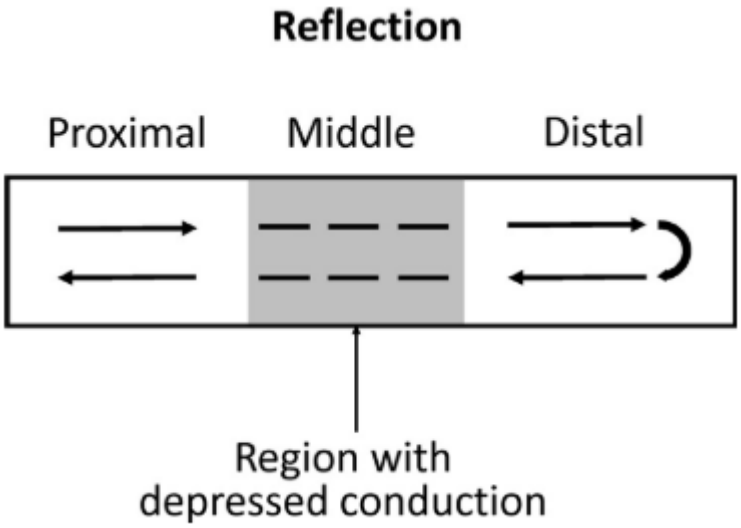

Figure 1.11. Illustration of reflection process. AP is elicits by stimulation of the proximal segment. The middle region is ion free and AP conduction there is slow. But it involves electrotonic current that through the cells. It reaches the distal area after delay and originates another AP. From (Tse, 2016).

Another re-entrant arrhythmia mechanism that does not depend on the obstacle is the Phase 2 arrhythmia (Di Diego and Antzelevitch, 1993). This type of events occurs in the settings of high heterogeneity in AP repolarization when the electrotonic currents can flow from sites with longer APDs to sites with shorter APDs. These currents could reactivate the AP when the latter sites have recovered from refractoriness (Dias et al., 2002). Phase 2 arrhythmias were shown in Brugada syndrome, where the resulting premature beat initiates spontaneous polymorphic VT (Moe, 1975). Heterogeneity in AP repolarization between cardiac regions leading to phase 2 re-entry occurs following exposure to the sodium channel inhibitor flecainide and under conditions of raised Ca^{2+} concentration and ischemia (Lukas and Antzelevitch, 1996).

Thus arrhythmogenic activity happens when a delicate balance between cell and tissue excitability and refractoriness is lost; understanding the mechanisms of arrhythmogenesis is very important for the interpretation of the experimental data.

1.5 Structural organisation of ventricular cardiomyocytes

Ventricular myocytes represent a rod shape cells with a regular striations and one/two nuclei (Figure 1.12). Cardiomyocytes connect with each other by the intercalated disks, where the gap junctions are located. These junctions are small channels that allow cells to exchange ions and small cytosolic molecules, like Na^{+} and Ca^{2+} and transmit the signals (Goodenough and Paul, 2009). Single human and rat ventricular myocytes have highly organized surface and internal structures (Lyon et al., 2009). The structure of myocytes is maintained by cytoskeleton which is composed of rigid filaments of actin and desmin and microtubules build up by α and β tubulin (Hein et al., 2000). Cardiomyocyte contractile proteins are organized in repeating functional units called sarcomeres. The length of each sarcomere is around 2 microns. Sarcomeres are delimited by Z-lines (Solaro and Stull, 2011).

The surface of cardiomyocytes has a complex pattern of Z-grooves, crests and T-tubule openings (Figure 1.12). Z-grooves presents a drains in surface membrane of cardiomyocytes separated by a dome-like structures, called crests (Gorelik et al., 2006).

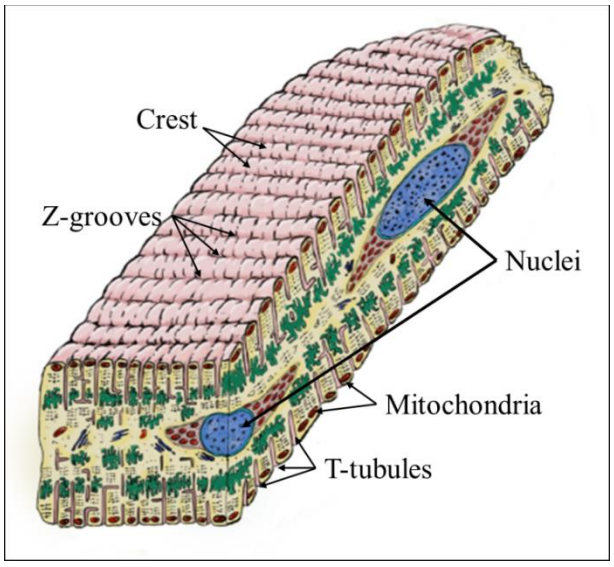

Figure 1.12. Structural organisation of ventricular myocyte. It shows a well- organized surface topography and repetitive sarcomeres Modified from (Sanchez-Alonso et al., 2019).

1.5.1 Transverse-axial tubular network

Plasma membrane of ventricular myocytes is folded into continuous invaginations through the cell interior, named transverse-axial tubular network (TAT) (Soeller and Cannell, 1999). The complex three-dimensional morphology of the TAT system in living rat ventricular cardiomyocytes was first revealed by Soeller and Cannell by using an extracellular dye solution together with two-photon microscopy (Soeller and Cannell, 1999). TAT network of ventricular myocytes predominantly consists of T-tubules, which are located close to the Z-lines between sarcomeres (Brette and Orchard, 2003). Axial or longitudinal tubules (A-tubules) are presented at between Z-lines and usually less frequent compared to T-tubules in ventricular myocytes (Asghari et al., 2009; Swift et al., 2012). Organisation and density of TAT network in cardomyocytes is highly dependent on the host heart rate. In rodents and other small animals, who has a high heart rate, myocytes possess a higher density of TAT network as compared to larger species who shows a relatively slower heart rate and less dense TAT network (Brette and Orchard, 2003; Louch et al., 2010; Song et al., 2005).

A high density of TAT network is important to maintain a rapid and synchronous Ca^{2+} release across the cell (Brette et al., 2005; Bu et al., 2009). This is achieved via a close proximity of TAT membrane to specialized terminals of SR, called junctional SR. The fine adjustment of the cardiomyocyte membrane forms a tight coupling between LTCC and RyR2 clusters, called dyadic couplons (Scriven et al., 2002). Among different parts of surface membrane, the coupling between LTCC and RyR2 was found predominantly within the TAT network in ventricular myocytes (Chen-Izu et al., 2006; Mackenzie et al., 2004).

Moreover, TAT network provides a regulatory function of ECC. TAT network accumulates a number of molecules that are important for Ca^{2+} signalling such as LTCC, NCX, β-2 adrenergic receptors (β_2AR), protein kinase A (PKA), and other regulatory proteins (Brette and Orchard, 2003). Thus, TAT network provides a rapid regulation of a cell contraction and relaxation (Richards et al., 2011). The TAT network furthermore limits the diffusion of ions which can enter into them and thereby establishes a microenvironment with relatively constant ion content (Brette et al., 2005).

1.5.2 Plasticity of TAT network

TAT network organisation varies in different type of myocytes, and depends on age and species (Jones et al., 2018). In contrast to adult ventricular cardiomyocytes with high TAT network organisation, neonatal cells lack a TAT network (Richards et al., 2011). The mechanisms responsible for the development of the TAT network and its maintenance during adulthood are not yet fully understood. An array of various proteins has been shown to participate in TAT formation and organisation. Caveolae, that are flask shape invaginations in sarcolemma membrane, are believed to be progenitors for T-tubule formation (Harvey and Calaghan, 2012; Wong et al., 2013; Woodman et al., 2002). T-tubular maturation was shown to coincide with the expression of junctophilin 2 (JPH2) (Munro and Soeller, 2016; Ziman et al., 2010). This protein anchors T-tubular membrane to junctional SR membrane producing stabilization of dyadic complexes. There is an evidence showing a role of JPH2 in the orientation of tubules (Pinali et al., 2013). Knock in of JPH2 in mouse showed an immature TAT network organisation (Chen et al., 2013; Reynolds et al., 2016). Another key protein for TAT network formation is amphyphisin-2 (BIN1) which can participate in tubule growth and intricate membrane folding (Hong et al., 2014). Telethonin (T-Cap) that is involved in sarcomere assembly, was proposed to play a role of mechanical stress transducer and load dependence in TAT network (Ibrahim et al., 2013).

Flexibility of TAT network is highly studied on diseased myocytes. TAT remodelling was studied in a big array of aetiologies, such as spanning myocardial infarction (Frisk et al., 2014; Louch et al., 2006; Lyon et al., 2009; Sanchez-Alonso et al., 2016; Swift et al., 2012; Wagner et al., 2012), aortic stenosis (Ibrahim et al., 2013; Pinali et al., 2013; Wei et al., 2010), heart failure (HF) induced by fast pacing (Balijepalli et al., 2003; He et al., 2001), hypertension (Singh et al., 2017; Song et al., 2006), chronic ischemia (Heinzel et al., 2008), and diabetes (Stølen et al., 2009; Ward and Crossman, 2014). Most of these studies reported a reduced TAT density and regularity in diseased myocytes, which sometimes is accompanied by an increased density of axial tubules. Resent works with more precise view on TAT structure revealed T-tubular swelling and fusion in failing LV myocytes (Pinali et al., 2013; Seidel et al., 2017; Wagner, 2012). Moreover, similar reduction of TAT

network organisation has been shown during right ventricular failure (Caldwell et al., 2014; Prins et al., 2017; Xie et al., 2012) and in the atria during heart failure (Dibb et al., 2009) and atrial fibrillation (Lenaerts et al., 2009). All these studies indicate a possible existence of the similar mechanism of TAT network remodelling in a variety of cardiac pathologies across the chambers of the heart.

1.5.3 Caveolae

Another important structure of cardiomyocyte sarcolemma membrane is caveolae. These lipid structures are flask shaped invaginations of the sarcolemma, enriched in cholesterol and glycosphingolipids. These nanostructures have a width around 50 to 100 nm, an can be clearly visualised in the electron microscopy images (Wright et al., 2014). In cardiomyocytes without a TAT network, like neonatal and some atrial myocytes, caveolae structures likely serve as a primary place of excitation-contraction coupling (Wong et al., 2013). They organise signalling microdomains in the sarcolemma membrane by attracting the palmitoylated transmembrane proteins, such as LTCC, β_2AR, adenyl cyclases (AC) and the α-subunit of G-proteins (Balijepalli et al., 2006; Brown and Borutaite, 2007). Through the accumulation of the signalling proteins, caveolae can modulate Ca^{2+} handling and β_2AR signalling (Bossuyt et al., 2006; Calaghan and White, 2006). Moreover, caveolae are involved in the stretch-induced regulation of different mechanosensitive ion channels such as volume regulated chloride channels (Egorov et al., 2019; Petroff et al., 2001).

The flask-like structure of caveolae serves as an ion reservoir, maintained by structural proteins called caveolins. Three isoforms of caveolins were found in different tissues. Caveolin 3 (Cav3) is predominantly expressed in cardiac, skeletal and smooth muscle cells (Song et al., 1996). Cav3 is important for maintaining cardiac function, as murine model of the Cav3 knockout develop a pronounced HF (Woodman et al., 2002).

1.6 L-type Ca^{2+} channels

Among other ion channels participating in the generation of AP in the heart, the voltage-gated L-type Ca^{2+} channels constitutes a major pathway for Ca^{2+} entry into

cardiac cells. The Ca^{2+} entry through the LTCC shapes the plateau phase of the ventricular AP and is required for the contraction as it induces CICR.

1.6.1 Classification of voltage-gated Ca^{2+} channels

Voltage-gated calcium channels (VGCCs) react to changes in the transmembrane potential. According to the activation voltage threshold, all VGCCs can be divided into high voltage-activated (HVA) Ca^{2+} channels, which include L-type, N-type, R type and P/Q type, and low voltage-activated (LVA) Ca^{2+} channels, such as T-type Ca^{2+} channels.

In the cardiac myocytes, there are two main types of VGCCs: L- type and T-type. L-type Ca^{2+} channels (LTCC, I_{CaL}) are characterized by a large conductance (25 pS in 110 mM Ba), long lasting openings, sensitivity to dihydropyridines (DHPs) and activation at more positive membrane potentials than T-type. In contrast, T type Ca^{2+} channels (I_{CaT}) have different characteristics: tiny conductance (8 pS in 110 mM Ba), insensitivity to DHPs and more negative potentials of activation. The relative amount of I_{CaL} and I_{CaT} varies among different types of cardiac myocytes. In normal ventricular myocytes I_{CaT} is almost absent, but it can become more prominent in hypertrophy. For example, Nuss and Houser reported a substantial I_{CaT} expression in hypertrophied cat ventricular myocytes (Nuss and Houser, 1993).

1.6.2 Subunit composition of VGCCs

Physiological and pharmacological properties of VGCCs are determined by the pore-forming α1 subunits. Three clusters of α1 subunits were named as Ca_v1 ($Ca_v1.1$, $Ca_v1.2$, $Ca_v1.3$ and $Ca_v1.4$), Ca_v2 and Ca_v3, which correspond to L-type, non-L-type (HVA) and LVA or T-type channels, respectively (Catterall et al., 2005). The pore-forming subunit is associated with the accessory subunits $Ca_v\beta$ (4 different isoforms), $Ca_v\alpha_2/\delta$ (4 different isoforms $Ca_v\alpha_2/\delta$ 1-4) and γ (8 isoforms) (Catterall, 2000). All these axillary subunits play important roles in the regulation of VGCCs activity and trafficking.

Schematic of LTCC channel subunit organisation is presented in Figure 1.13. The pore is formed by α subunit. β subunit interacts with a cytosolic conserved motif located at I-II loop of α subunit (Pragnell et al., 1994). α2 subunit is located extracellularly and is linked to δ subunit via a disulfide bridge which is connected

to the pore-forming subunit (De Jongh et al., 1990). The γ subunit consists of 4 transmembrane domains with intracellular N- and C- tails. Although the function of γ subunit in the heart is not determined; the expression of γ 4, 6,and 8 was detected at mRNA level (Yang et al., 2011).

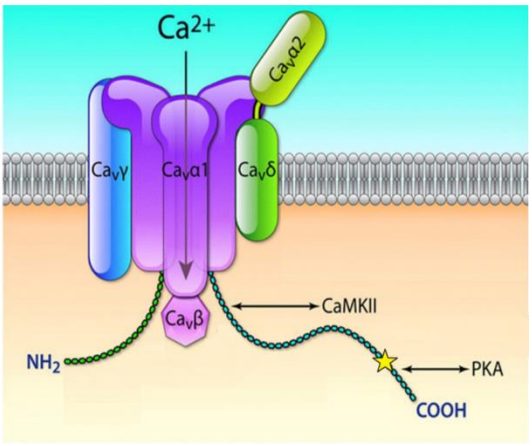

Figure 1.13. L-type calcium channel structure. The main pore-forming α1 and auxiliary β, α2δ and γ subunits integrated in membrane phospholipid bilayers. From (Rougier and Abriel, 2016).

1.6.3 Different roles of LTCC subunits

The Ca_vα1C subunit constitutes the pore of the calcium channel and mediates the influx of calcium ions into the cell upon membrane depolarization. Structural analysis of Ca_vα1 subunits revealed that the pore contains four repeated domains (I – IV), each of them includes six transmembrane regions (S1-S6) and a pore loop (Durell et al., 1998). The voltage sensor is located at S6 region which contains several positively charged residues. S3 contain a few charged residues and may play a role in the charge-charge interaction with S4. Ion selectivity is produced by the loop between S5 and S6 regions that dangles into the outer mouth of a channel.

The distal C-terminal part of the α1C subunit has been shown to have an auto-inhibitory effect on the calcium current (Crump et al., 2013; De Jongh et al., 1996). This subunit also included a phosphorylation site for PKA (Fuller et al., 2010; Mitterdorfer et al., 1998). However, this site, Ser1928, is located in the C-terminal portion of α1C that is cleaved off the full-length protein in *vivo* (Hell et al., 1996). But a minor expression of the full-length α1C was also observed in vivo, and biochemical and functional evidence indicates that the cleaved C-terminal fragment

remains tethered to the channel (Gao et al., 1997; Gerhardstein et al., 1999). Nevertheless to what extent PKA phosphorylation occurs in *vivo* of α1C remains unclear.

Although the α1 subunit largely determines the current gating, the auxiliary subunits affect the voltage-dependence, the rate of activation and the kinetics of current inactivation of the channel (Birnbaumer et al., 1998; Lacerda et al., 1991).

There are 4 β subunit genes (β_1-β_4) described, and the predominant cardiac isoform is β_2. All 4 types of beta subunits of LTCC enhance the L-type Ca^{2+} current when they are co-expressed with $Ca_v\alpha$ in heterologous expression systems. They modulate the kinetics of channels activation and inactivation, without affecting the channel conductance (Kamp et al., 1996; Singer et al., 1991). Moreover, $Ca_v\beta$ is involved in the regulation of LTCC by protein kinases, G proteins and ubiquitin ligases (Buraei and Yang, 2010; Gerhardstein et al., 1999). Three PKA phosphorylation sites (Ser459, Ser478, and Ser479) were also determined in this β_2 subunit (Gerhardstein et al., 1999) and two of them (Ser478, Ser479) were shown to contributes to channel regulation by PKA (Bünemann et al., 1999). Sites for PKC phosphorylation were found in both α1C and β_2 subunit and the expression of both α1C and β_2 was required for PKC induced reduction of I_{CaL} (Puri et al., 1997). Another important role of $Ca_v\beta$ is the channel drugs sensitivity. For example, the effective concentration of verapamil for cells $Ca_v1.2$ co-expressed with $Ca_v\beta$ was 14 times lower concentration than for the cells with $Ca_v1.2$ expressed alone (Lacinová et al., 1995). $Ca_v\beta$ also plays an important role in $Ca_v1.2$ trafficking to the plasma-membrane (Jiang et al., 2005; Josephson and Varadi, 1996) as well as channel internalization (Gonzalez-Gutierrez et al., 2007). Moreover, it was shown that different $Ca_v\beta$ subunits target LTCC to the specific subcellular domains (Foell et al., 2004). For example, $Ca_v\beta_1$, $Ca_v\beta_2$ and $Ca_v\beta_3$ isoforms localize predominantly in T-tubule membrane, while the expression of $Ca_v\beta_{1a}$ and $Ca_v\beta_4$ was found at surface membrane (Foell et al., 2004).

Several studies have shown that $Ca_v\alpha2/\delta$ has an effect on $Ca_v\alpha_{1C}$ and $Ca_v\beta$ channel trafficking. Co-expression of $Ca_v\alpha_{1C}$ with α_2/δ_1 in oocytes substantially increased the amount of α1 subunit protein associated with the plasma membrane (Shistik et

al., 1995). Moreover, co-expression of $Ca_v\alpha_{1C}$ and $Ca_v\beta$ with $\alpha_2\delta_1$ was found to increase the I_{CaL} and accelerate the activation and deactivation kinetics (Felix et al., 1997; Klugbauer et al., 2003). Interestingly, animals studies with $Ca_v\alpha_2/\delta1$ subunit knockout demonstrated a reduced basal myocardial contractility and relaxation along with decreased I_{CaL} peak current amplitude (Fuller-Bicer et al., 2009).

The $Ca_v\gamma$ subunit effects on $Ca_v1.2$ are incompletely elucidated. All 4 $Ca_v\gamma$ subunits that found in the human heart can differentially modulate the LTCC function when they are co-expressed with the $Ca_v\beta_{1b}$ and $Ca_v\alpha_2/\delta_1$ subunits in HEK-293 cells, altering both the activation and inactivation properties (Yang et al., 2011). The functional effects of $Ca_v\gamma$ on LTCC are dependent on the $Ca_v\beta$ subunit and the presence of $Ca_v\alpha_2/\delta_1$ subunit (Yang et al., 2011).

1.6.4 Properties and regulation of LTCC

The physiological conditions such as ion composition and membrane potential can significantly alter the amplitude and kinetics of I_{CaL}. In this chapter, a brief summary of the important LTCC properties is presented.

One of the important features of LTCC is Ca^{2+}-dependent inactivation (CDI), which provides a feedback control to limit the Ca^{2+} entry inside the cell. When the myocyte possesses a relatively high Ca^{2+} load and a large Ca^{2+} transient, CDI limits further Ca^{2+} influx. Conversely, when the myocyte's $[Ca^{2+}]$ is low and SR Ca^{2+} release is small, there is less CDI and enhanced Ca^{2+} entry which increases SR Ca^{2+} content. It was shown that CDI occurs through Ca^{2+} binding to calmodulin (CaM). CaM tethers to the $Ca_v1.2$ C- terminus. CaM activates by Ca^{2+} changes its position in C-terminus of $Ca_v1.2$, thereby accelerating I_{CaL} inactivation (Pitt et al., 2001).

On another side, LTCCs undergo a frequency-dependent facilitation (CDF). It was observed that with increased frequency of voltage-clamp pulses I_{CaL} showed a higher amplitude and prolongation of inactivation (Hryshko and Bers, 1990; Lee, 1987; Mitra and Morad, 1986). This increase of I_{CaL} was shown to be Ca^{2+}-dependent and the effect is modulated through the Ca^{2+}/calmodulin-dependent protein kinase II (CaMKII)- dependent phosphorylation (Yuan and Bers, 1994; Zygmuntt and Maylie, 1990). For the effective CDF, CaMKII should be closely localized to LTCC, so CDF does not happen equally throughout the sarcolemma

(Hryshko and Bers, 1990). The physiological impact of CDF becomes more important at high frequencies of contraction where it competes for the influence on I_{CaL} with CDI. These two effects have different speeds of activation. CDI responds rapidly (during the same beat), while Ca^{2+}-dependent activation occurs more slowly (from beat to beat). Phosphorylation sites of CaMKII was found in both α1C C-terminus and β_2 subunit (Pitt et al., 2001). Overexpression of CaMKIIδC in transgenic mouse myocytes and in rabbit myocytes produces higher I_{CaL} with a slower inactivation time (Kohlhaas et al., 2006; Maier et al., 2003).

β-adrenoreceptor stimulation produces a substantial increase in I_{CaL} (Reuter, 1967). The effect is mainly modulated through PKA stimulation (Mcdonald et al., 1994). PKA phosphorylation of $Ca_v1.2$ produces a two- to four time increase in basal I_{CaL} and shifts the voltage-dependence of channel activation and inactivation to more negative potentials (Hartzell, 1988; Tsien et al., 1986). Single channel studies showed that PKA phosphorylation significantly prolongs the open time of the channel without altering unitary conductance of the channel (Cachelin et al., 1983; Yue et al., 1990). PKA is anchored in close vicinity of the LTCC via "A-kinase anchoring protein" AKAP79 (Gao et al., 1997). The importance of this localization could be demonstrated by loss of the PKA-dependent activation of I_{CaL} in heterologous expressing systems (Zong et al., 1995).

One of the characteristic features of LTCC is their sensitivity to DHPs, such as nifedipine, amlodipine, nitrendipine, BayK8644, azidopine, iodopine. Most of these DHPs inhibit I_{CaL} and are used as LTCC antagonists. At the same time, some of them, such as BayK8644, CGP28392, benzoyl pyrrole are known LTCC agonists as they increase the whole cell LTCC current. The effect of LTCC agonists is produced by prolongation of the single-channel opening duration with a slight modification of single-channel conductance (Brown et al., 1984; Hess et al., 1984; Kokubun and Reuter, 1984). Thus, the application of agonistic DHPs results in long and large Ca^{2+} tail currents attributable to the abrupt increase in electrochemical driving force upon repolarization (Tsien et al., 1986). These could contribute to EADs during rapid depolarizations (January and Riddle, 1989).

To understand the LTCC behaviour Hess et al. proposed a model of three states or modes (Figure 1.14; (Hess et al., 1984)). In this model the bust of LTCC activity in one mode is faster than switching between modes. Under physiological conditions LTCC can be quiescent for many seconds (mode 0), switch to the mode 1 for a few seconds and return back to mode 0. Mode 1 has a short opening time. The mode 2 activity with very long LTCC openings is very rare in normal conditions (Hess et al., 1984). Binding of BayK8644 to the channel stabilizes the channel in mode 2, but the channel can still occur at mode 1. On the other hand, binding of antagonistic DHPs promotes channel to occur in mode 0. This state is characterized by channels being unavailable to open (Yue et al., 1990).

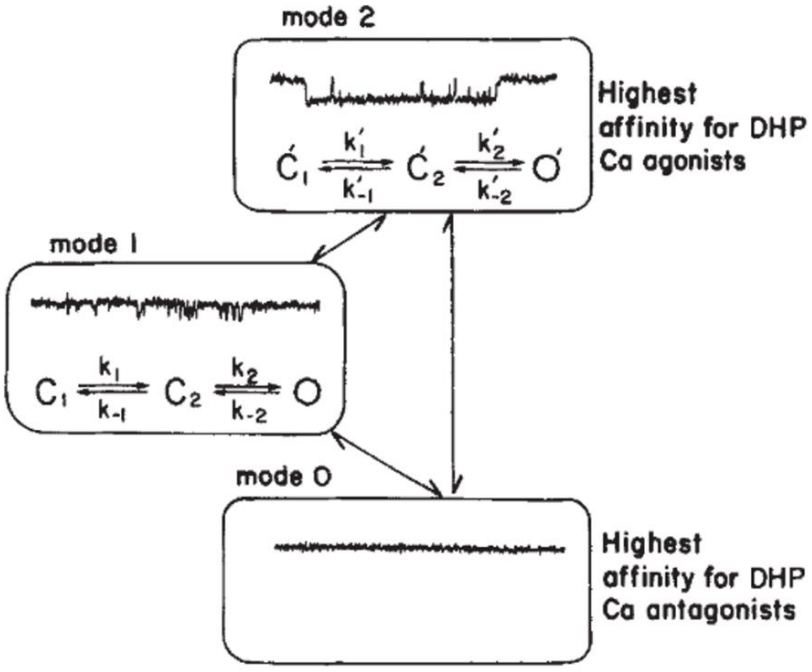

Figure 1.14 Model of the LTCC gating modes. The channels could exist in one of the three modes. The transition between modes is very slow compared to the gating within the mode. From (Hess et al., 1984).

1.6.5 Spatial localisation of LTCC in cardiac myocytes

Immunochemical studies revealed that LTCCs are not equally distributed in sarcolemma membrane in ventricular cells (Brette and Orchard, 2003; Scriven et al., 2000). Approximately 80% of all LTCCs are located in T-tubules in close

proximity to the calcium sensing and release units of SR (Smyrnias et al., 2010). Until recently, spatial distribution of LTCCs on the cellular membrane could be assessed only by immunolabelling or electron microscopy immunogold-labelling techniques. These methods lack functional information of the channel behaviour. Interesting approach was applied to understand the relative impact of T-tubular and surface membrane anchored LTCCs. Bryant et al. measured LTCC activity were performed in the normal cardiomyocytes before and after detubulation, induced by formamide treatment (Bryant et al., 2015). Such treatment induces a disconnection of TAT membrane from the surface sarcolemma. They showed that the density of I_{CaL} in T-tubules was around 3.2 times higher than the density of I_{CaL} originated from the detubulated part of surface membrane (Bryant et al., 2015).

Recently, the development of super-resolution patch clamp technique allowed a direct investigation of spatial clustering of ion channels, such as LTCCs, and functional analysis of the channels in relation to their localization (Bhargava et al., 2013; Novak et al., 2013). This methodology presents a combination of scanning ion conductance microscopy with the cell-attached configuration of the patch clamp technique (Figure 1.15; (Bhargava et al., 2013; Gu et al., 2002)). Recently, "smart patch-clamp technique" allowed to analyse a single channel density via measurement the chance to get the channel in the patch (occurrence). Bhargava et al showed a 30% occurrence of LTCC occurrence in T-tubule and less than 10% - on the surface sarcolemma membrane (crest) in rat LV myocytes (Figure 1.15C; (Bhargava et al., 2013)). This 3.5 higher prevalence of LTCC in T-tubule versus surface membrane was similar to the results observed by Bryant et al. in whole cell I_{CaL} experiments (Bryant et al., 2015).

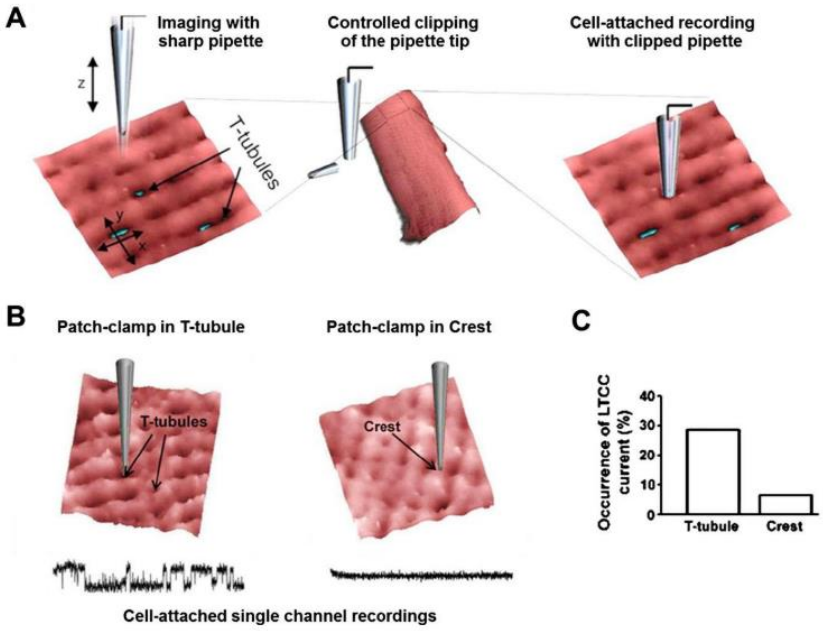

Figure 1.15 Schematic of the smart patch clamp technique. A sharp high resistance pipette used to resolve the topographical structure of the cardiomyocytes. The pipette is moved to a cell-free area on the dish and the fall rate is increased to clip the pipette tip. The pipette is then returned to the surface of choice, and patch clamp can be performed with a wider pipette tip. (B) Illustration of recordings of LTCC obtained at T-tubule (left panel) and sarcolemma membrane (crest, right panel). (C) Chance of recording of LTCC in patch represents as LTCC occurrence at T-tubules and crest in rat adult ventricular cardiomyocytes. From (Bhargava et al., 2013).

As most of the LTCC are located in the TAT membrane, the development and organisation of TAT network plays a crucial role in the distribution of LTCC across the membrane. In neonatal rat ventricular myocytes, that lack T-tubular structures, the chance of finding the LTCC current on sarcolemma membrane is 30% (Bhargava et al., 2013), almost the same as in T-tubule of adult ventricle. Interestingly, in rat atrial myocytes which have a disperse or almost absent TAT network, almost equal chance exists of obtaining the LTCC current at the T-tubule and at the crest (Glukhov et al., 2015). Moreover, loss of TATS in failing myocytes during HF was found to be associated with the re-distribution of LTCC from a predominant T-tubular localization to crests areas of surface sarcolemma (Sanchez-Alonso et al., 2016). The occurrence of single LTCC in T-tubules and crest areas

became similar after HF (Sanchez-Alonso et al., 2016) and the density of I_{CaL} was similar in these two membrane regions (Bryant et al., 2015).

Smart patch clamp technique allows not only investigating the spatial distribution of LTCC but also revealing functional properties of LTCC as well as local control of LTCC activity. For example, an unchanged whole cell $I_{Ca,L}$ was observed in HF conditions by many groups (Ibrahim et al., 2012; Louch et al., 2004). It has been found that crest subpopulation of LTCC in failing rat and human myocytes undergo phosphorylation by CaMKII and this subpopulation of LTCC could trigger abnormal electrical activity in failing hearts (Sanchez-Alonso et al., 2016). In failing atrial cells T-tubule-specific reduction of LTCCs conductance occurred, whereas crest channels remain unchanged (Glukhov et al., 2015). All these data showed the importance of investigation of microdomain-specific localization and functioning of LTCC. There is a lack of knowledge of LTCC localization in RV myocytes.

1.6.6 Functional roles of LTCC subpopulations.

It was shown that groups of LTCCs localized in different microdomains play a specific function in myocyte homeostasis (Best and Kamp, 2012). Subpopulations of LTCC and their roles are schematically presented in Figure 1.16. The channels that form dyads or couplons and participate in ECC represent the subpopulation of the LTCC which is the most crucial for cell contraction. Interestingly, only 75% of the dyadic LTCC were found in the TAT network, the other 25 % of the dyads are located at the surface membrane (Brette and Orchard, 2003; Scriven et al., 2010). Those LTCCs located at the surface membrane are believed to play a role in SR Ca^{2+} loading (Kawai et al., 1999).

Among all the LTCC located both in T-tubules and surface sarcolemma, there is a big group of channels that is anchored to caveolae. A strong colocalization was shown between $Ca_v1.2$ and Cav3 (Balijepalli et al., 2006; Cavalli et al., 2007; Shibata et al., 2006). Caveolae membrane accumulates several important signalling proteins such as G-protein coupled receptors, AC and PKA (Kamp and Hell, 2000), so it becomes a site of signal transduction and its regulation. Disruption of caveolae

leads to reduction of basal I_{CaL} and the loss of β_2AR-dependent Ca^{2+} current augmentation (Bryant et al., 2014).

Recently, a cleaved $Ca_v1.2$ C-terminus was found in the nucleus of cardiac myocytes, where it autoregulates CACNA1C transcription (Schroder 2009). It was hypothesized that different β subunits of LTCC could promote changes in the LTCC localization. For example, in ventricular myocytes, β4 fused to GFP showed a significant localization of in the nucleus; however, the significance of this pathway is currently unclear (Colecraft et al., 2002).

Moreover, it was proposed that a specific pool of LTCC is responsible for Ca^{2+}-dependent signal transduction to nucleus in the hypertrophic cardiomyocytes. The mechanism involves β_1AR, CaM and CaMKII which activates a number of hypertrophic transcriptional pathways (Maier and Bers, 2002).

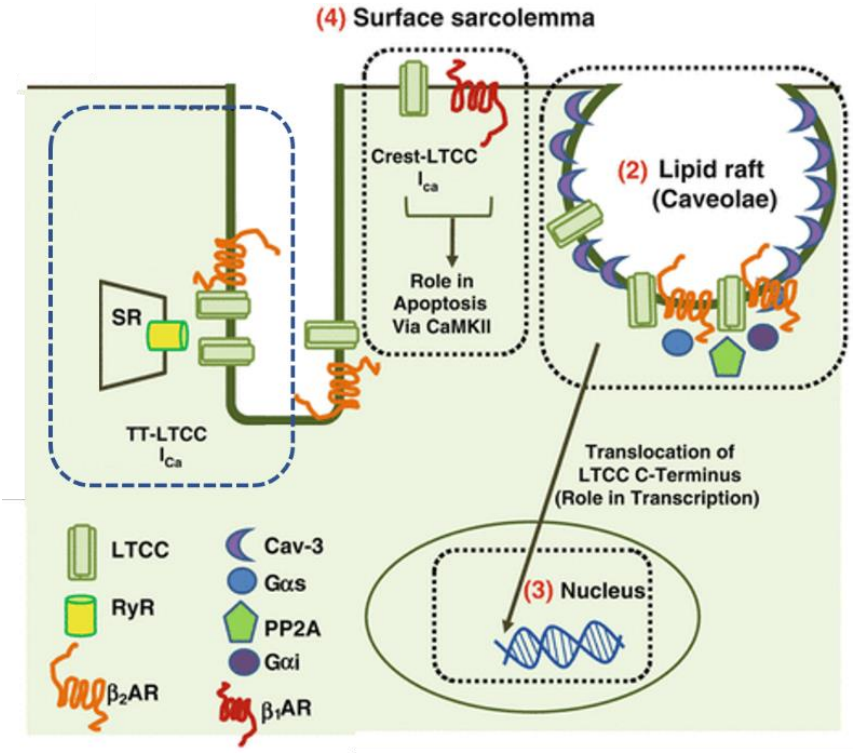

Figure 1.16 Subpopulations of LTCCs. Within T-tubules, LTCCs form dyadic junctions with ryanodine receptors (RyR2) that stay in the sarcoplasmic reticulum (SR). Caveolae is housed LTCC, β_2ARs, adenylyl cyclase (AC), protein kinase A (PKA), and A-kinase anchoring proteins (AKAPs) (2). These specialized domains contribute to cAMP production and signal transduction in cellular processes. Cleaved C-terminus of LTCCs can

translocate to nucleus and can act as a transcription factor (3). Non-caveolae LTCC mainly couple with ß1ARs which can induce CaMKII mediated apoptosis (4). From (Best and Kamp, 2012).

1.7 Sarcoplasmic reticulum Ca^{2+} release and sequestration. Role of Ryanodine receptors.

The main Ca^{2+} release channels involved in Ca^{2+} release from sarcoplasmic reticulum (SR) are represented by the ryanodine receptors (RyR) (Otsu et al., 1990) and inositol 1,4,5-triphosphate receptors (IP3Rs) (Nixon et al., 1994). IP3 receptors are involved in Ca^{2+} cycling, but their role in ECC is less clear (Borgatta et al., 1991). This section will focus on the structure and function of RyR.

1.7.1 RyR structure

RyR are called so due to their specific binding to ryanodine. This plant alkaloid was used to purify the RyRs from skeletal (Inui et al., 1987) and cardiac muscle (Lai et al., 1988; Inui et al., 1987). Three isoforms of the RyR have been identified. RyR1 was predominantly found in skeletal muscle cells with a lower expression present in smooth muscle cells, cerebellum, testis, adrenal gland, spleen, and ovary. RyR2 is the most abundant in the heart, lung, and brain (Nakai et al., 1990; Otsu et al., 1990). RyR3 is found in the brain, spleen, heart, and testis (Hakamata et al., 1992).

The RyRs have a molecular weights ~2260-kDa. They are present in homotetrameric complexes consisted of four ~565-kDa subunits. RyRs have large N-terminal cytoplasmic domains that modulates the gating of the channel pore located in the C-terminus. Electron microscopy studies showed the overall structure of the receptor (Figure 1.17). Shape of the complex resamples a mushroom with a large cytoplasmic cap, representing ~80% of the volume and the leg crossing the SR membrane. The dimensions of the head are ~280 x 280 x 120 Å and are much larger than the size of the transmembrane part of the channel (~120 x 120 x 60 Å) (Wagenknecht et al., 1989). These two major parts are connected via four thick columns. The head part represents not a rigid block but cavities filled with solvent. These structures allow the modulation of RyRs gating by interaction with solvent, small molecules and protein modulators. The corners of the cytoplasmic area are called “clamps”. They undergo conformational changes during openings and closes of RyR2 and participate in intermolecular interactions with close RyRs or modulators (Samsó et al., 2009; Serysheva et al., 2008; Wagenknecht et al., 1996).

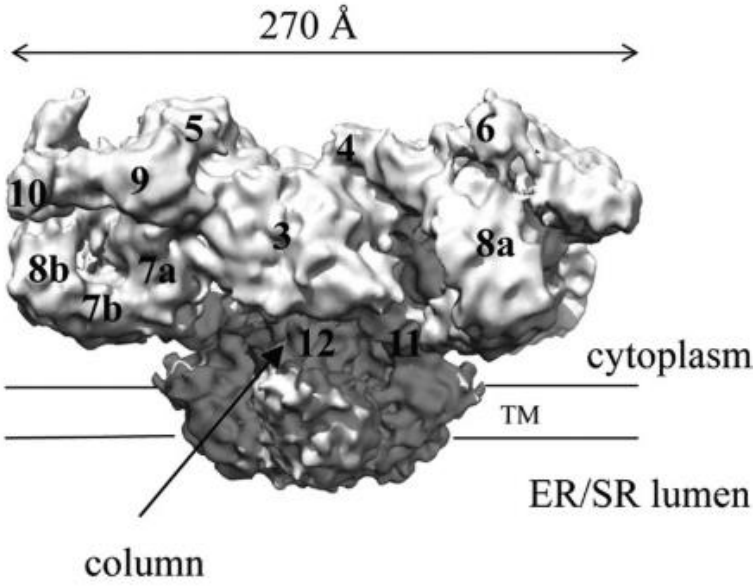

Figure 1.17 Schematic of RyR channel organisation. From (Lanner et al., 2010).

1.7.2 Regulation of RyR2

RyRs are approximately 10 times larger than the voltage gated Ca^{2+} and Na^{+} channels. In asymmetric solutions, RyR incorporated in a bilayer showed a high conductance of ~100 pS that is 5 times higher than the conductance of LTCC (Gao et al., 2000). N-terminal cytoplasmic domain serves as a scaffold for proteins and small molecules that regulates the function of RyR. Here is a summary of different regulators of RyR2.

First of all, Ca^{2+} has multiple direct effects on RyR2 and it can regulate receptor function through CaM and CaMKII. Ca^{2+} ions that reached the cytosolic part of RyR2, act as a ligand inducing opening of the receptor (Näbauer et al., 1989). Single channel experiments have shown that Ca^{2+} concentrations of ~1 µM are required to activate RyR2 openings (Meissner, 1986). In contrast to skeletal RyR, Ca^{2+}-induced inhibition of cardiac RyR2 requires a relatively high concentration of cytosolic [Ca^{2+}]. Luminal Ca^{2+}, which is stored in the SR, can stimulate Ca^{2+} release from the RyR2. Experiments on single RyRs have shown an increased Ca^{2+} release in the presence of cytosolic agonists such as ATP and caffeine (Sitsapesan and Williams, 1995; Smith et al., 1989; Xu et al., 1998). When SR [Ca^{2+}] is decreased, it inactivates RyR2 and contributes to the termination of CICR (Terentyev et al., 2002). The exact mechanism of SR [Ca^{2+}] RyR2 regulation is still unclear.

Another potent RyR2 regulator are Mg^{2+} ions. There are two proposed mechanism of Mg^{2+} regulation of RyR2. Mg^{2+} reduces the RyR2 open probability by competing with Ca^{2+} in high-affinity activation sites or it can bind to less selective low affinity Ca^{2+} sites to mediate Ca^{2+} inhibition (Laver et al., 1997; Meissner, 1986). The cytosol of most cells contains approximately 1 mM free Mg^{2+} and approximately 5 mM ATP, most of which is bound to Mg^{2+}. During pathology, such as ischemia, the concentration of ATP drops, so higher [Mg^{2+}] contributes to altered RyR2 Ca^{2+} sensitivity. RyR2 can be activated by ATP itself and some other adenosine nucleotides (ADP, AMP, cAMP, adenosine and adenine) (Meissner, 1984). Cardiac RyR2 are less effectively activated by ATP, than skeletal RyR1 (Xu et al., 1996).

Well known binding partners of RyRs are FK506-binding proteins (FKBPs) or castabins. Castabin2 (FRBP12.6) was co-purified with RyR2. It has a peptidyl-prolyl-*cis-trans* isomerase activity. Each monomer of RyR2 binds to one molecule of castabin2 (Jayaraman et al., 1992). Removal of castabin2 from RyR2 induces an increase in RyR2 open probability and appearance of subconductance states of the receptor. Thus, the role of Castabin2 in stabilizing the closed state of the RyR2 was proposed (Brillantes et al., 1994). It binds to a cytoplasmic portion of RyR close to the clamp regions and this binding induces significant conformational changes in the transmembrane domain (Marx et al., 1998). Moreover, castabin2 can be important for the oligomerisation of RyR2 monomers and interaction between tetramers (Brillantes et al., 1994; Kaftan et al., 1996). Castabin2 deficiency results in cardiomyopathy which mimics a human congenital heart disorder (Shou et al., 1998).

CaM is a 17 kDa Ca^{2+} binding protein that is ubiquitously expressed and binds to RyR2 at a 1:1 stoichiometry. Binding of CaM to RyR2 shifts the Ca^{2+} dependence of RyR2 activation to a higher [Ca^{2+}] and hence inhibits the receptor activity at all [Ca^{2+}] (Balshaw et al., 2001; Meissner and Henderson, 1987). Reduced affinity of CaM binding to RyR2 with PKA phosphorylation was shown in catecholaminergic polymorphic ventricular tachycardia (CPVT) mouse model increasing spontaneous local Ca^{2+} releases and arrhythmogenicity (Xu et al., 2010). In addition to CaM some other Ca^{2+} binding proteins were found in association with RyR2, including

calumenin, S100A1 and sorcin (Bers, 2004; Jung et al., 2006). However, their role in RyR2 functioning is still not fully clear.

Calcequestrin (CSQ) is a major Ca^{2+} buffering protein that is located in the SR. Due to a high binding capacity (40-50 $mol_{Ca^{2+}}/mol_{CSQ2}$) and low affinity, CSQ can not only buffer a large amount of Ca^{2+}, but can also release bound Ca^{2+} into the SR (Slupsky et al., 1987). At the same time, the free Ca^{2+} level inside the SR is maintained below the inhibitory level of the SERCA (Murphy et al., 2011). There are two genes encoding CSQ1 and CSQ2, with a predominant CSQ2 expression in the cardiac tissue. CSQ forms oligomers in the SR lumen and interacts with membrane associated proteins junctin and triadin. Together they modulate the activity of RyR2 (Beard et al., 2009; Györke et al., 2009). Mutation in CSQ2 gene were linked to exercise-induced cardiac death in CPVT, but not to alterations in cardiac contractility under basal conditions (Postma et al., 2002).

RyR activity can be strongly modulated by phosphorylation. The channel complex is associated with protein kinase A (PKA) and phosphatases PPI and PP2A. Interaction with kinases includes muscle mAKAP which is the target of PKA and phosphodiesterase 4D3 (PDE4D3) (Kapiloff et al., 2001). β-adrenergic stimulation induces PKA activation and RyR2 phosphorylation at Ser2808, that leads to a decrease in binding affinity of RyR to castabin2 and increases the open probability of the receptor (Doi et al., 2002; Wehrens et al., 2003). This is a part of "fight or flight" response to elevated stress. Chronic PKA activation in HF conditions can produce an incomplete channel closure and an enhanced Ca^{2+} leak during diastole. High diastolic Ca^{2+} leak depletes of SR Ca^{2+} stores and produces smaller Ca^{2+} transients (Wehrens et al., 2004). Association of RyR2 with PDE4D3 produces a local cAMP and PKA control loop to ensure a tight regulation of RyR2 activity (Lehnart et al., 2005).

Moreover, RyR2 association and regulation by CaMKII was shown (Witcher et al., 1991). Phosphorylation of RyR2 by CaMKII leads to an increased open probability of the receptor and an increased Ca^{2+} sensitivity (Wehrens et al., 2004). CaMKII activity is regulated by changes of intracellular [Ca^{2+}] through the CaM (Huke and Bers, 2007). It can phosphorylate Ser2808 and Ser2814 residues of RyR2 (Huke

and Bers, 2007; Witcher et al., 1991). In failing hearts, CaMKII -dependent phosphorylation of RyR2 was found to produce an enhanced Ca^{2+} leak with a reduction of SR Ca^{2+} load leading to arrhythmias and contractile dysfunction (Chelu et al., 2009; Curran et al., 2010).

RyR is an established redox sensitive channel. RyR redox state can induce both an activation (Stoyanovsky et al., 1997) or inactivation of the receptor gating(Boraso and Williams, 1994; Marengo et al., 1998). RyR has 80-100 cysteines per monomer and ~8 of them are ready for redox modifications by oxidation, nitrosylation, or alkylation by the redox active molecule glutathione (Xu et al., 1998; Zable et al., 1997). Production of reactive oxygen species promotes Ca^{2+} efflux from SR store with CaM – mediating effects on RyR2 (Kawakami and Okabe, 1998). High levels of reactive oxygen species and reactive nitrogen species are able to irreversibly modify and even damage proteins in cardiac ischemia-reperfusion injury (Ferdinandy and Schulz, 2003).

Caffeine increases both the RyR mean open time and open probability (Rousseau et al., 1987). This drug acts extremely rapidly and reversibly, which makes it a useful tool to study the SR Ca^{2+} loading. Application of 10 mM of caffeine induces a release of the full SR content, so it is widely used for SR content estimation (Bers and Perez-Reyes, 1999). Another important drug for RyR function is ryanodine, which has 2 binding sites on the receptor. At low concentrations (1nM- 10µM), it binds to a high affinity site and promotes RyR2 conduction at subconductance states (Rousseau et al., 1987) . At higher concentrations, (0.3-2 mM), it binds to a lower affinity site and induces a complete block of RyR2 (Rousseau et al., 1987). The binding of ryanodine is very slow and almost irreversible. The application of ryanodine to cells results in activation of a small fraction of RyR, and SR Ca^{2+} pump usually exceeds it to accumulate a higher SR Ca^{2+} content (Bers et al., 1987; Bers and Perez-Reyes, 1999).

1.7.3 Distribution of RyR2 in ventricle cardiomyocytes

Immunofluorescence studies of RyR2 from both fixed and live myocytes revealed a predominant localization of RyR2 along Z-lines (Figure 1.18, (Hiess et al., 2015; Jayasinghe et al., 2009; Soeller et al., 2007)). Only a small portion of RyR2 was

found between Z-lines, mostly on cell periphery. It was suggested to play a role in Ca^{2+} spread along the myofilaments (Subramanian et al., 2001).

Transversal tubules of TAT network in myocytes are highly colocalized with RyR2 (Hiess et al., 2015; Jayasinghe et al., 2010). Interestingly different types of myocytes can have a variable degree of TAT structure, but most of them have a highly regular organisation of RyR2 (Dries et al., 2013; Frisk et al., 2014; Hebisch et al., 2016). Differences in organisation of TAT structure and RyR2 indicate the presence of so called 'orphaned' RyRs along Z-line which do not colocalize with T-tubule (Figure 1.18; (Heinzel et al., 2008; Louch et al., 2006; Song et al., 2005)). Ca^{2+} release from these 'orphaned' RyRs is delayed, because they can't be activated by the Ca^{2+} release through the LTCC. Instead, their activation occurs via Ca^{2+} spread from the nearby RyRs (Frisk et al., 2014; Louch et al., 2006; Song et al., 2005). Thus, loss and reorganisation of TAT network occurred during the disease progression would promote the desynchronization and slowness of Ca^{2+} transients.

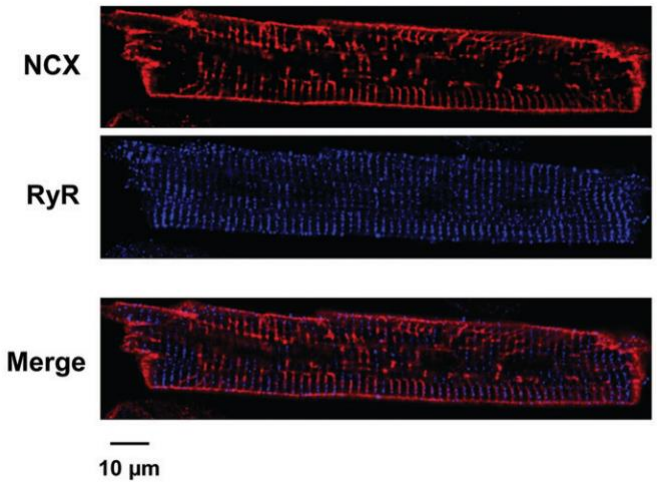

Figure 1.18. Example of a relative RyR2 alignment with TAT network in pig myocytes. A TAT system visualized by NCX antibody labelling, B) RyR2 signal, C. Merged signals. Obtained from (Dries et al., 2013).

1.7.4 Ca^{2+} sparks and Ca^{2+} transients

RyR2s are anchored to the SR membrane which makes patch-clamp investigations of their behaviour in live myocyte a very challenging approach. In contrary, optical methods with the Ca^{2+} sensitive dyes provides an easy and comprehensive way to

study the RyR2 functional behaviour (Cheng et al., 1993). Ca^{2+} sparks were firstly documented by Cheng et al., as a local, short lived Ca^{2+}- release events in cardiac tissue. These events can either occur spontaneously or be triggered by Ca^{2+} influx through the LTCCs (Cannell et al., 1995; Tsugorka et al., 1995). Ca^{2+} sparks are usually detected by the line-scan confocal imaging. The 3D illustration of Ca^{2+} spark activity is presented in (Figure 1.19, left panel). Ca^{2+} sparks are complex events with multiple factors affected their properties. One of the main determinants of Ca^{2+} spark behaviour is the frequency of sparks occurrence, which reflects the open probability of RyRs. The shape of the Ca^{2+} sparks is usually characterized by the amplitude, the width at half-maximum of amplitude (FWHM, Figure 1.19, top right panel), and the duration at half-maximum of amplitude (FDHM, Figure 1.19, bottom right panel). A typical cardiac Ca^{2+} spark may last for about 50 ms and have a width around 2 μm (Cheng et al., 1993). All the sparks parameters are tightly regulated. Moreover, Kolstad and co-authors suggested two additional parameters: spark mass can be calculated via multiplication of amplitude by FWHM and FDHM, and spark-mediated Ca^{2+} leak, can be calculated via multiplication of spark mass by frequency (Kolstad et al., 2018). These two parameters of Ca^{2+} sparks allow estimation of the amount of Ca^{2+} released thorough one spark.

The mechanisms underlying the spark formation are still not completely clear (Hoang-Trong et al., 2015). Most of the factors that can affect RyR2 behaviour, alter can influence the properties of the Ca^{2+} sparks (Bers, 2000).

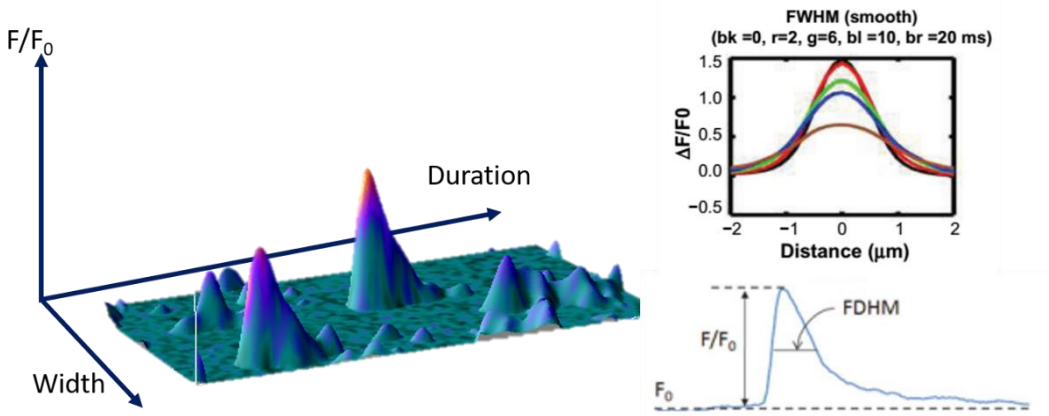

Figure 1.19. Representation of a typical Ca^{2+} spark recording illustrations Left: Line scan of fluorescence showing 3D Ca^{2+} sparks. Top right: spatial projection, Down right: time projection.

Ca^{2+} spark was proposed as an elementary event of so called "visible" Ca^{2+} leak (Cheng et al., 1996). Synchronous activation of Ca^{2+} sparks during AP causes the formation of Ca^{2+} transient and cell contraction (Cheng et al., 1996; Wier et al., 1997). Membrane TAT network largely determines the synchronization of Ca^{2+} transient via dyadic organisations. Dyads in ventricular myocytes contain a large cluster of RyRs (30-100 channels) in the SR membrane and a smaller cluster of LTCCs anchored to T-tubule. The high organisation of TAT network produces the synchronous activation of the most RyRs throughout the cell, but in atrial cells with a sparse TAT network, Ca^{2+} transient has a characteristic "U" shape (Figure 1.20, (Frisk et al., 2014)). Moreover, desynchronization of Ca^{2+} transients was frequently observed in failing ventricular myocytes due to membrane disorganisation and loss of LTCC- RyR2 communication (Song et al., 2006).

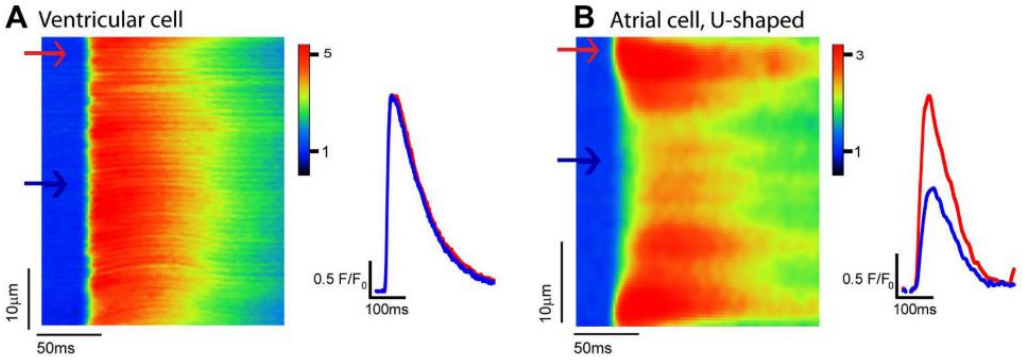

Figure 1.20. Differences in activation of Ca^{2+} transient in ventricular and atrial myocytes. From (Frisk et al., 2014).

The occurrence of orphaned RyR2 in myocytes, which have different properties and regulation that the normal receptors, drives the interest to separate the sparks occurred from RyR2 coupled with T-tubule from uncoupled ones (Heinzel et al., 2002). This relation is largely dependent on the type of myocytes. For example, Ca^{2+} sparks mainly occur close to T-tubules in rat ventricular myocytes (Lukyanenko et al., 2007), while in atrial cells Ca^{2+} sparks occur near the sarcolemma membrane and at the central area (Sheehan et al., 2006). Several groups have shown a correlation between the time of activation of Ca^{2+} release unit and its location to the sarcolemma membrane (Dries et al., 2013; Heinzel et al., 2002). They assigned the Ca^{2+} sparks as an early or delayed according to the time of activation (Figure 1.21, (Biesmans et al., 2011; Dries et al., 2013; Heinzel et al., 2002)).

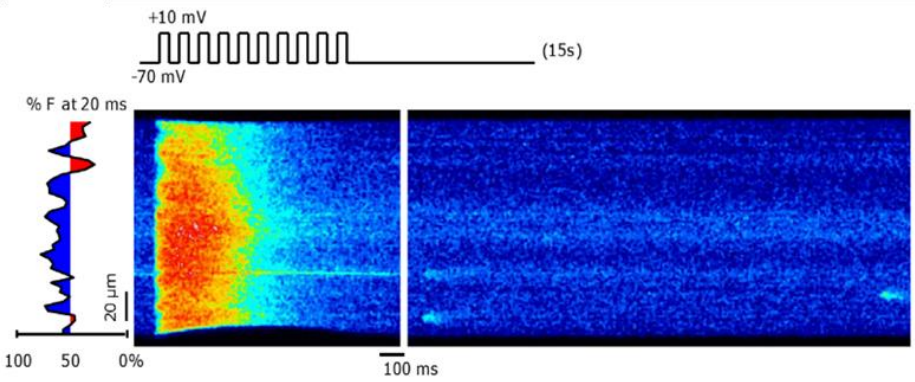

Figure 1.21. Example of a line scan of Ca^{2+} transient and following Ca^{2+} sparks in pig ventricular myocyte. Left graph represents a comparison of fluorescence of this pixel with

a mean fluorescence at 50 % of Ca^{2+} transient amplitude, lower values are colored in red, higher are in blue. From (Biesmans et al., 2011).

Investigation of the subcellular Ca^{2+} sparks heterogeneity is of particular importance, because it can provide the information on a local Ca^{2+} release control in health and disease. The work by Biesmans et al. has shown that in pig myocytes the coupled RyRs have a higher frequency of Ca^{2+} sparks as compared to the uncoupled ones (Biesmans et al., 2011). The duration of the coupled sparks was shorter than the uncoupled ones. HF does not affect the frequency of the sparks, but it changes the duration of coupled events. The authors proposed that in the number of active NCX produced longer Ca^{2+} sparks in these experiments.

Another interesting work was made by Dries et al. on pig myocytes: they have shown a direct correlation between the Ca^{2+} transient activation sites and their distance to the nearest membrane (Dries et al., 2013). They observed a similar frequency of Ca^{2+} sparks between coupled and uncoupled RyRs. The authors found the potentiation of coupled Ca^{2+} sparks by high speed stimulation via CaMKII phosphorylation that was not observed in uncoupled sparks. HF leads to loss of CaMKII – mediated potentiation of coupled Ca^{2+} sparks with the appearance of the effect on uncoupled Ca^{2+} sparks (Dries et al., 2013).

Determination of coupled and uncoupled Ca^{2+} sparks are usually performed on myocytes from big mammalians, such as dog and pig, which have a rather low T-tubular density (Biesmans et al., 2011; Dries et al., 2013; Heinzel et al., 2008). The work on rat and mice ventricle myocytes is challenging because of high degree of T-tubular organisation, which diminishes the fraction of uncoupled RyRs (Heinzel et al., 2002). Recent advantages of development of high speed oblique plane microscope allows to overcome these problems (Sikkel et al., 2016). Sikkel and colleagues observed a high frequency of the Ca^{2+} sparks in tubulated regions of rat ventricular myocytes as compared to non-tubulated regions (Sikkel et al., 2016).

1.7.5 Ca^{2+} efflux from the cytosol

Ca^{2+} removal from the cytosol plays an important role in the maintaining of low basal [Ca^{2+}] concentration. Cytosolic Ca^{2+} removal occurs through several routs: Ca^{2+} sequestration to SR by SERCA2, Ca^{2+} extrusion out of cell by NCX, and

mitochondrial Ca^{2+} loading via mitochondrial Ca^{2+} uniporter. The contributions of these proteins vary in different species. For example, in rat ventricular myocyte the main role is played by SERCA2 pump (~ 90% uptake) with a small contribution of others: NCX extrusion (~7%), by mitochondria (1%–2%) and by PMCA (Bers et al., 1996).

As most of Ca^{2+} release units are organized by TAT, Ca^{2+} removal also largely relies on TAT structure (Chase and Orchard, 2011). SERCA2 pumps are located close to junctional SR. NCX are predominantly located in T-tubules (~ 60 %), so the extrusion of Ca^{2+} occurs mostly from places close to TATS (Chase and Orchard, 2011; Scriven et al., 2010; Sjaastad et al., 2003). Interestingly, both LTCC and NCX were found to colocalize with Cav3, but they show no direct colocalization between each other (Scriven, et al 2005). Thus, Cav3 seems to organize different signalling microdomains through the T-tubule membrane. NCX can regulate the Ca^{2+} sparks activity via reduction of $[Ca^{2+}]$ near RyRs (Bovo et al., 2014). During its work, NCX exchanges one Ca^{2+} ion by three Na^{+} ions, and the depolarizing NCX current could serve as a trigger for arrhythmogenic activity (Pitts, 1979).

Another exchanger which is located in TAT is PMCA. This protein uses the ATP hydrolysis for Ca^{2+} extrusion (Chase and Orchard, 2011). The work of PMCA is very slow so its impact on the total Ca^{2+} removal is relatively small. The negligible amount of Ca^{2+} (~1%) could be uptaken to mitochondria via Ca^{2+} uniporter MIM (Lu et al., 2013).

1.8 Pulmonary hypertension and RV failure

1.8.1 Etiology of pulmonary hypertension

Pulmonary hypertension (PH) is a broad spectrum of disorders that affect both the pulmonary vasculature and the heart (Chesler et al., 2009). PH is characterized by an increased resistance of pulmonary circulation. This usually occurs through an excessive vascular proliferation and vasoconstriction. Clinical manifestation of PH is a substantial increase of the mean pulmonary pressure from 11-17 mmHg to the values above 25 mmHg (Subias et al., 2016). PH cases were classified into 5 groups

depending on the etiology of disease: 1) idiopathic pulmonary arterial hypertension (PAH), 2) pulmonary hypertension secondary to left heart failure, 3) pulmonary hypertension secondary to lung disease, 4) pulmonary hypertension caused by chronic embolism, and 5) pulmonary hypertension with unclear or multifactorial causes (Simonneau et al., 2009).

The most common cause of PH is the second type, due to the LV failure. Most of the patients with HF develop an increased pulmonary artery pressure > 25 mmHg with a pulmonary capillary wedge pressure >15 mmHg (Guazzi and Borlaug, 2012; Hoeper et al., 2013). The idiopathic PAH is relatively rare, with the incidence varies from 2.0 to 7.6 cases per million of adults per year (Mckee et al., 1971). The incidence of PAH is two to fourfold higher in women than in men (Hatton and Ryan, 2014). At the same time, women with PAH can survive much longer than men (Jacobs et al., 2014).

During the last two decades, the progress in PAH treatment significantly improved the survival of PAH patients. One year survival increased from 65% to 86-90% (D'Alonzo et al., 1991; Sitbon et al., 2010) and the median survival time in 2010 became around six years (Thenappan et al., 2018). Despite this, most of the treatments are still not able to stop the obstruction of pulmonary microvasculature that imposes an RV with a significantly higher pressure. The survival of the PAH patients is predominantly determined by the response of the RV to the increased afterload (D'Alonzo et al., 1991; Sandoval et al., 1994). Moreover, RV failure is the leading cause of death in PAH patients (Delcroix and Naeije, 2010). Interestingly, the RV status was shown to be a key determinant of survival in LV failure (Szwejkowski et al., 2012). Importantly, there is no current treatment in PH directed to fix RV (Thenappan et al., 2018).

1.8.2 RV hypertrophy and failure in pulmonary hypertension.

For the long time the research of heart disorders was concentrated in the LV, while little attention was given to study the RV progression in disease.Now, there is a growing amount of data regarding the RV behaviour in disease. The progression of RV to failure under high pressure is illustrated in Figure 1.22. In contrast to LV that works in generating pressure, RV is not prepared to work under a high pressure. In

circumstances of elevated ejection pressure, the stroke volume of the RV drops faster compared to the LV (Greyson, 2008). Several reasons could explain this. First, the thinner RV free wall faces with a greater wall tension under increments of pressure. Second, at end of LV contractions, the stress of the walls is significantly reduced because of the diminishing the curvature radius (Yin, 1981). On contrary, the contraction of RV leads to a higher radius of wall curvature, which increases the stress on the walls.

Several mechanisms of ventricular adaptation to the increased pressure was proposed, such as the Anrep effect (homometric autoregulation), the Frank-Starling mechanism (sometimes referred to as heterometric autoregulation), and catecholamine induced inotropy. The Anrep effect is mediated through the rapid changes in Ca^{2+} dynamics happened in the absence of external regulatory stimulation (Pawlush et al., 1989). It was believed to be a first adaptation response of RV to a high pressure (De Vroomen et al., 2000; Hon et al., 2001). According to Frank-Starling mechanism, a higher stretch of the walls will produce a larger stroke work (Karunanithi et al., 1992). However, at the baseline, a large increase in RV volume results in the increment of stretch, therefore, the Frank-Starling mechanism has a small impact on RV function at baseline (De Vroomen et al., 2000). Only when RV dilates and becomes more circular, the Frank-Starling mechanism can effectively determine the RV function (Szabo et al., 2006). Sympathetic stimulation permits the RV to further implement the pressure via an increase in inotropy (Handoko et al., 2010; Maughan et al., 1979; Naeije and Manes, 2014). When the most of the contractile reserve mechanisms are exhausted, systemic pressure begins to fall, with a dramatic, sudden, and irreversible reduction of RV contractile function (Guyton et al., 1954).

With increasing the pressure, RV is not able to maintain a high working load and becomes uncoupled from the load, making energy transfer inefficient, and ultimately RV failure develops (Vonk Noordegraaf et al., 2017). The wall stress determines the ventricular oxygen consumption (Sarnoff et al., 1958; Wong et al., 2011). Moreover, an increased wall thickness diminishes the oxygen delivery to the cells from blood, that affects the energy metabolism and changes the muscle contraction (Van Wolferen et al., 2008).

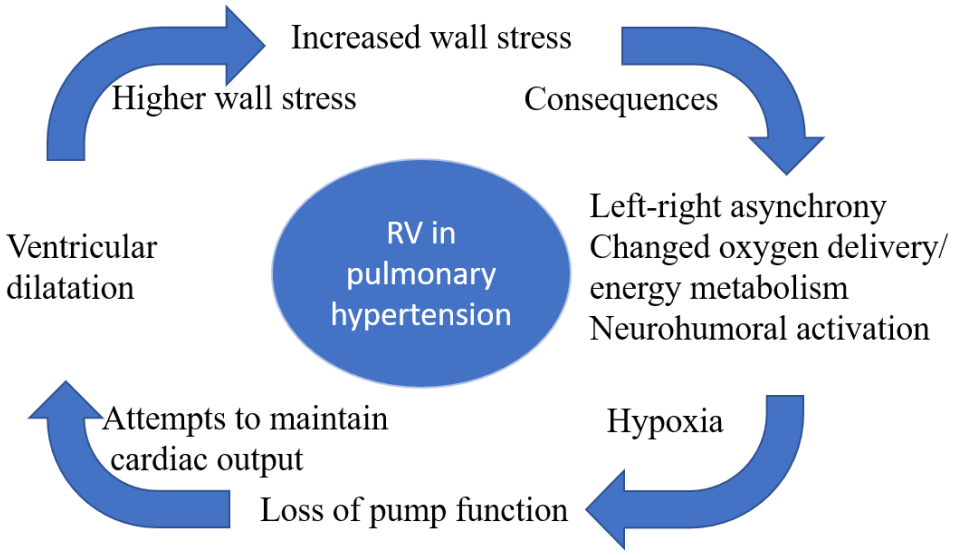

Figure 1.22. Schematic of the RV progression in pulmonary hypertension. Adapted from (Westerhof et al., 2017).

1.8.3 Models of pulmonary hypertension in rat

Investigations of the mechanisms of PH- related RV hypertrophy and failure are mostly performed in animal models (Nogueira-Ferreira et al., 2017). An ideal PH model should mimic the key clinical, hemodynamic and histopathological features of human disease (Ryan et al., 2011). PH is a complex disease of diverse etiology and so there is no single animal model that accurately reproduces the human disease, even focusing on just one of the PH groups (Das et al., 2012). Despite not fully replication of the aspects of human cardiovascular disease, animal models can provide invaluable insight into the processes and pathways underpinning pathological remodelling. A vast variety of PH animal models is currently available (Table 5). The models are grouped in the table according to the stimuli that result in PH development. Each model has its own characteristics and usage is highly dependent on the specific hypothesis of the study. Some of the models are commonly used as they recapitulate a broad spectrum of PH-related features and some could be used for investigation of the specific pathway and its role in disease progression.

Table 5. List of the commonly used animal models of PH

Experimental models	Animal species	Pathological findings	Advantages	Limitations	References
Chronic hypoxia	mouse, rat,	Chronic hypoxia results in vasoconstriction, muscularization of non- muscular arterioles, increased matrix deposition	• Widely used • Simple implementation	• Results in lung damages • Not included heart damage.	(Janssens, Thompson, Spence, & Hales, 1991; Meyrick & Reid, 1980; Steudel et al., 1998)
Pulmonary arterial binding	Mouse, rat	Pulmonary arterial binding leads to pulmonary arterial stenosis that causes RV hypertrophy	Model could mimic congenital heart diseases and investigation of the RV response to increased pressure	• Required highly technical skills • Generally associated with a high percentage of animal death	(Dias et al., 2002; Maarman, Lecour, Butrous, Thienemann, & Sliwa, 2013)

Vascular obstruction	Rat	Embolization of pulmonary arteries via intravenous administration of synthetic microspheres	• Allow to study chronic pulmonary thromboembolism • Possibility to target different size of microspheres	• Possible cellular reaction to microspheres • Effects are mostly on the lungs	(Marsboom & Janssens, 2004; Shelub, van Grondelle, McCullough, Hofmeister, & Reeves, 1984; Weimann et al., 1999)
Monocrotaline	Rat	PH induced via single MCT and characterized by vascular remodeling, increased muscularization, vascular inflammation and RV hypertrophy and failure	• Simple implementation • Commonly used • Relatively inexpensive • Recapitulate PH related problems of the heart and lungs	• MCT response vary among species, strain and animals • Could produce damage of liver	(Gomez-Arroyo et al., 2012; Hilliker, Bell, & Roth, 1982; Zeng et al., 2013)
Other chemical-induced PH	Mouse, rat	• A-naphthylthiourea- induced pulmonary vascular remodeling associated with RV hypertrophy. • Bleomycin–induced pulmonary fibrosis with increased lungs inflammation	• Simple implementation • Relatively inexpensive	• Mimic only a few features of a human PH, not commonly used	(Hill, O'Brien, & Rounds, 1984; Ortiz et al., 2002)

Genetic induced PH	Mouse, rat	• Mice overexpressing IL-6 develop PH with increased pulmonary arterial muscularization and RV hypertrophy. IL-6 effects are augmented by hypoxia • Transgenic rats overexpressing Ang-1 develop increased pulmonary arterial muscularization and vascular occlusion • 5-HTT overexpression leads to PH development and RV hypertrophy	• Useful for investigation of the specific pathways in PH development and progression	• Not reflex all the complex features of PH • Relatively expensive	(Chu et al., 2004; MacLean et al., 2004; Steiner et al., 2009)
Multiple stimuli					
SU5416 + chronic hypoxia	Mouse, rat	VEGFR-2 blockade with chronic hypoxia leads to PH development with a complex plexiform like lesions formation	Mimic more accurately human PH that single stimuli models: development more severe PH with vascular lesions	• Relatively expensive • Require technical skills • Associated with a high mortality	(Abe et al., 2010; Taraseviciele-Stewart et al., 2001)
Athymic + MCT	Rat	Athymic rats treated with MCT develop severe PH with a great number of mast cell and severer histopathologial changes			(Miyata et al., 2000)

MCT + pneumonectomy	Rat	Addititonal preunonectomy in MCT treated rats leads to RH with additional neointimal lesions formation			(Okada et al., 1997)
Endothelin receptor B deficiency + MCT	Rat	Monocrotaline administration in endothelin receptor-B deficiency rats leads to acceleration of PH progression, enhances the appearance of cellular and molecular markers related to PH progression and develops neointimal lesions			(Ivy et al., 2005)

5-HTT serotonin transporter, Ang-1: angiotensin 1, IL-6: Interleukin -6, VEGFR-2: vascular endothelial Growth Factor Reseptor-2,

1.8.4 The chronic hypoxia model of pulmonary hypertension

The chronic hypoxia model is one of the most used to study PH pathogenesis and treatment. Its pathological features of pulmonary vasoconstriction and vascular medial hypertrophy mimic the ones observed in human PH (Zhao, 2010). This model could be produced by exposing animals to oxygen-low air at normal pressure or to normal air at hypobaric pressure (Voelkel and Tuder, 2000). The decrease in oxygen pressure causes a strong pulmonary vasoconstrictor response that is characteristic of this model (Barman et al., 2009). However, there is little evidence of RV failure in this model (Zhao, 2010).

1.8.5 The surgical models of pulmonary hypertension

The surgical models are designed to mimic the increased blood flow and pressures imposed on the RV in Group 1 PH. There are two main surgical methods used: pulmonary artery banding (PAB) and aorto-caval shunt. The PAB produced a constriction imposed in the pulmonary artery, which leads to an increased afterload in the RV that drives the hypertrophic response. This produces only a cardiac disease, but not pulmonary. Thus PAB does not replicate the human pathology entirely, only the mechanisms of RV dysfunction (Ryan et al., 2013; Vonk Noordegraaf and Galiè, 2011).

The aorto-caval shunt is a volume overload method which displays a similar RV hypertrophy when compared with PAB. This model can be combined with the monocrotaline (MCT) model, leading to more severe disease development (Ryan et al., 2013; West and Hemnes, 2011). The main disadvantages of these surgical methods are related with the fact that they require highly technical skills and are usually associated with a high percentage of animal death (Ryan et al., 2011).

1.8.6 Monocrotaline induced pulmonary hypertension in rat

MCT is a pyrrolizidine alkaloid isolated from the seeds of the *Crotalaria spectabilis* plant. The model is produced by intraperitoneal MCT injection. MCT injection affects both lungs and heart, mimicking the two key pathological featured of human PH: vascular remodelling and inflammation (Umar et al., 2012).

Low doses around 30-40 mg/kg produced a compensated hypertrophy without the heart failure, and these doses are used for the investigation of the long term effects

of PH on the RV and LV (Benoist et al., 2012; Ruiter et al., 2013). A middle dose of 60-80 mg/kg the MCT produced a PH that leads to RV hypertension after 2 weeks and RV failure after 3-4 weeks (Abdul-Salam et al., 2019; De Man et al., 2012; Lamberts et al., 2007). The doses higher than 80 can cause an acute lung injury, interstitial pulmonary fibrosis and hepatic veno-oclusive disease (Copple et al., 2003).

The mechanism of MTC action is complex and not well understood. The MCT is not active by itself, but in the liver, it is oxidized by cytochromes P450 CYP3A4 to the short-lived, reactive MCT-pyrrole compound (Kasahara et al., 1997; Mattocks et al., 1990). The active compound is pumped by the RV to the lungs where it damages the endothelial cells of pulmonary arterioles. MCT-pyrrole causes the death of pulmonary vascular cells. When the barrier function of pulmonary vasculature is comprehended, it starts the inflammation leading to lung fibrosis (Pan et al., 1993; Sahara et al., 2007). Also, MCT-pyrrole promotes the proliferation, constriction and hypertrophy of smooth muscle cells (Huang et al., 2010; Ramos et al., 2007). Importantly, MCT-pyrrole has no direct action on the systemic circulation and peripheral resistance because of a small lifetime in the systemic circulation (Correia-Pinto et al., 2009). There is an evidence of significant liver and kidney damage by MTC-pyrrole (Huang et al., 2010), but it appears at the late stages of the disease. Moreover, there is a report indicating that MCT can cause myocarditis affecting both RV and LV, which complicates the evaluation of the direct effect of PH to the RV hypertrophy and failure at severe stages of PH (Miyauchi et al., 1993). Generally, MCT-pyrrole is proposed to produce the PH via acute/subacute damage of peripheral vasculature of the lungs and other organs.

1.8.7 Genetic animal models

In the past few years, there is a growing amount of animal PH models produced by genetic manipulation (Barman et al., 2009; Piao et al., 2010; Ryan et al., 2011). The transgenic and knockout models allow the evaluation of the role of a specific gene or protein modifications in the susceptibility to the development of PH. These models allow developing the molecular pathways underlying PH development rather than the PH-induced RV failure (Das et al., 2012; West and Hemnes, 2011).

1.9 Heart failure and the effect on the RV.

HF is a progressive clinical syndrome in which the heart is not pumping enough blood to the body. HF is associated with a high risk of morbidity and mortality; it causes more than 7.4 million of deaths annually (World health organisation, 2017). Moreover, many other cardiovascular diseases, including pulmonary arterial hypertension, atrial fibrillation, valve disease, and cardiomyopathy, can contribute to HF. As stated above, PH due to left heart disease is the most common cause of the pulmonary disease. It includes around 65-80 % of all the cases of PH (Rosenkranz et al., 2016). The prevalence of PH in HF varies from 36 to 83 %, because different estimations gave variable values. For example, echocardiography tends to overestimate the pulmonary arterial pressure so the detection of PH should be performed by right heart catheterization (Kalogeropoulos et al., 2011).

The presence of PH in the settings of left sided HF, predicts an increased morbidity and mortality (Guazzi and Borlaug, 2012; Salamon et al., 2014). Most of the efforts in the treatment of PH were concentrated on group one , i.e., PAH, leaving the second group of PH without a proper attention (Kalogeropoulos et al., 2011). However the treatments of PAH can be partially beneficial or ineffective for the treatment PH due to the HF. Deeper understanding of the mechanisms of RV pathophysiology in PH can help to find a better treatments.

The pathophysiology of PH in this case is related to the backward transmission of LV filling pressures into the pulmonary circulation that is followed by pulmonary vasoconstriction, decreased nitric oxide availability and desensitization to natriuretic peptide-induced vasodilatation (Rosenkranz et al., 2016). Pulmonary vascular remodelling leads to RV strain and dysfunction. Uncoupling of RV from pulmonary artery leads to RV dilatation, increased wall stress, tension and elevated myocardial oxygen consumption that result in ischemia and failure (Kalogeropoulos et al., 2011).

If PH occurs during LV failure, the disease progresses from a predominantly LV cardiomyopathy phenotype to biventricular or RV dysfunction predominant phenotype. At certain stage of disease, it is hard to establish what is the reason or the cause of dysfunction. At the beginning, LV dysfunction can produce PH, but

later the worsening of PH can worsen the disease progression. For example, dilatation of RV at the late stages of PH shifts the septum leftwards and impairs the global ventricular function (Haddad et al., 2008).

1.9.1 Animal models of heart failure

Small animal models are commonly used for deeper the understanding of various aspects of HF (Goh et al., 2016). Mice and rats are the most commonly used as they have a relatively short breeding cycle, low housing costs, and share a high degree of homology to the human genome (Riehle and Bauersachs, 2019). However, the pathogenesis of HF is multifactorial and is not a model that can recapitulate the whole range of HF induced remodelling. Thus, there are numerous small rodent HF models have been developed that allowed investigating HF induced remodelling and specific molecular pathways (Riehle and Bauersachs, 2019). These models could be grouped according to the stimulus into surgical, toxic and genetic models. The main characteristics of the commonly used rodent models are summarized in the Table 6.

In this work, we used a model of the myocardial infarction (MI) induced via left anterior descending (LAD) artery ligation. This model was established by Pfeffer et al. (Pfeffer et al., 1979). LAD showed good reproducibility, as rats with infarctions greater than 46% developed congestive HF after 21 days with elevated filling pressures, reduced cardiac output, and minimal capacity to respond to pre- and after-load stress (Pfeffer et al., 1979). The degree of impairment of LV function is directly related to the extent of myocardial loss (Pfeffer et al., 1979). This model was thoroughly characterized in our group showing that after sixteen weeks of infarction animals had developed significantly increased heart weight/body weight ratios, ventricular dilatation, with reduced ejection fraction and elevated end-diastolic pressure (Lyon et al., 2009).

Importantly, RV hypertrophy was shown in 30-60% cases in this model (Pfeffer et al., 1979).In MI, the degree of RV hypertrophy correlated to increases in the LV end-diastolic pressure and RV systolic pressure . In addition, the change of the pulmonary circulation resistance due to MI can influence RV function (Sicard et al., 2019). Another evidence of declined RV contractile function was observed in

coronary ligated MI mouse and pig (Danton et al., 2001; Toldo et al., 2011). Thus, there is a remodelling occurring in the RV due to the LV MI and this model is suitable to investigate the cellular and molecular mechanisms of the adaptation RV myocytes in the settings of LV failure.

Table 6. Characteristics of animal models of HF.

Experimental models	Animal species	Pathological findings	Advantages	Limitations	References
LV pressure overload via transverse aortic constriction (TAC)	Mouse, rat	TAC increases LV after-load, which results in concentric cardiac hypertrophy and, ultimately, HF.	Reliable model to induce cardiac hypertrophy and HF	The acute increase in afterload does not reflect the gradual progression observed in human patients	(Grund et al., 2019; Riehle et al., 2011; Schwarzer et al., 2014)
LV pressure overload via ascending aortic constriction	Rat	In this model, LV hypertrophy is observed by 6 weeks and overt HF by 18 weeks post-surgery.	Gradual onset of pressure overload that mimics the gradual onset of arterial hypertension in patients	Induced in young animals, whereas arterial hypertension is primary observed in elderly patients The technical challenge of such a delicate procedure	(Schunkert et al., 1990)
Myocardial infarction (MI) via left anterior descending (LAD) artery ligation	Mouse, rat	Myocardial scar and dilated cardiomyopathy develop several weeks post-surgery.	This model mimics the effects of a completed human myocardial infarction in patients	Model does not reflect the clinical settings with reperfusion of the occluded vessel during coronary angiography High perioperative mortality Variations in the size of infarct	(Fraccarollo et al., 2011; Pfeffer et al., 1979)

Ischemia/reperfusion (I/R) injury via temporary LAD ligation	Mouse, rat	I/R model typically exhibits less tissue damage compared to permanent LAD occlusion.	Close to scenario with reperfusion of the occluded vessel during coronary angiography performed after acute MI	More complex and challenging surgery	(Lindsey et al., 2018; Yeang et al., 2019)
Volume overload via aorto-caval fistula (shunt)	Mouse, rat	Volume overload in rats initially decreases LV function. The subsequent compensatory hypertrophy normalizes contractile function at one month post-surgery.	Model mimic the volume overload observed in patients with mitral valve regurgitation	The acute increase in volume overload does not reflect the gradual progression of mitral valve regurgitation in patients The time course of HF development strongly dependent on the shunt volume Shunt create an artificial mix of arterial with venous blood	(Liu et al., 1991; Toischer et al., 2010)
Toxic cardiomyopathy via doxorubicin injection	Mouse, rat	Doxorubicin causes dilated cardiomyopathy in a dose-dependent manner that is typically irreversible and progressive.	Potent stimulus to induce dilated cardiomyopathy	Systemic toxic effects, especially on bone marrow cells and gastrointestinal system	(Hayward and Hydock, 2007; van der Vijgh et al., 1988)

Chronic activation of adrenergic signalling by Isoproterenol injections	Mouse	Chronic activation of adrenergic signalling with isoproterenol provokes cardiomyocyte hypertrophy and fibrosis	Potent stimulus to induce cardiac hypertrophy	Model mimic only one factor contributing to HF development in patients	(Thum et al., 2008)
Chronic stimulation of angiotensin II Type 1 receptor (AT1R) signalling	Mouse, rat	Chronic AT1R stimulation causes hypertension and cardiomyocyte hypertrophy	Reliable model of cardiac hypertrophy; Technically easy surgery to implant osmotic mini-pumps	Unspecific side effects on organ systems, especially kidney	(Joseph et al., 2002)
Dahl rats that are susceptible to hypertension following a high salt diet	Rat	When fed with a high-salt diet containing 8% NaCl, this model rapidly develops hypertension, diastolic dysfunction, and HF	No surgery needed Slow progression of hypertension as observed in patients	Slow progression of disease requires long housing for the animals	(Dahl et al., 1962)
Spontaneous hypertensive rats	Rat	Spontaneously progress to hypertension and HF	Slow progression of hypertension as observed in patients	High housing costs based on the slow progression of hypertension	(Okamoto and Aoki, 1963)

1.9.2 Structural changes in cardiomyocytes during heart failure

Cardiac myocytes are terminally differentiated cells (de Tombe, 1998). Thus the adaptation to a high working load is going through the changes of cell shape (increase cell mass, hypertrophy) rather than the cell proliferation (de Tombe, 1998). Different loading conditions can modulate variable changes of myocytes geometry (Tamura et al., 1998). In circumstances of pressure overloaded, myocytes tend to become wider, as it helps to reduce the wall stress. When the ventricle experiences the volume overload, the myocytes tend to elongate to maintain the stroke volume (Grossman et al., 1975). At the same time, the capacity of cells to adapt to stress is very limited. If the initial stimuli remain and myocytes cannot sustain it, the pump failure will happen at certain point (Gerdes and Capasso, 1995).

When the hypertrophy of the ventricle is established, it produces a mismatch of oxygen supply and demand, and development of hypoxic and unexcitable regions unable to contribute the contraction. Hypoxia promotes myocytes apoptosis fibrosis. Both of these factors have been observed in PH rats (Campian et al., 2009). Progressive fibrosis replaces the myocardium in order to maintain the structure organisation of the heart; however, it impairs heart pump function (Cingolani et al., 2004).Adrenergic stimulation via βARs plays an important role in disease progression. There are three main subtypes of βARs expressed in the heart. The most abundant is β_1ARs, with a β_1/β_2 ARs ratio of around ~80/20 found in ventricle. The β_1ARs effectively regulate the contraction providing positive lusitropic and inotropic effects. From the other side, β_2ARs are involved only in the inotropic response (Nikolaev et al., 2010). In pathology, the βAR system usually became overstimulated because of constitutive demand of increased contractility that leads to desensitization (Sato et al., 2015) and internalization of the βARs (Luttrell and Lefkowitz, 2002). Reduction in βAR inotrope results in hypophosphorylation of key Ca^{2+} handling proteins and reduction of the contractile reserve to adapt for acute stress, such as exercise (Holubarsch et al., 1996).

Hypertrophic stimuli were shown to be associated with the reappearance of the fetal genes expression (Alpert and Gordon, 1962; Chien, 1999). An altered myosin heavy chain (MHC) expression is one of the most important changes (Alpert and Gordon, 1962). β-MHC is expressed in the embryonic/fetal ventricles of all mammals. In

small mammals it is replaced (at approximately three weeks of age) by α-MHC (Schaub et al., 1998). In hypertrophy, a decreased myofibrillar ATPase activity makes a slow β-MHC more suitable for the contraction demands (Pope et al., 1980; Swynghedauw, 1986; VanBuren et al., 1995). Therefore in larger mammals, including humans, β-MHC remains the predominant ventricular isoform throughout adulthood, so the heart is already in low gear and there is little potential for a change as compared with the smaller mammals (Cooke, 1997; Schaub et al., 1998). The contractile dysfunction of the myocytes rises also from the changes in thin filaments and their associated proteins (LeWinter and VanBuren, 2002; Lowes et al., 1997). These include expression of alpha-skeletal actin (α-SKA) and alpha-smooth muscle actin (α-SMA) (Long et al., 1989; Swynghedauw, 1986). The enhancement of α-SKA expression is associated with increased myocyte stretch, high wall stress, and pressure overload (Machackova et al., 2006). Another important protein that appears in hypertrophied myocardium is atrial myosin light chain 1 (ALC1). It is normally found in the developing heart and skeletal muscle (Price et al., 1980). The main consequence of ALC1 re-expression in the ventricle is the increase of Ca^{2+} sensitivity of the contractile apparatus (Morano et al., 1997). ALC1 modulates ventricular contractility by increasing the cross-bridge kinetics of the β-MHC isoform. Expression of β-MHC in combination with ALC1 produces a faster contraction with a higher ATPase efficiency (Morano et al., 1996). Failing myocardium has an altered expression of cardiac troponin T isoforms expression (Adamcová and Pelouch, 1999).

Significant changes in the contractile apparatus of failing cardiomyocytes occur due to the endogenous phosphorylation status of thin and thick filament proteins (Suematsu et al., 2001; Van Der Velden et al., 2003). These alterations may be determined by the activity of different protein kinases, such as the PKA, protein kinase C (PKC), and myosin light chain kinase, as well as phosphatases, in the failing myocardium (Machackova et al., 2006). Most of these kinases are activated via βAR and can regulate the activity and Ca^{2+} sensitivity of the contractile proteins affecting the rate and force of contraction.

During the progression of HF, many research groups have seen the disorganisation and loss of TAT system (Heinzel et al., 2002; Schobesberger et al., 2017; Wei et

al., 2010). JPH2 and BIN-1 that are the key proteins for T-tubular maintenance undergo significant down-regulation in HF (Hong et al., 2014; Schobesberger et al., 2017). Disorganisation of TAT network was shown to uncouple the LTCC from RyRs which decreases a spatial synchrony of Ca^{2+} transients and reduce the contraction force (Louch et al., 2006). $Ca_v1.2$ expression and Ca^{2+} current density are usually not changed in HF, but single LTCC channels showed the redistribution from a predominant T-tubular localization to the surface sarcolemma (Bryant et al., 2015; Sanchez-Alonso et al., 2016). Redistribution of LTCCs could be induced by the reduction of JPH2 and Cav3, that are essential for the maintenance of LTCC in T-tubular membrane (Bennett et al., 2015).

1.9.3 Progression changes of RV myocytes Ca^{2+} handling in hypertrophy and failure

The pathophysiology of RV in hypertrophy and failure is not clear. It can significantly vary depending on the model and the specie. Most of the studies were concentrated on the MCT model of PH (Nogueira-Ferreira et al., 2017) and we aiming to study this model, so results produced in MCT rats will be described here. The most consistent finding in failing RV myocytes is the prolonged action potentials and a steeper AP duration restitution that were described in PH rats (Benoist et al., 2011; Sabourin et al., 2018). The steep AP restitution can lead to the formation of altering long and short AP durations (namely, AP alternants) which can generate ventricular fibrillation (Rosenbaum et al., 1994).

In the studies of Ca^{2+} handling in RV there are many contradicting results. At the early stages of PH, some have found the prolongation of contractions and Ca^{2+} sequestration (Brunner et al., 2002). In contrast, others have observed higher amplitudes and shorter durations of contraction and Ca^{2+} transients in RV (Kuramochi et al., 1994; Sabourin et al., 2018). In the late-stage PH in MCT rats, some groups observed smaller and slower Ca^{2+} transients (Kuramochi et al., 1994; Xie et al., 2012), but others reported an increase of SR Ca^{2+} loading, Ca^{2+} transients and cell shortening (Benoist et al., 2012).

From molecular point of view, in PH the prolongation of Ca^{2+} transients in RV myocytes was supported by the reduction of SERCA2a expression and the reduced phosphorylation of its inhibitor, phospholamban (Benoist et al., 2014; Xie et al.,

2012). Moreover, the reduction of SERCA2a activity provokes the decrease in SR Ca^{2+} loading and consequently Ca^{2+} transient amplitude. In contrary, Sabourin et al. found the unchanged levels of SERCA2a expression and increased phosphorylation of phospholamban by PKA in MCT model of PH, which produced higher levels of SR Ca^{2+} loading (Sabourin et al., 2018).

Progressive loss of TAT structure was shown in hypertrophied RV myocytes (Wei et al., 2010; Xie et al., 2012). It was accompanied by down-regulation of two T-tubule scaffolding proteins, BIN1 and JPH2 (Wei et al., 2010; Xie et al., 2012). TAT network loss resulted in the reduction of synchronous Ca^{2+} release, prolongation of Ca^{2+} transients and diminishing the force of contraction (Ferrantini et al., 2014; Xie et al., 2012). The mRNA and protein levels of LTCC were downregulated at severe PH (Benoist et al., 2011; Xie et al., 2012) whereas the whole-cell LTCC current was not altered (Benoist et al., 2012). It raises the question to what extend the mismatch of the expression and whole-cell current data could be attributable to single LTCC spatial localization or functioning.

Higher rate of spontaneous Ca^{2+} waves and sparks release were shown in hypertrophied and failed RV myocytes (Benoist et al., 2012; Sabourin et al., 2018). Such enhanced Ca^{2+} activity promoted the loss of SR Ca^{2+} contents, participated in the formation of ectopic AP (Fujiwara et al., 2008) and provoked ventricular fibrillation (Benoist et al., 2011).

1.10 Hypothesis and aims of the study.

As indicated before RV is involved in several severe disorders, such as pulmonary hypertension and left ventricular failure. The adaptation RV was shown to be an important predictor of patient survival in PH (Thenappan et al., 2018). The behaviour and mechanism of LV progression in failing heart are well studyed, but the differences between the chamber and their working conditions did not allowed a direct translation of the results obtained from LV studies to the RV.

Myocytes membrane is organized in microdomains that serve for synchronous contraction and regulation of ECC. TAT network plays an important role in organizing such signalling microdomains (Kamp and Hell, 2000). Cardiac disorders

usually promotes the disorganisation of TAT network and signalling complexes involving ion channels and associated signalling molecules that further contribute to the pathophysiology of disorder (Dibb et al., 2009; Schaper et al., 2002).

Here we hypothesize that in rats RV myocytes have a distinct ECC organisation than LV myocytes which could be responsible for a different adaptation of RV myocytes to the disease conditions.

The main aims of this thesis were:

1. To compare myocyte membrane microdomain organisation and to reveal how the differences of microdomain organisation influence Ca^{2+} handling in normal RV and LV myocytes
2. To analyse the influence of PH on RV and LV microdomain structure, in a rat model of the MCT-induced PH, to investigate the effect of PH on electrical conduction in-*vivo*, and on cellular ECC.
3. To investigate RV microdomain changes after left-sided heart failure in a rat model of HF (in 16 weeks after myocardial infarction); to compare RV myocytes progress towards failure, relative to the LV myocytes.

2 General methods

2.1 Animals

2.1.1 Sprague Dawley rats

All animals were treated and maintained under conditions fulfilling the criteria of Animals in Scientific Procedures Act 1986 (UK Home Office, ASPA 1986). The male outbred, Sprague Dawley rats (*rattus norvegicus*) were obtained from Harlan Laboratories (Wyton, UK). They were fed standard rat diet, which they had access to *ad libitum*. Rats were housed at a density of 4-6 per cage and maintained on a 12-hour light/dark cycle at 21^{o}C. The adult cardiomyocytes were isolated from males above 250g.

2.1.2 Monocrotaline model of pulmonary artery hypertension

Pulmonary hypertension was induced via monocrotaline injection accordingly to the protocol described (Abdul-Salam et al., 2019; Wojciak-Stothard et al., 2014). Rats were injected and carried out by Dr. Vahitha Abdul-Salam in Imperial College London and by Dr. Stefano Rossi in University of Parma. Monocrotaline (MCT; Sigma, UK) injections were prepared before the experiments by dissolving 80 mg of MCT in a 250 µL of 1 M HCl. After full dissolvent of MCT the volume was adjusted by a normal saline up to 3 ml. The pH was adjusted to 7.4 with 5 N NaOH. The final concentration of MCT was 20 mg.mL^{-1}. Male Sprague-Dawley rats weighing 240 ± 10 g were injected intraperitoneally of 60 mg/kg MCT to induce the PH. Equivalent volume of 140 mM saline was injected in control rats (CON). Rats were weighed and checked for signs of HF daily after the MCT injection up to 10-14 days after the injection (Abdul-Salam et al., 2019). Loss of more than 10% weight was used as sign of distress and the animal should be killed. Rats were checked for the other signs of distress, such as cachexia, lethargy, dyspnoea, cold extremities or piloerection. Experiments in control rats were performed on temporally equivalent days.

2.1.3 Myocardial infarction model of heart failure

The study of the effect of the failure LV on the Ca^{2+} handling in RV myocytes was performed in the model of chronic myocardial infarction (MI) in rats as described previously (Lyon et al., 2009; Vescovo et al., 1989).

Rats were anesthetized with isoflurane and placed in ventral recumbence. The thorax was shaved and sterilized. Then a left thoracotomy was performed, and the ligation was performed of the left anterior descending coronary artery. Sham ligation operation was performed for CON rats. The animals placed back to the cages and stayed 16 weeks to develop the MI. At that time, hearts were explanted, weighed, and prepared for cell isolation.

MI has been established as model of congenital HF (Glukhov et al., 2015; Lyon et al., 2009; Sanchez-Alonso et al., 2016). The operation lead to extensive left ventricle dilatation reduced ejection fraction and increased LV myocytes length. The effect of chronic increase in afterload has been studied in LV myocytes, but not in RV.

2.2 Myocytes isolation and plating

2.2.1 Ventricular myocyte isolation

The isolation of cardiomyocytes was performed by Mr. Peter O'Gara via enzymatic digestion as described previously (Gorelik et al., 2006). The rats were killed accordingly to UK Home Office Schedule 1 method. This method includes the animal being anesthetized with 5% isoflurane and then killed via cervical dislocation. The heart and lungs were removed from the body and rapidly placed in ice cold Krebs-Henseleit (KH) buffer (119mM NaCl, 4.7mM KCl, 0.94mM MgSO4, 1mM CaCl2, 1.2mM KH2PO4, 25mM NaHCO3, 11.5mM glucose; 95% O2, 5% CO2). Then the lungs were removed and the heart was cannulated through the aorta at the Langendorff perfusion system. Heart was perfused with KH at 37°C for 5 minutes, and then the solution was switched to low calcium (LowCa) buffer. This solution contained: 15μM CaCl2, 120mM NaCl, 5.4mM KCl, 5mM MgSO4, 5mM pyruvate, 20mM glucose, 20mM taurine, 10mM HEPES, 5mM nitrilotriacetic acid; 100% O2). After the 5 min of LowCa buffer perfusion, the perfusion was switched to an enzyme (Enz) buffer with 1mg/ml Collagenase II and

0.6mg/ml Hyluronidase for 10 min. Enzyme buffer composited of 12- 15µM CaCl2, 120mM NaCl, 5.4mM KCl, 5mM MgSO4, 5mM pyruvate, 20mM glucose, 20mM taurine, 10mM HEPES, 5mM nitrilotriacetic acid; 100% O2. After 10 min of perfusion with the Enz solution, the heart was removed from the perfusion system and placed in a petri dish with some enzyme free solution. The RV, LV and septum were carefully dissected, weighed and placed in separate tubed with 4 mL Enz solution containing Collagenase and Hyluronidase. The tubes were shaken mechanically for 5 min at 35 ºC, and then the solutions were filtered through 200 μm^2 nylon mesh and replaced with new Enz buffer for isolation. After 30 min of mechanically shaking, the tissue has been almost completely digested. The tubes were centrifuged for 1 minute at 700 rpm. The supernatant was removed and the pellets were re-suspended in Enz buffer without the enzymes. Cardiomyocytes stayed in Enz buffer before the plating and the beginning of the experiments

2.2.2 Cardiomyocytes plating and fixation

In accordance to the type of experiment freshly isolated cardiomyocytes was plated on the 35 mm Petri dishes (for SICM and patch clamp investigation), 35 mm MatTek (MatTek Corp) dishes for TAT network visualization and 13 mm glass coverslips for the immunolabelling. All the dishes were coated with 20 µl of 1mg/ml laminin (Sigma-Aldrich, UK) and left for 30 min. When the laminin was completely dried, a drop (200-300 µL) of cardiomyocyte solution was placed on the laminin area and left to stick for at least 30-45 minutes. Then the cells were washed with appropriate buffer to remove not attached dead cells. For the functional experiments and TAT network visualization cardiomyocytes were used on the same day of isolation. For the immunochemical staining myocytes were fixed in 4 % formaldehyde or methanol and kept at 4 ºC.

2.3 Methods of structural investigations

2.3.1 TAT labelling and investigation

Myocytes were stained according to the protocol described (Schobesberger et al., 2017). To prepare the solvent for Di-8ANEPPS, 0.5 g of Pluronic acid was dissolved in 1.5 µL of DMSO under mild heating in water bath (70-80ºC). Then 630 µL of the warm mixture was added to the 5mg of the Di-8-ANEPPS powder.

When the dye completely dissolved, it was aliquoted by 10 microliter each and stored at -20°C until used. To stain the cells, one of the aliquots was dissolved in 1 ml of Tyrode normal solution (contained in mM: 140 NaCl; 6 KCl; 10 Glucose; 10 HEPES; 1 $MgCl_2$; 1 $CaCl_2$ and pH was adjusted to 7.4 by 1M NaOH) or any other suitable physiological buffer, i.e. Hank balanced salt solution (HBSS, Sigma-Aldrich) and placed in water bath (Fisher Scientific, model FB15047) at 55^{o}C for 5 min and then cooled down to room temperature. Glass part of the Mat-Tek dishes with myocytes was covered with enough amount of dye suspension and left for 1 min. Then the cells were washed 2 times with enough amount of Tyrode solution.

Visualization of the membrane was performed with an inverted confocal microscope (Zeiss LSM-780). The excitation was performed with argon laser at 488 nm and the fluorescence was collected through the filter centred at 615 nm and maxima at 635 nm. The Z-stack was taken of optical images at every 0.8 microns.

2.3.1.1 Analysis of cell dimensions

Cells were visualised using a phase contrast mode of confocal microscope in parallel with TAT network visualisation. The images were later analysed in FIJI according to the steps illustrated in Figure 2.1.

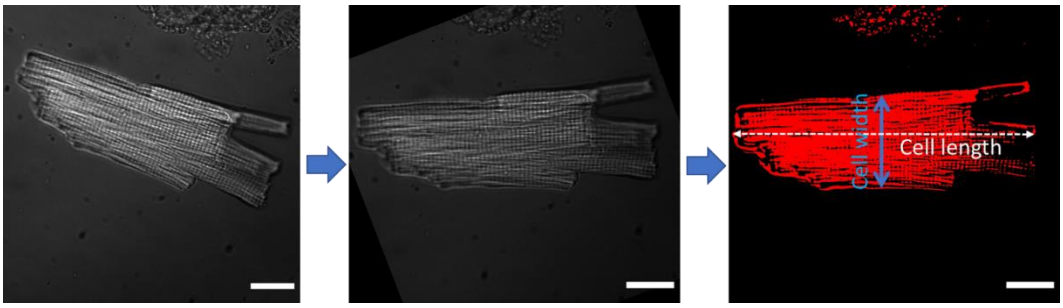

Figure 2.1. Schematic illustration of the cell dimension analysis. Left. Original phase contrast image of LV myocyte. Middle. Image was rotated to place myocyte horizontally. Right. Image was thresholded to highlight the borders. Double arrows selected width and length. Bars -15 µm.

2.3.1.2 The TAT network analysis

Offline analysis of the TAT network parameters was performed simultaneously in Fiji (Schindelin et al. 2011) using a custom made macro. The macro combines the analysis of TAT density as described (Schobesberger et al., 2017), image processing for power of regularity analysis and image processing for analysis of

TATS skeleton and directional analysis accordingly to the protocol in (Wagner et al., 2014). The power of regularity of T-tubules was counted by Fast Fourier Transformation in a custom-made Matlab2016 (The MathWorks, Inc., Natick, MA, USA) accordingly to a protocol of (Lyon et al., 2009).

The image processing and analysis steps of this macro are present in Figure 2.2.

Steps 8 and 9 were performed in custom-made Matlab macro (Lyon et al., 2009). Briefly, macro converted the waveform obtained on the step 7 into power-frequency graphs by a Fast Fourier transformation as described before (Ibrahim et al., 2011). The output of the calculation is a power peak (Figure 2.2), which maximum serves as an indicator of how regular T-tubules appear at a physiological distance of ~2µm.

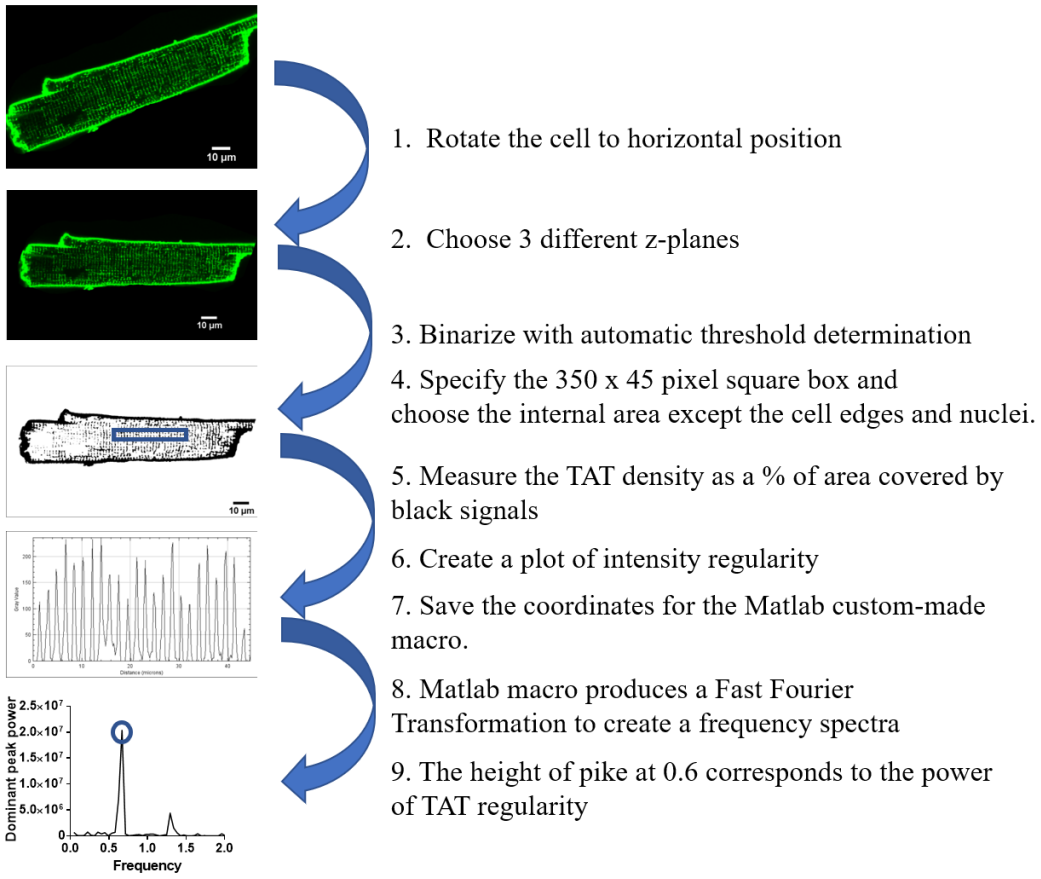

Figure 2.2. Image processing steps for the analysis of TAT density and regularity.

Then the macro turned back to the step 2 and performed a directionality analysis accordingly to (Wagner et al., 2014). The main steps are present in Figure 2.3.

The “Analyse Skeleton (2D/3D)” plugin was used to analyse the skeletonized TAT structure. The typical data table produced by this analysis contained the following skeleton parameters: #branches, #junctions, #end-point voxels, average branch length, #triple points, #quadruple points, and maximum branch length. Two main parameters were derived from this table: the total skeleton length per area and the number of junctions per area. Normalized skeleton length per area was calculated by the following formula:

$$Total\ length\ per\ area = \frac{\sum(\#\text{branches} \times \text{average branch length})}{area} \quad (1)$$

Total number of triple junctions per area was calculated using the following formula:

$$Number\ of\ junctions\ per\ area = \frac{\sum \#\text{tripple points}}{area} \quad (2)$$

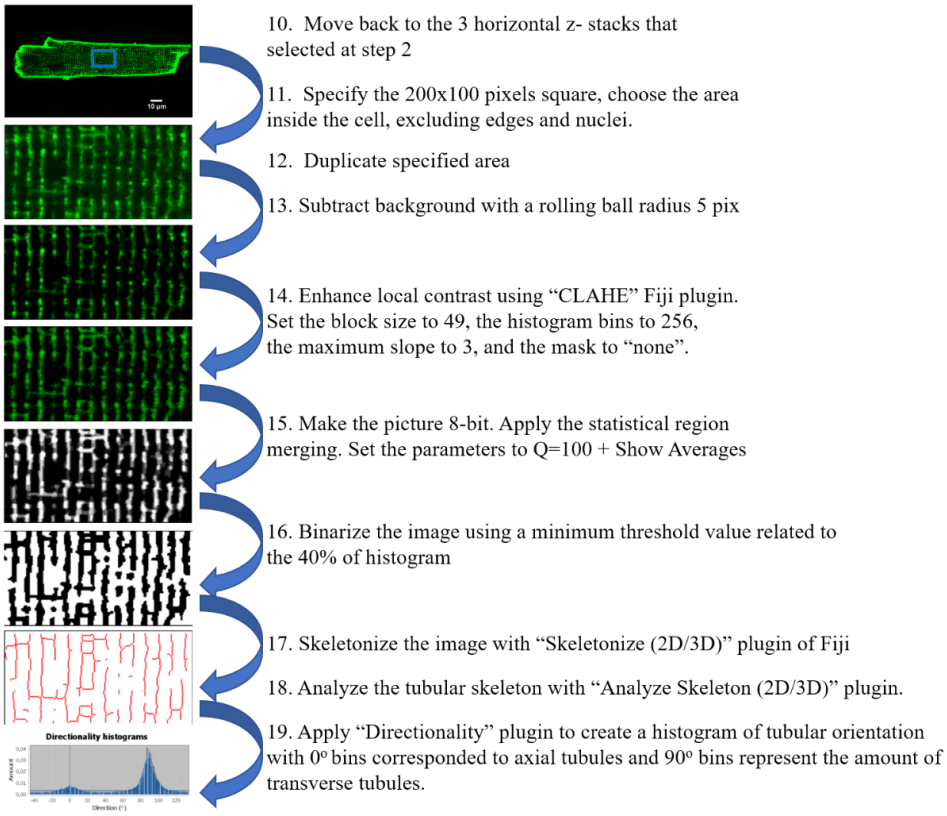

Figure 2.3. Image processing steps for the study of TAT skeleton and directional analysis of TATS.

The “Directionality” plugin (http://fiji.sc/Directionality) was used at step 19 to calculate the histogram of the TATS distribution in different directions. The cell image was rotated into horizontal position that made the A-tubules were represented around the 0° bin, whereas the transversal components were groupped around the 90° bin. The healthy ventricular myocytes have a double peak histogram (Figure 2.3 step 19) with a higher peak of transverse TATS than the axial TATS. The analysis of peaks was performed in Fiji, by summarizing all the values corresponding to the 0±10° bin for the axial and 90±10° bin for the transverse tubules. Then the obtained sums were multiplied by the normalized skeleton length from step 18 to get the normalized length of TATS aligned axially or transversally, respectively.

2.3.2 Immunofluorescence labelling

Immunocytochemical staining of fixed myocytes was performed accordingly to the protocol described in (Schobesberger et al., 2017). The primary antibodies were used against: the main pore forming subunit LTCC $Ca_v1.2$, ryanodine receptor type 2, RyR2 and the caveolae protein Cav3. **Error! Reference source not found.**Table 7 contains the list of antibodies used and corresponding concentrations and fixation type used. The myocytes suspension contained approximately 2000-3000 cells was plated at the laminin-coated 13 mm borosilicate glass coverslips. After 40-50 min of attachment, the cells were washed with PBS, and then fixed for 10 min with 4 % PFA in PBS at room temperature or for 10 min with pure methanol at -20 ^{o}C. Then the coverslips were washed 3 times with PBS containing 0.1 % tween (PBS-T). In case of PFA fixation 15 min of permeabilization step with the 0.1 % Triton X-100 was performed. Then the cells were washed two times with PBS-T. The blocking step was performed by incubating the coverslips in PBS-T contained 3 % of goat serum and 0.3% of Triton X-100 for 1 h. After that, the blocking solution was aspirated and without washing the cells the primary antibody in blocking buffer was applied overnight at 4^{o}C. On the next day the coverslips were washed three times with PBS-T for 5 min each. The secondary antibodies solution in blocking buffer was applied to the myocytes for 2 hours at room temperature and in the dark. As negative control myocytes were stained following the same protocol but without the application of the primary antibody. After two washes with PBS-T the

coverslips were mounted onto partly frosted coverslides (Thermo Scientific, Shandon TM # 6776108) using mounting medium (Vector Labs, Vectashield mounting medium). At the end the coverslips were sealed onto the coverslides with transparent nail polish and kept at 4°C prior to imaging.

2.3.2.1 Confocal imaging of protein arrangement

The imaging of the immunocytochemical staining molecules was performed in the Facility for Imaging by Light Microscopy of Imperial College London with a Zeiss LSM780 Laser Scanning Confocal Microscope (Carl Zeiss, Germany) equipped with a x63 magnification Zeiss DIC Plan-Apochromat oil-immersion objective (numerical aperture 1.4; Carl Zeiss, Germany). Also $Ca_v1.2$ and RyR2 colocalization visualization was performed at Unit of Advanced Optical Microscopy in Humanitas Research Hospital equipped with Leica SP8 Laser Scanning Confocal Microscope, equipped with a diode white laser. To visualize the specific secondary dyes 488, 552 and 638 lines of the white laser were used. Z-stack images were recorded at a distance of 0.5-1 μm. Image processing was performed with the freeware Fiji (Schindelin et al., 2012). The image analysis included two parts. First part included the signal density estimation according to the steps № 1-9 from TAT network analysis, the second was related to the colocalization between two proteins. The colocalization of two dyes was performed in Imaris (Ver. 7.4.2, Andor Technology Ltd) or Jacob plugin of Fiji (Bolte et al., 2006).

Table 7. List of antibodies used for immunolabelling experiments

Antibody	Company and number	Species	Concentration	Fixation
$Ca_v1.2$	Alomone labs, ACC-013	Polyclonal rabbit	1:200	Methanol
Ca_vb2	Abcam, ab93606	Monoclonal mouse	1:200	PFA
RyR2	Sigma HPA020028	Polyclonal rabbit	1:200	Methanol
RyR2	Thermo-scientific, C3-33	Monoclonal mouse	1:150	Methanol
Cav3	BD biosciences, 610421	Monoclonal mouse	1:1000	PFA
Alexa Fluor 488	Invitrogen,	Goat anti -rabbit	1:1000	
Alexa Fluor 594	Invitrogen,	Donkey anti-mouse	1:1000	
Abberior Star 580	Abberior	Goat anti -rabbit	1:1000	
Abberior Star 635	Abberior	Goat anti-mouse	1:1000	

2.3.2.2 Super-resolution stimulation emission depletion microscopy (STED) of $Ca_v1.2$ and RyR2 colocalization in ventricular myocytes

STED experiments were performed with assistance of Dr. Tilo Schorn at the Unit of Advanced Optical Microscopy of Humanitas Research Hospital, Milan, Italy. STED xyz images were acquired in bidirectional mode with a Leica SP8 STED3X confocal microscope system. Anti-rabbit Abberior STAR 580 antibody was excited with a 580 nm-tuned white light laser (WLL) and emission collected from 583 to 634 nm, anti-mouse Abberior STAR 635 antibody was excited with a 635 nm-tuned

WLL and emission collected from 640 to 797 nm. Line sequential acquisition was applied to avoid fluorescence overlap. It was applied a gating between 0.3 to 6 ns to avoid collection of reflection and autofluorescence. 775 nm pulsed-depletion laser was used for Abberior STAR 580 excitations (60% of power) and Abberior STAR 635 excitations (10% of power). Images were acquired with Leica HC PL APO CS2 100x/1.40 oil STED White objective. Gated pulsed-STED was applied to Abberior STAR 580 and Abberior STAR 635 fluorophore. Signal density and regularity were analysed in the same manner as described above for the TAT system. Colocalization analysis was performed by Jacob plugin (Bolte et al., 2006) in Fiji. The Pearson and Manders colocalization coefficients were determined.

2.3.3 Scanning Ion conductance microscopy

Scanning ion conductance microscopy (SICM) is a non-contact scanning microscopy technique, which empowers three-dimensional imaging of surface structures on live cells with resolution of up to ≤ 20 nm (Figure 2.5; (Novak et al., 2009)). This methodology is based on the evidence that the ion current through the glass pipette filled with electrolyte drops down when the pipette goes close to the surface of the sample (Ion-conductance et al., 1987; Korchev et al., 1997). Non-contact scanning is provided by a hopping mode of scanning with a distance-modulated feedback control system which keeps the ionic conductance and sample-pipette distance constant. The hopping mode of SICM with the usage of nano-pipette (internal diameter (I.D.) of 100 nm) allows visualizing even a very tiny nano-structures such as microvilli (Novak et al., 2009)

The sharp pipette (with I.D. of 100 nm) was generated from the borosilicate glass capillaries BF100-50-7.5 (IntraCel) with the P-2000 laser puller (Sutter Instrument). The dish with isolated cells was placed on the piezoelectric stage which is able to move in X and Y directions. The nano-pipette was filled with electrolyte and fixed in the piezo-actuator that can move in Z- direction. When the tip of the pipette reached the solution the ion current was established between the nano-pipette and the electrode in the bath. The software IonView (IonScope, UK) was used to position the pipette on top of the cell and surface topography reconstruction. The map of surface is stored then on PC allows to precise position

of pipette to desired location for local drug application (Nikolaev et al., 2010) or switching to cell-attached patch-clamp recordings (Bhargava et al., 2013).

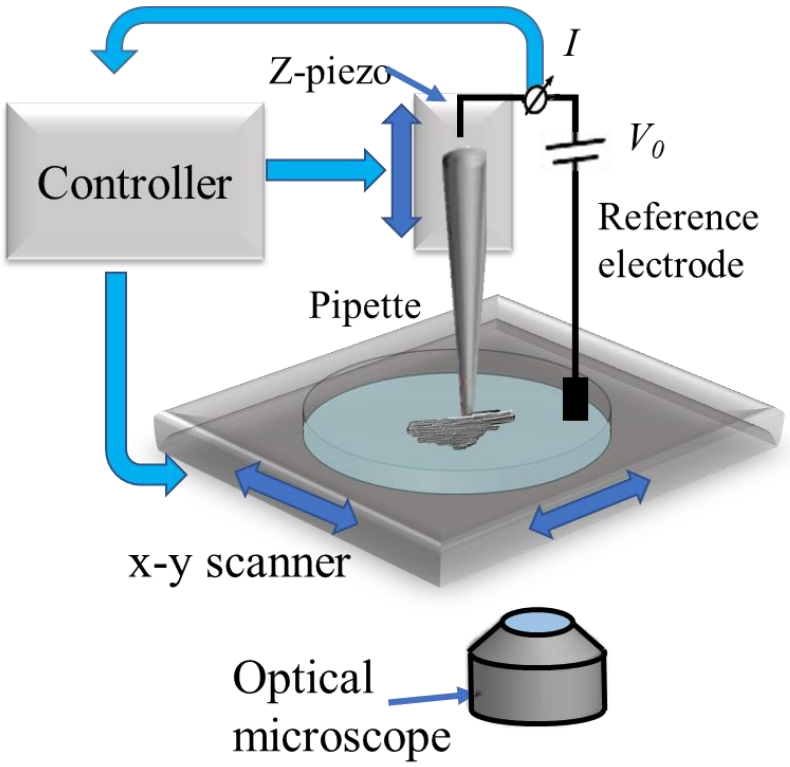

Figure 2.4 Scanning Ion Conductance Microscope. The scanning pipette is mounted on a piezo- translation platform and connected to a patch-clamp amplifier (controller). The amplifier's output drives a feedback control for the pipette's piezo, which provides a Z-only directional movement (top and bottom). Samples are placed on the stage which can make a scanning in 2 directions (X Y). Computer-controlled software provides a user interface to control the set-up. From (Bhargava et al., 2013).

2.3.3.1 Surface structure analysis. Z-groove index

Surface topography was analysed in SICM Image Viewer. To quantify surface structure development Z-groove index was used (Gorelik, Yang et al. 2006). Z-groove index is a ratio of total length of the Z-grooves present on 10 x 10 µm scan (Figure 2.5) to the hypothetical value which represent the length of Z-grooves on the ideal ventricle myocyte (50 µm). Normally healthy ventricular cardiomyocyte

has 65-80% Z-groove index (Gorelik et al., 2006; Schobesberger et al., 2017). Also the amount of T-tubule openings per image was counted manually.

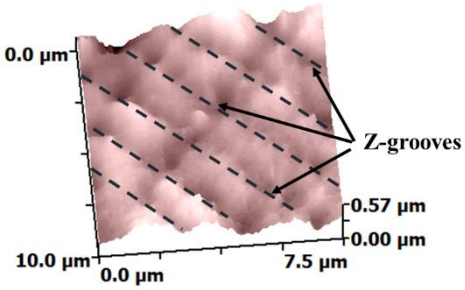

Figure 2.5. SICM: a typical scan of 10x10 µm showing the Z - grooves.

2.4 Functional investigations

2.4.1 Super-resolution scanning patch-clamp technique

Super-resolution scanning patch-clamp is a novel technical approach which allows direct investigation of ion channel clustering in the cell surface with a high resolution up to 20 nm (Bhargava et al., 2013). This technique presents a combination of Scanning Ion Conductance Microscopy with a cell-attached mode of a patch-clamp technique (Korchev et al., 1997). The major advantage of this methodology is that SICM could visualize surface membrane topography and piezo-actuator can bring the pipette to desired location of the surface membrane. The main steps of Super-resolution patch clamp technique are illustrated in Figure 2.6. SICM requires a very sharp (~100 nm I.D.) pipette to detect a nanoscale changes in cell topography. On the other side, the probability of obtaining the ion current during patch clamp recordings is direct proportional to the size of pipette. Controlled clipping of the tip of pipette allows precise widening of the pipette I.D. to ~300-400 nm that significantly increases the probability of channel occurrence (Bhargava et al., 2013).

The setup of Super-resolution Patch Clamp technique were based on the Axopatch 200A patch-clamp amplifier (Molecular Devices, USA), the currents were digitized using Digidata 1200B and a pClamp 10 data acquisition system (Axon Instruments; Molecular devices).

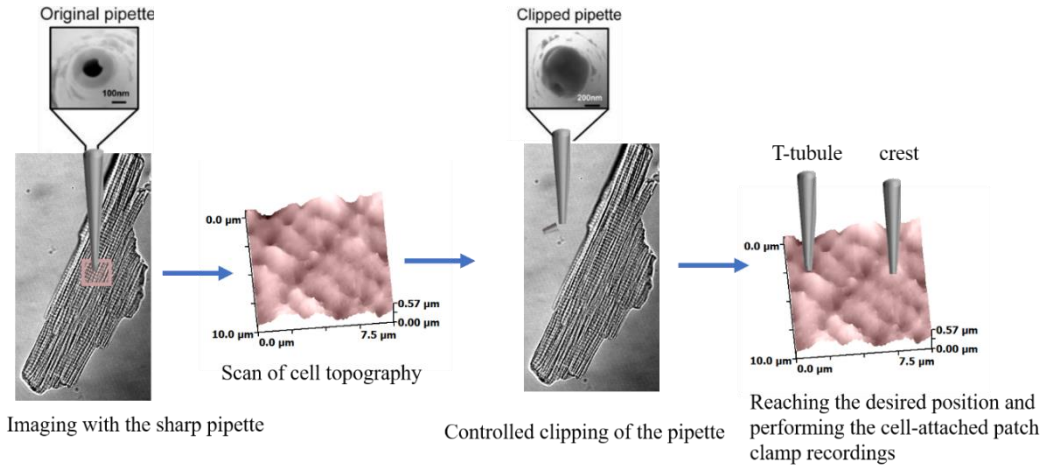

Figure 2.6 Main steps of the Super-Resolution Patch Clamp technique

2.4.1.1 Pipette clipping procedure

Pipette clipping procedure is applied directly after the generation of cell topography. The pipette is positioned 10-20 um out of the cell surface, on the place free from cells. The piezo-control is switched to manual mode, in which it doesn't control the distance to the surface. Then, the pipette is moved down with high velocity (10 times higher the normal rate). This high speed movement results in the crushing of the pipette tip by the bottom of the dish. The tip is become wider which is monitored by changes of the pipette resistance. To obtain desired resistance can require several clipping steps. The most important feature of this technique is a preserved shape of the pipette tip which allow than to perform gigaseal attachments.

Depending of the size of desired patching area pipette size was adjusted. For example T-tubule openings have a restricted size, so the pipettes should have resistance around 30 MΩ (corresponding to ~350 nm ID) to patch only desired area. From the other side, crests are not so restricted in size, so wider pipettes can be used (16-30 MΩ) to increase the chance of channel occurrence.

After clipping the pipette can be positioned back to the cellular microdomain of choice (in this case T-tubule or crest) by clicking the desired place on topography image. Then the feedback was turned off; pipette was lowered until it touches the cell surface and a gentle suction was applied to form a seal. Cell- attached single channel recordings are then performed by the conventional patch-clamp technique.

2.4.1.2 Patch Clamp technique

The patch-clamp technique is used to record the single channel ion currents though the pipette electrode under voltage-clamp. In this condition voltage is constant and the current is directly proportional to the changes of the conductance. When the seal is established the measured current through the electrode is assumed to flow exclusively across the cell membrane proportionally to the membrane conductance (mediated by plasma-membrane ion channels). Patch clamp technique allows studying single ion channel and receptor properties under basic conditions or under drug interaction.

The pipette for ion current recording were used the same as for SICM, pulled from borosilicate glass capillaries BF100-50- 7.5 (IntraCel) with the P-2000 laser puller (Sutter Instrument). Working and reference electrodes were Ag/AgCl electrodes, they were kept and checked to be fully chlorinated. The internal pipette solution contained in mM: 90 BaCl2, 10 sucrose, 10 HEPES, pH=7.4 adjusted with TEA-OH. The external solution includes in mM: 120 K- gluconate, 25 KCl, 2 $MgCl_2$, 1 $CaCl_2$, 2 EGTA, 10 Glucose, 10 HEPES, pH=7.4 was adjusted with NaOH.

The surface of the cell were reached by manual or piezo-controlled approaching which used a small voltage pulses (1–5 mV, 2–10 ms) to check the current through the pipette. Near the surface the resistance substantially (by 10-15 %) increases and approaching stops. Then a small gentle suction through the syringe is applied and a high resistance of contact between surface and pipette is established. The contact is monitored in Clampex software as rise in pipette resistance, a formation of gigaseal (1-16 GΩ) is an evidence of a good contact with the membrane. We worked in cell-attached patch-clamp configuration. This mode allows recording of single channel fluctuation with the range of several picoamperes. We applied this methodology to study single LTCC current behaviour in ventricle myocytes.

2.4.1.3 Single L-type calcium channels analysis

Single LTCCs were characterized and identified by their voltage dependent properties (Rosenberg et al., 1988). The current-voltage relationship is characterized by -30 mV to 30 mV voltage pulses applied from the held potential -80 mV. Analysis was performed according to established protocol from (Bhargava

et al., 2013). Single channels were sampled at 10 kHz and filtered at 2 kHz (-3 dB, 8-pole Bessel). The analysis of channels data was performed by Clampfit version 10.6. A liquid junction potential, -16.7 mV, was calculated before, in (Sanchez-Alonso et al., 2016). All the potentials presented in this work are shown after subtraction of the liquid junction potential.

To determine the presence or absence of LTCC in the patch the sweeps from holding potential to a step with maximal availability (-6.7 mV) were checked for stepwise- like current fluctuations. To characterize the LTCC at least 100 sweeps from holding potential to -6.7 mV and three protocols of different voltages were performed. When no second level of spikes is observed in any of the sweeps the recording is classified as one channel. Then several parameters of LTCC behaviour were analysed.

Occurrence of LTCC was calculated as a percentage of the recordings showing the LTCC activity to the total number of seals made in this position. Occurrence of single- channel L-type calcium current can characterize the distribution of channels across the different microdomains. It can be useful to show, for example redistribution of LTCC in failing myocytes versus normal ones. The occurrence of the channels doesn't take into account the possible multichannel patches. To overcome this limitation we used a single channel density which calculated as the total number of channels found in that cellular microdomain to the sum of all the patched membrane area (Poulet et al., 2020). We estimated the pipette diameter (d) from the pipette resistance (Ω) by the following formula:

$$d = 2/(0.18759125141643 * \Omega) \quad (3)$$

The membrane area under the patch pipette was calculated according to the following formula:

$$area = \pi \times (d/2)^2 \quad (4)$$

And the density of the channels was calculated via the ratio between the total numbers of recorded channels to the total patched area. This approach takes into account the multiple number of channels and variations of the pipette resistance.

Functional analysis of LTCC included the determination of the open probability (P_o) and voltage- current characteristics. Open probability characterizes fast gating between channels "modes" (Cavalié et al., 1986) and how the available channel moves between the closed, open, and inactivated states during depolarization (typically in order of milliseconds, to 10 ms). We determined the Po by the Clampfit automatic analysis from 10-20 sweeps at -6.7 mV for each cell. Each cell was recorded only once, and only one value of Po per cell was used. In case of multichannel patches, Po calculated from multichannel fluctuation was divided by the n of the channels.

Channel conductance was calculated from protocols with sweeps to different voltages in the range of -30 to +5 mV. Then the amplitudes of fully resolved openings plotted against the test potential and the channel conductance determined as a slope of I-V curve.

2.4.2 Optical mapping of intracellular Ca^{2+} waves in single myocytes

Optical mapping of Ca^{2+} waves was performed in single cell preparations according to the protocol described in (Glukhov et al., 2015). Freshly isolated myocytes were placed at 13 mm glass coverslips as described in paragraph 2.2.2. Firstly 100 mg of Pluronic Acid was dissolved in 4 ml of DMSO under heating in water bath. Fluo-4AM stocks were prepared in advance by dissolving 5 mg of Fluo4-AM (Invitrogen) in 91 µL of DMSO with Pluronic acid. Then it was vortexed and aliquoted by 5 µL. The working dye solution contained 10 µmol/L Fluo4-AM was prepared via dilution of one aliquot in 500 µL of HBSS. The cover glasses were placed in petri dishes and covered with enough dye solution. After 30 min, the cells were washed with a dye-free HBSS and left for 20 min to allow dye de-esterification. Then the cover glass was placed in the chamber of inverted microscope equipped with a MiCam Ultima-L CMOS camera (SciMedia, USA Ltd, Costa Mesa, CA). Fluo-4 was excited with 488 nm filtered light and fluorescence was collected through 520 nm filter at frequency 500 fps. Acquisition was performed with 20X objective that produced a resolution 1.5–2 µm/pixel. Two experimental protocols were used: 1) recordings of induced Ca^{2+} waves under the field stimulation with square 10 ms pulses at rising frequencies from 0.5 to 4 Hz

and 2) study of spontaneous Ca^{2+} activity during 16 s rest period after 1 min of 4Hz stimulation.

Analysis of Ca^{2+} waves and transients parameters was produced in Brainvision Ana v. 1208. Spontaneous Ca^{2+} waves that occupy only a piece cell surface (local) were separated from ones propagated through the cell surface (propagated waves). Their frequencies were analysed separately.

2.4.3 Confocal measurements of intracellular Ca^{2+} changes

The experiments of confocal measurements of intracellular Ca^{2+} changes were performed according to established protocol (Bannister et al., 2016; Lyon et al., 2009). Fluo4-AM dye stock solution was prepared as described above. Myocytes dye loading was performed in suspension by addition of 500 µL of cells in Enz buffer to 5 µL of Fluo4-AM stock. After 30 min, the cells were centrifuged at 600 rpm for 1 min and supernatant was discharged. The pellets were re-suspended in the Tyrode normal solution, which contained in mM: 140 NaCl; 6 KCl; 10 Glucose; 10 HEPES; 1 $MgCl_2$; 1 $CaCl_2$; pH was adjusted to 7.4 by 1M NaOH. After 20 min, the suspension was placed on the glass bottom of experimental chamber equipped with perfusion system. The imaging was performed with 40x objective of inverted microscope equipped with a laser scanning confocal system (BioRad Microscience Ltd., Hemel Hempstead, Hertfordshire, UK). Ca^{2+} imaging was performed along the line placed near the centre of the cell and parallel to its long axis at 500 fps. Myocytes were perfused with Tyrode solution at 37ºC. Experimental protocol included 1 min of myocytes field-stimulation at 1 Hz, and recording of 3-5 Ca^{2+} transients and 16-18 s of Ca^{2+} activity at rest. The analysis of Ca^{2+} transients and Ca^{2+} sparks was made in custom-made macro in Fiji.

2.4.3.1 Ca^{2+} transient analysis

Custom-made macro was used to determine the Ca^{2+} transient parameters, as shown (Lyon et al., 2009). It produced the average profile of the fluorescence (Figure 2.7B) and determined the starting point, endpoint and maximum for each of the transients, then produced the general parameters, such as normalized amplitude (F/F0), duration (ms), time to peak (ms), time to F50 (ms), time to 80% of repolarization (ms) and time constant of decay or Tau (ms).

To determine synchronicity of Ca^{2+} releases across the cell we applied the method similar to (Louch et al., 2006). Briefly, the steps of the macro code included: determination of the half-maximum of the peak Ca^{2+} fluorescence (F50 value) for each of the transient. Then the part of the scan starting from the beginning of the transient till the maximum was duplicated for each transient and the threshold was applied using F50 value (Figure 2.7C). Then for each pixel of the line it determined the time from staring point to reach F50. The resulting profile of time to F50 was averaged across all Ca^{2+} transients. Standard deviation of this profile was used as desynchrony-index of Ca^{2+} release (Louch et al., 2006).

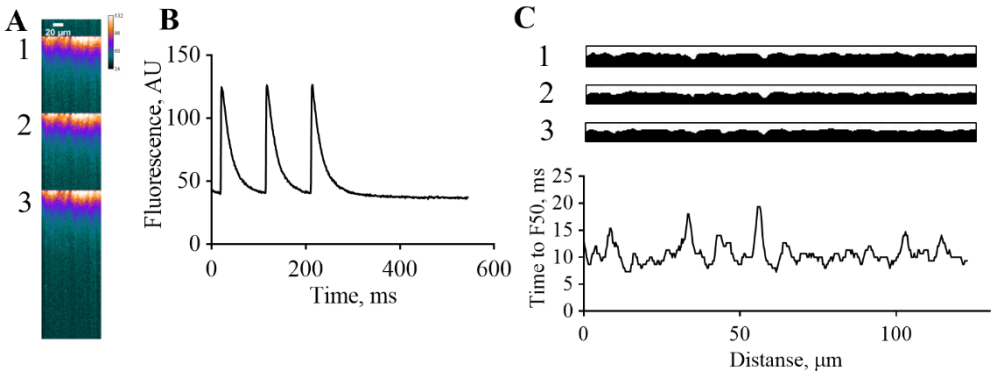

Figure 2.7. Main steps of the Ca^{2+} transient analysis. A) Linescan of 3 consecutive Ca^{2+} transients. B) Fluorescence profile that used for the analysis of Ca^{2+} transients parameters. C) Time to peak parts from each transient showed in A binarised with threshold F50 value. Bottom: the mean of 3 TTF50s obtained from Ca^{2+} transients showed above.

2.4.3.2 Ca^{2+} sparks analysis

The SparkMaster plugin (Picht et al., 2007) in Fiji with 4.2 determination criteria and 25 background was used to analyse Ca^{2+} sparks. SparkMaster plugin automatically calculates several parameters of Ca^{2+} sparks such as: amplitude (F/F0); Half maximum full width (µm); Half maximum full duration (ms); time to peak (ms); and Tau (ms). The linescan image was cut horizontally to exclude the parts with waves and better Ca^{2+} spark determination. According to literature data (Cheng et al., 1993) sparks are local Ca^{2+} releases, so we excluded a very long (>150 ms duration) and wide events (>4 µm full width).

Two additional important parameters were estimated according to the (Kolstad et al., 2018): Ca^{2+} spark mass, a parameter that is proportional to the amount of Ca^{2+} released through an average Ca^{2+} spark and total Ca^{2+} spark mediated Ca^{2+} leak. The mass of Ca^{2+} spark was calculated according to the following formula:

$$Mass = Amplitude \times Full\ Width\ Half\ Maximum \times Full\ Duration\ Half\ Maximum\ \left(n\left(\frac{F}{F_0}\right) \cdot m \cdot s\right) \quad (5)$$

Spark-mediated Ca^{2+} leak was counted by the following formula:

$$Ca^{2+}\ leak = Mass \times Frequency\ \left(p\left(\frac{F}{F_0}\right)\right) \quad (6)$$

2.4.4 Cell shortening measurements with Ionoptix system

These experiments were performed by Dr. Ivan Diakonov. Cardiomyocyte contractions were measured by the Ionoptix system in which the IonWizard 6.0 software was able to follow the movement of the cell edges, imaging was performed with IonOptix Myocam camera (Ionoptix Corp. Milton, MA). Myocytes in suspension were placed on the glass bottom of the chamber that connected to perfusion system and field stimulator. During experiments cells were perfused with KH buffer at 37 ºC and field stimulated at 0.5 Hz. Single myocytes were selected for the experiments that have a rod shape and followed the stimulation pulses. The contractions were measured at the baseline and after application of the pharmacological agents, when the steady-state contraction was established.

For each condition 10-15 contractions were analysed. The software measured the amplitude of contraction as deflection of cell length during contraction as compared to baseline. Time parameters of contraction were also investigated, such as time to peak and 90 % repolarization time.

2.5 Molecular study

2.5.1 Western blot

The protein expression was studied by western blot analysis. The proteins were extracted from the snap-frozen cell pellets (~4-5 millions of cells). The cells were lysed with 50 µl of RIPA buffer (Sigma) contained protease inhibitor and 1mM dithiothreitol (DTT). Then concentrations of proteins were determined by Bio-Rad

DC™ Protein Assay Kit (Bio-Rad) according to the manufacturer's instructions. 20 mg of proteins were mixed with 4 x loading buffer, heated at 70 °C for 15 minutes, centrifuged and then loaded in 8-10 % polyacrylamide gels. The run was performed at 120 V for 2-3 h depending on the protein size. When the run was finished the proteins were transferred in PVDF membrane during 1 h t 70 V (most of the proteins or overnight at 30 V ($Ca_v1.2$) using Bio-Rad wet transfer system. The transfer was checked by Punseau S (Sigma Aldirich # P7170) staining. Then the membranes were washed with Tris buffer saline (TBS) contained 0.1% of Tween and blocked for 1 h with 5 % non-fat milk. Then the membranes were incubated with the corresponding primary antibodies and left in a rochet at 4 °C overnight. The following antibodies were used: $Ca_v1.2$ (Alomone), Cav3 (BD), pCaMKII (ThermoScientific), pPKA substrate (Cell Signalling) and GAPDH (Invitrogen).

On the next day, the membranes were washed 3 times by TBS-T. Then the membranes were incubated at room temperature with the corresponding secondary antibodies for 1 h goat anti-rabbit (1:100; Thermo Fisher Scientific #31460) and goat anti-mouse -HRP (1:1000; Thermo Fisher Scientific #31430). Secondary antibodies were washed out 3 times with TBS-T. Then the membranes were incubated with the Immobilon™ Western Chemiluminescent HRP Substrate (Merck Millipore) and the chemiluminescence was detected on a Chemidoc™ MP System (Bio-Rad). Analysis of bands density was performed in Image Studio Lite ver. 5.2.1 (LiCOR Biosciences).

2.6 Statistical analysis

All graphs in this work were produced and statistical analysis was performed using GraphPad Prism 6. Normality was tested using the Kolmogorov–Smirnov test. For double comparisons the unpaired Student t-test or nonparametric Mann–Whitney test was used according to the result of normality test. Statistical differences of more than two groups were assessed with the analysis of variance (ANOVA) with Bonferroni correction or Kruskal–Wallis test with Dunn's post-hoc, depending on the normality of the samples. All data are expressed as mean± standard error of the mean (S.E.M.). A value of $P<0.05$ was considered statistically significant.

3 Structural organisation of RV myocytes and comparison with LV

3.1 Introduction

First, we started with the evaluation of cellular membrane organisation and Ca^{2+} handling in healthy RV myocytes. We used LV myocytes as a control because the membrane organisation and Ca^{2+} handling of LV myocytes are well studied (Gorelik et al., 2006; Louch et al., 2004, Lyon et al., 2009).

Differences between ventricles are described in the general introduction; here we summarise the most important ones. Alterations between the RV and LV start from their different embryological origin (Zaffran et al., 2004). Then a huge difference between systemic and pulmonary circulation and chambers shape lead to a complete different working conditions in LV and RV myocytes (Greyson, 2008). Contraction of RV produces large volume changes whereas LV work produces pressure generation (Pouleur et al., 1980).

On the cellular level interventricular differences are species dependent. In rodents, longer AP duration in LV myocytes produces larger Ca^{2+} transients than in RV myocytes. In large mammalians RV myocytes have only deeper notches than LV (Molina et al., 2016). Differences in SERCA2a expression and regulation between ventricles in rats produced longer Ca^{2+} transients in RV myocytes as compared to LV ones (Sathish et al., 2006). Cell contraction is significantly dependent on the amount of Ca^{2+} released, so LV myocytes have stronger and larger contractions as compared to RV myocytes (Sabourin et al., 2018).

Abovementioned differences in cell behaviour could arise from the distinct organisation of Ca^{2+} release microdomains in RV and LV myocytes. ECC in ventricular myocytes relies on the membrane organisation. Sarcolemma membrane in ventricular myocytes folds in a very organized TAT network to maintain a fast propagation of excitation for the simultaneous contraction of the cells (Bers & Despa, 2013). TAT concentrates several important proteins for ECC such as LTCC, NCX, βAR and many others (Bers and Despa, 2013). However, there are many

types of myocytes that lacks of organized TAT network, probably due to a distinct working condition (Richards et al., 2011).

In LV myocytes TAT membrane is the primary place of LTCCs localization (Bhargava et al., 2013; Scriven et al., 2000). This subgroup of LTCCs is coupled with RyR2 in dyads, where the CICR occurs. When the TAT network is sparse, for example, in atrial cell or in failing cells, LTCC distribution become more equalized across different membrane structures and that leads to a characteristic Ca^{2+} cycling properties and makes these cells to be more prone to arrhythmia (Glukhov et al., 2015; Sanchez-Alonso et al., 2016).

Thus, the sarcolemma membrane serves as the organisational scaffold for the ECC in myocytes. We hypothesized that RV and LV myocytes have a profound differences in membrane organisation which promoted alternative Ca^{2+} handling functioning and myocytes contraction.

The main objectives of this chapter were:

1. To study the cell dimensions, surface topography and TAT system organisation in healthy rat RV and LV myocytes.
2. To determine the distribution and colocalization of LTCC, RyRs and Cav3 in RV and to compare it with those in LV myocytes
3. To investigate contraction properties of the RV and LV myocytes.
4. To assess the chamber - specific differences in Ca^{2+} transients and spontaneous Ca^{2+} activity in RV and LV myocytes.
5. To figure out the spatial localization of LTCCs in RV myocytes and characterize their functional behaviour.

3.2 Methods

3.2.1 Surface topography characterisation

Surface topography of live cardiomyocytes was visualized by SICM that used a nano-pipette (ID ~80-100 nm) for non-contact scanning of the topography (Novak et al., 2009). The experiments were performed on freshly isolated myocytes as described in section 2.3.3.

3.2.2 Confocal microscopy of live cardiomyocytes

The TAT network of single myocytes was stained by 10 mM Di-8ANEPPS and visualized by confocal microscopy as describes previously (Section 2.3.1). The images of TAT structure were analysed in Fiji (Schindelin et al., 2012) by custom-made macro, as described in section 2.3.1.1.

3.2.3 Confocal study of Cav3 and $Ca_v1.2$ protein colocalization

Visualization of signal $Ca_v1.2$ with Cav3 arrangement and colocalization was performed at faculty of imaging unit Imperial College London. Cells were plated on a glass 13 mm coverslips and fixed with 4 % PFA. After fixation myocytes were permeabilized (0.2 % Triton X-100, 10 % bovine calf serum in PBS) for 1 h after the PBS washing steps. Then the RV and LV myocytes were incubated with mouse monoclonal anti-Cav3 (dilution 1:200, BD instruments) and rabbit polyclonal anti-$Ca_v1.2$ (dilution 1:200, Alomone labs, ACC-013). After overnight incubation with primary antibodies, secondary Alexa Fluor 488 anti-rabbit (dilution 1:1000) and Alexa Fluor-546 anti-mouse (dilution 1:1000) antibodies were applied. Visualization of protein arrangement was performed with Zeiss LSM-780 inverted confocal laser scanning microscope.

3.2.4 STED study of $Ca_v1.2$ and RyR2 localization

Stimulation emission depletion experiments were performed at the Unit of Advanced Optical Microscopy of Humanitas Research Hospital, Milan, Italy with assistance of Dr. Tilo Schorn. For these experiments cardiac myocytes were fixed with methanol at -20^{o}C. Cells were incubated over night with the following primary antibodies and dilutions: rabbit anti-$Ca_v1.2$ 1:200 (Alomone labs, ACC-013), mouse anti-RyR2 1:500 (Thermo Fisher Scientific, C3-33). After washing, myocytes were incubated for 1 h with the following secondary antibodies and

dilutions: anti-rabbit Abberior STAR-580 1:1000 and anti-rabbit Abberior STAR-635 1:1000. Samples were imaged using a Leica a Leica SP8 STED3X confocal microscope system using a 100x oil objective and a pixel size of 40 nm. Images were analysed in Fiji using Jacob colocalization plugin.

3.2.5 In vivo epicardial mapping

Epicardial multiple-lead recordings were performed by Dr. Stefano Rossi as describes elsewhere (Savi et al., 2016). Briefly, the measurements were performed in anesthetized rats placing an 11×11 electrode array. The array was positioned on the surface of the LV and then moved to the RV. Unipolar electrograms were recorded during normal sinus rhythm or during ventricular pacing via specific protocols at three selected electrodes of the array, using near-threshold, 1-ms cathodal current pulses. Standard procedures (Carnevali et al., 2013; Rossi et al., 2008) were applied to measure conduction velocity (CV), excitability, refractoriness, and mean parameters of ECG.

3.2.6 Ionoptix measurements of cell contraction

Measurements of cell shortening of ventricular myocytes were performed by Dr. Ivan Diakonov. Detailed description is presented in section 2.4.4. Briefly, cells were placed at the glass bottom of a custom-made perfusion chamber and left for 5 min to settle down. Perfusion was performed with KH buffer saturated with oxygen/CO_2 mixture (95%/5%) at 37ºC temperature controlled. Only cells which were following the pace but which did not exhibit spontaneous contractions were selected. The contractions were measured at steady-state.

3.2.7 In *vivo* epicardial mapping

Epicardial multiple-lead recordings were performed by Dr. Stefano Rossi as describes elsewhere (Savi et al., 2016). Briefly, the measurements were performed in ane anesthetized rats placing an 11×11 electrode array. The array was positioned on the surface of the LV and then moved to the RV. Unipolar electrograms were recorded during normal sinus rhythm or during ventricular pacing via specific protocols at three selected electrodes of the array, using near-threshold, 1-ms cathodal current pulses. Standard procedures (Carnevali et al., 2013; Rossi et al.,

2008) were applied to measure conduction velocity (CV), excitability, refractoriness, and mean parameters of ECG.

3.2.8 Optical mapping of Ca^{2+} transients

Optical mapping of Ca^{2+} transients was performed on live cardiac myocytes stained with the Ca^{2+}-sensitive fluorescent dye Fluo-4AM. Detailed description can be found in section 2.4.2. Myocytes studied placed on the glass bottom chamber of inverted microscope equipped with CMOS camera ULTIMA-L (SciMedia, USA Ltd, CA; 500 fps, 1.5–2 μm/pixel). Myocytes were constantly perfused with HBSS and 2 stimulation protocols were applied: 1) to measure Ca^{2+} transients properties: 5 min of 1 Hz followed by 5 s of recording; 2) Analysing the spontaneous Ca^{2+} waves 1 min of 4 Hz stimulation followed by stimulation cessation and 16 s recording.

Ca^{2+} transient properties were analysed in a custom- made code in Fiji, that was applied before for a line scan Ca^{2+} transient analysis (Lyon et al., 2009). Spontaneous Ca^{2+} events were divided into propagated waves (occupied the entire cell surface) and non-propagated waves (occurred only at certain place of cell). Ca^{2+} wave frequency was counted as the number of each Ca^{2+} event per observation time.

3.2.9 Confocal measurements of Ca^{2+} transients and Ca^{2+} sparks

Ca^{2+} sparks and Ca^{2+} transients were analysed from line-scan images acquired by the confocal microscope as described before in (Lyon et al., 2009). Briefly, myocytes were loaded with Fluo4-AM via 30 min incubation in 10 mol/L solution of Fluo4-AM. After washing cells were placed in the glass bottom of a specific chamber of inverted microscope equipped with a laser scanning confocal system (BioRad Microscience Ltd., Hemel Hempstead, Hertfordshire, UK).

Experiment protocol included 1 min of 1 Hz field stimulation followed by recording of few (3-5) Ca^{2+} transients and 16-18 s of rest spontaneous Ca^{2+} activity.

Ca^{2+} sparks were analysed with a SparkMaster plugin (Picht et al., 2007). Ca^{2+} transients were analysed in terms of synchronicity of activation as described (Louch et al., 2006).

3.2.10 Super resolution patch clamp technique with pipette clipping modification

This methodology is described in detail in section 2.4.1. It included the generation of surface topography image by SICM using pipette with ~ 80-100 nm diameter tip, controlled widening of the tip diameter out of the cell surface (Novak et al., 2013) to increase the probability of channel occurrence and approaching the desired topological position (T-tubule or crest). Then the pipette was lowered down until it reached the membrane and a high resistance seal was established. Recordings were performed in cell attached mode of patch-clamp technique as described (Sanchez-Alonso et al., 2016).

In experiments with BayK8644, the 10 mmol/L of drug was added to pipette internal solution. To exclude the rapid LTCC internalization that was observed when cells were bathed in BayK8644.

3.3 Results

3.3.1 Myocytes characterization

To characterize the differences between RV and LV myocytes we first compared their shape. The measurements of cell dimensions were performed in images obtained with phase contrast. The examples of RV and LV myocytes are shown in Figure 3.1.

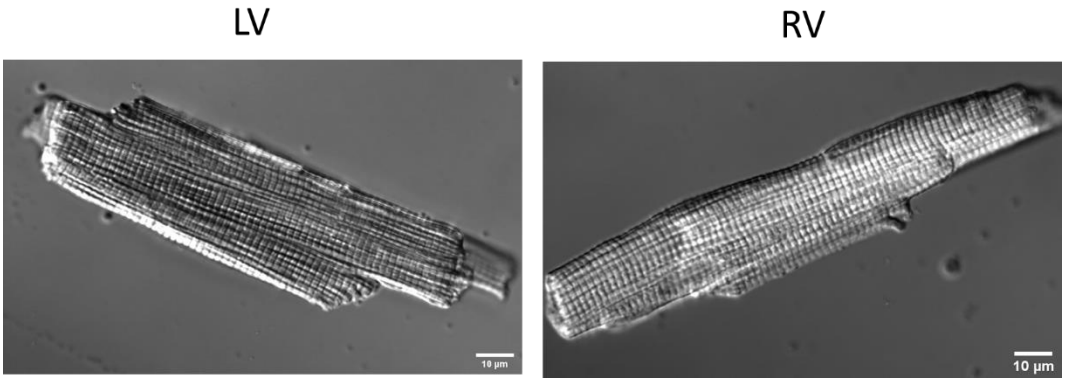

Figure 3.1. Representative images of RV and LV myocytes. Bars are 10 µm.

Analysis of cell dimensions of RV and LV myocytes have shown, that both ventricles have myocytes with a similar length (Figure 3.2A), but RV myocytes are significantly thinner than LV myocytes (Figure 3.2B).

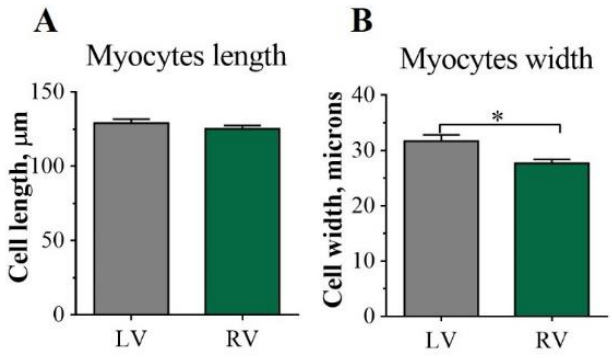

Figure 3.2. Characterization of RV and LV myocytes. A) Cell length and B) cell width (n=40-58 cells, N=3-5 rats, *P<0.05, by unpaired Student t test).

3.3.2 Surface topography

Previously LV myocyte surface topography was characterized by SICM imaging (Gorelik et al., 2006). As has been shown in previous work, LV myocytes have a regularly organized surface with repetitive Z-grooves and doomed crests structures and clear T-tubule openings present in Z-grooves. Surface topography of RV myocytes was found to be pretty much the same as of LV myocytes, with regular structures and Z-grooves (Figure 3.3A). To analyse the surface regularity, we calculated Z-groove ratio as a ratio of the total length of observed Z-grooves to the extrapolated Z-groove length (See 2.3.3.1; (Gorelik et al., 2006)). The average Z-groove ratio is not different between LV and RV myocytes (Figure 3.3B). The density of T-tubule openings that are present on a 10x10 scan was counted manually. RV and LV showed the same mean density of T-tubule opening at the surface (Figure 3.3B).

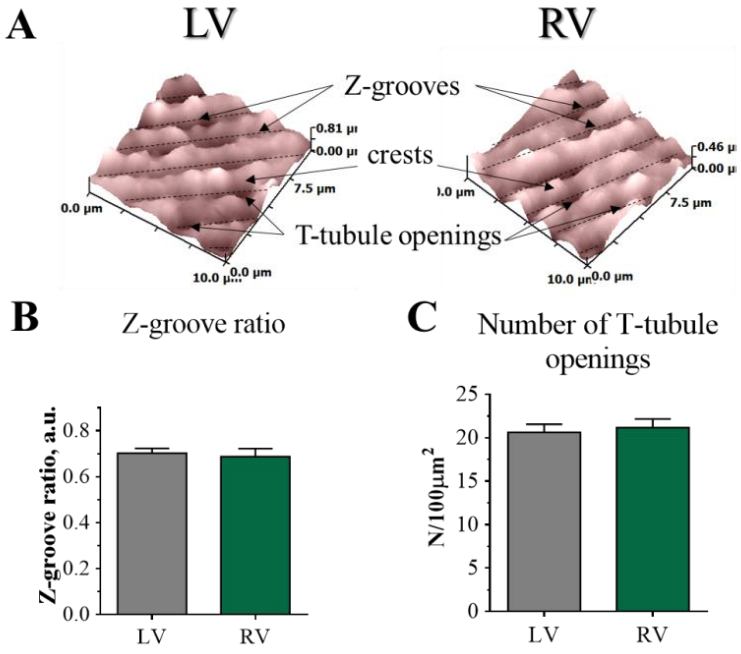

Figure 3.3. Characterization of surface topography of control myocytes. A) 10x10 µm surface scans of the LV (right) and RV (left) topography. Z-grooves, crest and T-tubule openings are marked by the arrows. B) Bar graph, representing the average Z-groove ratio of the LV and RV myocytes. C) Bar graph representing the average number of T-tubule openings per 100 μm^2 area. (n=24-33 cells, N=5-6 rats)

3.3.3 Transverse-axial tubular system

To assess the internal membrane organisation, myocytes were stained with 10 mM Di-8ANEPPS. The examples of confocal images obtained from RV and LV myocytes are shown in Figure 3.4. Internal structure of LV myocytes was well characterized before (Ibrahim et al., 2013). RV myocytes have a well-developed TATS, comparable with TATS of the LV myocytes.

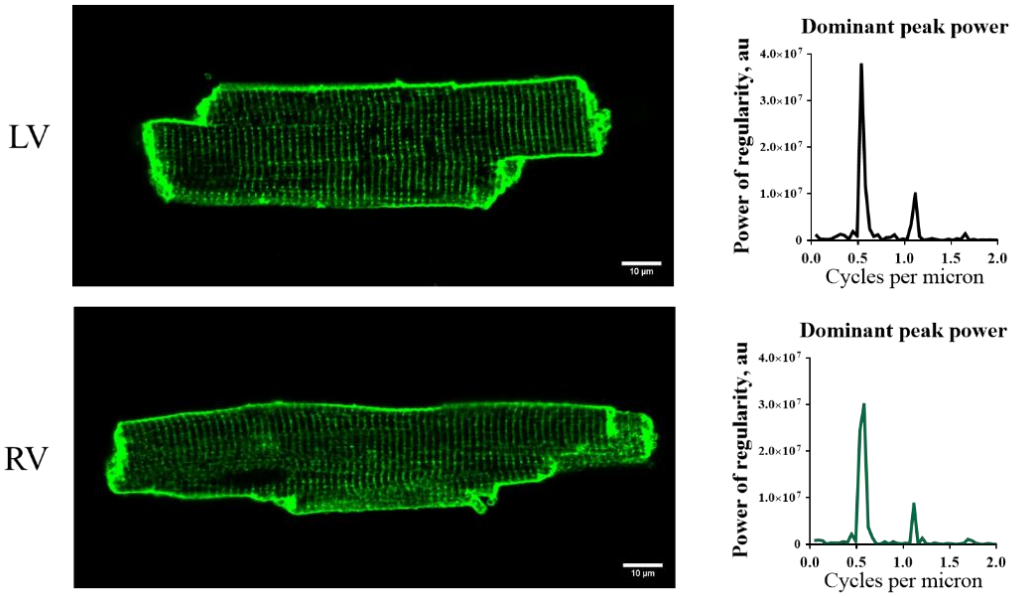

Figure 3.4. Representative images of the TATS of control LV (top) and RV (bottom) myocytes, visualized by Di-8ANEPPS staining and corresponding power peaks of T-tubular regularity.

Statistical analysis of the TAT density and power of transverse oriented tubules (T-tubules) regularity is presented in Figure 3.5. TAT network has similar density in RV and LV myocytes and slightly (not significantly) lower T-tubule regularity in RV as compared to LV myocytes.

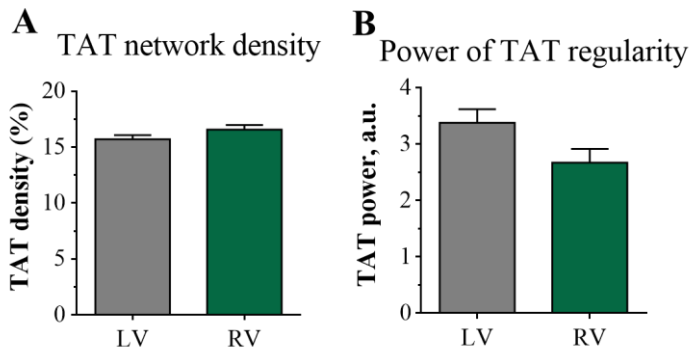

Figure 3.5. Average TAT density and regularity in control RV and LV myocytes. A) Average TAT system density, B) Average T-tubule regularity (n=50-70 cells, N=5-7 rats).

To have a more complete view on the possible differences between RV and LV TAT structure, the new methodology was applied (Wagner et al., 2014). According to this protocol, TAT network image converted into skeletonized picture, the examples of fragments of TAT network before and after skeletonization are shown in Figure 3.6. The length of skeletonized TATS per area was determined, Figure 3.6C. RV myocytes showed a significantly longer length of TATS per area compared to LV myocytes, probably due to the extensive branching. Another parameter that was estimated from the TATS skeletons is the density of triple junctions as a number of triple junctions of three individual, continuously connected tubule components. This parameter was used to characterize the branching complexity of the TATS membrane network (Wagner et al., 2012). RV myocytes showed significantly higher number of triple junctions per area compared to LV myocytes.

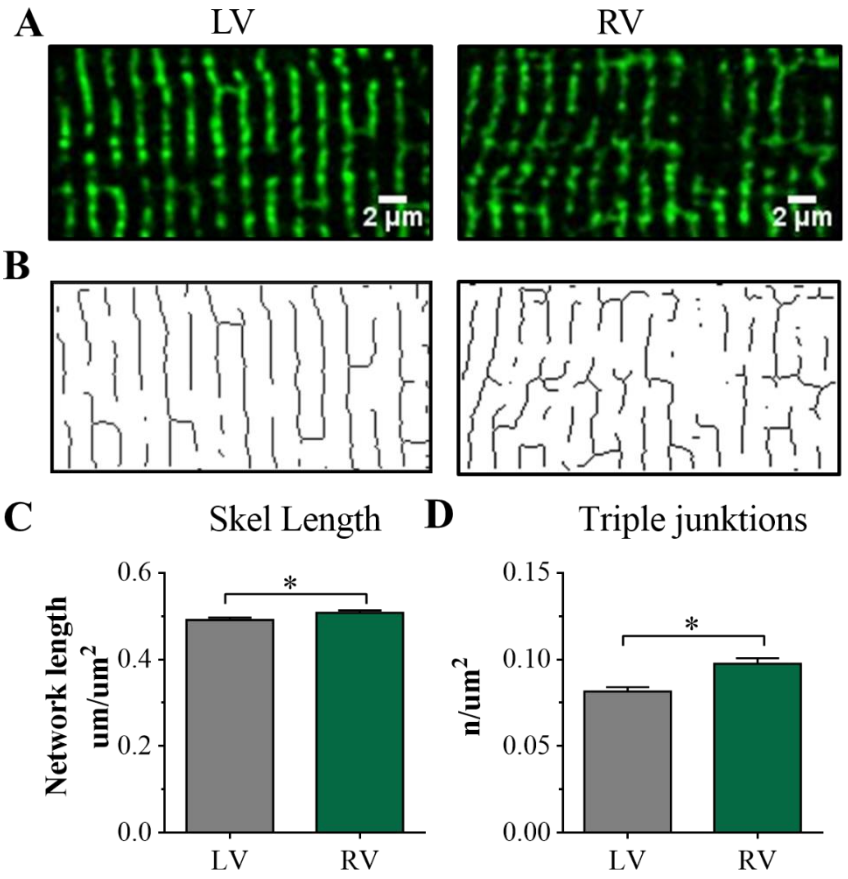

Figure 3.6. Analysis of TAT network skeleton organisation in RV and LV myocytes. **A)** Representative fragments of the confocal images of LV (left) and RV (right) cardiomyocytes. B) TAT network of LV and RV myocytes displayed in A after the skeletonization. C) Average TAT network length in LV and RV myocytes. D) Average density of triple junctions in TAT network. (n=66-70 cells, N=6-7 rats, *p<0.05, by Mann-Whitney test).

Moreover, the TATS skeleton was analysed in terms of tubules directional orientation. This analysis provided information regarding the relative number of tubules arranged in transversal and axil directions. The histograms of the LV and RV myocytes TATS distribution across different directions are shown in Figure 3.7. Both RV and LV myocytes have a two peak distribution with a higher peak of T-tubules and smaller peak of A-tubules. On the right panel in Figure 3.7 histogram subtraction is indicated that LV myocytes have a higher frequency of T-tubules and lower frequency of A-tubules as compared to RV myocytes. Statistical analysis of

the average T-tubule length aligned in transversal and axial directions (Figure 3.8) proved the observations from Figure 3.7.

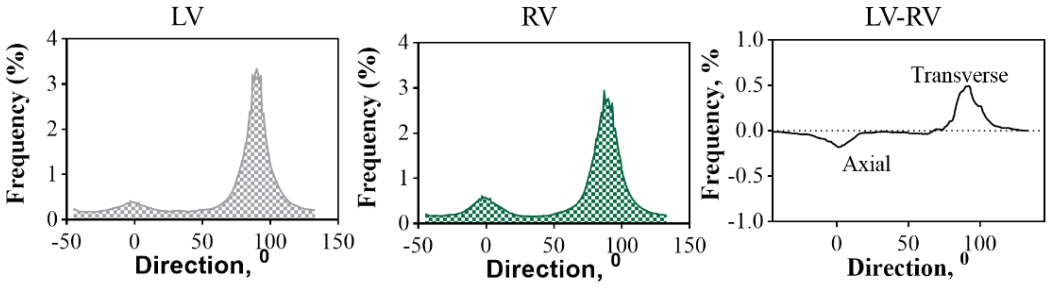

Figure 3.7. Representative histograms of directional distribution of TAT network from LV (left) and RV (middle) myocytes. On the right: histogram subtraction (LV – RV), showing the differences between them.

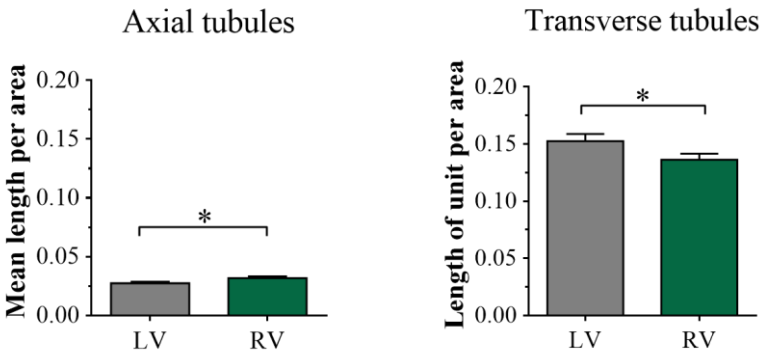

Figure 3.8. Statistical analysis of the TAT distribution in different directions. Left: Mean total length of axial tubules in LV and RV myocytes. Right: average length of transverse elements of TAT system in control LV and RV myocytes. (n=56-70 cells, N=6-8 rats, *p<0.05, by unpaired Student t test).

3.3.4 L-type Ca^{2+} channels and ryanodine receptors immunostaining

TAT network in ventricular myocytes brings LTCC in close proximity to RyRs to ensure simultaneous activation of all the Ca^{2+} release channels (Bers, 2008). We hypothesize that differences in TAT network organisation found between LV and RV myocytes produce alterations in L-type Ca^{2+} channels distribution and their colocalization to ryanodine receptors. In order to study protein arrangement and colocalization we applied STED microscopy. Representative images of control LV and RV myocytes stained by $Ca_v1.2$ (green) and RyR2 (red) are presented in Figure

3.9. Myocytes from both ventricles showed a well-organized arrangement of $Ca_v1.2$ and RyR2, that has in a regular pattern with a ~2µm distance.

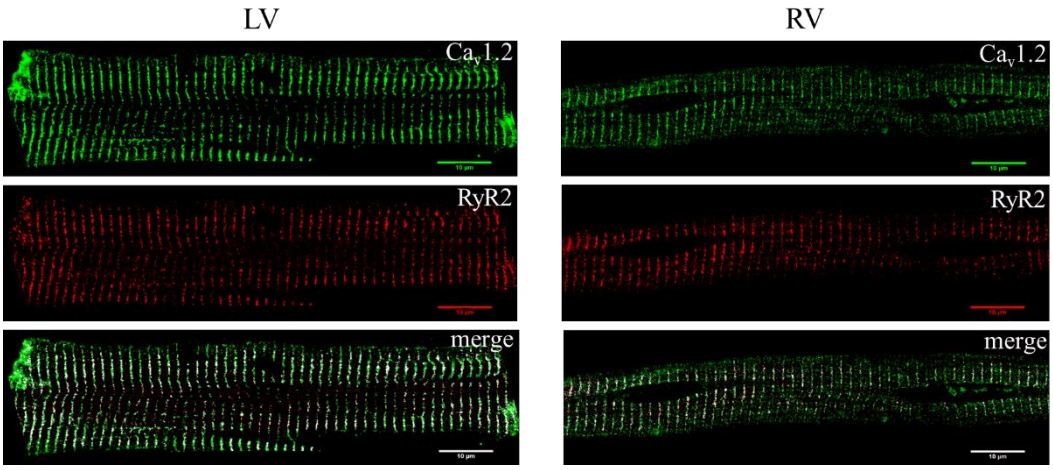

Figure 3.9. Representative STED images of LV and RV myocytes stained with $Ca_v1.2$ and RyR2 antibodies. Scale bar 10µm.

In order to determine the relative levels of the proteins, we analysed the protein signal density as a percentage of cell area occupied by the immunofluorescence signal. LV myocytes have a 21% higher $Ca_v1.2$ density as compared to RV myocytes ($P<0.05$, Figure 3.10). The signal density of RyR2 is similar between LV and RV myocytes (Figure 3.10).

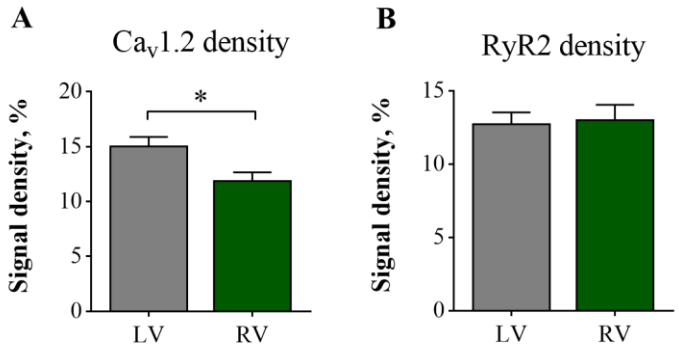

Figure 3.10. Average density of A) $Ca_v1.2$ signals and B) RyR2 signals from control LV and RV myocytes. (n=28-29 cells, N=5 rats, by Mann-Whitney test)

The relative colocalization between $Ca_v1.2$ and RyR2 was analysed via determination of Pearson and Manders coefficients (Figure 3.11, (Manders et al., 1993)). LV and RV myocytes showed similar mean Pearson correlation

coefficients. Also the Manders coefficients for the $Ca_v1.2$ colocalization with RyR2 were close in control LV and RV myocytes. At the same time, the Manders coefficient for the colocalization of RyR2 with $Ca_v1.2$ showed a 3 times higher value in LV myocytes versus RV myocytes ($p<0.01$, Figure 3.11).

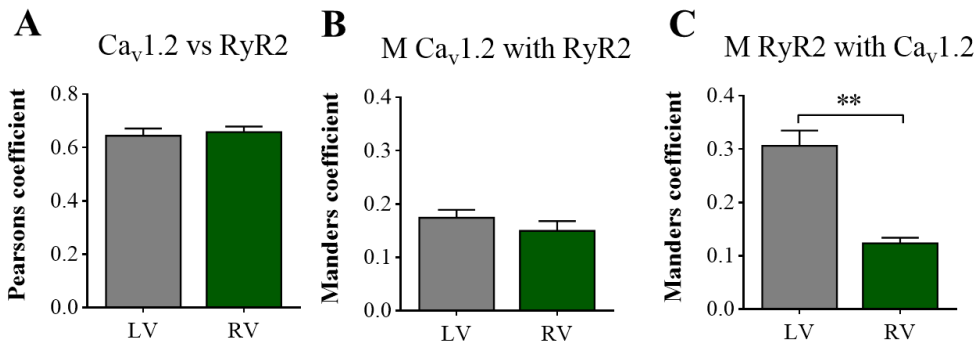

Figure 3.11. Colocalization analysis of $Ca_v1.2$ and RyR2 in control LV and RV myocytes. (n=28-29 cells, N=4-5 rats, **p<0.01, by Mann-Whitney test).

3.3.5 Colocalization of $Ca_v1.2$ with Cav3

Previous studies of LTCC localization in ventricular myocytes showed a great colocalization of this channels with Cav3, the main protein of caveolae (Scriven et al., 2005). Moreover cells with the absent or sparse TAT network, such as atrial myocytes, our recent results indicated a great importance of caveolae for LTCC localization and function (Glukhov et al., 2015). We hypothesize that for RV myocytes which have less organized TAT network, caveolae play a more important role. We studied an immunofluorescence images of RV and LV myocytes stained against $Ca_v1.2$ and Cav3 antibodies. Representative pictures are shown in Figure 3.12.

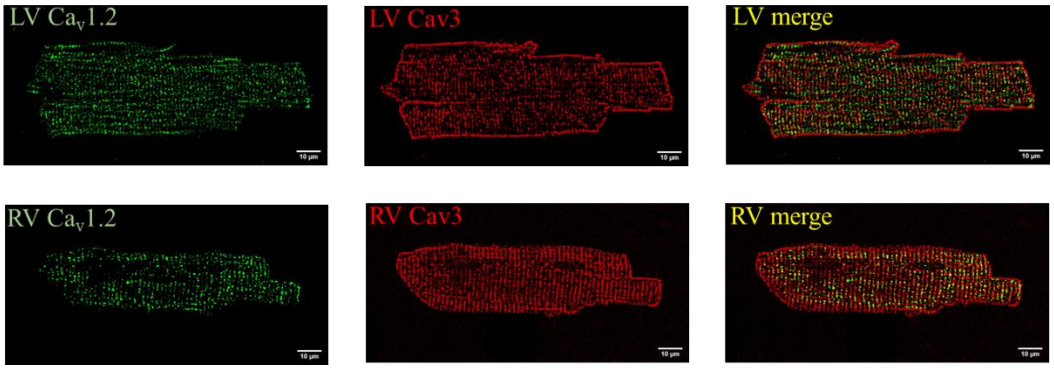

Figure 3.12. Representative confocal images of RV and LV myocytes showing $Ca_v1.2$ (green), Cav3 (red) and merged images (yellow). Bar -10 µm.

The analysis of Cav3 signal density showed that RV and LV myocytes have similar amount of Cav3 (Figure 3.13A). The colocalization analysis of $Ca_v1.2$ and Cav3 revealed no differences in Pearsons coefficient between RV and LV myocytes. Manders coefficients for both $Ca_v1.2$ and Cav3 were higher in RV myocytes than in LV myocytes ($p<0.01$, Figure 3.13C and 3.13D).

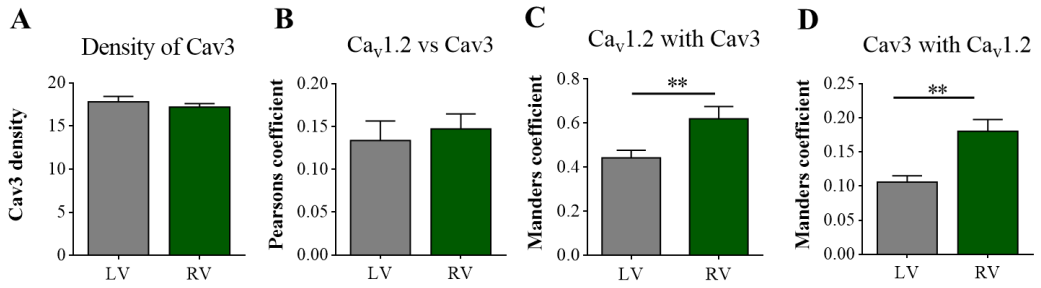

Figure 3.13. Statistical analysis of Cav3 density and colocalization with $Ca_v1.2$.A) Signal density of Cav3 antibody. B) Pearson correlation coefficient of $Ca_v1.2$ with Cav3 in control LV and RV myocytes. C) Manders colocalization coefficient for $Ca_v1.2$. D) Manders colocalization coefficient for Cav3. (n=20-21 cells; N=4 rats; **p<0.01 by unpaired Student t test).

3.3.6 Functional studies of tissue refractoriness, cells contraction and Ca^{2+} transients

As described in section 1.3.1, differences in contraction and Ca^{2+} handling between control RV and LV myocytes have been observed previously in several species.

These alterations are very species-dependent but there are some common changes (Kondo et al., 2006; Sathish et al., 2006).

Firstly we measured the durations of AP *in vivo* using an 11by 11 multielectrode grid placed on the RV and LV. Effective refractory period is mainly determined by APD as the period of membrane depolarization where the sodium currents cannot be activated. QT interval is also connected to the APD and it represents an algebraic sum of all APD (Vaughan Williams, 1982). Both of these parameters were significantly longer in LV compared to the RV (Figure 3.14A and B).The same trend was observed for the activation time and T-wave duration, in LV these parameters were significantly longer than in the RV (Figure 3.14C and D).

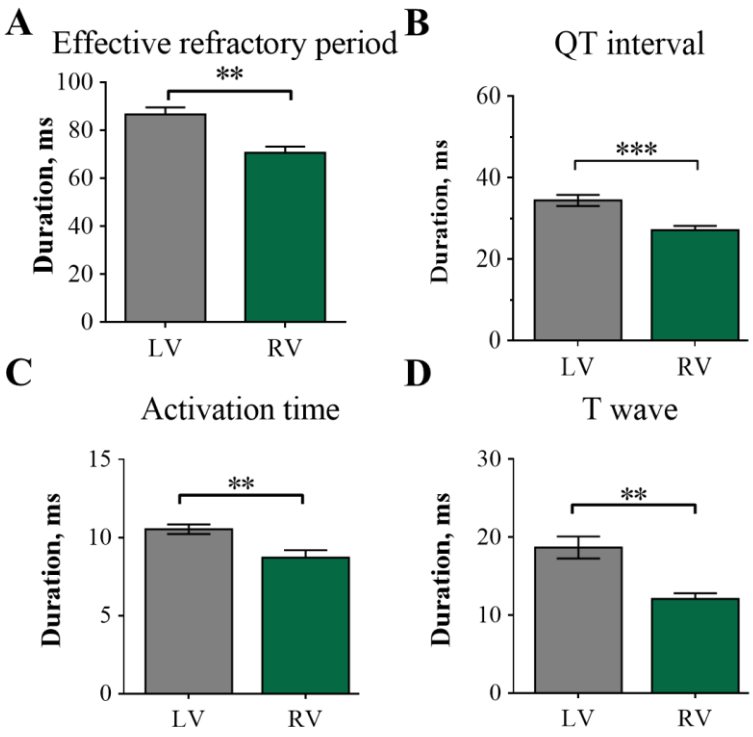

Figure 3.14. Analysis of the electrocardiogram in control tissue. A) The effective refractory period. B) QT interval (an index of ventricular action potential duration), C) QR interval as an indicator of activation time, D) T-wave duration (an indicator of the ventricular repolarization time). (N= 7 rats, * P < 0.05, ** P <0.01, *** P <0.001, by unpaired t test).

Then we characterized the contractions in the rat RV and LV myocytes. The examples of LV and RV contraction traces measured by IonOptix microscope

technique are presented in Figure 3.15A. The amplitude of contraction was similar in RV and LV myocytes (Figure 3.15B). Duration of a RV contraction is longer that in LV myocytes that is seen from a 13 % higher time to peak ($p<0.05$, Figure 3.15C) and a 21% longer decay time ($p<0.01$, Figure 3.15D) of contractions in RV myocytes as compared to the LV myocytes.

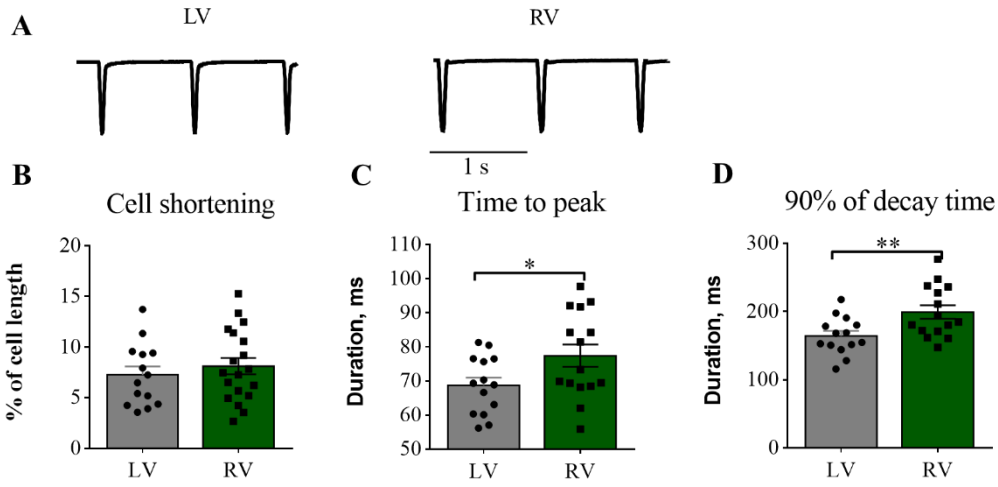

Figure 3.15. Characterisation of RV and LV myocytes shortening. A) Examples of contraction recordings obtained from LV and RV contractions. B) maximal cell shortenings during contractions. C) Time to contraction peak measured in control LV and RV myocytes. D) Duration of 90% of relaxation time observed control LV and RV myocytes. (n=14-19 cells, N=4 rats, *p<0.05, **p<0.01, by unpaired Student t test).

Ca^{2+} transients properties in RV and LV myocytes were analysed from optical mapping (OM) traces of myocytes stained with Fluo-4AM. Representative examples of OM Ca^{2+} transients are shown in Figure 3.16A. The measurements of Ca^{2+} transient amplitude using non-ratiometric dye - Fluo4-AM has a potential risk of false changes due to the alterations in background cell fluorescence, quality of staining, however, there are several reports including this analysis(Louch et al., 2006; Sabourin et al., 2018; Xie et al., 2012). We provide here and in the next chapters the analysis of the amplitude of the Ca^{2+} transients, but without including them into conclusions. RV myocytes have lower amplitude of Ca^{2+} transient than LV myocytes ($p<0.01$, Figure 3.16B). The durations of both time to peak (Figure

3.16C) and 90% of decay time (Figure 3.16D) were similar in control RV and LV myocytes.

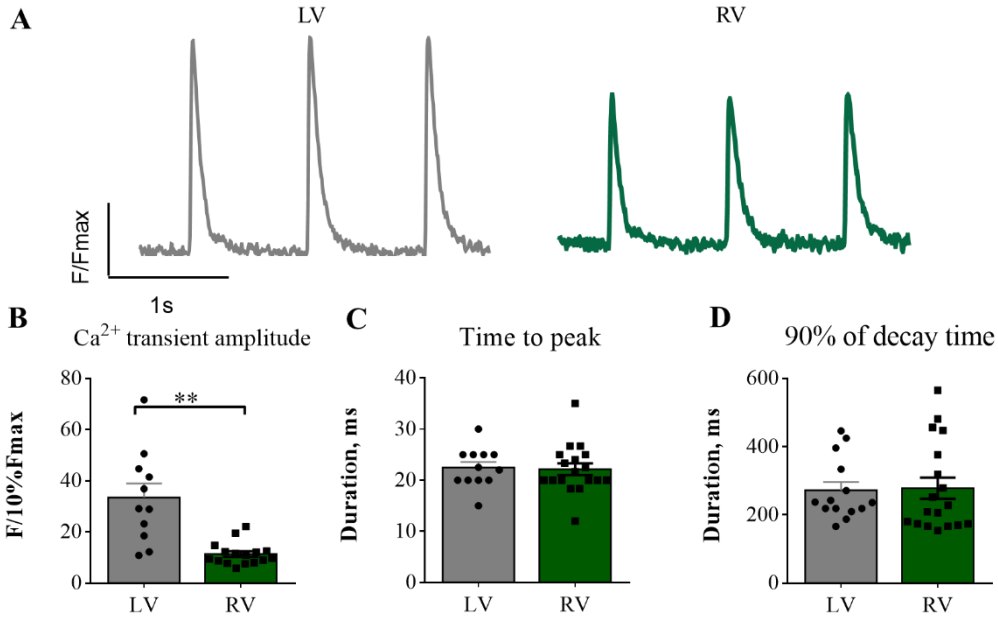

Figure 3.16. Differences in Ca^{2+} transients properties between RV and LV myocytes. A) Example of Ca^{2+} transient measured in control LV and RV myocytes. B) Mean Ca^{2+} transient amplitude in control LV and RV myocytes. C) Average time to peak in control LV and RV myocytes. D) Average decay time measured in control LV and RV myocytes. (n=14-19, N=4, *p<0.05, **p<0.01, by unpaired Student t test).

3.3.7 Spontaneous Ca^{2+} activity in control RV and LV myocytes.

To estimate the value of a spontaneous Ca^{2+} activity in control RV and LV myocytes we applied two methods OM of Ca^{2+}waves and confocal linescan Ca^{2+} sparks measurements. The first protocol included 1 min of 4 Hz field stimulation of myocytes loaded with Fluo-4AM and then optical recording of Ca^{2+} changes (Glukhov et al., 2015). An example of optical traces obtained from one myocytes is shown in Figure 3.17A. Statistical analysis of non-propagated Ca^{2+} waves revealed no differences between control LV and RV myocytes. The frequency of propagated Ca^{2+} waves were 3 times higher than the frequency of non-propagated waves in control LV myocytes Figure 3.17B. RV myocytes have similar frequencies of propagated and non-propagated waves (NS, Figure 3.17B). The

frequency of propagated waves was slightly higher in LV than in RV myocytes (NS, Figure 3.17B).

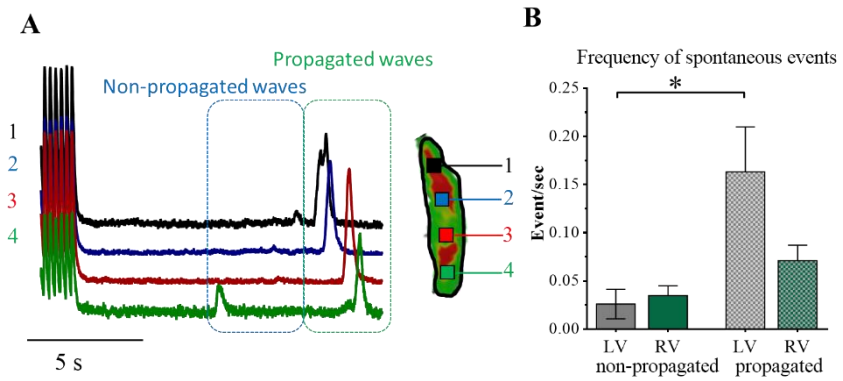

Figure 3.17. LV myocytes have a higher frequency of spontaneous Ca^{2+} waves. A) Representative traces showing changes in [Ca^{2+}] from 4 consistent points (1–4) selected in a single cardiomyocyte. Cells were electrically paced at 4 Hz for 1 minute to enhance sarcoplasmic reticulum Ca^{2+} loading. Propagating and non-propagating Ca^{2+} waves were recorded during a 16-s rest period after cessation of pacing. On the left, optical traces. B) Bar graphs showing the frequency of propagated and non-propagated waves in single LV and RV myocytes. (N=4-5 rats, *p<0.01, by Kruskal- Wallis test with Dunn's post-hoc).

For understanding of spontaneous Ca^{2+} activity in control RV and LV myocytes we analysed Ca^{2+} sparks using the established protocol of line-scans analysis (Lyon et al., 2009). The protocol included 1 min of the field stimulation to establish the high SR loading and then 16-18 s of spontaneous Ca^{2+} activity recording. The representative Ca^{2+} sparks images are shown in Figure 3.18A. Characterization of the Ca^{2+} sparks properties in control RV and LV myocytes are shown in the Table 8 and Figure 3.18. We calculated two values of Ca^{2+} sparks: mass (amplitude X FWHM X FDHM) and spark- mediated Ca^{2+} leak (mass X frequency) as described in (Section 2.4.3.2; (Kolstad et al., 2018)). RV myocytes slightly but not significantly lower frequency of Ca^{2+} sparks as compared with a sparks in LV myocytes. The shape of Ca^{2+} sparks was also different in RV vs. LV myocytes with a lower amplitude and width, producing ~ 20 % reduction in Ca^{2+} spark mass in RV myocytes (p<0.001, Figure 3.18C). Lower Ca^{2+} spark mass and a slight variation in frequency of Ca^{2+} sparks in RV versus LV myocytes produced ~ 40% lower spark-

mediated Ca^{2+} leak in control RV myocytes then in LV myocytes ($p<0.05$, Figure 3.18D).

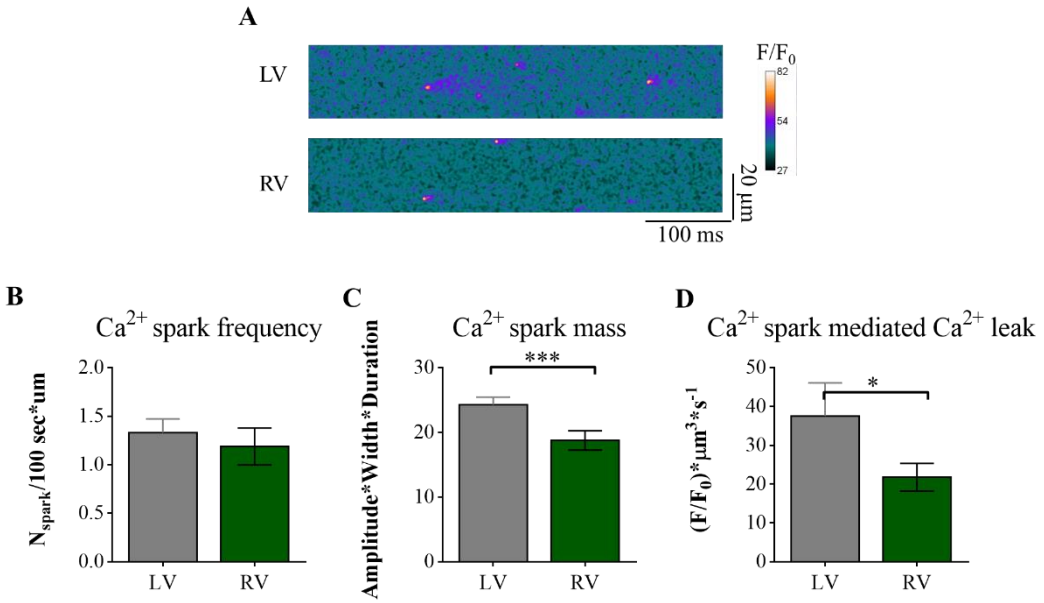

Figure 3.18. RV myocytes have lower frequency of Ca^{2+} sparks. A) Representative Ca^{2+} sparks images recorded in control LV and RV myocytes. B) Statistical analysis of Ca^{2+} sparks frequency, C) Ca^{2+} sparks mass, D) Ca^{2+} spark mediated Ca^{2+} lead. (n=35-42 cells, N=5-6 rats, by Mann- Whitney test).

Table 8. Ca^{2+} spark properties observed in control LV and RV myocytes.

	LV	RV
Frequency, N_{spark}/µm/100s	1.33±0.14	1.19±0.18
Amplitude, F/F0	0.35±0.01	0.29±0.01**
HMFW, µm	2.65±0.05	2.35±0.06**
HMFD, ms	25.1±0.6	24.3±1.2
Time to peak, ms	12.6±0.6	11.7±0.5
Tau, ms	26.3±1.4	26.5±2.0
Ca^{2+} spark mass, n(F/F0)*m*s	24.3±1.1	18.8±1.5*
Ca^{2+} spark induced Ca^{2+} leak, p(F/F0)	30.5±4.9	21.8±3.5*

Values are means ± SE; n = 35-42 cells, N= 4-5 hears, *P < 0.001 vs. the Control LV. HMFW- Half maximum full width, HMFD- Half maximum full duration.

3.3.8 Analysis of synchronicity in control RV and LV myocytes.

Observed differences in Ca^{2+} sparks and waves activity in control LV and RV could generally indicate distinct properties of RyR2 that are responsible for the intracellular Ca^{2+} releases. Moreover, our findings of the reduced TAT organisation in RV vs. LV myocytes drive us to check the synchronization of the Ca^{2+} release through the cell. The work of Louch et al. proposed the analysis of synchronization of activation though the cell via measurements of variability of the half rise time (TTF50) (Louch et al., 2006). Figure 3.19A shows the representative examples of Ca^{2+} transients recorded in control LV and RV myocytes. The histograms of TTF50 distribution in control LV (grey) and RV (green) (Figure 3.19B) clearly indicates that RV myocytes have lover pike with more broad distribution of TTF50 as compared to LV myocytes. To quantify these differences we used 'desynchrony index' which defined as a standard deviation of TTF50. RV myocytes showed a significantly higher "desynchrony index' than LV myocytes ($p<0.05$, Figure 3.19C).

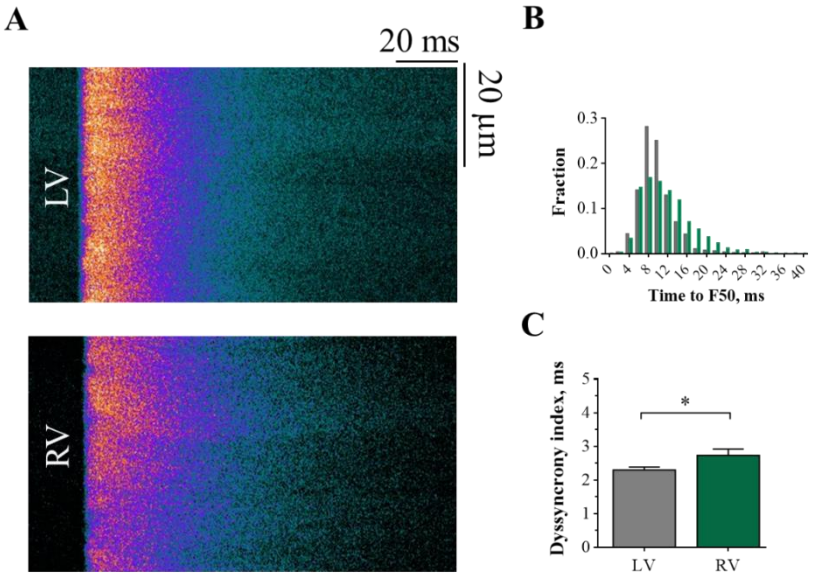

Figure 3.19. Analysis of the shape of Ca^{2+} transients. A) Example line scans of Ca^{2+} transients recorded in control LV and RV myocytes. B) Frequency distribution of time to 50 % of Ca^{2+} transient amplitude (TTF50) analysed in control LV (grey) and RV (green) myocytes (n=30-40 cells, N-3 rats). C) Analysis of a standard deviation of these values, defined as the desynchrony index (Louch et al., 2006) (n=30-40 cells, N-3 rats, *$p<0.05$, by unpaired Student t test).

Moreover, the TTF50 values have been used to define the early and delayed RyRs (Biesmans et al., 2011; Heinzel et al., 2002). Following this methodology, we used the cumulative histograms of TTF50 (Figure 3.20A) to determine the point where 50% of the sites of the line scan have F>F50. Statistical analysis of this time to 50 % values in LV and RV myocytes (Figure 3.20B) showed slightly less value in LV then in the RV. When the values from both RV and LV we put together, we got the mean of around 9.9±0.4 ms and for simplicity, we used 10 ms as a reference value to divide RyR2 into early (TTF50<10 ms) and delayed (TTF50 >10 ms).

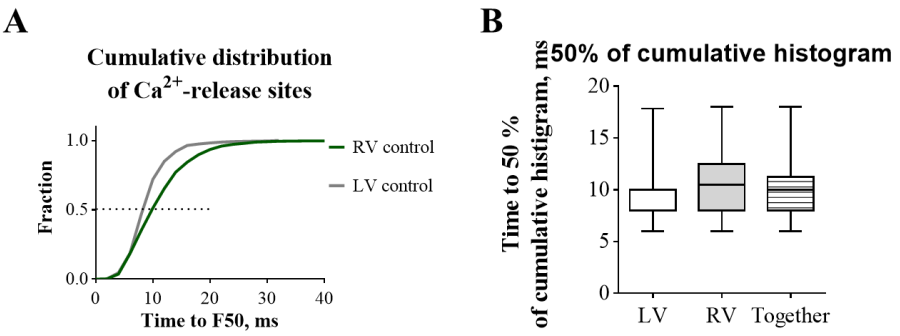

Figure 3.20. Cumulative distribution of TF50 in control LV and RV myocytes. A) Cumulative histograms of TF50 distribution in control RV and LV myocytes (n= 30-40 cells). B) Statistical analysis of 50% of TF50 histogram from every from LV and RV myocytes and both of them.

Identification of early and delayed Ca^{2+} release points could be useful for checking the spatial distribution of RyR2 in myocytes and their colocalization with the tubular membrane. Work of Heinzel et al. provides evidence that early Ca^{2+} release sites are arise from RyRs located within a higher TAT density regions and late Ca^{2+} release sites are originated from RyRs located far from tubular membrane (Heinzel et al., 2002). Biesmans et al. used this approach to study the properties of Ca^{2+} sparks related to the early or delayed Ca^{2+} release sites (Biesmans et al., 2011). We applied this methodology to study the differences of Ca^{2+} sparks in relation to their origin. The example of Ca^{2+} transient, corresponding TTF50 trace and Ca^{2+} sparks are presented in Figure 3.21A. Interestingly, in LV myocytes, so called early and delayed Ca^{2+} sparks showed similar properties. On the contrary, in RV myocytes, Ca^{2+} sparks occurred more frequently in the early sites than in delayed sited

(p<0.05, Figure 3.21B). Moreover, Biesmans and co-workers showed that early and delayed Ca^{2+} sparks have different duration (Biesmans et al., 2011). We observed here similar differences between sparks in RV myocytes (p<0.05, Figure 3.21C). In RV myocytes, lower frequency and duration of the delayed Ca^{2+} sparks leads to a less spark induced Ca^{2+} release in delayed regions than in early sites (p<0.05Figure 3.21D). Interestingly, delayed Ca^{2+} sparks in RV myocytes produce significantly less Ca^{2+} release than delayed Ca^{2+} sparks in LV myocytes (p<0.01, Figure 3.21D).

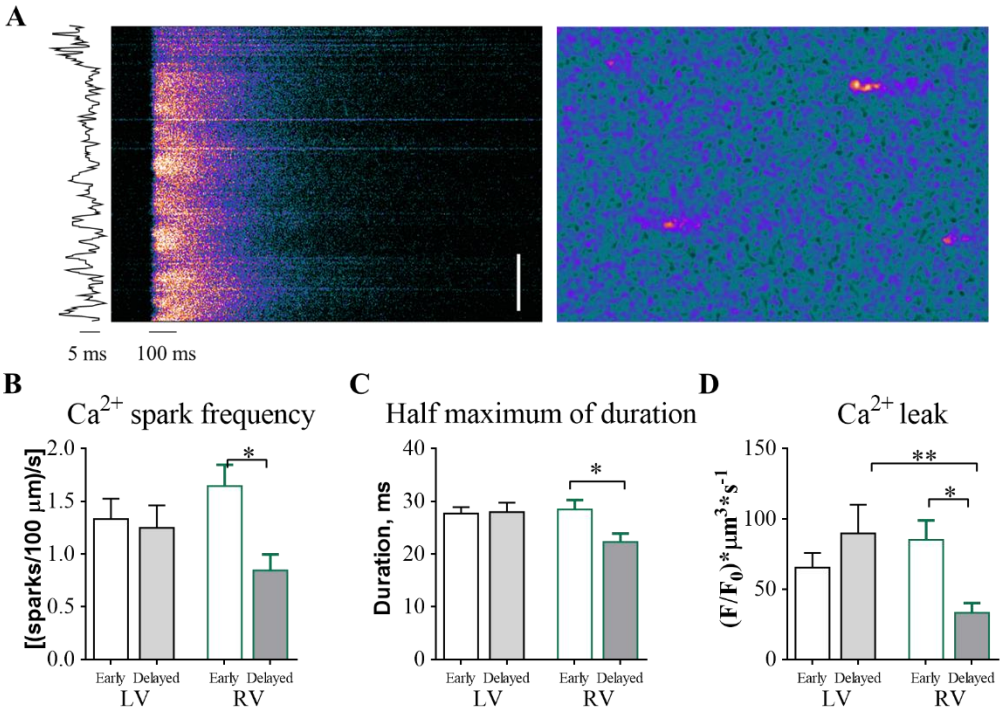

Figure 3.21. Characterization of two subpopulations of Ca^{2+} sparks in LV and RV myocytes. A) Illustration of Ca^{2+} transient analysis. Ca^{2+} sparks were assigned to early and delayed areas of Ca^{2+} transients using the TTF50 values. The TTF50 profile is shown on the left. Bar – 20 µm. B) Average frequency of Ca^{2+} sparks, C) Half maximum of duration, D) Ca^{2+} spark mediated Ca^{2+} leak analysed in control LV and RV myocytes. (n=36-46 cells, N=4-5 rats, *p<0.05, **p<0.01, by Kruskal- Wallis test with Dunn's post hoc).

3.3.9 Spatial localization and properties of L-type Ca^{2+} channels in control RV myocytes

It was shown before by several methods, that LTCC are not equally distributed across sarcolemma membrane in LV myocytes, with much higher chance of obtaining LTCC current at T-tubule than at the surface membrane (Bhargava et al., 2013). In contrast, in atrial myocytes, equal distribution of LTCC between T-tubule and sarcolemma membrane have been shown recently (Glukhov et al., 2015). We found in literature no data regarding LTCC spatial distribution in RV. We hypothesized that alterations of ECC observed between LV and RV could involve different distribution of LTCC and altered regulation of the channels.

To characterize LTCC localization and properties in RV myocytes we applied super resolution scanning patch-clamp technique to two different compartments of the myocyte membrane TT and crest. Typical LTCC single channel activity was observed at T-tubule (Figure 3.22**Error! Reference source not found.**) and crests (Figure 3.23**Error! Reference source not found.**) of RV myocytes. Single LTCC behaviour was close to that observed before in LV myocytes (Bhargava et al., 2013).

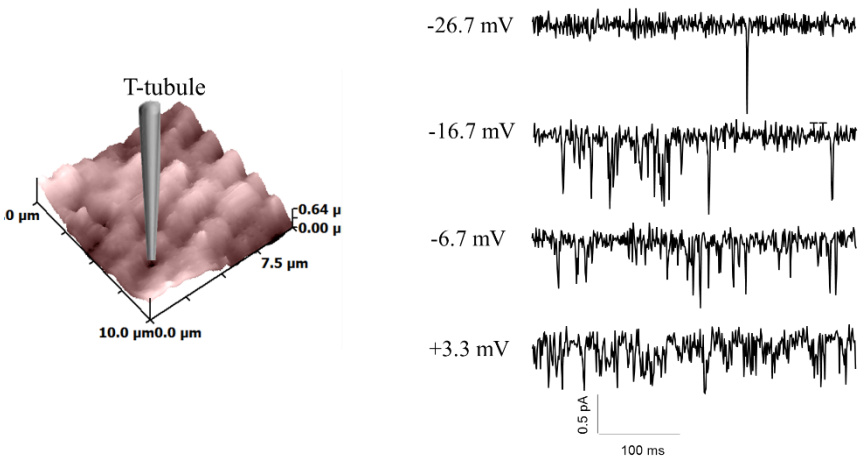

Figure 3.22. Single LTCC activity recorded at T-tubule of RV myocytes. On the left, example of cardiomyocyte 10x10 µm surface scan shoving the pipette approaching the T-tubule for the giga-seal formation. On the right, representative LTCC current traces recorded at T-tubule applying variable voltages.

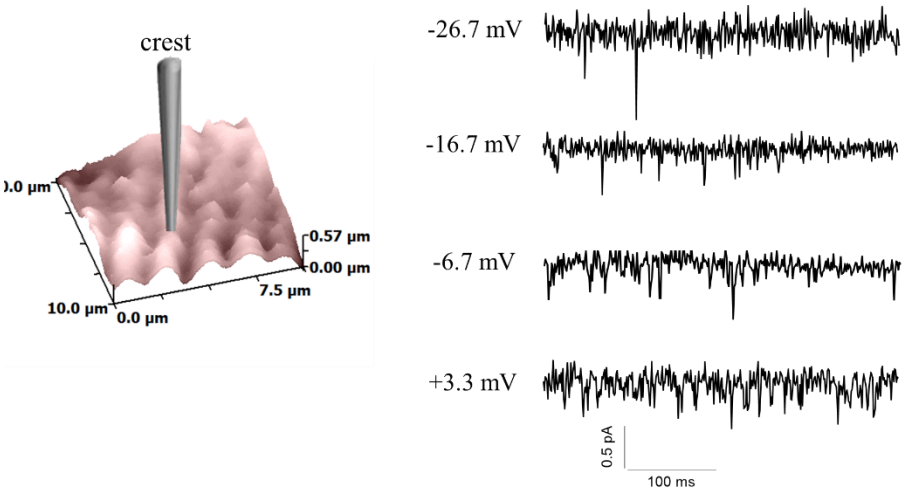

Figure 3.23. Single LTCC activity recorded at crest of control RV. On the left, typical example of 10x10 µm surface scan of RV myocyte with a pipette placed at crest position. On the right, representative current traces recorded at crest of RV myocyte holding variable potentials.

Localization and properties of LTCC at T-tubule and crest was characterized using the comparison with the corresponding LTCC in LV myocytes. The main characteristics of LTCC were analysed applying -6.7 mV (Figure 3.24).

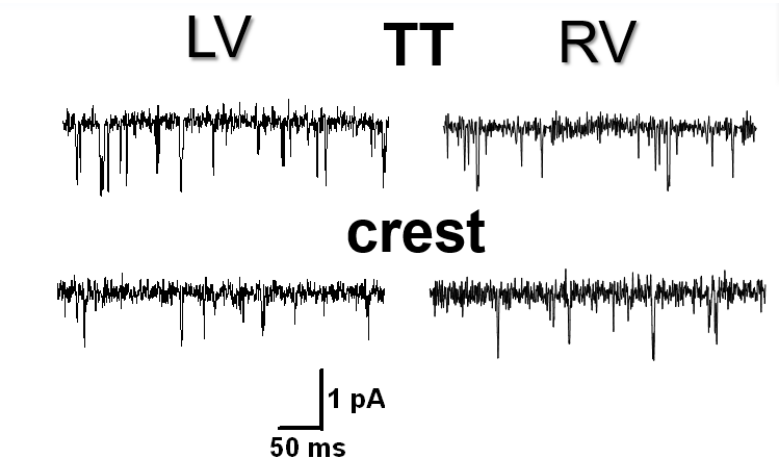

Figure 3.24. Single LTCC recordings performed in T-tubule and crest of LV and RV myocytes applying -6.7 mV.

LTCC localization in RV was characterized with two parameters: occurrence and density (Figure 3.25A-3.25B). Single channel LTCC recordings in LV myocytes showed almost 3 times higher chance to obtain LTCC at T-tubule compared to the crest (Figure 3.25A), as it was shown before (Bhargava et al., 2013). Surprisingly, in RV myocytes the occurrence of LTCC at T-tubule and crest membrane domains was almost equal (21.1% of 95 successful patches in T-tubules vs. 21.8% of 78 successful patches, Figure 3.25A).

The occurrence of the LTCC doesn't take in consideration the number of LTCC obtained in the patch. To include also the number of channels in the patch, the ingle channel density analysis was performed. LTCC single channel density was calculated as total number of the channels to the total patched area (Figure 3.25B). The density of LTCC in LV myocytes was almost 4 times higher at T-tubule as compared to crest region. RV myocytes showed almost similar density of LTCC at T-tubule (2.7 channel/μm^2) and crest (2.1 channel/μm^2).

Also to check LTCC clustering in control RV and LV percentage of multiple channels was calculated (Figure 3.25C). In both LV and RV myocytes the chance of multichannel LTCC recording was higher at crest that at T-tubule (not significant).

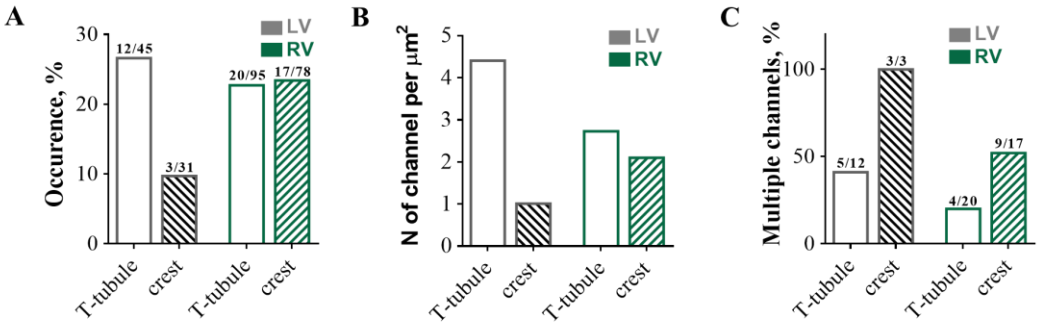

Figure 3.25. LTCCs spatial localization in RV and LV myocytes. A. LTCC current occurrence at T-tubule and crest of LV and RV myocytes. n/m- number of patches with LTCC/ total number of successful patches. B) Single channel LTCC density at T-tubule and crest in LV and RV myocytes. C) Percentage of multi-channel LTCC recordings from

the total number of patches with a LTCC current. n1/n = number of patches with more than one LTCC/ total number of patches showing LTCC activity.

Functional properties of LTCC recorded at T-tubule and crest in LV myocytes have similar Po Figure 3.26A) and amplitude Figure 3.26B). In RV myocytes the LTCC recorded at T-tubule have lower open probability (P_o) compared to the crest of RV and T-tubule of LV myocytes: RV: 0.029±0.004 at T-tubule vs. 0.049±0.009 at crest, $p<0.05$; and vs. 0.043±0.006 at T-tubule in LV myocytes, $p<0.05$, Figure 3.26A). The amplitude of the LTCC at -6.9 mV measured at crest of RV myocytes was significantly lower than amplitude of LTCC at crest of LV myocytes (amplitude: RV crest: 0.56±0.04 vs. LV crest: 0.69±0.01 pA, $p<0.05$, Figure 3.26B).

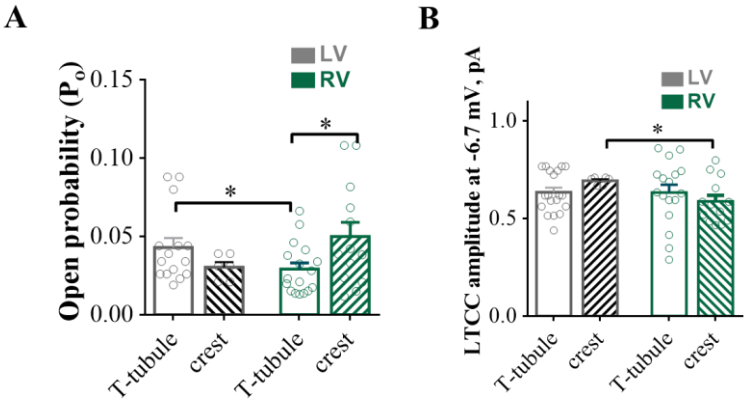

Figure 3.26. Properties of LTCC in control RV and LV myocytes. A) Open probability of single LTCC recorded at T-tubule and crest in LV and RV myocytes holding -6.7mV. (N=6-17 channels, from 31-95 cells, *P<0.05, by unpaired Student t test). B) Amplitude of single LTCC recorded at T-tubule and crest of LV and RV myocytes with potential set -6.7 mV. (N=6-17 channels, from 31-95 cells, *P<0.05, by Mann-Whitney test).

3.3.9.1 Total membrane LTCC density study with LTCC agonist BayK8644.

To characterize total membrane density of LTCC in control RV and LV myocytes an LTCC agonist BayK8644 (BayK) was applied. This drug increases the mean time of channel opening with a slight modification of the channel conduction (Brown et al., 1984; Hess et al., 1984). Representative traces of LTCC recorded at

-6.7mV in T-tubule and crest of LV and RV myocytes are shown in Figure 3.27. It is clear, that LTCC after BayK application opens at high conductance state with a longer open time as compared to recordings in normal external buffer (Figure 3.27).

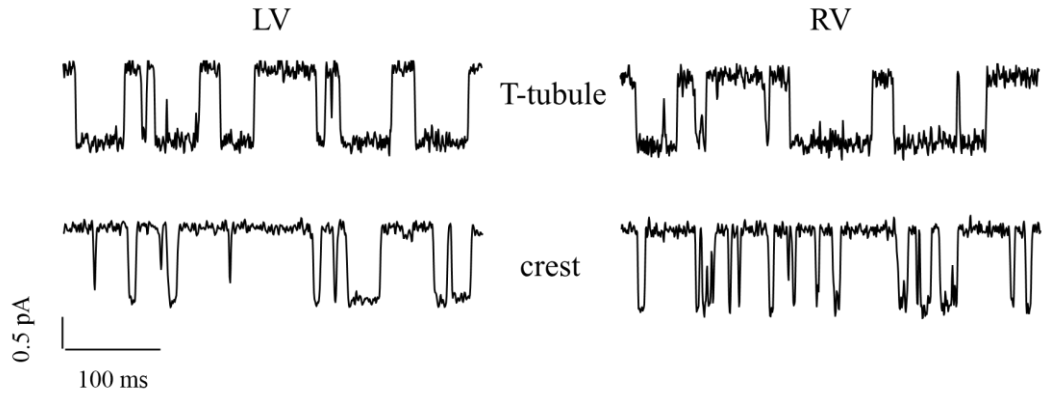

Figure 3.27. Traces of single LTCC activity recorded at-6.7mV in T-tubule or crest of LV and RV myocytes in presence of BayK.

Membrane density of LTCC in RV and LV myocytes in absence and presence of BayK is shown in Figure 3.28. The density of LTCC at T-tubule and crest of LV myocytes was similar with and without the BayK. On the contrary, LTCC membrane density was ~40% higher at T-tubule and crest of RV myocytes in presence of BayK. It could be a sign of existence of some LTCC in RV myocytes that are inactive or having very low Po under the normal conditions, to detect them.

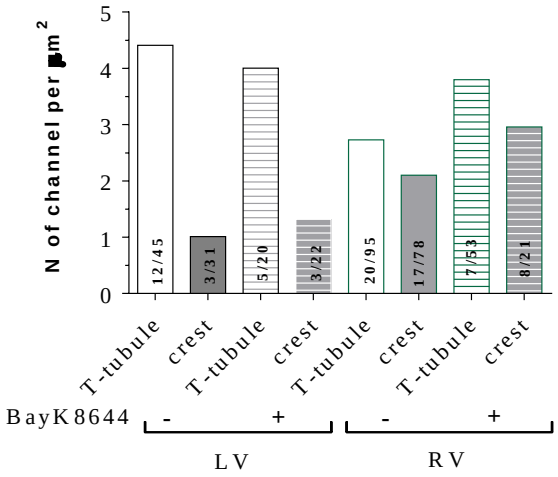

Figure 3.28. Single LTCC density measured in LV and RV myocytes in absence and presence of BayK. (n/m = number of patches with channels/total number of successful patches).

Analysis of functional properties of LTCC in the presence of BayK showed some differences between the channels in RV and LV myocytes. Application of BayK increased the open probability of LTCC located at T-tubule and crest of both RV and LV myocytes by an order (Figure 3.26A vs. Figure 3.29A). Interestingly, the Po of LTCC located at T-tubule of RV was less than Po of LTCC located at T-tubule of in presence of BayK (LV T-tubule: 0.43±0.07 vs. RV T-tubule: 0.29±0.01, $p<0.05$, Figure 3.29A).

Another analysed parameter of LTCC single channel activity was channel amplitude (Figure 3.29B). As was mentioned before, BayK induces long openings of LTCCs up to the highest conductance state around 1 pA (at -6.7 mV). LTCCs located at T-tubule and crest of LV myocytes and crest of RV myocytes are forced to open at highest level (Figure 3.29B). However, LTCCs located at T-tubule of RV myocytes in presence of BayK had smaller amplitude, than those of LTCCs located at crest areas of RV or at T-tubule of LV myocytes (RV T-tubule: 0.67±0.08 pA vs. RV crest: 1.12±0.09, $p<0.01$; vs.LV T-tubule: 1.05±0.03 pA, $p<0.001$; Figure 3.29B). We hypothesize that actually two subpopulations of LTCCs could be present in T-tubule of RV myocytes, one with amplitude ~ 1pA and another – with amplitude ~ 0.4pA. Finding the reason for observed differences requires additional experiments.

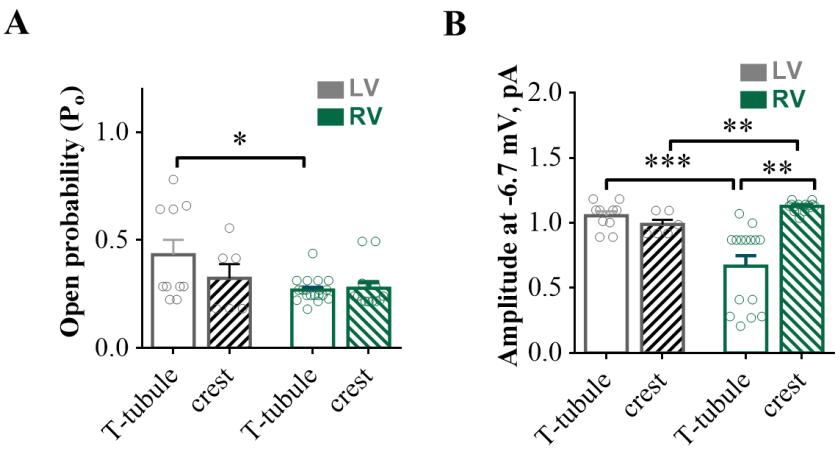

Figure 3.29. Properties of LTCC observed in control LV and RV in presence of BayK. **A)** Open probability of LTCC recorded at-6.7mV in presence of BayK8644. (N=3-8 channels, 20-53 cells, *p<0.05, by unpaired t test). B) LTCCs mean amplitude at -6.7 mV in presence of BayK. (N=3-8 channels, 20-53 cells, **p<0.01, ***p<0.001 by Kruskal-Wallis test with Dunn's post-hoc).

3.4 Discussion and conclusions

In this chapter we characterized the structural organisation and Ca^{2+} handling in RV myocytes and compared these properties to those of LV myocytes. Both ventricles have a pronounced differences starting from by embryological origin and working condition. The physiology and hemodynamic functions of RV in the normal state differ considerably from those of LV (Dell'Italia et al., 1995). Our results and previous papers from other laboratories showed the huge differences between organisation and function of RV and LV myocytes. Generally, we observed altered contraction and Ca^{2+} transients in RV and LV myocytes (Figure 3.14 and 3.15). Contractions were longer in RV then in the LV myocytes, but the Ca^{2+} transients were much higher in LV then in RV myocytes. As was mentioned before, we could not fully rely on our measurements of Ca^{2+} transient amplitude. Also in literature there are contradicting data about the differences between RV and LV Ca^{2+} transient amplitude (Table 4). For example, Sabourin et al. showed that in rat LV myocytes Ca^{2+} transient amplitude is higher than in the RV (Sabourin et al., 2018), but in the different study the amplitude of Ca^{2+} transients has been shown to be similar in control RV and LV myocytes with the longer contractions found in RV myocytes (Sathish et al., 2006). It is unclear whether this differences are attributable for the problems with Fluo4-AM Ca^{2+} transient measurements or intrinsic differences between RV and LV myocytes. Higher Ca^{2+} transients in LV myocytes could be produced via longer APD, observed in these cells by many groups (Di Diego et al., 1996; Ramakers et al., 2005).

To understand if the differences observed were related to internal myocytes structure we studied their TAT network and surface topography. Analysis of the shape of cardiac myocytes showed that LV myocytes were significantly wider that RV ones (Figure 3.2). Our recent findings in atrial myocytes, which possess a variable TAT network organisation from almost absent to highly regular tubules, showed the correlation of the TAT density and myocyte width (Glukhov et al., 2015). But RV myocytes showed similar density of TAT network to the LV one (Figure 3.5). Moreover, the index of surface regularity (Z-groove ratio) was similar in myocytes from both ventricles (Figure 3.3). Detailed investigation of TAT

skeleton revealed a significant difference between myocytes. RV myocytes have higher skeleton length per area than LV myocytes. Moreover, the complexity of TAT network, a parameter indicating the amount of branching was also higher in RV myocytes than in LV (Figure 3.6). Directional investigation TAT alignment showed that RV myocytes have less frequency of T- tubules appearance with a higher amount of A- tubules. Exact roles of T- tubules and A- tubules in ECC are not defined. A- tubules are abundant in atrial cells, where they are very long and wider then T- tubules (Hund and Mohlerp, 2016). Moreover in atrial myocytes the active highly phosphorylated clusters of RyRs are found to locate close to A-tubules so they are believed to serve as a place of initial Ca^{2+} transient onset (Brandenburg et al., 2016). In ventricular myocytes the role of A- tubules are not so clear. The width of A- tubules was found to be similar to that of T- tubules (Wagner et al., 2012). Moreover electron microscopy studies showed formation of dyadic junctions between axial tubules and junctional SR as it is happen in T-tubules (Asghari et al., 2009).

The TAT network is a very flexible system in cardiac myocytes, it can easily react to changes in stress or loading condition (Jones et al., 2018). Rearrangement of TATS during pathology is usually accompanied by an increase of A- tubules formation (Schobesberger et al., 2017; Wagner et al., 2012)). This was suggested as a first compensatory mechanism which attributed to help with the impaired contractility. The density and regularity of TAT network in RV myocytes were close to those in unloaded LV myocytes, from the model heterologous heart implantation in systemic circulation (Wright et al., 2018). So differences in TAT structure between RV and LV could be linked with ventricle-specific loading conditions, such as, for example, six times lower afterload, lower pressure in systemic circulation (Dell'Italia et al., 1995).

Altered TAT network has pronounced effects on the Ca^{2+} cycling in RV versus LV myocytes. Firstly we studied the general Ca^{2+} activity in the heart. Both of our experimental setups revealed similar frequency of Ca^{2+} waves (Figure 3.16) and Ca^{2+} sparks (Figure 3.17) in RV myocytes when compared to LV. However, the analysis of Ca^{2+} sparks mass and spark-induced Ca^{2+} lead was higher in LV myocytes. (Figure 3.17C and 3.17D). The reason for higher mass of Ca^{2+} sparks

could be the higher SR Ca^{2+} loading in LV myocytes, as indicated higher amplitude and HMFW of Ca^{2+} sparks (Table 2). However, our preliminary results and literature data shows that it is not the case, caffeine-evoked Ca^{2+} releases showed similar amplitude in RV and LV myocytes (Sabourin et al., 2018; Sathish et al., 2006). RyRs phosphorylation has a great impact on the sparks activity under the rest condition, in the work of Sathish et al. the phosphorylation level of RyR2 was significantly higher in LV myocytes than in RV ones (Sathish et al., 2006). Phosphorylated RyRs could be opened for a longer time, increasing amount of Ca^{2+} released through Ca^{2+} spark.

Another consequence of disorganized TAT network in RV myocytes is an alteration of LTCC- RyR coupling. The analysis of LTCC and RyRs density in RV and LV myocytes showed that density of LTCC was lower in RV myocytes (Figure 3.10). Moreover the colocalization analysis of $Ca_v1.2$ with RyRs in RV and LV myocytes showed less Manders coefficient for RyRs with $Ca_v1.2$ in RV myocytes compared to LV myocytes. That could be an indicator of fewer couplons in RV versus LV myocytes. Recent studies showed that sparks originate from RyRs coupled and uncoupled from LTCC have different activity and regulation (Biesmans et al., 2011; Dries et al., 2013). These higher amount of uncoupled RyRs could lead to a more disorganize Ca^{2+} transients activation. We studied the synchronisation of Ca^{2+} transient activation via variability in time to half-maximal fluorescence (TTF50) across the cell. Analysis of line-scans of Ca^{2+} transients showed a wider and right-shifted distribution of TTF50 values in RV versus LV myocytes and significantly larger desynchrony index in RV myocytes compared to LV ones (Figure 3.18). Similar situation was observed in failing LV myocytes by Louch and co-workers (Louch et al., 2006). Desynchronization of Ca^{2+} transient was addressed to reduction of TAT organisation which is leading to formation of inhomogeneous impulse propagation and “orphaned” RyR2 formation (Frisk et al., 2014; Song et al., 2006). Resent work has also linked inhomogeneous Ca^{2+} transients with a Ca^{2+} spark kinetics (Kolstad et al., 2018). Sparks with a longer rise time were more frequent in places with higher TTF50.

To address the question about the spatial inhomogeneous Ca^{2+} spark formation we used an approach established in previous works (Biesmans et al., 2011; Heinzel et

al., 2002). The approach is based on the analysis of TTF50 distribution across the cell surface. The regions with smaller TTF50 have higher T-tubule density whereas when TTF50 in larger this was accompanied with lower TAT density (Heinzel et al., 2002). Recently Dries and colleagues directly visualized two subpopulations of RyR2 - ones located close to T-tubule and another one - far from it (Dries et al., 2013). Dries et al. analysed the myocytes from large animals (pigs) that possess low TAT density. We addressed the same methodology to study rat cells. Firstly, 50% TTF50 cumulative distribution showed a mean value 10 ms, that we used as a criteria to assign the Ca^{2+} release site as early (close to T-tubule) or late (further from it). The sparks were assigned to early or delayed according to their location with the TTF50 of Ca^{2+} transient. Frequency and shape of early and late Ca^{2+} sparks were similar in LV myocytes (Figure 3.20). In RV myocytes we observed significant alterations in properties of Ca^{2+} sparks located in early and delayed sites (Figure 3.20). The frequency and half maximum duration of early sparks were higher as the corresponding parameters of delayed sparks. Similar differences only in frequency and duration of Ca^{2+} sparks have been previously observed (Biesmans et al., 2011). Higher frequency of Ca^{2+} sparks in early places was addressed to communications of RyR2 with LTCC. Ca^{2+} that reaches RyR2 in diastole is higher close to T-tubule, than far away from it. Interestingly, the experiments of Biesmans et al. showed that blocking of LTCC didn't change the sparks activity in early release areas, but application of LTCC agonist increased the Ca^{2+} sparks rate at early areas. This was suggested that sparks were indeed 'spontaneous' and did not require sarcolemmal Ca^{2+} influx. Moreover RyR2 close to T-tubule could be exposed with an elevated local [Ca^{2+}], that could promote the activation of CaM and CaMKII, that enhance the RyR2 openings (Dries et al., 2013; Saucerman and Bers, 2008; Song et al., 2005). In LV we did not see any differences between early and delayed sparks that could be attributed to a higher membrane organisation in LV myocytes and larger amount of T-tubule.

We next characterized the spatial localization and function of LTCC in RV myocytes. Interestingly, the distribution of LTCC between T-tubule and crest was almost equal (Figure 3.24). This distribution of LTCC was strictly different from the distribution in LV myocytes, where we and other observed much higher

occurrence and density of LTCC in T-tubule than in the crest (Bryant et al., 2015; Sanchez-Alonso et al., 2016). Moreover, atrial myocytes have also almost equal chance to get LTCC current in T-tubule and crest (Glukhov et al., 2015). Firstly, we hypothesize, that as in atria myocytes, RV myocytes have higher density of caveolae, membrane domain where LTCC predominantly anchored (Scriven et al., 2000) then LV myocytes. But it was not a case, as the immunostaining showed similar density of Cav3 in both RV and LV (Figure 3.13) and our preliminary results from electron microscopy showed similar levels of caveolae in RV and LV myocytes (data not shown). But the colocalization between $Ca_v1.2$ and Cav3 in RV myocytes was higher than in LV myocytes. Thus with the same amount of caveolae, the amount of LTCC linked with it was higher in RV myocytes than in LV myocytes. However, further functional experiments needed to understand the consequences of these findings, such as, for example, incubation of the cells with MβCD, that is capable to remove the cholesterol out of membrane and flatten the caveolae.

As indicated before, RV myocytes in terms of their TAT network structure were close with unloaded LV myocytes. Unloaded LV myocytes were showed a similar occurrence of LTCC in T-tubule and crest (Wright et al., 2018). Moreover, a large part of LTCC were silent or possess a very low Po under the normal conditions in unloaded LV myocytes, but were active in presence of LTCC agonist BayK. Application of BayK on RV myocytes revealed a ~40% higher density of LTCC located at both T-tubule and crest, whereas it doesn't affect the density of LTCC in LV myocytes. The exact reasons for this silent subpopulation of LTCC in RV are not clear, but we can hypothesize that RV need to adapt to variable loading conditions during the rest or exercise and for this it should have some resources to easy increase the contractility. A similar picture was observed by (Sathish et al., 2006) with SERCA2a level. RV myocytes in his work have a significantly slower Ca^{2+} uptake than LV myocytes because a large portion of SERCA2a in RV was inhibited via association with phospholamban (PLB).

Not only spatial localization of LTCC was different between RV and LV myocytes, the properties of the channels were also altered in RV and LV myocytes. The analysis LTCC located in T-tubule of RV myocytes showed less Po than LTCC

located in crest of RV and T-tubule of LV myocytes (Figure 3.25). This could indicate a lower Ca^{2+} influx thorough LTCC in T-tubule, that could be responsible for the less triggering of sparks in RV vs. LV myocytes.

The amplitude of LTCC was measured at maximum activation step to -6.7 mV. When recorded in normal solutions, LTCC in crest of RV myocytes have slightly lower average amplitude that LTCC at crest of LV myocytes (Figure 3.25). Interestingly, in the presence of BayK, the mean amplitude of LTCC in T-tubule of RV was significantly lower than LTCC in any other locations (Figure 3.28). This could be due to the existence of 2 pools of LTCC – one with normal amplitude ~ 1pA and another one – with amplitude ~ 0.45 pA. This smaller LTCC behaved like normal ones, they have voltage dependence like LTCC, and in the presence of BayK they opened in "mode 2" with long lasting open states and high open probability (Hess et al., 1984). Firstly, we checked the reports and find out the low frequent occurrence of this type of LTCC in T-tubule of rat LV myocytes after 4 days in culture and in human LV myocytes from patients with dilated cardiomyopathy. A peculiar group of LTCC that possess low amplitude has been described in cerebellar granule cells; these channels were built of $Ca_v1.2$ subunits and they have been proposed to play a specific role in gene regulation (Koschak et al., 2007). Our hypothesis was related to a specific membrane compartment and most of the membrane compartments are organized by cholesterol- rich lipid rafts. The understanding of the nature and the role of this "peculiar" LTCC in myocyte physiology will require additional investigations.

3.4.1 Conclusion

In summary, differences in working load and contractions between the RV and the LV are probably responsible for the lower TATS regularity in RV myocytes with a higher proportion of A-tubules, and that in turn leads to a more atrial-like uniform distribution of LTCC on the membrane. In RV myocytes, LTCCs are less co-localised with RyR2 than in LV myocytes, which is due to the lower TATS organisation, and that could be responsible for a more desynchronised Ca^{2+} transient activation in RV myocytes and higher differences between early and delayed Ca^{2+} sparks. On the other side, a higher co-localisation of LTCC with Cav3 and T-tubular subpopulation of LTCC in RV have a low Po that could indicated a different

microdomain organization and regulation of LTCC in RV versus LV myocytes. Thus, we observed a significantly altered Ca^{2+} signalling microdomain organisation in RV and LV myocytes, so we could expect a different remodelling of these structures in disease.

4 Structural changes in calcium microdomains in RV and LV cardiomyocytes in pulmonary hypertension.

4.1 Introduction

We observed the differences in microdomain organisation between healthy RV and LV myocytes. However, the most important question is how ECC in RV myocytes will be changed in pathological conditions. In this chapter, we characterized the modification of RV and LV structure and function in pulmonary hypertension (PH). PH is a complex disorder which could have a variety of aetiologies as it was described in chapter 1. Generally, PH is induced by the proliferation of pulmonary vasculature and narrowing of the pulmonary vessels, which results in a profound increase in the RV load. The survival of patients with PH is largely dependent upon the ability of RV to adapt to the pressure overload (Thenappan et al., 2018). In patients with PH, increased resistance of pulmonary vessels leads to profound reorganisation of the RV. Crescent-shaped normal RV undergoes significant remodelling into a spherical chamber, with thicker walls and a four-times higher chamber pressure (Bogaard et al., 2009; Voelkel et al., 2006). During disease progression, an excessive electrical remodelling and arrhythmogenicity were also observed in the RV, including the prolongation of QT interval and T-wave, an appearance of T-wave alternants (Folino et al., 2003; Hlaing et al., 2005). Moreover, the pressure overload in the RV could affect the function of the LV as well. There is an evidence indicating LV atrophy in PH patients with an impaired stroke volume and systolic pressure (Han et al., 2018; Hardziyenka et al., 2011).

Despite these alterations found in PH hearts, so far there is no specific treatment targeted to the RV. Treatments applied for LV hypertrophy have been also proposed for the RV (Handoko et al., 2010), but their suitability is still under debate (Thenappan et al., 2018). It is clear that a better understanding of the mechanisms of RV and LV remodelling in PH is needed.

In this work, we analysed the changes that occur in both RV and LV in a MCT-induced rat model of PH. This is a commonly used model (Benoist et al., 2011; Sabourin et al., 2018; Wojciak-Stothard et al., 2014) because it is easy to produce

and it mimics several important aspects of PH in rats, such as APD prolongation and the occurrence of T-wave and Ca^{2+} transient alternants (Benoist et al., 2012). Despite a high interest to this disease, there are some discrepancies about the progression of the disease. For example, Ca^{2+} characterized by confocal imaging in isolated ventricular myocytes, were found to be smaller and slower in PH rats compared to control (Benoist et al., 2012; Xie et al., 2012). In contrast, others studies revealed an increase in the magnitude of Ca^{2+} transients as well as their shortening in PH vs. control (Sabourin et al., 2018). Different protocols and durations of MCT exposure between groups make a direct comparison between those studies more complicated. The reduction of TAT network density was observed in some works (Fowler et al., 2018; Sabourin et al., 2018; Xie et al., 2012). This was accompanied by an increase of spontaneous Ca^{2+} activity in PH RV myocytes. Moreover, there are some studies that showed changes in mRNA and protein expression levels of LTCC in PH RV myocytes (Benoist et al., 2011; Xie et al., 2012). At the same time, a whole-cell LTCC current density was reported to be preserved in PH RV myocytes (Benoist et al., 2012; Rocchetti et al., 2014).

Investigation of alteration of Ca^{2+} signalling microdomain organisation of RV in PH could provide more insights in disease progression. Our resent findings from failing LV myocytes and failing atria myocytes indicate the importance of microdomain-specific changes in the whole heart physiology (Glukhov et al., 2015; Sanchez-Alonso et al., 2016). In ventricular myocytes Ca^{2+} signalling microdomains are maintained by an elaborate organisation of TAT, surface sarcolemma and their adjustments to junctional sarcoplasmic reticulum (Fearnley et al., 2011). Reduction of TAT in HF has been associated with desynchronization of Ca^{2+} transients, a pronounced increase in Ca^{2+} spark rate, redistribution of LTCCs and their hyperphosphorylation (Louch et al., 2006; Lyon et al., 2009; Sanchez-Alonso et al., 2016). We hypothesized that that PH leads to arrhythmogenicity that could be studied at many levels, and that RV and LV myocytes undergo a significant remodelling in Ca^{2+} signalling microdomains that will affect the rate and synchronicity of Ca^{2+} release and produce hyperactivation of LTCCs. All together these alterations could promote arrhythmogenicity in the PH heart.

The main objectives of this chapter were:

1. To analyse electrical and arrhythmogenic activity of the RV and the LV of PH rats.
2. To study the structural changes in the LV and RV shape, surface topography and TAT membrane organisation after PH.
3. To characterize the alterations in $Ca_v1.2$, RyRs and Cav3 protein arrangement and colocalization in PH.
4. To assess the PH-induced modifications of myocytes in cell-shortening, Ca^{2+} transients and spontaneous Ca^{2+} activity in RV and LV myocytes.
5. To examine how the spatial localization of LTCCs in PH RV myocytes affects their functional behaviour.
6. To determine the modulations of the expression of $Ca_v1.2$, PKA and CaMKII in PH rats.

4.2 Methods

4.2.1 Monocrotaline model of pulmonary hypertension

Adult male Sprague Dawley rats (weight <250g, n=12, Charles River, Margate, UK) underwent monocrotaline (MCT; 60 mg/kg, Sigma) injection in order to induce pulmonary hypertension as described previously (Abdul-Salam et al., 2019; Wojciak-Stothard et al., 2014). Age and weight matched rats were used as control (n=12). Experiments were performed at 10-12th days after injection. Catheterization through the jugular vein was made to measure a right ventricle systolic pressure (RVSP). The weight of RV to LV+septum wet tissue was measured to assess the right ventricle hypertrophy.

4.2.2 In vivo epicardial mapping

Epicardial multiple-lead recordings were performed by Dr. Stefano Rossi as describes elsewhere (Savi et al., 2016). Briefly, rats were anesthetized, artificially ventilated and subjected to middle thoracotomy. Temperature was maintained constant at 37°C. One hundred twenty-one unipolar electrograms (EGs) were simultaneously recorded from the epicardial surface via an 11×11 electrode array with 0.5 mm interelectrode distance (Figure 4.1A). The array was positioned on the surface of the LV and then moved to the RV in both control and treated animals. Unipolar electrograms were recorded during normal sinus rhythm or during ventricular pacing via specific protocols at three selected electrodes of the array, using near-threshold, 1-ms cathodal current pulses. Standard procedures (Carnevali et al., 2013; Rossi et al., 2008) were applied to measure conduction velocity (CV), excitability, refractoriness, and mean parameters of ECG.

Conduction velocity. Activation times were estimated using the instant of the minimum time derivative of unipolar EGs during QRS complex, and were referenced to stimulus onset during a pacing beat. The activation sequence (isochrone map) was determined from the activation times of paced beats. Two CV were computed: longitudinally (CV-l) and transversally (CV-t) to fibre orientation. Anisotropic ratio was determined as CV-l/CV-t. These measures were evaluated after stimulation in 3 different areas in the RV and LV from control and MCT animals.

Refractoriness. Eight baseline stimuli (S1), 1ms duration and twice diastolic threshold strength each, were delivered at each of the 3 selected electrodes of the array at a frequency slightly higher than sinus rhythm. This programmed stimulation protocol was performed in 7 control and 7 MCT animals. The S1 pacing sequence was followed by an extra-stimulus S2 (four times higher than S1 strength) at the same site whose delay from previous S1 was first progressively decremented by 10 ms steps until capture was lost and then progressively incremented by 2 ms steps till capture was resumed. We defined an effective refractory period as the longest S1–S2 time interval at which impulse initiation failed (Rossi et al., 2008).

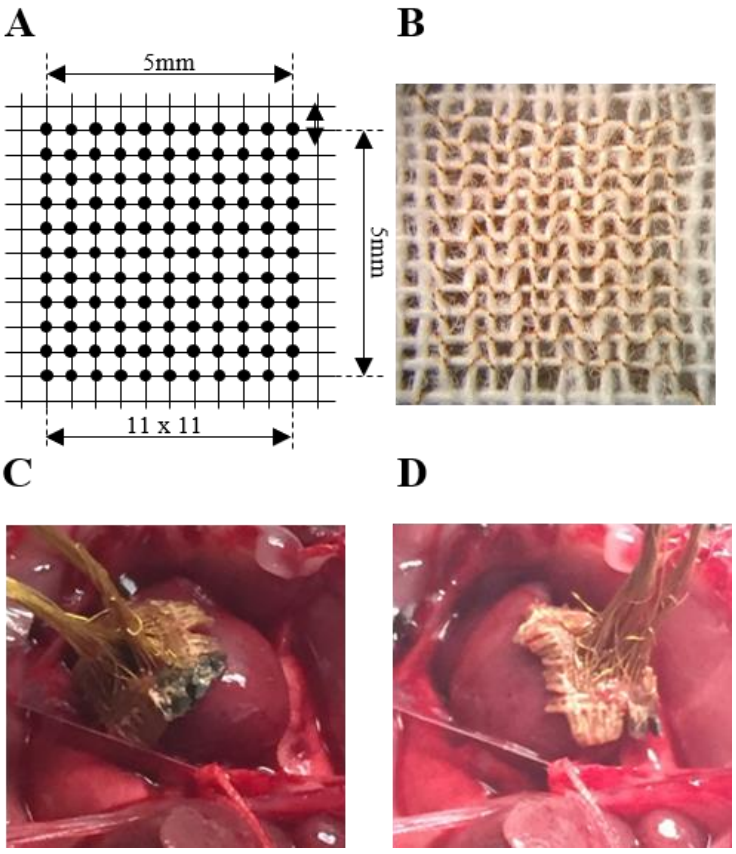

Figure 4.1 Multi-electrode 11x11 grid for the epicardial mapping. A) Schematic illustration of the electrode arrangement and size, **B)** bottom view of the grid, **C)** Multielectrode grid placed on the RV, **D)** Multielectrode grid placed on the LV.

4.2.3 Surface topography

Surface topography of freshly isolated cardiomyocytes was acquired by SICM as described in section 2.3.3. Myocytes were scanned at the day of isolation by a sharp

(100 nm diameter) nano-pipette using a hopping mode of SICM (Novak et al., 2009).

4.2.4 Confocal microscopy of TAT network

The internal TAT network of freshly isolated ventricular myocytes was stained by Di-8ANEPPS and visualized by confocal microscope, as described before (Ibrahim et al., 2013; Lyon et al., 2009). The TAT structure was analysed in Fiji in terms of signal density, regularity of the t-tubules, the skeleton length, number of triple junctions per area and directional distribution of t-tubules as described in section 2.3.1.

4.2.5 Confocal visualization of $Ca_v1.2$ and Cav3 protein arrangement

Immunofluorescence study of $Ca_v1.2$ and Cav3 arrangement and colocalization was performed in faculty of Imaging Unit, Imperial College London, as described in section 2.3.2.2. Briefly, cells were fixed with 4 % PFA and were permeabilised with 0.2 % Triton X-100. Then the cells were incubated with 10 % bovine calf serum. Then cardiac myocytes were incubated with mouse mono-clonal anti-Cav3 (dilution 1:500, BD biosciences, 610421) and rabbit polyclonal anti-$Ca_v1.2$ (dilution 1:200, Alomone labs, ACC-013). After overnight incubation with primary antibodies, secondary Alexa Fluor 488 anti-rabbit (dilution 1:1000) and Alexa Fluor-546 anti-mouse (dilution 1:1000) antibodies were applied. Visualization of protein arrangement was performed with Zeiss LSM-780 inverted confocal laser scanning microscope using a 64x 1.4 NA oil objective and a pixel size of 80 nm.

4.2.6 STED study of $Ca_v1.2$ and RyR2 localization

Stimulation emission depletion experiments were performed at the Unit of Advanced Optical Microscopy of Humanitas Research Hospital, Milan, Italy with the assistance of Dr. Tilo Schorn. Cardiac myocytes were fixed with methanol at -20^{o}C for 5 min. Cells were incubated overnight with the following primary antibodies and dilutions: rabbit anti- $Ca_v1.2$ (1:200, Alomone labs, ACC-013), mouse anti-RyR2 (1:200, Thermo Fisher Scientific, C3-33). After washing step, cardiac myocytes were incubated for 1 h with the following secondary antibodies and dilutions: anti-rabbit Abberior STAR 580 (1:1000) and anti-rabbit Abberior STAR 635 (1:1000). Samples were imaged using a Leica SP8 STED3X confocal

microscope system with a 100x oil objective and a pixel size of 40 nm. Images were analysed in Fiji using Jacob colocalization plug-in.

4.2.7 Optical mapping of Ca^{2+} transients

Optical mapping of Ca^{2+} waves and transients was performed on freshly isolated cardiac myocytes stained with Fluo-4AM Ca^{2+}-sensitive dye. A detailed description of the method can be found in section 2.4.2. Myocytes were placed on the glass bottom chamber of inverted microscope equipped with a CMOS camera ULTIMA-L (SciMedia, USA Ltd, CA; 500 fps, 1.5–2 μm/pixel). Chamber was constantly perfused with HBSS solution at constant temperature of 37ºC. Two stimulation protocols were applied: 1) 5 min of 1 Hz followed by 5 s of recording to measure Ca^{2+} transients' properties, and 2) 1 min of 4 Hz stimulation followed by stimulation cessation and recording of spontaneous Ca^{2+} waves.

Ca^{2+} transient properties were analysed by using a custom- made code in Fiji. It was applied before for a line scan Ca^{2+} transient analysis (Lyon et al., 2009). Spontaneous Ca^{2+} events were divided into propagated waves (occupied all the cell length) and non-propagated waves (occurred only at certain place of cell).

4.2.7.1 βAR stimulation of Ca^{2+} transients

The effect of βAR stimulation on Ca^{2+} transients was measured by the comparison of Ca^{2+} transient amplitude measured at 1 Hz stimulation in free HBSS with that measured in HBSS containing 100 nM of isoprenaline (ISO) (Wright et al., 2014). When the perfusion buffer was changed to HBSS + ISO, cell left for 3 min and then 3 consecutive 5 s recordings were performed at 3, 4, and 5^{th} min after ISO application. The effect of ISO on the Ca^{2+} transient amplitude was measured at the same cell before and after the application of ISO.

4.2.8 Ionoptix measurements of cell contraction

Measurements of cell shortening of ventricular myocytes were performed by Dr. Ivan Diakonov. Detailed description can be found in section 2.4.4. Myocytes were attached to the glass bottom of a custom-made perfusion chamber and superfused with a KH buffer bubbled with oxygen/CO2 mixture (95%/5%) at a constant temperature of 37ºC. Only cells with a rod-shape that followed the pacing and haven't exhibit spontaneous contractions were selected. Baseline contractions were

measured at least for 10 min to establish a steady-state. After measurements of baseline contractions, perfusion was switched to a KH buffer containing 100nm of ISO for the stimulation of the βARs. Only steady-state contractions were used in analysis.

4.2.9 Confocal measurements of Ca^{2+} transients and Ca^{2+} Sparks

Ca^{2+} transients and Ca^{2+} sparks were recorded in a line-scan mode of a confocal microscope as described in section 2.4.3. Briefly, cells were loaded with Fluo4-AM for 30 min and placed on a glass bottom of a stimulation chamber equipped with a perfusion system. Myocytes were paced at 1 Hz for 1 min and then the fluorescence was recorded with 500 lines/s and 0.2-0.4 µm resolution. Analysis of Ca^{2+} sparks and shape of Ca^{2+} transient was performed in a custom-made macro in Fiji as described in 2.4.3.1.

4.2.10 Super resolution patch clamp technique with pipette clipping modification

Single LTCC recordings were performed using super resolution scanning patch clam technique in cell attached mode, as described in section 2.4.1 (Bhargava et al., 2013).

In experiments with LTCC, a channel agonist BayK8644 in concentration 5 µM was added to internal pipette solution.

4.2.11 Western Blot

Western blot analysis was performed on protein extracts from tissue lysates as described in section 2.5.1. Briefly, the proteins were extracted from cell pellets using RIPA buffer, protease inhibitor, and DTT (around 500 µL for each samples). The protein concentration was quantified with BioRad DSK+ kit using a BSA standard curve. Custom-made Tris-Glycine gels 6%- 10% were used for the blots. Running protocol included 20 min of pre-run at 70V and 1-2 h of run at 120 V, depending on the protein size. After the run, the proteins were transferred on the PVDF membrane using a wet transfer system. Membranes were stained with the Ponceau S solution (Sigma Aldirich # P7170) to check the quality of a transfer. After this, the membranes were washed with PBS + 0.1% Tween. Then they were blocked with 5% skim milk and incubated with the primary antibodies overnight at 4^{o}C (Table 2). On the next day, the membranes were washed with PBS-T and

incubated with the corresponding secondary antibodies in 5% milk for 1 hour at room temperature. At the end, the membranes were washed and covered with ECL detection solution (BioRad). The development was performed using the ChemiDoc XRS+ Imaging System (BioRad).

4.3 Results

4.3.1 Physiological data of MCT rats

The characterization of the monocrotaline model of pulmonary hypertension in rats was performed by Dr. Vahitha B. Abdul-Salam. The results are presented in Figure 4.2. A profound increase of the mean pulmonary pressure was found in rats after 10-12 days of MCT treatment (P<0.01, Figure 4.2A). The heart weight to body weight ratio was not changed after the MCT treatment (Figure 4.2C), but the lungs had an increased weight, which can be seen from the Figure 4.2B. Elastic van Gieson staining of peripheral arteries showed a significant increase in the proportion of muscularised vessels in MCT-treated rats (p<0.01, Figure 4.2E and 4.2F). Fulton index, as a ratio of the RV weight to LV plus septum weight was used to characterize RV hypertrophy. It was markedly increased in MCT-treated rats versus control ones (P<0.01, Figure 4.2D). Thus, the observed phenotype was close to hypertrophic state of RV described for MCT model.

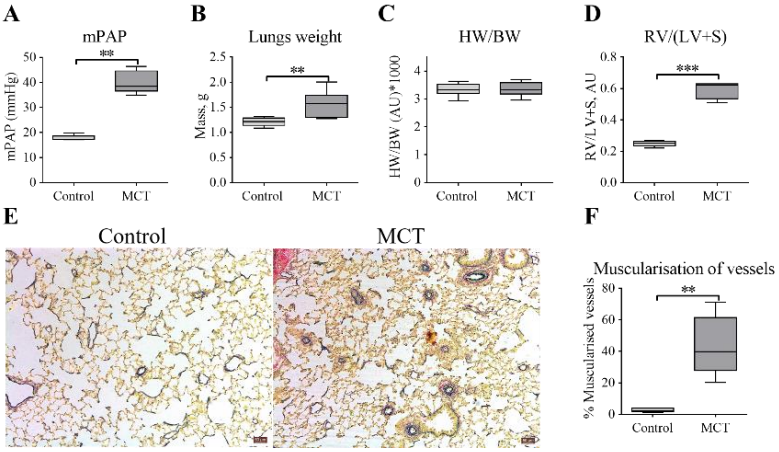

Figure 4.2 Physiological data of MCT rat model of pulmonary hypertension. A) Mean pulmonary arterial pressure measured in control and MCT treated rats. **B)** Graph representing the weight of the length from control and MCT treated animals. **C)** Graph representing the ratio of heart weight to lungs weight in control and MCT treated animals. **D)** Proportion of RV weight to LV+septum weight in control and MCT treated animals. **E)** Elastic van Gieson (EVG) representative staining of peripheral arteries in control and MCT treated animals. **F)** Graph summary of the percentage of muscularised vessels in control and MCT treated rats. **D)** (N =7-12 rats, * P <0.05, **P<0.01, by Mann-Whitney test).

4.3.2 PH produce changes in electrical properties of the RV and LV.

The electrophysiological properties of the RV and the LV from control and PH rats were studied by Dr. Stefano Rossi via epicardial multi lead recordings. The basic cardiac electrophysiological properties were assessed, such as CV and refractoriness according to (Savi et al., 2016).

The velocity of impulse propagation along (CV-1) and across the fibre directions (CV-t) were evaluated from isochrone maps (Figure 4.3A). Representative examples are shown in Figure 4.2A. PH led to a significantly slower CV-1 in LV tissue, but not in the RV ($p<0.05$, Figure 4.3B). We found no changes in CV-t between the RV and the LV from control and PH rats (Figure 4.3C). Interestingly, when conduction anisotropy was calculated by the CV-1/CV-t ratio (Figure 4.3D), it showed a significant reduction in PH RV (1.83±0.08) than in control RV (2.22±0.09, $p<0.01$).

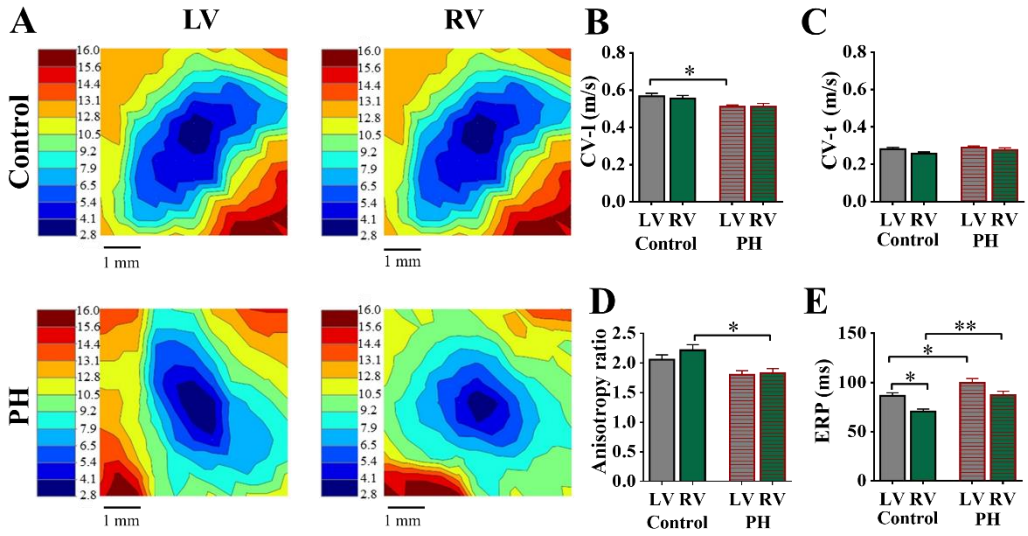

Figure 4.3 The electrophysiological properties of the RV and LV in control and PH rats. A) Representative isochrone maps of RV and LV from control and PH rats. **B)** Conduction velocity (CV-l) computed longitudinally to fibre orientation, **C)** CV-t, computed transversely to fibre orientation, **D)** anisotropy of CV (CV-l/CV-t), **E)** the effective refractory period. (N=7 rats, * $P < 0.05$, ** $P < 0.01$, by one-way ANOVA test with Bonferroni correction).

The refractoriness of the cardiac tissue was assessed by the effective refractory period (ERP). The ERP was significantly shorter in control RV than in control LV

($p<0.01$, Figure 4.3E). PH led to different prolongations of ERP in the RV (by 20%, $p<0.01$) and the LV (by 15%, $p<0.05$). Thus, ERP in RV and LV in PH rats became not statistically different.

For the analysis of arrhytmogenic activity we analysed the data from S1-S2 stimulation protocol for the appearance of extra systolic beats. There was a tendency to increase the appearance of extrasystole in PH RV where 5 on 7 rats showed at least one extrasystole whereas is was seen only in 3 on 7 animals in control RV. We did not observe in the appearance of extrasystole in control and PH LV.

The ECG parameters were evaluated to study the heart rate and propensities of the arrhythmias (Figure 4.4). The R-R interval represents a time between the activation of the ventricles at heart rate and is produced by a single sinoatrial node. Thus, there we did not expect to have the differences between RV and LV in terms of R-R interval (Figure 4.4B). Moreover there were no changes in R-R interval between control and PH rats (Figure 4.4B). Similar R-R interval in all conditions allowed us to use the QT interval as an index of cardiac action potential without frequency correction (Figure 4.4A). Both control and PH rats showed longer QT intervals in the LV than in the RV ($p<0.001$). PH produced a 20% prolongation of QT interval in the LV ($p< 0.001$) and 18% prolongation in the RV ($p<0.05$). Statistical analysis of QR duration (activation time) and T-wave duration (repolarization phase) showed their longer durations in the LV as compared to the RV in both control and PH rats ($p<0.05$, Figure 4.4C-4.4D). PH did not produce alterations of activation time and T-wave duration in both RV and LV.

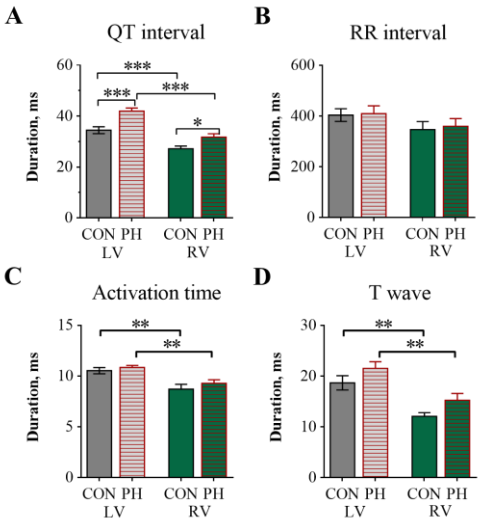

Figure 4.4. Analysis of the electrocardiogram parameters. A) QT interval (an index of ventricular action potential duration), B) RR interval (inversely related to the heart rate), C) QR interval as an indicator of activation time, D) T-wave duration (an indicator of the ventricular repolarization time). (N= 7 rats, * P < 0.05, ** P<0.01, *** P <0.001, by one-way ANOVA test with Bonferroni correction).

4.3.3 Alteration of the cardiomyocytes shape

To understand the influence of PH on the myocytes shape, we applied a phase contrast light microscopy to freshly isolated myocytes. RV myocytes in PH rats have significantly different shape with a shorter length (P<0.001, Figure 4.5A) and wider width (P<0.01, Figure 4.5B), that suggested a pronounced hypertrophic process. The length to width ratio of RV myocytes was pronouncedly decreased (P<0.01, Figure 4.5C). LV myocytes in PH rats became thinner (LV PH: 24.3+0.9 vs. LV CON: 31.7±1.1, p<0.01), that led to a higher LWR in PH LV myocytes (p< 0.05).

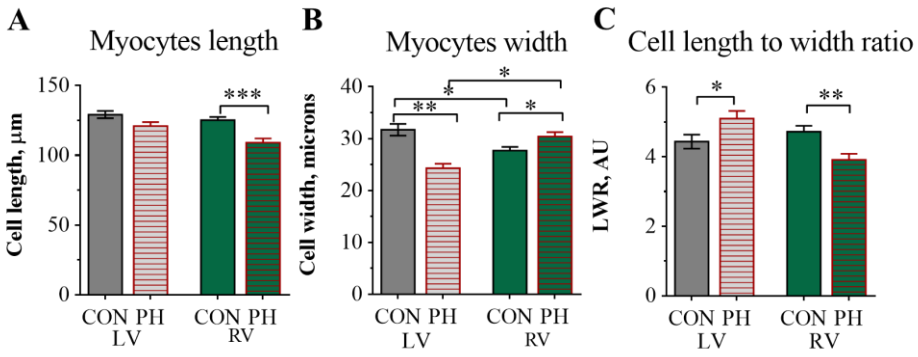

Figure 4.5. Myocytes shape characterization. Graph summary shown differences in the **A)** length, **B)** width and **C)** length to width ratio between RV and LV from control and PH rats. (n=40-58, N=3-5 rats, *P<0.05, **P<0.01, ***P<0.001 by one-way ANOVA test with Bonferroni correction).

4.3.4 Pulmonary hypertension promoted flattering of RV surface topography

We used the SICM microscopy to visualize the surface topography of live cardiomyocytes isolated from control and PH rats. Representative examples of surface scans are shown in Figure 4.6A. LV myocytes showed a similar regular striated topography in PH rats and in control ones. The surface regularity analysis of RV myocytes showed a significant reduction of z-groove ratio in PH myocytes compared to control ones. Z-groove ratio of PH RV myocytes was 0.59±0.03 A.U. vs. 0.68±0.02 A.U. in control RV ($p<0.05$). Density of T-tubule openings was analysed from LV and RV myocytes surface scans. This analysis showed similar mean T-tubule densities in RV and LV myocytes from control and PH rats.

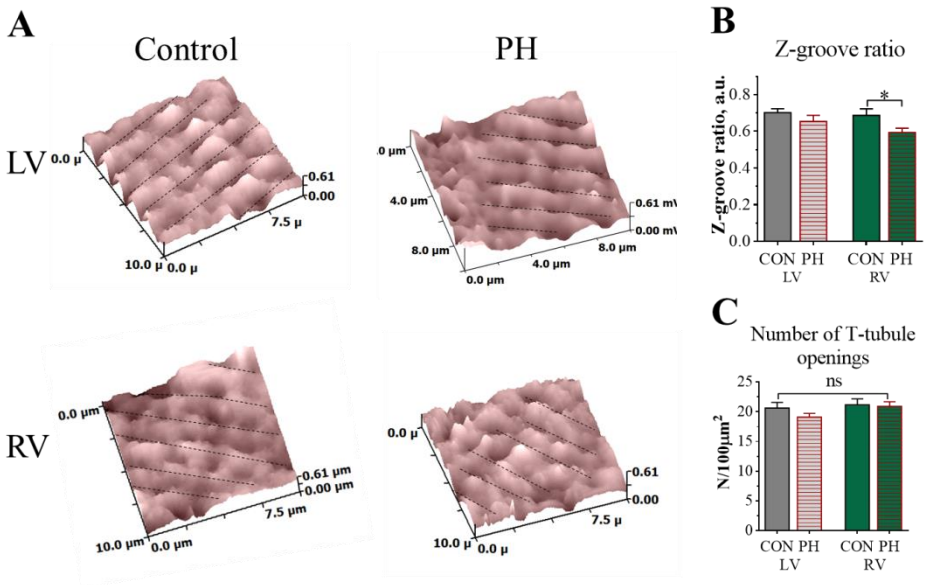

Figure 4.6. Study of myocytes surface topography. A) Scans of 10x10 surface regions of LV (up) and RV (bottom) from control (left) and PH (right) rats obtained by SICM. B) Average Z-groove ratio of LV and RV myocytes from control and PH rats. C) Average number of openings counted on 100 μm^2 surface counted on RV and LV myocytes from control and PH rats. (n=23-34, N=4-6, $p<0.05$, by Kruskal- Wallis test with Dunn's post-hoc).

4.3.5 Reorganisation of TAT network in PH myocytes.

Several studies reported a reduction of TAT network of RV myocytes in severe PH (Sabourin et al., 2018; Xie et al., 2012). The initial changes of TAT network at early stages of PH are less characterized. Representative images of the TAT structure of RV and LV myocytes from control and PH rats are shown in Figure 4.7. Myocytes from both ventricles undergo TAT remodelling process that can be seen from the dominant frequency graphs (Figure 4.8). The density of TAT network of RV myocytes was reduced in PH by 26 % ($p<0.05$ for RV, Figure 4.8C). The regularity of T-tubules was reduced significantly in PH RV myocytes compared to control ones (by 27 %, $p<0.05$, Figure 4.8D). In contrast, the density and regularity of T-tubules in LV myocytes did not change significantly ($p=0.2$).

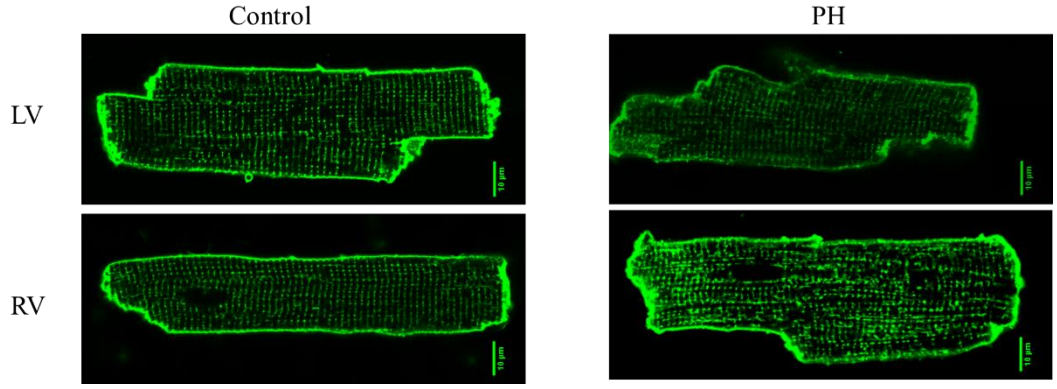

Figure 4.7. Representative images of LV (top) and RV (bottom) myocytes from control (left) and PH (right) rats.

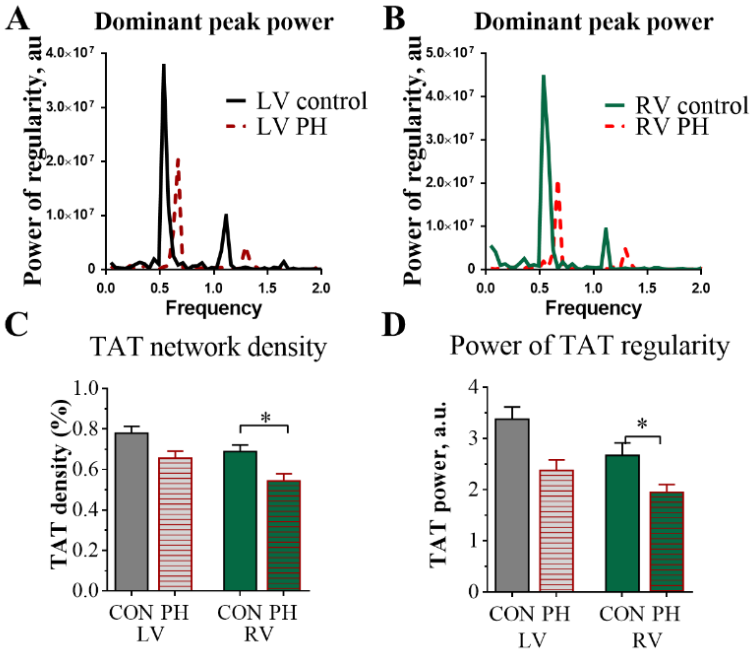

Figure 4.8. Analysis of TAT network changes in PH myocytes. A) Power peaks of the T-tubular regularity of LV myocytes from control and PH rats. B) Power peaks of the T-tubular regularity of RV myocytes from control and PH rats. C) Average TAT density of LV and RV myocytes from control and PH rats. D) Mean power of T-tubular regularity of LV and RV myocytes from control and PH rats. (N=5-8 rats, *p<0.05, by one-way ANOVA with Bonferroni correction).

To understand detail changes of TAT organisation, we applied protocol from (Wagner et al., 2014). Representative fragments of TAT structure of LV and RV myocytes from control and PH rats and corresponding skeletonized pictures are shown in Figure 4.9. Analysis of TAT skeleton length per area showed that in PH rats RV myocytes have a 6% increase of the skeleton length as compared to control ones ($p<0.05$, Figure 4.9C). The complexity of the TAT network was assessed by a number of triple junctions per area (Wagner et al., 2012). In PH rats, both RV and LV myocytes have an increased number of triple junctions compared to control ones (by 20%, $p<0.05$ and 25%, $p< 0.001$, accordingly, Figure 4.9F).

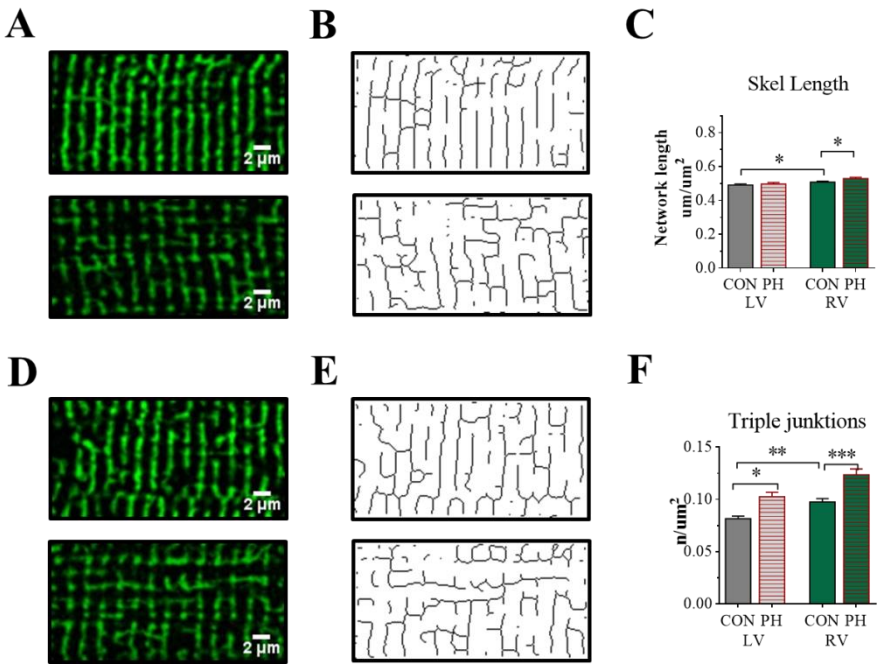

Figure 4.9. Representative fragments of TAT images of control and PH rats. A. Fragments of LV myocytes from control (top) and PH (bottom) rats. B) Skeletonized images that presented in A. C) Bar graph showing average skeleton length per area measured in RV and LV myocytes from control and PH rats. D) Fragments of TAT images of RV myocytes from control (top) and PH (bottom) rats. E) Skeletonized images that presented in D. F) The average density of triple junctions of TAT network measured in RV and LV myocytes from control and PH rats. (n=20-70 cells, N=3-7 rats, *p<0.05, **p<0.01, ***p<0.001, by one-way ANOVA with Bonferroni post hoc).

The directional distribution of TAT network was obtained via directionality histograms created in Fiji, as described in (Wagner et al., 2014). Representative histograms of TAT network directional distribution in RV myocytes from control and PH rats and subtraction histogram are shown in Figure 4.10. Subtraction histogram highlighted that in PH RV myocytes the average frequency of A-tubules become higher, than in control RV myocytes. At the same time the frequency of the T-tubules was lower in PH RV myocytes compared to control ones. Statistical analyses of the average length of tubules aligned transversally and axially to the cell main axis are presented in Figure 4.10B and 4.10D. In PH RV myocytes have a higher length of axial tubules whereas the length of transverse tubules was reduced ($p<0.05$, Figure 4.10).

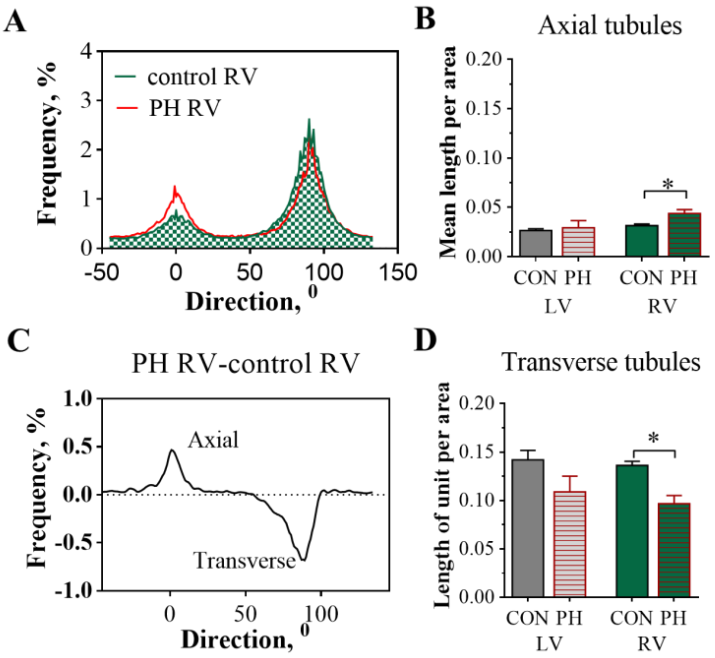

Figure 4.10. Directionality analysis of TAT network changes in PH rats. A) Representative histograms of directional distribution of TAT network of RV form control (green) and PH (red) rats. B) Average length of axial tubule in LV and RV myocytes from control and PH rats. C) Histogram subtraction PH RV – control RV), highlighting the differences between control and PH RV myocytes. D) The average length per area of transverse tubules in TAT network of LV and RV myocytes from control and PH rats. (n=20-73 cells, N 4-6 rats; *P < 0.001 by unpaired Student t test.)

4.3.6 PH lead to increase in colocalization of $Ca_v1.2$ with RyR2 in RV myocytes

Disturbance and reorganisation of TAT network observed in PH myocytes could produce changes in the membrane-anchored proteins. To understand the impact of PH on the ECC we studied the LTCC α subunit $Ca_v1.2$ density and its colocalization with RyR2 by super-resolution STED microscopy. The representative images of RV and LV myocytes stained against $Ca_v1.2$ and RyR2 antibodies are shown in Figure 4.11A. On the right side of the Figure 4.11 the presented the magnified 10x10 µm areas of the corresponding whole cell images are shown.

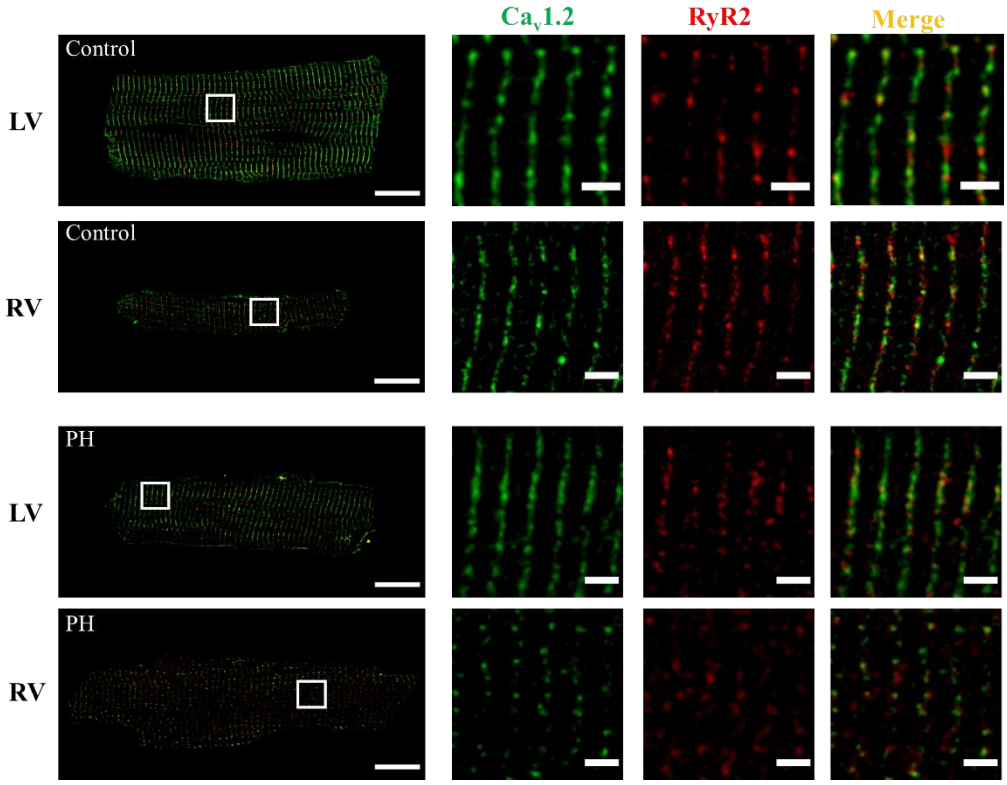

Figure 4.11. Representative images of LV and RV myocytes stained with Ca$_v$1.2 (green) and RyR2 (red) antibodies. A) Whole cell images showing merged signals. Bar equals to 20 µm. B) Magnified 10 x 10 µm portions of the images marked by a white box in A. Bar equals to 2 µm

We characterized the density of the signals from both Ca$_v$1.2 and RyR2. In PH rats, RV myocytes had a 20% lower Ca$_v$1.2 density compared to control RV myocytes ($p<0.05$, Figure 4.12A). There were no changes in RyR2 density in both RV and LV myocytes after PH (Figure 4.12B).

Then, we aimed to determine the structural alterations of Ca^{2+} interplay between LTCC and RyR2 and studied the colocalization changes in RV and LV myocytes after PH. Pearson correlation coefficient was 30% higher in PH RV myocytes than in control ones ($p<0.05$, Figure 4.13A). Manders coefficient in PH RV become higher than in control RV myocytes for Ca$_v$1.2 colocalization with RyR2 ($p<0.01$, Figure 4.13B) but not for the RyR2 colocalization with Ca$_v$1.2 (Figure 4.13C). There were not significant changes in colocalization of Ca$_v$1.2 with RyR2 in PH LV myocytes versus control LV (Figure 4.13).

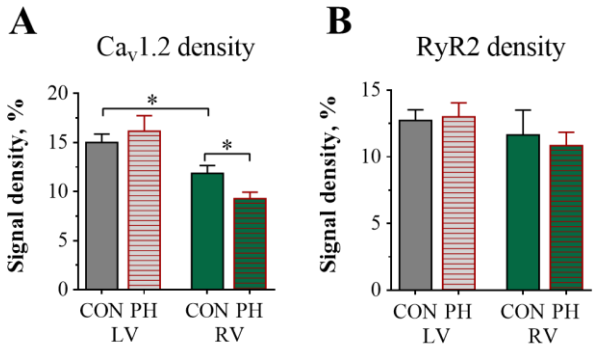

Figure 4.12. Analysis of changes in signal densities after PH. A) Average $Ca_v1.2$ signal density in LV and RV myocytes from control and PH rats. B) Average RyR2 signal density measured in LV and RV myocytes from control and PH rats. (n=10-20 cells, N=3-5 rats, *by* one-way ANOVA test with Bonferroni correction).

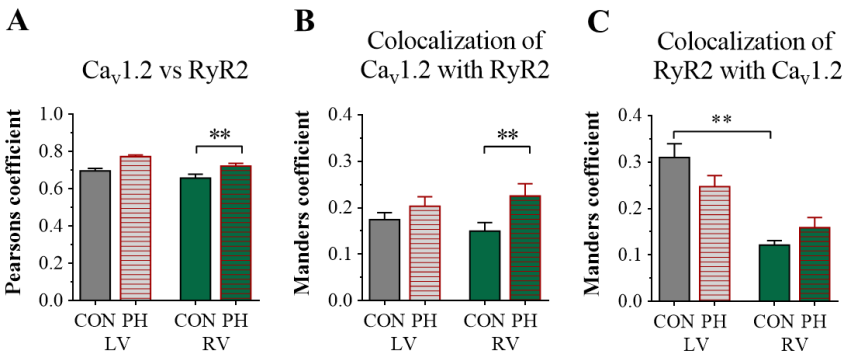

Figure 4.13. Increased colocalization between $Ca_v1.2$ and RyR2 in RV PH cells. A) Analysis of Pearson correlation coefficient between $Ca_v1.2$ and RyR2 in RV and LV myocytes. B) Manders colocalization coefficient of $Ca_v1.2$ colocalization with RyR2. C) Manders colocalization coefficient of RyR2 colocalization with $Ca_v1.2$. (n=10-25 cells, N=3-4 rats, **p<0.01, by one-way ANOVA test with Bonferroni correction).

4.3.7 PH lead to reduction of Cav3 density and colocalization with $Ca_v1.2$

LTCC main pore subunit $Ca_v1.2$ is mostly anchored to caveolae in cardiac myocytes which regulates its functioning (Balijepalli et al., 2006; Scriven et al., 2005). We hypothesized that the reduction of $Ca_v1.2$ is caused via down-reduction of caveolae structures in PH RV myocytes. The representative images of LV and RV myocytes labelled with $Ca_v1.2$ and Cav3 antibodies are shown in Figure 4.14.

Analysis of Cav3 signal density showed a 25 % reduction of this parameter in PH RV myocytes compared to control RV ($p<0.05$, Figure 4.15A). LV myocytes from control rats has a similar Cav3 density as control LV myocytes.

Colocalization of $Ca_v1.2$ with Cav3 was performed in IMARIS (Oxford instruments). The Pearson coefficients were lower in PH LV and RV myocytes as compared to the corresponding control myocytes ($p<0.05$, Figure 4.15D). To have a second verification of the data, we determined the Manders coefficients and percentage of protein volume colocalization. Both parameters were lower for $Ca_v1.2$ colocalized with Cav3 in PH RV myocytes versus control ones ($p<0.05$, Figure 4.15B and 4.15E). Similar reduction was observed in Manders coefficient and % of colocalized Cav3 with $Ca_v1.2$ in PH RV myocytes as compared to control RV cells ($p<0.05$, Figure 4.15C and 4.15F). In LV myocytes there were no changes in both Manders coefficients of $Ca_v1.2$ and Cav3 colocalization.

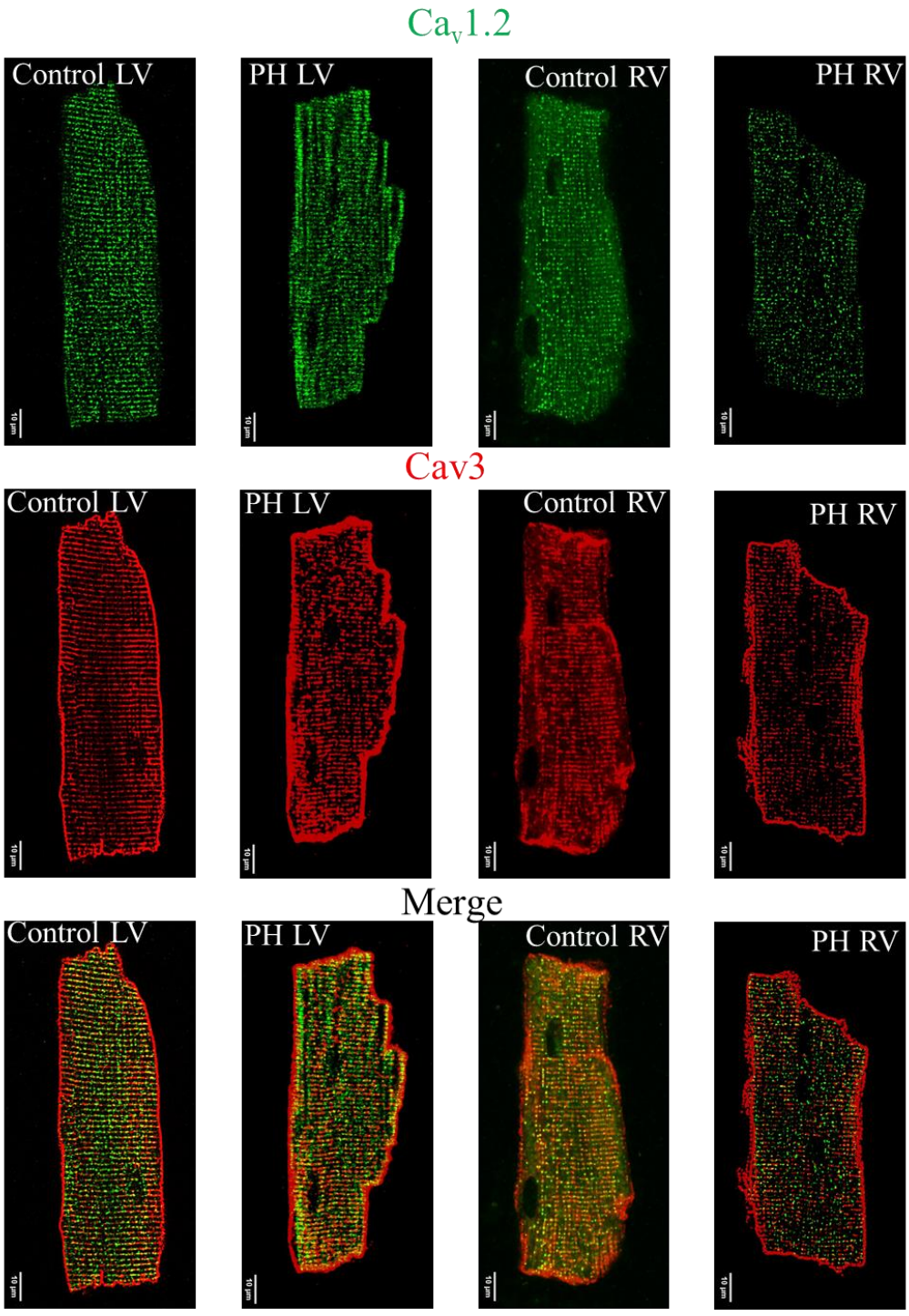

Figure 4.14. Representative images of RV and LV myocytes from control and PH rats stained with $Ca_v1.2$ (green) Cav3 (red) and merged images.

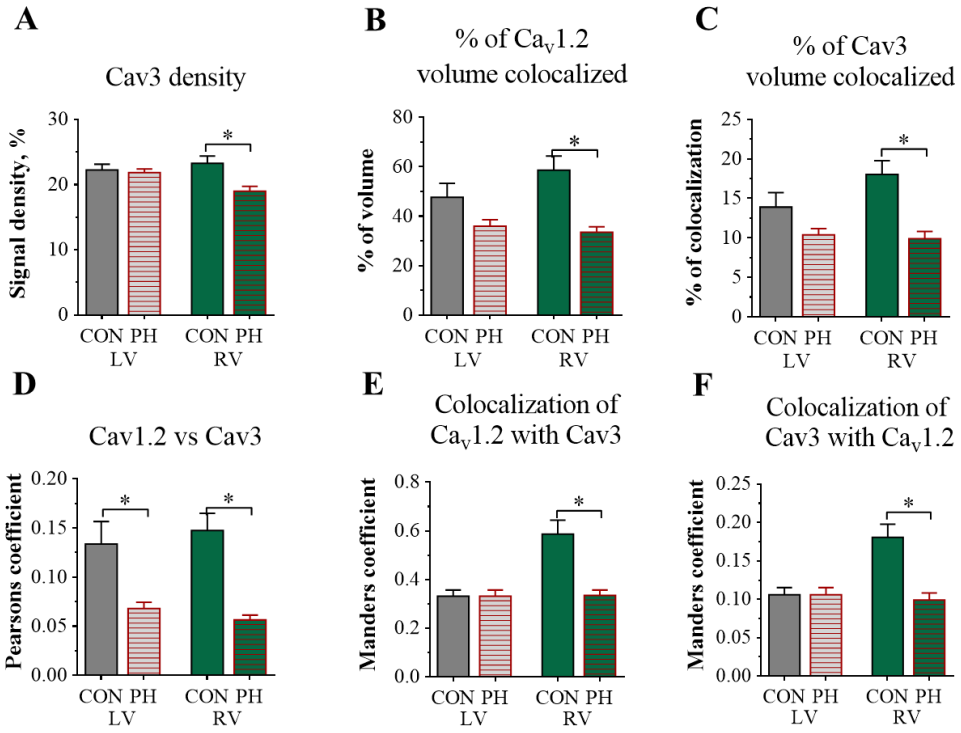

Figure 4.15. Reduction of Cav3 density and colocalization diminishing of Cav3 with $Ca_v1.2$. A) Average density of Cav3 signal measured in LV and RV myocytes from control and PH rats. B) Graphs showing the % of $Ca_v1.2$ colocalized with Cav3 in LV and RV myocytes from control and PH rats. C) Graphs showing the % of Cav3 colocalized with $Ca_v1.2$ in LV and RV myocytes from control and PH rats. D) Statistics of the Pearson coefficient of $Ca_v1.2$ colocalization with Cav3. E). Manders coefficient analysis for the $Ca_v1.2$ colocalized with cav3. F) Manders coefficient of the Cav3 colocalization with $Ca_v1.2$. (n=20-30 cells, N=3-4 rats, $p<0.05$, by one-way ANOVA test with Bonferroni correction).

4.3.8 PH induced prolongation of myocytes contraction and Ca^{2+} transients.

Characterization of functional changes in myocytes from PH rats was started with cell contraction and Ca^{2+} transients. Literature data about the Ca^{2+} transient changes are controversial (Benoist et al., 2012; Sabourin et al., 2018; Xie et al., 2012). Most of the studies were concentrated on changes in RV myocytes at severe stages of PH. We focused on the alterations in both RV and LV myocytes in early stage of PH. Contraction experiments for PH myocytes were performed with the same settings as for control cells (section 3.3.6). PH led to a ~40% increase of the cell

shortening amplitude in RV myocytes ($p<0.05$, Figure 4.16A) but not in LV myocytes. Prolongation of relaxation time was observed in PH RV myocytes compared to control ones ($p<0.01$, Figure 4.16C). LV myocytes had similar contraction properties in control and PH rats.

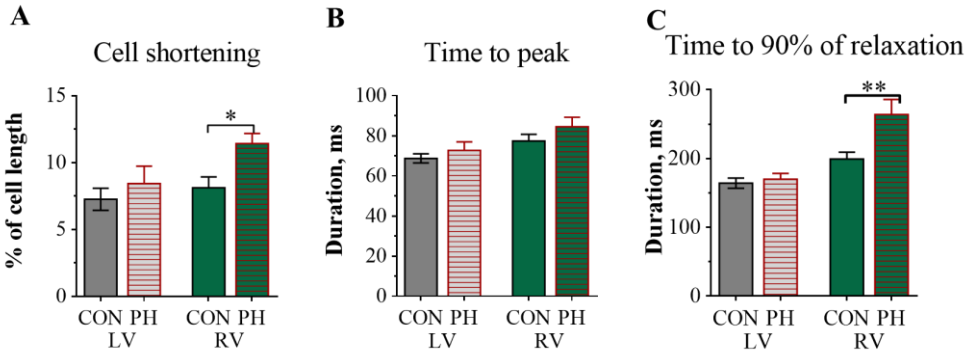

Figure 4.16. Changes in cell shortening in PH rats. A) Maximal cell shortening changes in LV and RV myocytes in PH rats. B) Time to peak of contraction, studied in control and PH myocytes from RV and LV. C) Time to 90% of relaxation measured in LV and RV myocytes from control and PH rats. (n=11-19 cells, N=4 rats, *p<0.05, **p<0.01 by one-way ANOVA test).

Alterations of Ca^{2+} transient properties were studied by optical mapping of single myocytes. The examples of Fluo-4AM optical traces recorded in LV and RV myocytes from control and PH rats are presented in Figure 4.17A. As it was mentioned in section 3.3.6, we cannot fully rely on the measurements of the Ca^{2+} transient amplitude produced using Fluo4AM, so we will not use the amplitude measurements for any conclusions (Figure 4.17B). However, other parameters of Ca^{2+} transients could be estimated from these experiments. RV myocytes in PH rats had a larger duration of time to peak ($p<0.01$, Figure 4.17C) and a longer decay time ($p<0.001$, Figure 4.17D) than in control RV myocytes. PH also changed LV Ca^{2+} transients. In PH LV myocytes duration of decay time was significantly longer than in control LV ($p<0.05$, Figure 4.17D).

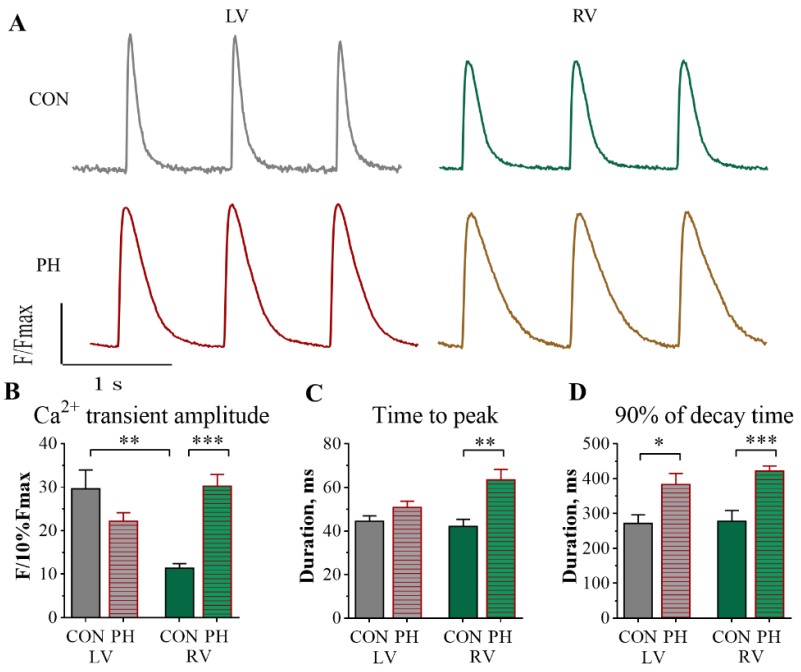

Figure 4.17. Prolongation of Ca^{2+} transients in PH RV myocytes. A) Representative examples of Ca^{2+} transient traces measured in LV and RV myocytes paced at 1 Hz. B) Average Ca^{2+} transient amplitude alterations in LV and RV myocytes from control and PH rats. C) Time to peak of Ca^{2+} transient measured in control and PH rats. D) Duration of Ca^{2+} transient decay (90%) observed in LV and RV myocytes from control and PH rats. (n=10-30 cells, N=3-4 rats, *p<0.05, ***p<0.01, ***p<0.001, by one-way ANOVA test).

4.3.9 The effect of βAR stimulation on cell contractions.

The observed alterations of cardiomyocyte contraction and Ca^{2+} transient properties could be partially induced by βAR stimulation. There are some reports indicating a high level of catecholamines in PAH patients that would lead to a persistant βAR stimulation (Sato et al., 2015). We thus hypothesized that myocytes from PH rats are less sensitive to βAR stimulation. To answer to this question, we analysed the effect of the nonselective βAR agonist (ISO) on contraction and Ca^{2+} transients of RV and LV myocytes. In these experiments we measured the amplitude of contraction and Ca^{2+} transient before and after ISO application on the same cell that excludes the potential problems with the dye loading.

The traces of cells contraction before and after application of ISO are shown in Figure 4.18A. Statistical analysis of the ISO effect on sarcomere shortening indicated that PH RV myocytes had almost a 2 times lower response to βAR than

control RV myocytes ($p<0.05$, Figure 4.18B). At the same time, application of ISO produced a ~50% reduction of Ca^{2+} transient amplitude in PH RV myocytes as compared to control RV myocytes. We did not find any differences for ISO stimulation of control and PH LV myocytes.

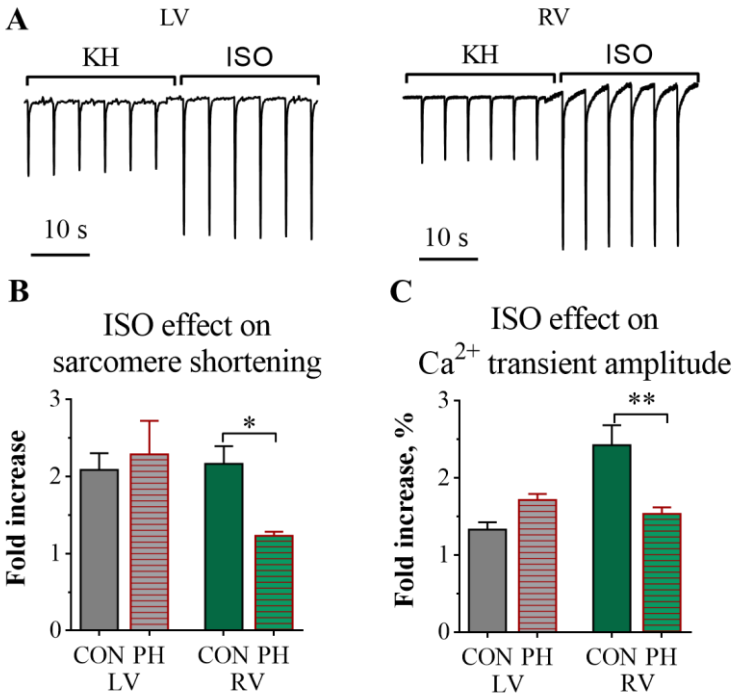

Figure 4.18. Alterations of maximal βAR stimulation in PH LV and RV myocytes. A) Representative changes in RV and LV myocyte contractions after application of ISO. (KH-Krebs-Henseleit buffer). B) The effect of ISO stimulation on the contraction amplitude in LV and RV myocytes from control and PH rats. (n=11-18 cells, N=4 rats, *p<0.05, one-way ANOVA with Bonferroni correction). C) Changes induced by ISO application in the amplitude of Ca^{2+} transients measured in RV and LV myocytes from control and PH rats. (n=27-35 cells, N=4 rats, **p<0.01, by one-way ANOVA with Bonferroni correction).

4.3.10 Increase in spontaneous Ca^{2+} activity in PH myocytes

Several pathologies were associated with the Ca^{2+} handling dysregulation, and an increased spontaneous Ca^{2+} activity was observed in PH RV myocytes (Sabourin et al., 2018; Xie et al., 2012). We hypothesized that observed alterations in myocytes structure in PH will change the spontaneous Ca^{2+} activity in PH myocytes. We applied two methods for investigation of a spontaneous Ca^{2+} activity: OM for Ca^{2+} waves and line scan microscopy for Ca^{2+} sparks.

For the first type of experiments, myocytes loaded with Fluo-4AM were electrically paced at 4 Hz for 1 min, and then spontaneous Ca^{2+} waves were recorded during 16-s rest period. Figure 4.19 presented the optical image of a myocyte loaded with Fluo-4AM and optical traces of Ca^{2+} waves showing non-propagated and propagated Ca^{2+} waves. Statistical analysis of the frequency of non-propagated Ca^{2+} waves showed a two times higher value in PH RV myocytes as compared to control ones ($p<0.01$, Figure 4.19C). The frequencies of propagated Ca^{2+} waves in RV and LV myocytes were preserved in PH. (Figure 4.19D).

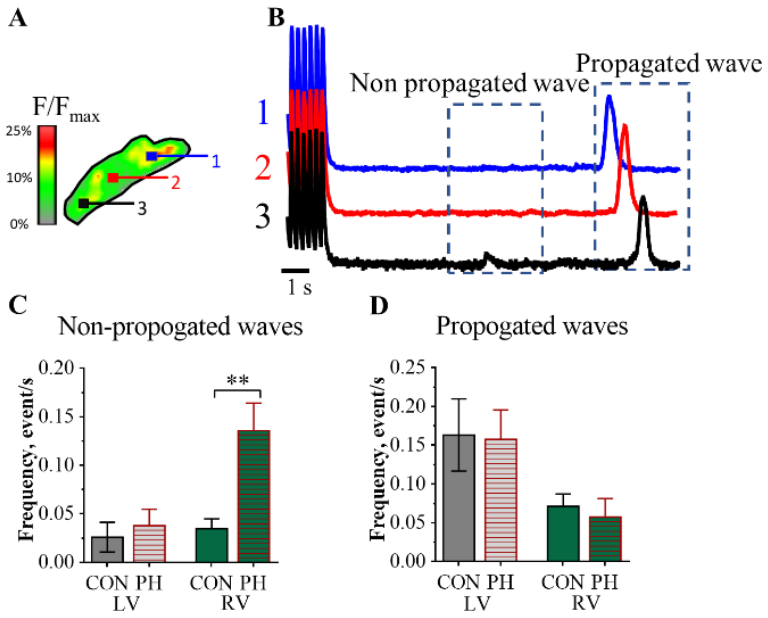

Figure 4.19. Increased spontaneous Ca^{2+} wave activity in PH myocytes. A) Optical imagine of cardiac myocyte loaded with Fluo-4AM. B) Representative traces of spontaneous Ca^{2+} activity measured in isolated ventricular myocytes during 16-s rest period after 1 min of 4Hz pacing. Optical traces of Fluo-4AM florescence changes recorded from 3 different points (1–3) selected in the cardiomyocyte. C) Bar graph showing statistical analysis of frequency of non-propagated waves in control and PH myocytes. D) Bar graph indicating statistical analysis of propagated Ca^{2+} waves frequency in control and PH myocytes. (N=4-7 rats, *p<0.05, ***p<0.001 by Kruskal- Wallis test with Dunn's post hoc).

The second method used a line-scan mode of confocal microscope to visualize spontaneous Ca^{2+} sparks (Lyon et al., 2009). Representative line-scans of Fluo4-AM fluorescence are presented in Figure 4.20A. Basic properties of Ca^{2+} sparks are

presented in Table 9 and Figure 4.20. The frequency of Ca^{2+} sparks was two times higher in PH RV myocytes as compared to control ones ($p<0.01$, Figure 4.20B). PH did not change the frequency of Ca^{2+} sparks in LV myocytes (Figure 4.20B). PH led to alteration of the Ca^{2+} spark shape in RV myocytes, they had a higher amplitude ($p<0.05$) and a longer duration ($p<0.05$) than control RV myocytes. This variations produced a significantly higher mass of the spark in PH RV myocytes than in control RV myocytes ($p<0.001$). Consequently, spark-mediated Ca^{2+} leak was 2.5 times higher in PH RV myocytes than in control RV myocytes ($p<0.01$, Figure 4.20D). The mass of Ca^{2+} sparks and spark-mediated Ca^{2+} leak were similar between control and PH LV myocytes (Figure 4.20C and 4.20D).

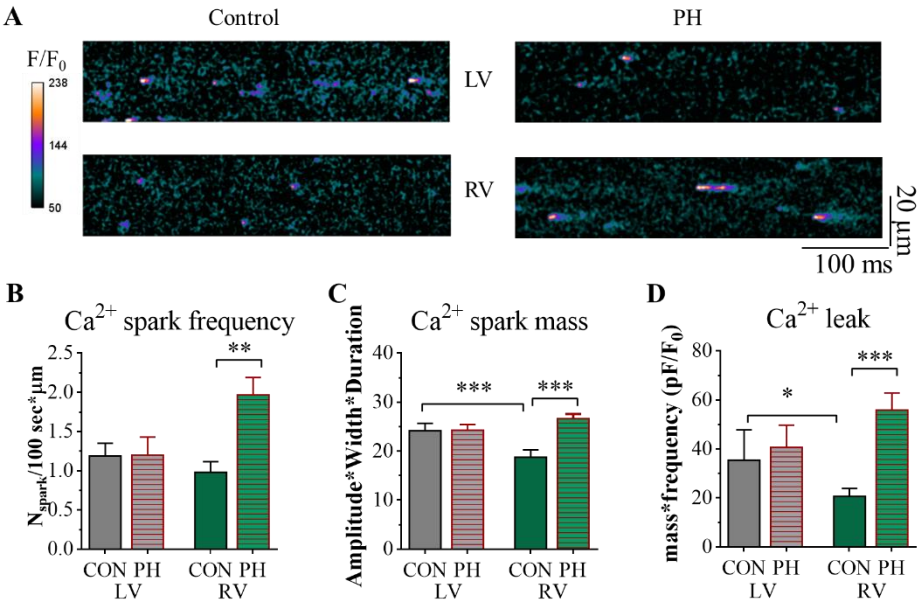

Figure 4.20. The modulation of Ca^{2+} sparks parameters induced by PH. A) Representative line scans of Fluo4- AM fluorescence recorded in LV and RV myocytes from control and PH rats. B) Analysis of Ca^{2+} sparks frequency, B) Ca^{2+} spark mass and C) Ca^{2+} leak in control and PH myocytes. (n= 26-49 cells, N=3-5 hearts/group., by one-way ANOVA test with Bonferroni correction).

Table 9. Ca^{2+} sparks properties in RV and LV myocytes from control and PH rats.

	LV		RV	
	CON	PH	CON	PH
Frequency, $N_{spark}/\mu m/100s$	1.3±0.1	1.4±0.3	1.18±0.18	2.0±0.2*
Amplitude, F/F_0	0.35±0.01	0.34±0.01	0.29±0.01	0.36±0.01*
HMFW, µm	2.65±0.05	2.67±0.07	2.35±0.06	2.51±0.03
HMFD, ms	25.1±0.6	26.9±1.1	24.3±1.2	28.6±0.6*
Time to peak, ms	12.6±0.6	12.6±0.9	11.7±0.5	14.3±0.5*
Tau, ms	26.3±1.4	27.3±1.7	26.5±2.0	32.4±1.0*
Ca^{2+} spark mass, $n(F/F_0)*m*s$	24.3±1.1	24.2±1.1*	18.8±1.5	26.7±0.9*
Ca^{2+} spark induced Ca^{2+} leak, $p(F/F_0)$	30.5±4.9	24.9±5.5	21.8±3.5	55.8±7.0*

Values are mean±SEM, n = 26-49, N=3-5 hearts/group. Spark mass was calculated as amplitude*width*duration, and spark leak was calculated as mass*frequency. *p<0.05, **p<0.001 vs. the corresponding CON group, by one-way ANOVA test.

4.3.11 RV myocytes from PH rats exhibit less synchronous Ca^{2+} transients

The observed different Ca^{2+} handling properties of PH myocytes and the disorganisation of TATS can lead to the uncoupling of RyR2 from TAT network, producing "orphaned" RyRs (Song et al., 2006). This could result in a different pattern of Ca^{2+} release in PH myocytes as compared to control ones. We compared the shape of Ca^{2+} release using TTF50 profiles. The representative images of Ca^{2+} transients are presented in Figure 4.21A. The histograms of TTF50 distribution in LV (Figure 4.21B) and RV myocytes are shown in (Figure 4.21B and 4.21C). PH had no effect on the TTF50 histogram of LV myocytes (Figure 4.21B), whereas in PH RV myocytes TTF50 had a right-shifted distribution of values as compared to control RV myocytes (Figure 4.21C). We applied the methodology of (Louch et al., 2006) to estimate the de-synchronization of the Ca^{2+} transient. The average 'desynchrony index' values are presented in (Figure 4.21D). PH RV myocytes have

a ~19% higher ‘desynchrony index’ than control RV myocytes ($p<0.05$, Figure 4.21D).

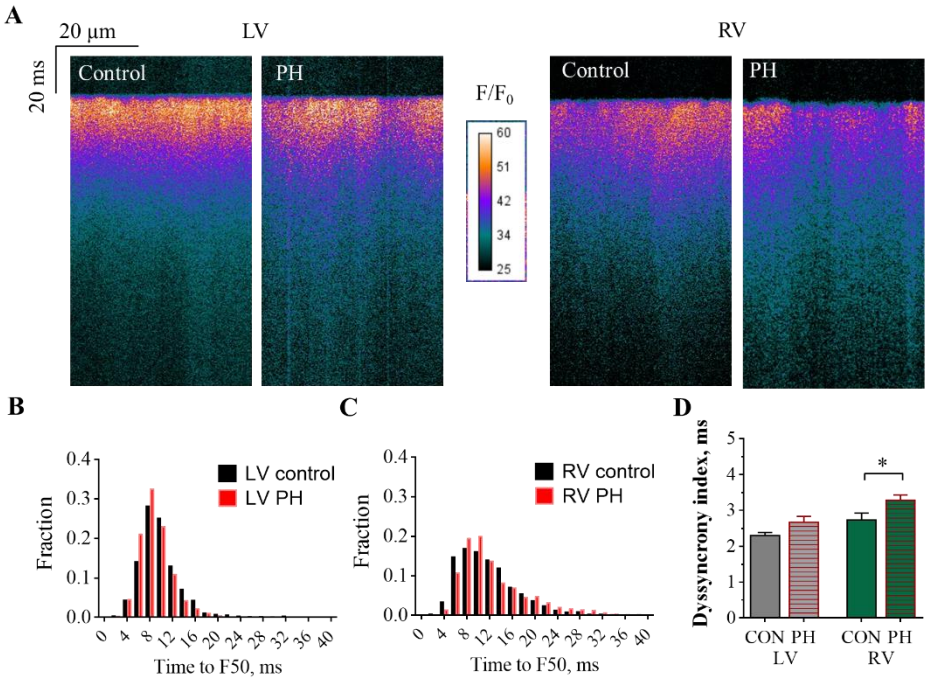

Figure 4.21 Analysis of Ca^{2+} transient activation in LV and RV myocytes. A) Representative examples of Ca^{2+} transient line scans recorded in LV and RV myocytes from control and PH rats. B) Histogram of TF50 distribution in control and PH LV myocytes. C) Histograms of TTF50 distribution in control and PH RV myocytes. D) Analysis of desynchrony index in RV and LV myocytes from control and PH rats (n=24-51 cells, N=3-5 rats, *$p<0.05$ by one-way ANOVA with Bonferroni post hoc).

As discussed before in section 3.3.8, we applied the method of Biesmans et al. to divide the observed Ca^{2+} sparks in accordance with their TTF50 position. Using this approach, we looked at the modifications of early and delayed sparks separately. As we did not observe the differences in a general Ca^{2+} sparks properties in LV myocytes, we did not found the alterations of both early and delayed sparks in LV myocytes (Figure 4.22 B-4.22D). In the RV, PH lead to significant alterations in the properties of delayed Ca^{2+} sparks (Figure 4.22). Delayed Ca^{2+} sparks from PH myocytes had a larger amplitude than control RV myocytes ($p<0.05$, Figure 4.22F) and became significantly wider ($p<0.01$, Figure 4.22G).

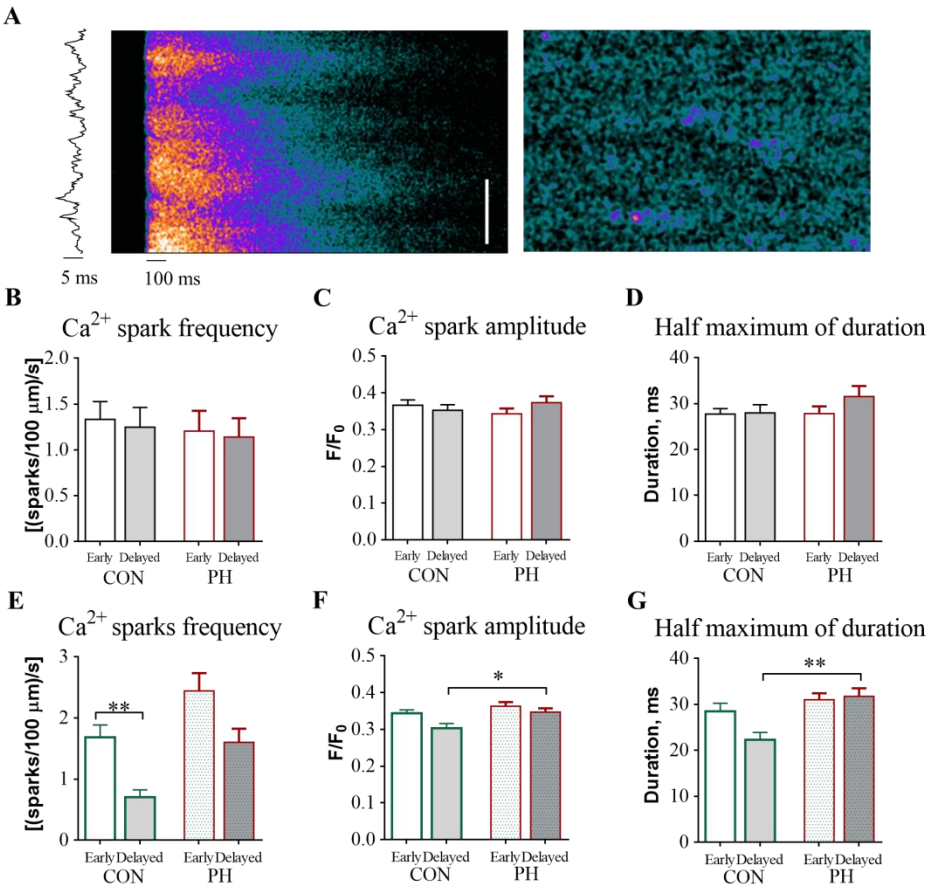

Figure 4.22. Analysis of early and delayed Ca^{2+} sparks in control and PH myocytes. A) Typical example of a line scan image during and after 1 Hz stimulation. On the left the TTF50 profile is presented. Sparks were assigned to early and delayed release areas corresponding to their position on the scan line. Statistical analysis of Ca^{2+} sparks parameters in LV myocytes from control and PH rats: frequency, B) Ca^{2+} spark amplitude, C) Half maximum of duration. (n=20-37, N=3-4). D) Analysis of Ca^{2+} sparks frequency, E) amplitude and F) half maximum of duration in control and PH RV myocytes. (n=35-47 cells, N=4-5 rats, *p<0.05, **p<0.01, *p<0.001, by one-way ANOVA test with Bonferroni correction).

4.3.12 L-type Ca^{2+} channels redistribution in PH RV myocytes

Spatial localization of L-type Ca^{2+} channels was assessed by the super resolution scanning patch-clamp technique. Representative traces of LTCC single channel activity recorded in normal external solution at -6.7 mV are shown in Figure 4.23. Single LTCC activity was also recorded in the presence of a channel agonist BayK.

Traces of LTCC activity recorded in the presence of BayK in T-tubules and crests of RV myocytes from control and PH rat are shown in Figure 4.24.

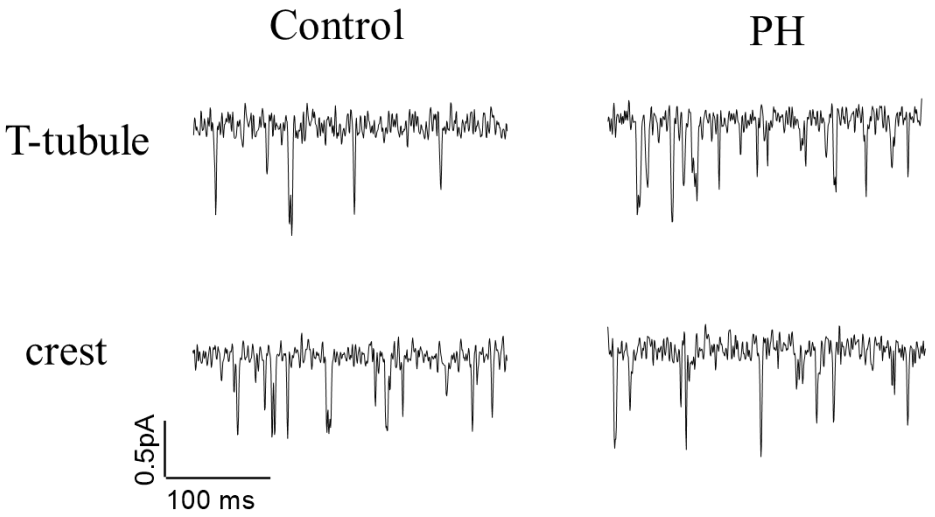

Figure 4.23. Traces of single LTCC activity recorded at -6.7 mV in T-tubule and crests of RV myocytes from control and PH rats.

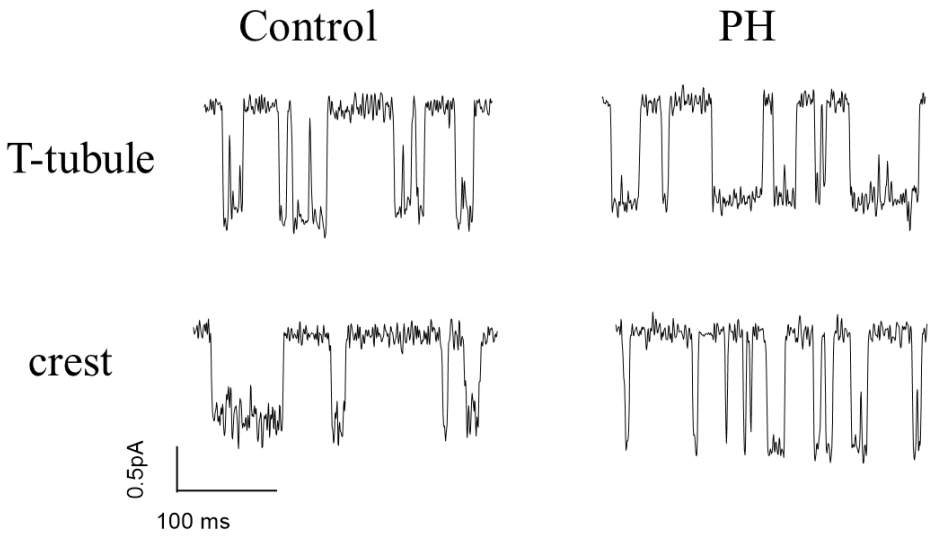

Figure 4.24 Single LTCC recordings acquired at T-tubule or crest regions of RV myocytes from control and PH rats in presence of LTCC agonist BayK8644.

Analysis of spatial localization of LTCCs after PH in RV myocytes was performed in normal external solution and with BayK in the bath (Figure 4.25). Density of LTCC was reduced in PH RV myocytes by ~2.1 times in T-tubule and ~2.3 times at the crest. The density of LTCC in T-tubule in the presence of BayK was reduced by 28% in PH RV myocytes versus control RV myocytes. LTCC density was 40 % higher at the crest of PH RV myocytes as compared to control ones. Application of the LTCC agonist showed that the observed reduction of LTCC density during the physiological recordings could be attributed to the redistribution and silencing of the channels.

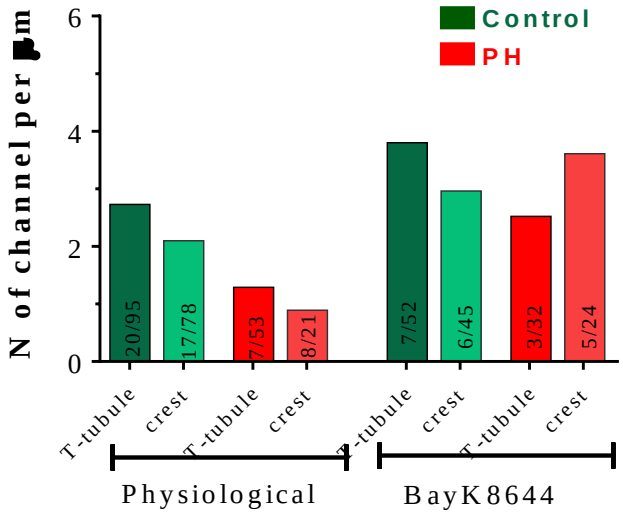

Figure 4.25. Density of LTCC measured in control and PH RV myocytes in absence and presence of BayK8644. n/m- number of patches with LTCC / total number of successful patches.

LTCC open probability and amplitude were studied (Figure 4.26A and 4.26B). In normal external solution, LTCCs had an 80% higher Po in T-tubules of PH myocytes than in T-tubules of control myocytes ($p<0.05$, Figure 4.26A). The same higher Po of LTCCs located in T-tubules of PH rats than in T-tubules of control RV myocytes was observed when channels were recorded in the presence of BayK ($P<0.05$, Figure 4.26A).

Single channel activity can be analysed in terms of current-voltage relationship (Figure 4.27 and Figure 4.28) or using amplitude at single voltage, in this case at -

6.7 mV (Figure 4.26B). In both cases, when LTCCs were recorded in normal external solution, no alterations of LTCC amplitude or conductance in PH RV myocytes were observed. As it was shown in control RV myocytes, the presence of BayK LTCCs had a lower amplitude in T-tubules that in the crest. PH lead to an increase in LTCC amplitude in T-tubule compared to the corresponding LTCCs in control RV myocytes ($p<0.05$, Figure 4.26B). Conductance of LTCCs was also higher at T-tubules of PH rats versus T-tubules of control rats ($p<0.05$, Figure 4.28). On the contrary, LTCC conductance and amplitude measured at -6.7 mV for the channels recorded at crests of PH RV myocytes were significantly lower as the conductance and amplitude at -6.7 mV measured at the crests of control RV myocytes ($p<0.01$, Figure 4.28, $p<0.01$, Figure 4.26B).

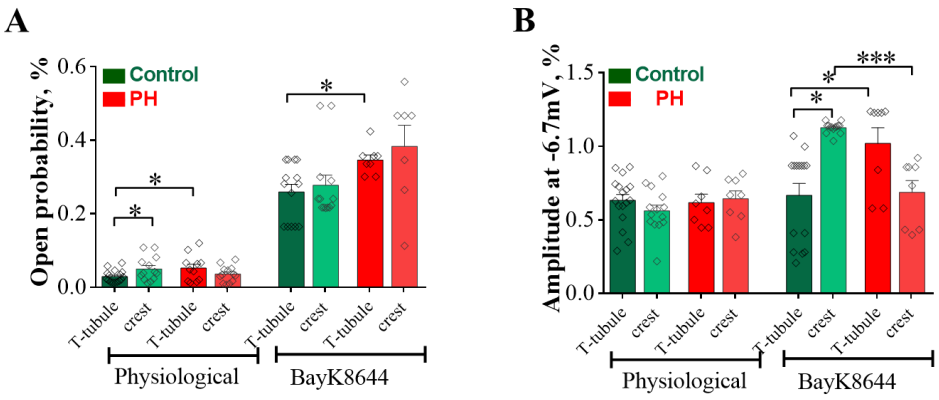

Figure 4.26. Alteration of LTCC properties in PH RV myocytes. A) Open probability of single LTCC measured at-6.7mV in absence and presence of BayK8644. (Number of successful patches used in physiological control: T-tubule-20, crest 17, PH T-tubule-7, crest-8; BayK: Control T-tubule-7, crest-6, PH: T-tubule-3, crest 5 channels, *$p<0.05$, by Kruskal- Wallis test with Dunn's post-hoc). B) Average single LTCC amplitude measured at -6.7 mV in myocytes with and without BayK (*$P<0.05$, ***$P<0.001$ by Kruskal- Wallis test with Dunn's correction).

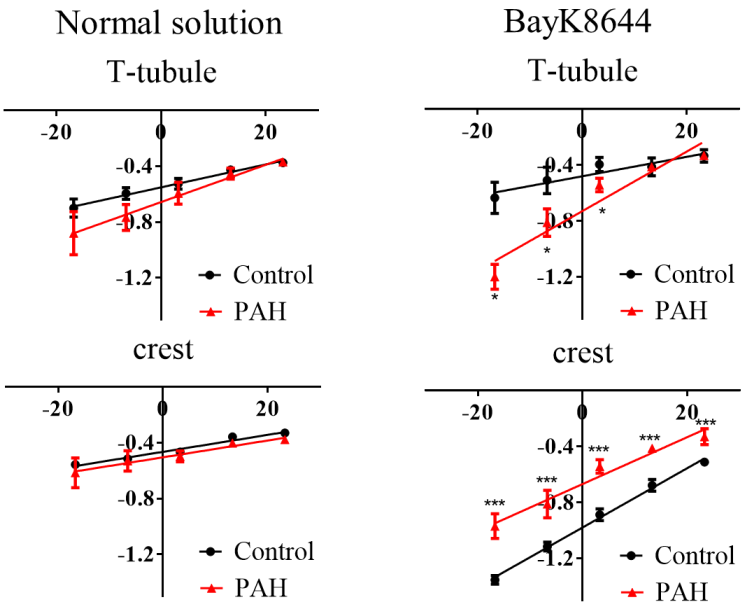

Figure 4.27. Current-voltage LTCC dependence measured at T-tubule (top) and crest (bottom) of control and PH RV myocytes in absence (left) and presence (right) of BayK. Normal solution: control: T-tubule-20, crest 17, PH T-tubule-7, crest-8; BayK: Control T-tubule-7, crest-6, PH: T-tubule-3, crest 5 channels, *p<0.05, ***p<0.001 vs. control LTCC amplitude at corresponding voltage, by unpaired t-test.

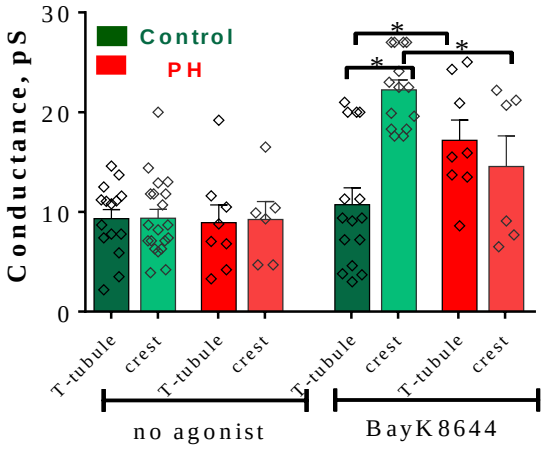

Figure 4.28. Conductance of single LTCC measured at T-tubule and crest of RV myocytes from control and PH rats in absence and presence of BayK. (Physiological: control: T-tubule-20, crest 17, PH T-tubule-7, crest-8; BayK: Control T-tubule-7, crest-6, PH: T-tubule-3, crest 5 channels, *p<0.05, by one-way ANOVA test with Bonferroni correction).

4.3.13 Average expression of $Ca_v1.2$, Cav3 and levels of kinase activity in RV and LV myocytes

Finally, we performed the western blot analysis of $Ca_v1.2$ and Cav3 expression and the level of phosphorylation of CaMKII and PKA in control and PH RV and LV myocytes (Figure 4.29 and 4.30). PH had no effect on the expression of $Ca_v1.2$, in both RV and LV myocytes. As LTCC and RyR2 are both the targets of PKA and CaMKII phosphorylation, we checked the activity of these kinases in control and PH myocytes. To investigate the level of the PKA activity, we applied the antibody specific to pPKA-substrate, as it was performed in (Seul Han et al., 2018). PH RV myocytes had a slight (by 10%, not significant) increase of the PKA substrate density than control RV myocytes (Figure 4.29B). pCaMKII phosphorylated at Thr286 was used to assess CaMKII activity. RV myocytes from PH rats showed about 20% higher level of pCaMKII than the control ones (not significant, Figure 4.29B). PH did not change the expression of both pPKA and pCaMKII in LV myocytes (Figure 4.30).

As discussed before, Cav3 is important for maintenance of LTCCs and their function, as it brings together LTCC with many signalling proteins and regulatory units, such as PKA (Balijepalli et al., 2006). Expression of Cav3 in PH RV myocytes was ~ 35% smaller than in control RV myocytes (not significant, Figure 4.29B).

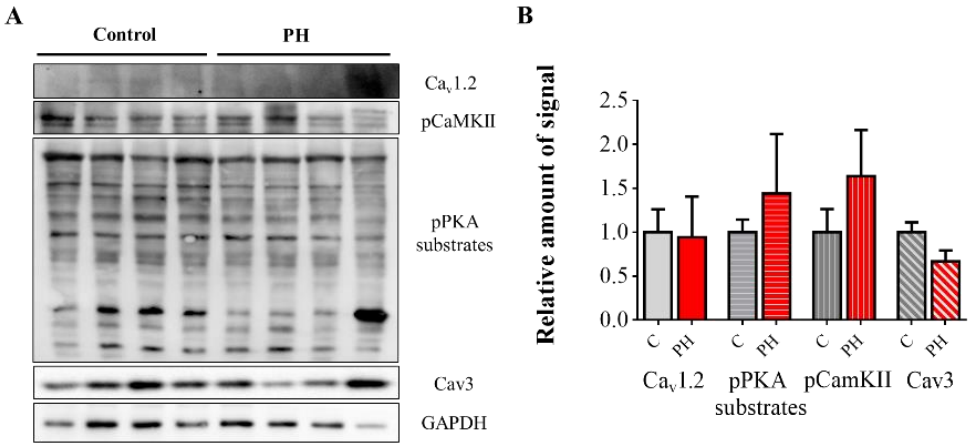

Figure 4.29. Western blot analysis of the protein expression in control and PH RV myocytes. A) Blots showing the relative levels of $Ca_v1.2$, pCaMKII, pPKA substrate, Cav3 and GAPDH in control and MI RV myocytes. B) Average density of $Ca_v1.2$, pCaMKII, pPKA substrates, and cav3 normalized to GAPDH. (Control (C) n=4, PH n=4 rats).

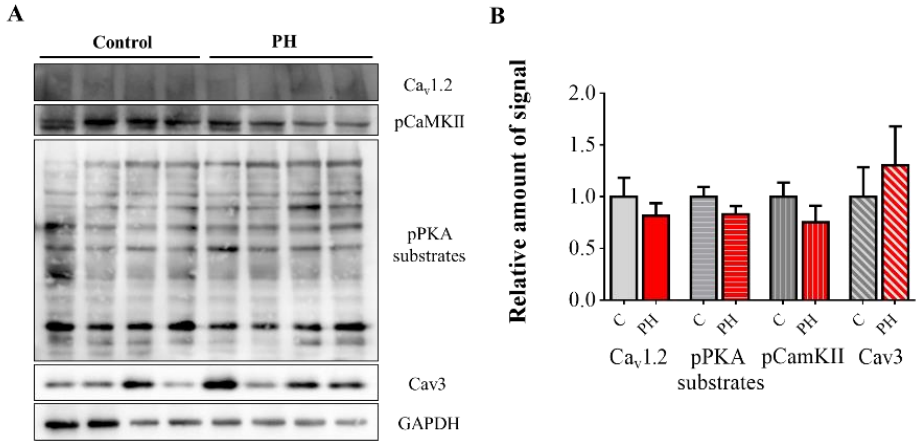

Figure 4.30. Western blot analysis of protein expression in the LV myocytes from control and PH rats. A) Representative blots of $Ca_v1.2$, pCaMKII, pPKA substrate, Cav3 and GAPDH performed on samples from control and PH LV myocytes. B analysis of mean protein density from the blots showed in A. (Control (C) n=4, PH n=4 rats).

4.4 Discussion

This chapter was devoted to investigate the PH-induced alterations in RV and LV function on different levels. To make a better description of PH in rats we studied it effects on molecular, cellular and whole organ levels.

First, we analysed the phenotype of PH induced in rat by MCT. Despite a wide usage of this model, the protocols of MCT applications differ from one publication to another. Benoist et al. proposed that MCT injection of 30 mg/kg will lead to RV hypertrophy, whereas 60 mg/kg would produce RV failure (RVF) (Benoist et al., 2012). The common protocols include a 60 mg/kg injection and animals were sacrificed around 20-25 days after the injection when the pronounced RVF was established (Benoist et al., 2011; Rocchetti et al., 2014; Xie et al., 2012). Monitoring the changes of RV dynamics and shape at several time points after 60 mg/kg of MCT injection showed that the pronounced hypertrophy of RV is usually developed after 2 weeks (Abdul-Salam et al., 2019; Sabourin et al., 2018). We followed the protocol of (Abdul-Salam et al., 2018) and treated the rats with MCT for 10-12 days. The physiological measurements that are shown in Figure 4.2, indicated a significant increase of PAP, muscularisation of the vessels in the lungs and RV / LV+ septum ratio in MCT treated rats. These results indicate an appearance of PH with a RV hypertrophy, similar to that described by (Abdul-Salam et al., 2019; Sabourin et al., 2018).

Progression of PH in humans is accompanied by the formation of the arrhythmogenic activity at the last stages of the disease (Handoko et al., 2010). In rats with RVF, arrhythmogenicity was also observed by Benoist et al. (Benoist et al., 2011). Here, we investigated the formation of pro-arrhythmogenic substrates at the early stage of PH in rats via analysis of impulse propagation and tissue refractoriness. The velocity of impulse propagation along a fibre orientation was lower in PH LV than in control LV tissue and there were no changes observed in the CV of the RV. However, the formation of pro-arrhythmogenic substrates depends on the anisotropy of CV in the tissue. In healthy ventricular tissue, the anisotropic ratio is around 1:2 and the increase of the anisotropic ratio was linked to the generation of unidirectional conduction block and sink to source mismatch

(Van Rijen et al., 2004; Volders et al., 1999). Here, we found a decrease in CV anisotropy in the PH RV (Figure 4.3) that cannot be considered as pro-arrhythmic (Linnenbank et al., 2014).

We also observed prolongation of ERP in the RV and LV from PH rats, which could be related to the prolongation of QT interval (reflects APD in ECG, Figure 4.4), and to the increase of Ca^{2+} transient duration observed in RV and LV myocytes (Figure 4.17). Prolonged ERP could either increase or decrease arrhythmogenesis (Linnenbank et al., 2014). Increasing the ERP can precipitate *torsades de pointes*, a type of ventricular tachycardia caused by EADs or DADs (Cleland and Krikler, 1992; Volders et al., 1999). On the other side, a longer ERP could interrupt tachycardia caused by re-entry mechanisms by prolonging the length of the re-entrant circuits (Wiener and Rosenblueth, 1946). Thus, both of the observed alterations in CV anisotropy and ERP prolongation solely cannot produce a pro-arrhythmogenic substrate. We did not see a significant increase in occurrence of extrasystole in the PH RV as compared to the control RV, so we could assume this stage of the disease is not severe enough for the development of pro-arrhythmogenic substrates.

We observed pronounced changes in the shape of both RV and LV myocytes in PH rats, while RV myocytes became more hypertrophic and the LV myocytes became atrophied (Figure 4.5). As it is an early stage of the disease, we observed a significant change of the RV mass, but not the LV mass (Figure 4.2). The changes in the RV mass could be due to the adaptation to the work in conditions of increased PAP (Figure 4.2). On the other side, if the RV is dilated, the interventricular septum shifts toward the left, altering LV geometry and increasing pericardial constriction (Foschi et al., 2017). In our case, the hypertrophied RV could already shift the septum towards the left that induce the changes of cell shape and Ca^{2+} handling, however it is not enough for a significant changes in the ventricular mass. This trend could be responsible for the significant atrophy of the LV observed at severe PH (30 days after MCT injection; (Han et al., 2018)).

Changes in myocytes shape lead to the damage of the membrane structures. In our studies we found that a surface topography was altered only in RV myocytes but

not in LV (Figure 4.6). Sarcolemma membrane flattering was studied by our group on LV myocytes during the progression of HF (Lyon et al., 2009; Schobesberger et al., 2017). It was shown that reorganisation of surface sarcolemma is correlated with an impaired contractility of cells and a high rate of spontaneous Ca^{2+} activity (Heinzel et al., 2008; Lyon et al., 2009). Both impaired contractility and altered Ca^{2+} handling were observed in RV myocytes, but not in LV cells after PH (Figure 4.16-4.19).

The internal TAT network is more flexible than the surface sarcolemma. It changes to adapt to the alteration in the load and stress (Heinzel et al., 2008). We showed that in PH, RV myocytes have a reduced density and regularity of T-tubules (Figure 4.8). Significant reduction of both TAT density and regularity was found at later stages of PH hypertension by (Fowler et al., 2018; Rocchetti et al., 2014; Xie et al., 2012). Sabourin et al. also observed the reduction of TAT regularity in the RV after 14 days of PH as well as in LV myocytes after 21 of PH (Sabourin et al., 2018). Moreover, the TAT skeleton analysis showed a higher complexity of the network in both RV and LV myocytes (Figure 4.9), probably due to an increase of A-tubules formation and a reduction of T-tubules (Figure 4.10). As discussed before (section 3.4) and in the work by (Schobesberger et al., 2017), A-tubules are appeared during the hypertrophic state of disease. They were proposed to be a compensatory mechanism that serves to maintain the ECC under the stress when initial T-tubules organisation is destroyed (Jones et al., 2018). In ventricular myocytes, new tubules formation in axial direction could be driven by actin filaments formation, which was observed in HF (Lichter et al., 2014). Higher proliferation of actin filaments was also found in RV myocytes of PH hypertensive rats (Stones et al., 2013).

Reduction of surface regularity and reorganisation of TAT network in PH RV myocytes were accompanied by a pronounced increase of cell shortening (Figure 4.16) and Ca^{2+} sparks amplitude (

Table ***9***). As discussed in the introduction, there are some discrepancies in the literature about the effect of PH on myocytes cell shortenings and Ca^{2+} transient that could be related to different protocols of MCT treatment. We hypothesize that high neurohormonal activity observed in PH, could be responsible for a higher basal βAR stimulation in PH RV myocytes. Application of non-selective βAR agonist, ISO, showed a less potent effect on cell contraction and Ca^{2+} transients of PH RV myocytes then on control RV cells (Figure 4.18). LV myocytes from control and PH rats had similar cell shortenings, and potentiation under the βAR stimulation (Figure 4.16-4.18).

Membrane reorganisation and surface flattering in PH RV and LV myocytes could promote a higher rate of spontaneous Ca^{2+} activity. We used two separate methodologies to investigate the spontaneous Ca^{2+} events in RV and LV myocytes: optical mapping and line modification of confocal microscopy. Both approaches showed a pronounced increase in the frequency of Ca^{2+} waves and Ca^{2+} sparks in RV myocytes after PH, but not in LV myocytes (Figure 4.19 and 4.20). A higher sparks rate was observed at 14 days of PH (Sabourin et al., 2018), and at 30 days of MCT treatment (Benoist et al., 2014; Xie et al., 2012). The shape of Ca^{2+} sparks was also modified in PH. Ca^{2+} sparks in RV had a higher amplitude and a longer duration than in control RV myocytes (Table 4.1) producing a larger mass of Ca^{2+} spark and spark-mediated Ca^{2+} leak. In the work of Sabourin et al. Ca^{2+} sparks in PH RV myocytes have a similar amplitude, but a wider and a longer duration than in control RV myocytes (Sabourin et al., 2018). However, Benoist et al. reported a pronounced increase of both Ca^{2+} spark mass and spark mediated leak in hypertrophic stage of RV (Benoist et al., 2012). Increased spontaneous Ca^{2+} releases through RyR2 could be induced via phosphorylation of the receptors by CaMKII and PKA (Bers and Perez-Reyes, 1999). The levels of pCaMKII and pPKA substrate were slightly but not significantly higher in PH RV myocytes as compared to control ones (Figure 4.29). Phosphorylation of RyR2 at Ser 2808 and Ser 2814 was not changed in RV and LV myocytes after PH (Sabourin et al., 2018). Ca^{2+} sparks rate could be altered by variation of the SR Ca^{2+} loading. However our preliminary study and others showed the unchanged SR Ca^{2+} loading in RV myocytes after 14 and 30 days of PH (Benoist et al., 2014; Sabourin et al., 2018).

Thus, we hypothesize that an increased [Ca^{2+}] in cytosol due to the prolonged Ca^{2+} transient or increase influx through LTCC could be responsible for triggering of RyR2 openings.

Disorganisation of TAT network in HF was associated with a slower and more desynchronous activation of Ca^{2+} transients (Louch et al., 2006). We analysed the shape of Ca^{2+} transients by TTF50, distribution and variability. RV myocytes from PH rats showed a right-shifted distribution of TTF50 with a significantly higher desynchrony index as compared with control RV myocytes (Figure 4.21). LV myocytes possessed a similar TTF50 distribution and desynchrony index. Fowler et al. reported the magnification of desynchrony in RV Ca^{2+} transients but at the late stages of PH (Fowler et al., 2018). First, we hypothesized that the reorganisation of TAT network removed LTCCs from the coupling with RyR2 that will became "orphaned" as it happened in HF (Song et al., 2006). However, it is not the case, the analysis LTCC and RyR2 arrangement and colocalization by STED microscopy showed no reduction of RyR2 colocalization with $Ca_v1.2$ (Figure 4.13). A recent study proposed that desynchronization of Ca^{2+} transients is one of the consequences of reorganisation of RyR2 clusters in HF (Kolstad et al., 2018). Smaller RyR2 clusters were shown to produce an invisible non-spark Ca^{2+} leak, and large clusters were responsible for the irregular and slow Ca^{2+} sparks that could be attributed to the delayed regions of Ca^{2+} transients. The analysis of the Ca^{2+} sparks properties in early and delayed sites of Ca^{2+} transient showed that Ca^{2+} sparks that originated in delayed regions was significantly longer and higher in PH RV myocytes as compared to control (Figure 4.22F and 4.22G). This could be a consequence of reorganisation of RyRs clusters in RV following PH.

Investigation of LTCC expression and density in PH showed that expression of the pore-forming protein, $Ca_v1.2$, was preserved in both RV and LV myocytes (Figure 4.29 and 4.30). At later stages of PH, a significant reduction of $Ca_v1.2$ expression was observed in RV myocytes by (Benoist et al., 2011; Xie et al., 2012), although during the hypertrophic stage of the disease it was still unchanged (Benoist et al., 2012; Rocchetti et al., 2014). Immunocytochemical study and functional patch clamp investigation showed a potential silencing of LTCC in PH RV myocytes (Figure 4.13). Analysis of LTCC density in T-tubules and crests in the presence of

BayK showed a pool of non-active LTCC in both membrane domains (Figure 4.25). LTCC in both T-tubules and crests are mainly anchored in caveolae (Cavalli et al., 2007; Shibata et al., 2006). We analysed the expression and the density of Cav3 immunofluorescence in control and PH RV myocytes. Expression level of Cav3 was slightly reduced in PH (Figure 4.29). The density of Cav3 immunofluorescence was analysed inside the cell and thus could be proportional to the T-tubular fraction of Cav3. This Cav3 density and its colocalisation with $Ca_v1.2$ was significantly reduced in PH RV myocytes, as compared to control RV myocytes (Figure 4.15), which could indicate the redistribution of Cav3 from T-tubules to the outer membrane among with the LTCC.

The observed reduction of the number of active LTCC in the membrane could be compensated by an increased activity of the remaining ones. The open probability of T-tubule LTCCs of PH myocytes was significantly higher than in control RV myocytes (Figure 4.26). This could be a compensatory mechanism to maintain the loading conditions in terms of loss of some LTCCs.

We did not find any differences in LTCC mean amplitude and conduction under the normal conditions, but in the presence of BayK, LTCCs in T-tubules had a smaller mean amplitude and conductance as compared to the crest LTCC (Figure 4.26 and 4.28). PH lead to a significant increase of the LTCC conductance in the presence of BayK in T-tubules and reduction of average LTCC conductance in the crest, making T-tubules and crest LTCCs not different (Figure 4.28). It is possible that down-regulation of Cav3 during PH and the redistribution of LTCC from their native location to non-canonical regions produced these functional alterations. This question will be addressed in further investigations.

4.4.1 Conclusion

In summary, at the early stage of PH, we found that an elevated PAP in PH rats causes a significant cell structural remodelling in RV myocytes, which includes cell hypertrophy, reduction of TAT network, z-groove flattening and LTCC redistribution. This structural reorganization is accompanied by the adaptive changes in cell shortening, desynchronization of Ca^{2+} transients, higher Po of LTCC and increased Ca^{2+} spark rate. The cellular changes could in part be responsible for the electrical remodelling observed *in vivo*, such as prolongation of ERP and

reduction of CV anisotropy, however, these changes are not severe enough for an increase in arrhythmias in the tissue. In LV myocytes, PH leads to prolongation of Ca^{2+} transients but without changes in the TAT organization. Altogether our findings suggest that at this stage of PH significant cellular structural and functional remodelling occurs. However the arrhythmogenic activity in RV that reported at later stages of the disease in RV is not present. Suggesting that these changes observed at the cellular level could be the first stage before the development of arrhythmias in the long term.

5 Alterations in microdomain organisation of RV in left sided HF.

5.1 Introduction

Idiopathic pulmonary arterial hypertension is not the most common cause of RV dysfunction (Thenappan et al., 2018). The leading case of PH in the world is due to left sided HF (La Vecchia et al., 2001; Thenappan et al., 2018). The patients with HF who developed signs and/or symptoms of RV failure have a very poor prognosis and median survival is usually less than two years (Anavekar et al., 2008; Di Salvo et al., 1995; Larose et al., 2007; Oakley, 1988). Moreover, RV hypertrophy and failure showed to be an independent risk factor for morbidity and mortality of HF patients (Ghio and Tavazzi, 2005). The exact mechanisms how LV failure could promote RV pathological changes are not clear. It was proposed that septal dyssynergia, pulmonary hypertension, neurohormonal activation or inflammation can provoke RV hypertrophy and failure in HF (Haddad et al., 2008; Quaife et al., 1998). Some studies proposed that pulmonary pressure was elevated due to the elevated left-sided filling pressures in failing LV (Jiang et al., 2011; Kalogeropoulos et al., 2011; La Vecchia et al., 2001). However, others have not reported the appearance signs of RV ischemia/infarct, septal infarct, or pulmonary hypertension in HF patients (Quaife et al., 1998; Voelkel et al., 2006).

The mechanism of RV progression in disease in the settings of LV dysfunction is of key importance in understanding the disease. Pathophysiological remodelling of cardiac function in HF occurs at multiple levels. As was shown in previous chapter we attempt to study alterations of RV myocytes structure and function in HF to compare it with progression of LV myocytes. We used a well-studied model of myocardial infarction in rats induced by coronary artery ligation (Lyon et al., 2009). Recently in our laboratory and other groups was found that 16 weeks after MI LV myocytes undergo significant destruction of membrane organisation that lead to increased irregular Ca^{2+} activity, LTCC redistribution and hyperphosphorylation (Bryant et al., 2015; Louch et al., 2006; Lyon et al., 2009). Moreover, progressive

reorganisation of Ca^{2+}-signalling microdomains was shown to capable to produce an arrhythmogenic triggers in the whole heart (Sanchez-Alonso et al., 2016).

Specifically, we wanted to investigate the local control of LTCC in RV myocytes. In LV myocytes from MI rats LTCCs were relocated from their predominant localization (in T-tubule) to surface membrane (crest) where LTCCs become hyperphosphorylated and arrhythmogenic (Sanchez-Alonso et al., 2016). Different regulation of two subpopulations of LTCC was found (Bryant et al., 2015; Sanchez-Alonso et al., 2016).

Therefore, we hypothesized that MI induced the rearrangement of the sarcolemma membrane in RV myocytes that leads to altered function of single LTCCs and higher spontaneous Ca^{2+} activity in failing RV myocytes.

The main objectives of this chapter were:

1. To study alteration of RV myocytes shape, surface topography and internal TAT network organisation after MI.
2. To investigate the effect of MI on the properties of Ca^{2+} transients, spontaneous Ca^{2+} waves and Ca^{2+} sparks in RV myocytes.
3. To assess the spatial localization and functional behaviour of LTCCs in MI RV myocytes
4. To check the expression levels of $Ca_v1.2$, Cav3 and phosphorylation activity of pCaMKII and pPKA in MI RV myocytes.

5.2 Methods

5.2.1 Rat myocardial infarction HF Model

The study of HF effect on single RV myocytes was performed in a model of chronic MI in adult Sprague-Dawley rats. The model was produced by Dr. Catherine Mansfield in Imperial College London. This is an established model frequently produced in our laboratory via ligation of the left anterior descending coronary artery. Myocytes were isolated 16 weeks after the operation. Our group validated this model before (Lyon et al., 2009; Sanchez-Alonso et al., 2016), showing a pronounced increase of LV weight, dilatation and elevated levels of brain natriuretic peptide in serum (Lyon et al., 2009).

5.2.2 Myocytes isolation

Myocytes were isolated from control and failing hearts according to the protocol described in section 2.2.1.

5.2.3 Scanning ion conductance microscopy

Surface topography of live cardiomyocytes was assessed by SICM as described in 2.3.3. RV and LV myocytes were plated on petri dishes covered with laminin. The recordings were made in hopping mode of microscope with 100 nm I.D. borosilicate pipettes. Z-groove ratio was used for the regularity analysis of surface membrane (Gorelik et al., 2006).

5.2.4 Confocal microscopy investigation of TATS in the live cardiomyocytes

The subcellular TAT system was visualized by confocal imaging of live cells stained with Di-8-ANEPPS as described previously (Lyon et al., 2009). Analysis of TAT network density, regularity skeletons length and complexity was performed as described in method section 2.3.1.

5.2.5 Optical mapping of Ca^{2+} events in isolated myocytes

Optical mapping of Ca^{2+} waves and transients was performed as described in section 2.4.2. Briefly, freshly isolated cardiac myocytes were stained with Fluo-4AM and placed in perfusion chamber of inverted microscope equipped with CMOS camera ULTIMA-L (SciMedia, USA Ltd, CA; 500 fps, 1.5–2 μm/pixel). Chamber was constantly perfused with HBSS temperature was controlled to 37ºC. Two stimulation protocols were applied: 1) 5 min of 1 Hz followed by 5 s of recording to measure Ca^{2+} transient's properties. 2) 1 min of 4 Hz stimulation followed by stimulation cessation and recording of spontaneous Ca^{2+} waves

Ca^{2+} transient properties were analysed using a macro code in Fiji. Spontaneous Ca^{2+} events were visualized in BraviAna (Brainvision Ana v. 120) and manually checked for the propagation of the waves. Frequency of propagated and non-propagated Ca^{2+} waves was counted separately.

5.2.6 Calcium sparks and transients investigation with line mode of confocal microscope

Ca^{2+} sparks and Ca^{2+} transients were analysed from confocal line-scans of Fluo4-AM fluorescence. Detailed protocol is described in section 2.4.3. Briefly, cells were field-stimulated at 1 Hz for enhancement of SR Ca^{2+} loading, then few (3-5) Ca^{2+} transients were recorded together with 8-16 s rest Ca^{2+} activity. Analysis of Ca^{2+} sparks and Ca^{2+} transients was performed in custom made macro in Fiji.

5.2.7 Super-resolution patch clamp technique

This methodology was described in detail in section 2.4.1. Briefly, the protocol included the visualization of a myocyte surface topography by SICM then the tip of pipette was precisely widened by clipping (Bhargava et al., 2013). After pipette moved to a desired surface region (T-tubule or crest) and lowered down until it reached the membrane. A high resistance seal then was established and single LTCC recordings were performed in a cell-attached modification of path-clamp technique.

For experiments when PKA activity needs to be blocked 10µM of PKA antagonist, H89, was added in external LTCC buffer prior to experiments. Solution of drug was used only at the day of preparation. Myocytes during LTCC recordings were kept in H89 solution no longer than 30 min, than a new dish with myocytes were treated with a drug.

5.2.8 Western blot

Detailed procedure is described in the section 2.5.1. Proteins were extracted from cell pellets and the level of proteins was determined with BioRad DSK+ kit using BSA as standard protein. The following primary antibodies were used for immunoblotting: $Ca_v1.2$ (1: 200), pPKA substrate (1: 1000), pCaMKII (1:500); Cav3 (1:1000) and GAPDH (1:1000). Secondary antibodies were anti-mouse and anti-rabbit linked with HRP in dilution 1:2000. Density of the bands was normalized to GAPDH levels.

5.3 Results

5.3.1 Alterations of the cell shape after MI

The shape of myocytes was analysed after the MI. RV and LV myocytes became markedly hypertrophied in MI rats (Figure 5.1). Failing LV myocytes became 21% longer (Figure 5.1A) and 35% wider (Figure 5.1B) with a decreased LWR (Figure 5.1C) than control ones. Similar changes but with less extend happened with RV myocytes in MI rats. They became an 8 % longer (Figure 5.1A) and 28 % wider (Figure 5.1B) but the LWR was not altered compared to the myocytes from control rats (Figure 5.1C).

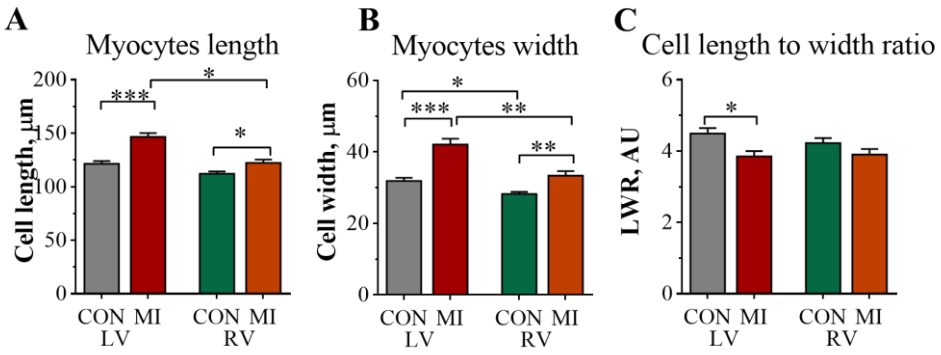

Figure 5.1. Characterization of changes in the myocytes shape in MI rats. A) Myocyte length, B) myocyte width and C) length to width ratio in RV and LV myocytes from control and MI rats (n=60-100 cells, N=6-10 rats; by one-way ANOVA test with Bonferroni corrections).

5.3.2 Surface topography study

Surface structure of life cardiomyocytes was assessed by SICM. Representative 10x10 µm scans are presented in Figure 5.2. Analysis of surface topography was performed with Z-groove ratio determination (Figure 5.3). Failing LV myocytes possessed a pronounced reduction of Z-groove ratio from 0.69±0.02 au in control LV myocytes to 0.40±0.02 au in failing ones ($p<0.001$). RV myocytes undergo similar reduction of Z-groove ratio but for a less extend. Z groove ratio reduced from 0.68±0.03 au in control RV to 0.49±0.02 au in MI rats

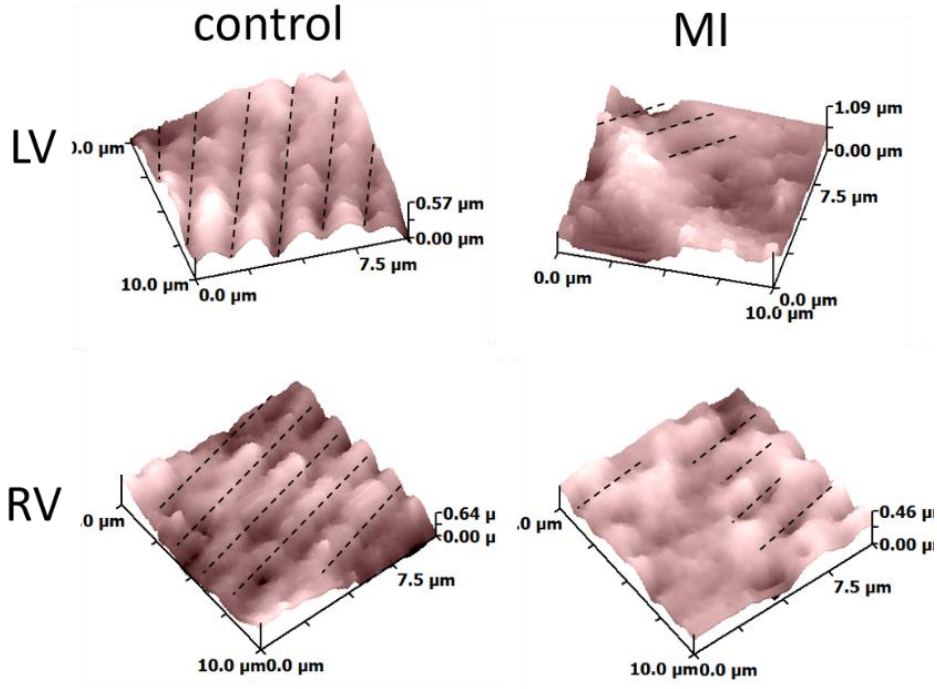

Figure 5.2. Representative surface scans of myocytes topography of LV (top) and RV (bottom) myocytes from control (left) and MI (right) rats.

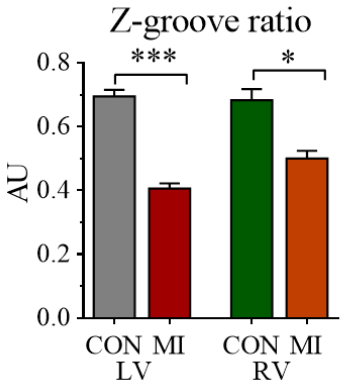

Figure 5.3. Bar graphs showing the average Z-groove ratio of LV and RV myocytes from control and MI rats. (n=40-100 cells, N=4-10 rats, *p<0.05, *** p<0.001, by one-way ANOVA with Bonferroni correction).

5.3.3 Changes of TAT network parameters of RV in failing hearts

The reduction of TAT network density and its reorganisation after MI in rats were well studied by our group (Ibrahim et al., 2011; Schobesberger et al., 2017) and

others (Louch et al., 2006; Wei et al., 2010). Most of the works agreed that LV myocytes undergo gradual reduction of TAT density and regularity, which fist accompany with initial increase in the amount of A-tubules, that lost in the end stages of HF (Schobesberger et al., 2017). RV myocytes TAT network from control and 16 weeks post-MI stage are presented in Figure 5.4. The reorganisation of TAT structure in MI can be mentioned from the corresponding power peak plots that shown in Figure 5.4 and statistical analysis of TAT density (Figure 5.5). In failing rats RV myocytes have a 12 % ($p<0.001$) reduction of TAT density and a 42% ($p<0.001$) reduction of T-tubule regularity.

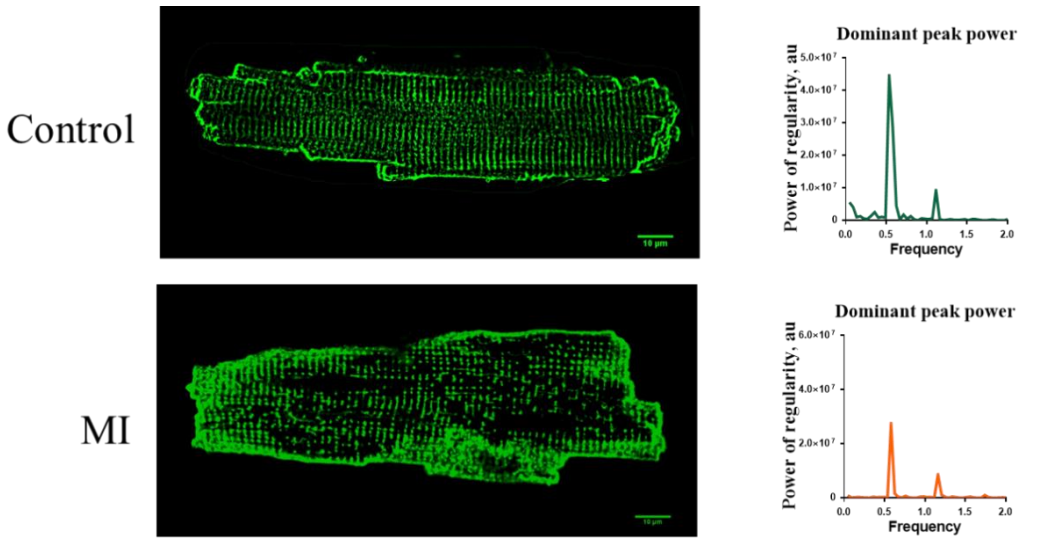

Figure 5.4. Representative Di-8ANEPPS images of TAT network in control and MI RV myocytes and corresponding power frequency graphs of T-tubule regularity.

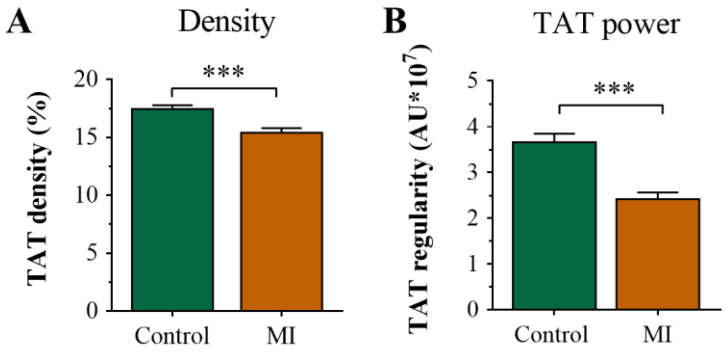

Figure 5.5. Statistical analysis of TAT parameters changes in MI. A) TAT network density of control and MI RV myocytes. B) Power of T-tubule regularity analysis of control and MI RV myocytes. (N=9-10 rats, $p<0.001$ by unpaired Student t-test).

The portions of TAT images were processed accordingly to the protocol of (Wagner et al., 2014). Representative portions of TAT network of RV myocytes from control and MI rats and corresponding TAT skeleton images are presented in Figure 5.6. The analysis of the TAT skeleton length per area indicated that in MI rats RV myocytes have a slightly (by 4 %) but significantly ($p<0.05$) less length of TAT skeleton as compared to RV myocytes from control rats. Complexity analysis of TAT network by the number of triple junctions per area showed similar values in RV myocytes from control and failing rats (Figure 5.6C).

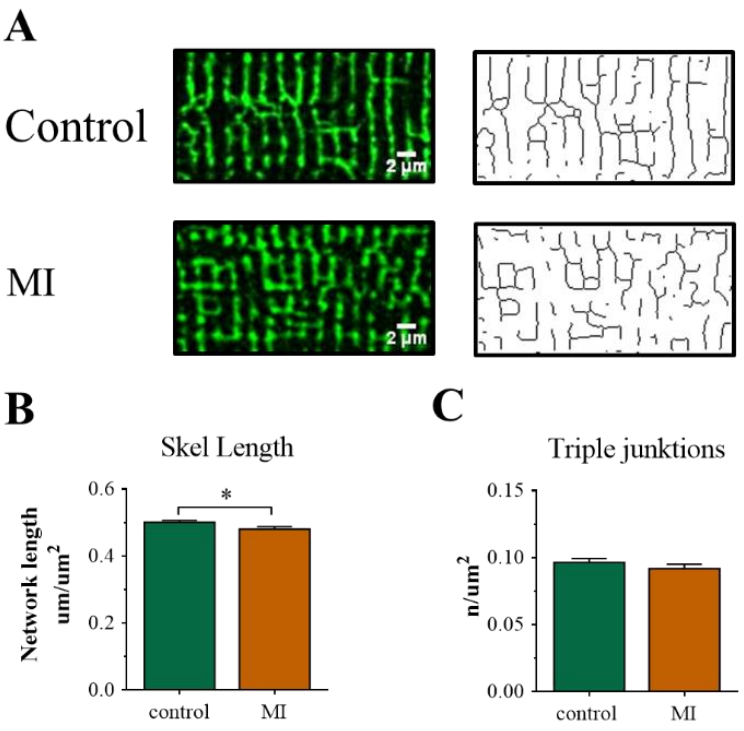

Figure 5.6. RV TAT skeleton changes in MI. A) Representative fragments of the TAT network images of RV myocytes from control (top) and MI (bottom) rats and corresponding skeletonized TAT structures. B) Average TAT network skeleton length per area measured in RV from control and MI rats. C) Average number of triple junctions in TAT network found in RV myocytes from control and MI rats. (n=50-60 cells, N=5-6 rats, *$p<0.05$, by Mann-Whitney test).

Directional distribution of TAT in control and MI RV myocytes was obtained by the directionality histograms created by Fiji. Representative examples of directional histograms of RV myocyte TAT network are presented in Figure 5.7A. The analysis

of average length of A-tubules and T-tubules revealed preserved levels of both A-tubules and T-tubules in RV myocytes from MI rats (Figure 5.7B).

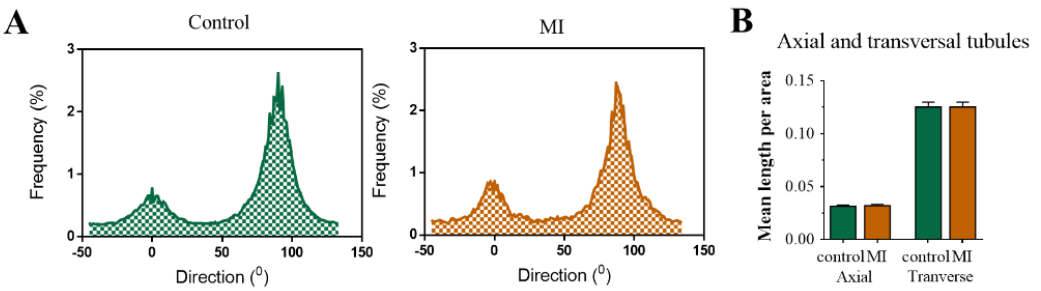

Figure 5.7. Directionality study of TAT network changes in RV after MI. A) Representative histogram of directional distribution of TAT network of control RV myocyte. B) Representative histogram of directional distribution of TAT network in RV myocyte from MI rat. B) Average length of A-tubules and T-tubules found in RV myocytes from control and MI rats. (n=40-50 cells, N=4-5 rats).

5.3.4 Failing RV cells have higher and longer Ca^{2+} transients.

During the progression of HF many groups observed alterations of ECC coupling that is caused by changes in Ca^{2+} transients parameters. Our recent study revealed that Ca^{2+} transients became more prolonged with reduced amplitude in failing LV myocytes. Here we studied the changes 16 weeks post MI in RV myocytes. The OM traces recorded in control and MI RV myocytes are shown in Figure 5.8A. As discussed before, we cannot rely on Ca^{2+} transient amplitude measurements. Thus the values of Ca^{2+} transient amplitude are shown here only for comparison. (Figure 5.8B). No changes were found in Ca^{2+} transient time to peak in MI (Figure 5.8C). Comparison of a 90 % decay time between control and failing RV myocytes showed a significant prolongation of the Ca^{2+} transient decay in failing RV myocytes ($p<0.05$, Figure 5.8D).

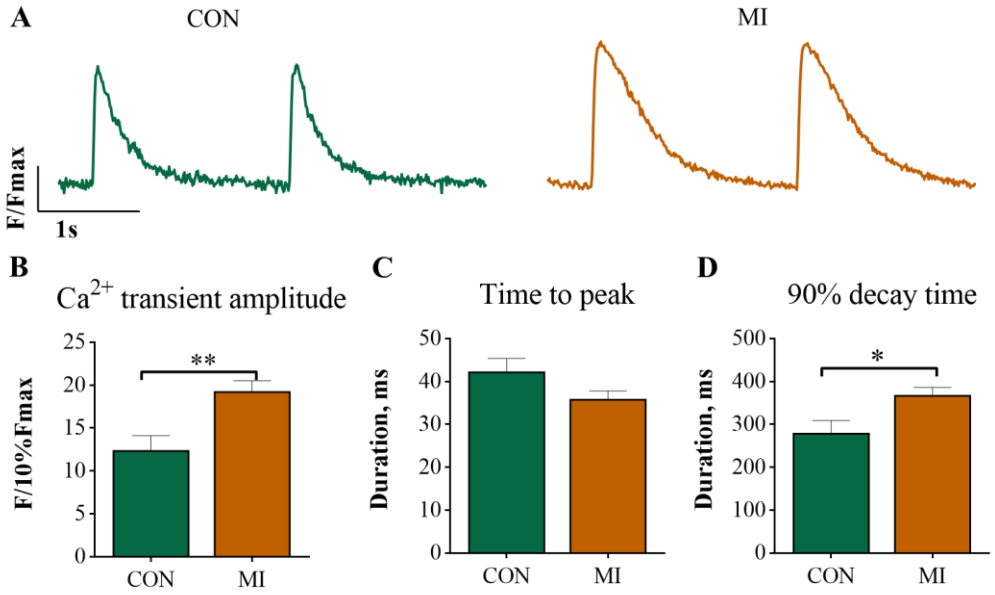

Figure 5.8. Failing RV myocytes have higher and longer Ca^{2+} transients compared to control RV myocytes. A) Representative traces of Ca^{2+} transients measured in control and MI RV myocytes. B) Average Ca^{2+} transient amplitude in control and MI RV myocytes. C) Statistical analysis of time to peak of Ca^{2+} transient in control and MI RV myocytes. D) 90% of Ca^{2+} transient decay time observed in control and MI RV myocytes. (n=18-28 cells, N=3-4 rats; *p<0.05, **p<0.01, by unpaired Student t test).

Significant prolongation of Ca^{2+} transients observed by optical mapping and reduction of TATS density and regularity in MI RV myocytes drives us to hypothesize that MI RV myocytes should have more desynchronized activation. The examples of line-scans of Ca^{2+} transients recorded in control and MI RV myocytes are presented in Figure 5.10. Analysis of TTF50 histograms (Figure 5.10B) and 'desynchrony indexes' (Figure 5.10C) showed that RV myocytes from post-MI rats have a right shifted distribution of TTF50 with a slightly higher (p=0.1) 'desynchrony index'.

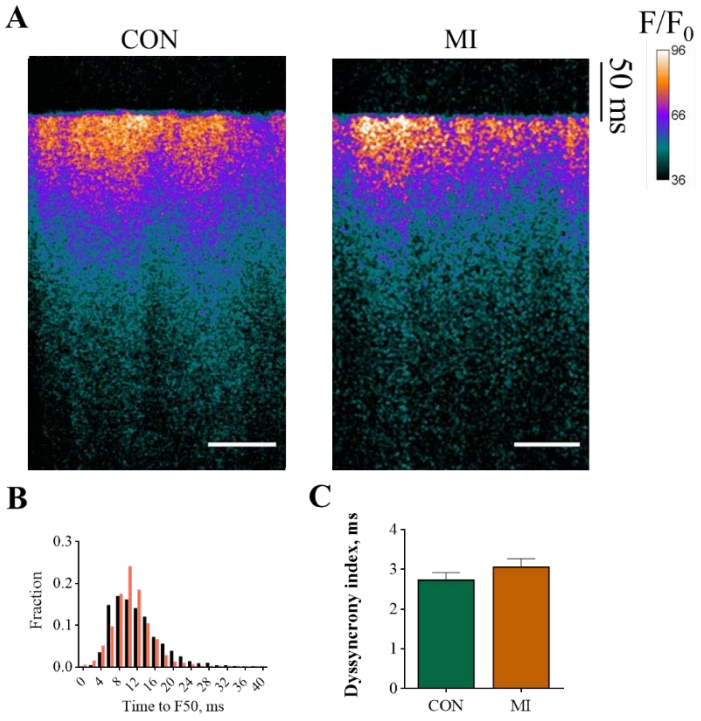

Figure 5.9. Analysis of synchronicity in control and MI RV myocytes. A) Examples of Ca^{2+} transient line scans recorded in control and MI RV myocytes. Bar – 20 µm. B) Histograms of TF50 distribution in control (black) and MI (red) RV myocytes. C) Average 'desynchrony index' of Ca^{2+} transient measured in control and MI RV myocytes. (n=24-27 cells, N=3-4 rats, p=0.1, by unpaired t test).

5.3.5 MI lead to an increase of a spontaneous Ca^{2+} activity in RV myocytes

To analyse spontaneous Ca^{2+} behaviour we applied two methods. Optical mapping of Ca^{2+} waves was applied after 1 min of 4 Hz field stimulation to ensure the equal SR loading in all the experiments. The optical Ca^{2+} traces recorded from control and failing RV myocytes are shown in Figure 5.10A. Statistical analysis of the non-propagated Ca^{2+} waves frequency showed two times higher frequency in failing RV myocytes as compared to control ones ($p<0.05$, Figure 5.10B). The propagated waves had the reduced frequency in MI ($p<0.05$).

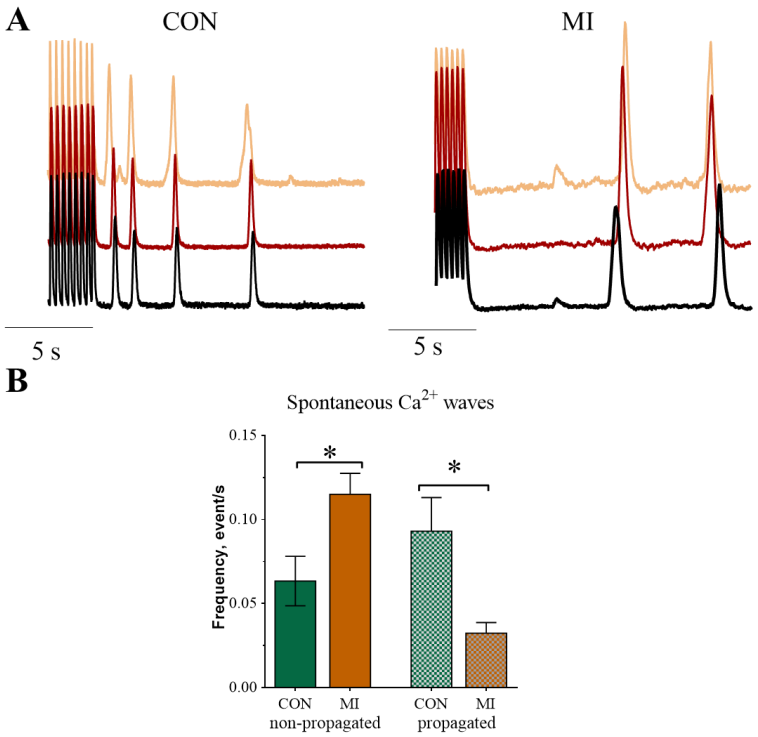

Figure 5.10. Increased frequency of spontaneous Ca^{2+} waves in failing RV myocytes. A) Examples of spontaneous Ca^{2+} waves acquired in control and MI RV myocytes during a 16-s rest period after 4Hz stimulation. B) Bar graph showing the analysis of non-propagated and propagates Ca^{2+} waves frequency measured in control and MI RV myocytes (N= 4-7 rats, *P<0.05, by one-way ANOVA with Bonferroni post hoc).

The study of Ca^{2+} sparks using line-scans also indicated an increase in Ca^{2+} activity in MI RV myocytes as compared to control RV myocytes (Table 10). Line-scans of Fluo4-AM fluorescence recorded in control and MI RV myocytes are shown in Figure 5.11. In MI rats RV myocytes had higher frequency of Ca^{2+} sparks ($p<0.05$, Figure 5.11B), higher mass ($p<0.05$, Figure 5.11C) and as a consequence, Ca^{2+} leak induced by the sparks was significantly higher than observed in control RV myocytes.

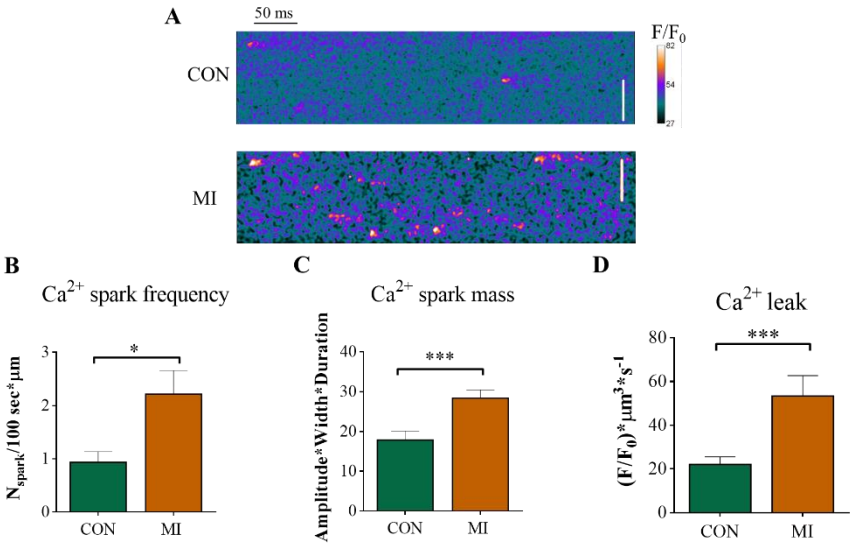

Figure 5.11. Alteration on Ca^{2+} sparks properties in RV from 16 weeks post MI rats. A) Representative line scans of Fluo4-AM fluorescence recorded in control and MI RV myocytes. Bar – 20 µm. B) Bar graphs showing the average Ca^{2+} sparks frequency, C) Ca^{2+} sparks mass, D) Ca^{2+} leak in control and MI RV myocytes. (n=19-21 cells, N=3 rats, *p<0.05, ***p<0.001, by Mann-Whitney test).

Table 10. Ca^{2+} sparks parameters measured in control and MI RV myocytes.

	RV CON	RV MI
Frequency, N_{spark}/µm/100s	0.9±0.2	2.2±0.4*
Amplitude, F/F_0	0.28±0.02	0.345±0.007**
HMFW, µm	2.33±0.08	2.61±0.09*
HMFD, ms	22.3±1.2	27.1±1.1*
Time to peak, ms	11.7±0.5	13.5±0.7
Tau, ms	26.5±2.0	27.8±1.7
Ca^{2+} spark mass, $n(F/F_0)*m*s$	18.8±1.5	28.4±2.0**
Ca^{2+} spark induced Ca^{2+} leak, $p(F/F_0)$	22.2±4.9	53.4±9.3***

Values are means ± S.E.M.; n = 19-21 cells, N= 3 rats, *P < 0.05, **P < 0.01, ***P < 0.001 vs. the CON RV. HMFW- Half maximum full width, HMFD- Half maximum full duration.

5.3.6 Hyperphosphorylation of LTCC in T-tubule of RV in post MI rats.

Our resent work (Sanchez-Alonso et al., 2016) showed that MI in LV myocytes lead to redistribution of LTCC from a predominant localization at T-tubule to a crest domain. Moreover this relocalisation of LTCC from T-tubule to surface membrane was accompanied by hyperphosphorylation of crest LTCC via CaMKII. We hypothesize that changes of intracellular Ca^{2+} behaviour in RV could be promoted by relocalisation of LTCC in RV myocytes.

The action of MI on spatial localization of LTCC in RV myocytes was analysed by super resolution scanning patch-clamp technique. Typical single LTCC recordings obtained holding -6.7 mV are presented in Figure 5.12. Higher activity of T-tubule LTCC can be mentioned in MI RV myocytes.

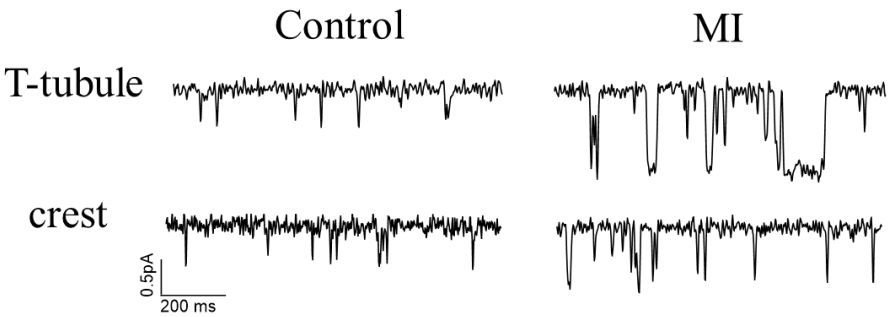

Figure 5.12. Traces of single LTCC activity recorded at T-tubule or crest of RV myocytes from control and post MI rats.

Study of LTCC spatial distribution in MI RV myocytes showed a ~30 % reduction of LTCC occurrence at T-tubule and a ~43 % reduction at crest as compared to T-tubule and crest of control RV myocytes (Figure 5.13A). Analysis of LTCC density in T-tubule showed a slight (15%) increase of the channel density in post MI RV myocytes as compared to control ones (Figure 5.13B). Density of LTCC at T-tubule of RV was slightly changed in MI (Figure 5.13B), as the higher chance was to obtain multiple LTCC in the patch (Figure 5.13C).

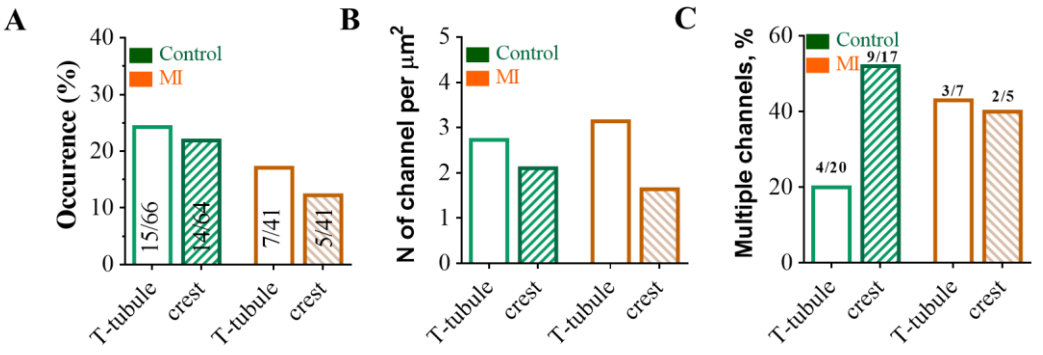

Figure 5.13. LTCCs localization analysis in control and post MI RV myocytes. A) Single channel LTCC occurrence observed at T-tubule and crest of RV myocytes from control and post- MI myocytes. n/m- number of patches with LTCC/ total number of successful patches. B) Density of single channel LTCC activity observed at T-tubule and crest of control and post MI myocytes. C) Percentage of multi-channel LTCC patches from the total number of seals with a LTCC current. n1/n = number of patches with more than one LTCC/ total number of patches showing LTCC activity

Open probability of T-tubule LTCC was significantly increased in MI RV myocytes as compared to control RV myocytes (MI: 0.26±0.05 vs. Control T-tubule: 0.029±0.004, $p<0.05$, Figure 5.14). LTCC at crest of MI RV myocytes have similar open probability as LTCC at crest of control RV myocytes.

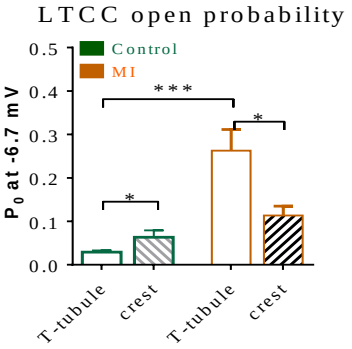

Figure 5.14. Open probability of LTCC recorded at T-tubule and crest of RV myocytes from control and post MI rats. (n=5-15 channels from 41-66 myocytes, 10 rats; *p<0.05, ***p<0.001, by Mann-Whitey test).

Current−voltage dependence of LTCC located at T-tubule (Figure 5.15A) and crest (Figure 5.15B) of RV myocytes from control and MI rats was analysed. MI produced in RV myocytes a significant increase in conductance of the channel (MI T-tubule: 8.8±1.1 pS vs. control T-tubule: 17.8±2.1 pS, p<0.01, Figure 5.15C).

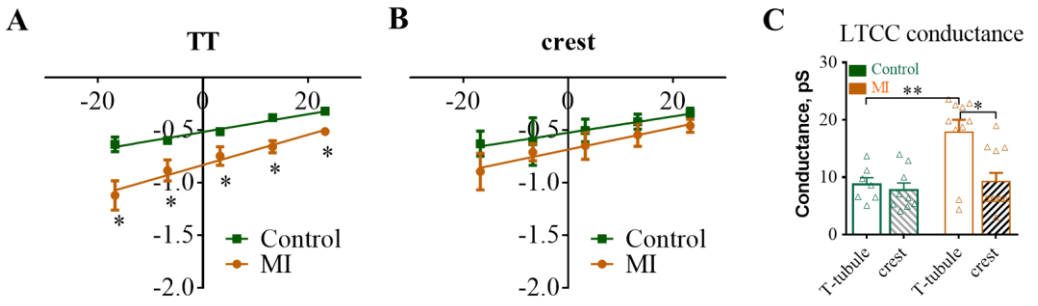

Figure 5.15. Current-voltage (IV) characteristics of LTCC recorded at T-tubule or crest of control and MI RV myocytes. A) IV properties of LTCC recorded at T-tubule of Control and post MI RV myocytes, B) IV graphs of LTCC recorded at crest of control and post MI RV myocytes. (n=5-15 channels from 41-66 myocytes, 10 rats; *p<0.05 to the corresponding amplitude of LTCC in control RV myocytes, by Mann-Whitney test). C) LTCC conductance analysed at T-tubule and crests of control and post MI RV myocytes (n=5-15 channels from 41-66 myocytes, 10 rats; *p<0.05, **p<0.001, by Kruskal - Wallis test).

5.3.6.1 Inhibition of PKA activity in T-tubule of RV myocytes return the properties of LTCC to control level

In our previous work high open probability of LTCC located at the crest of MI LV myocytes was explained through the hyperphosphorylation of these channels via CaMKII (Sanchez-Alonso et al., 2016). Studies in human cardiomyocytes from HF patients recently indicated that in ischemic cardiomyopathy LTCC became highly activated at T-tubule of LV myocytes due to an increased PKA phosphorylation (Sanchez-Alonso et al., 2018). Here we tested the hypothesis that in MI RV myocytes LTCC was hyperphosphorylated by PKA.

MI RV myocytes was treated with H89 to block PKA activity. Typical traces of single LTCC activity at T-tubule of Control, MI and MI treated with H89 are presented in Figure 5.16. Analysis of functional LTCC behaviour showed significant reduction of open probability of LTCC observed at T-tubule in MI

myocytes treated with H89 (MI + H89: 0.039±0.009 vs. MI: 0.26±0.05, p<0.001, Figure 5.17A). Open probability of control and MI treated with H89 are not significantly different. Conductance of T-tubule LTCC recorded in MI RV myocytes treated with H89 was significantly lower compared to conductance of LTCC in MI myocytes (MI+ H89 10.6±1.2 pS vs. MI 17.8±2.1 pS, p<0.001, Figure 5.17B). Current-voltage characteristics of T-tubule LTCC in MI myocytes treated with H89 are similar to the characteristics of T-tubule LTCC of control RV myocytes (Figure 5.17B).

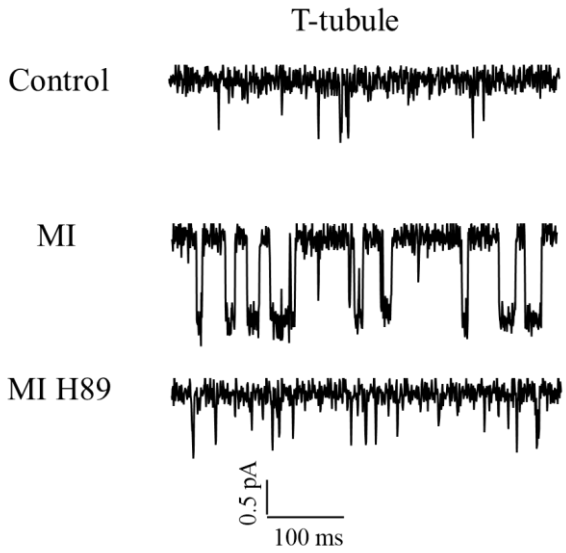

Figure 5.16. Traces of LTCC recorded at T-tubule of RV myocytes isolated from control, MI and MI myocytes treated with H89 to block PKA activity.

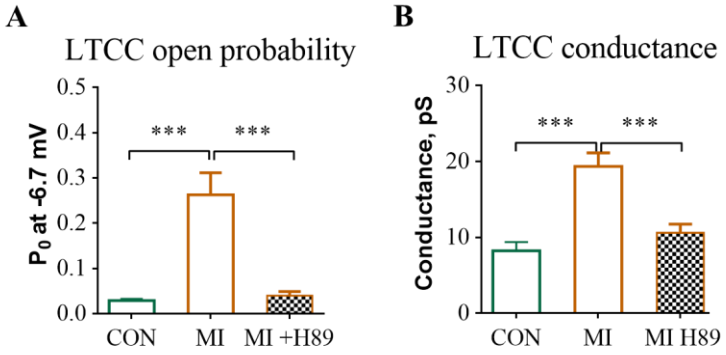

Figure 5.17. Inhibition of PKA returned the properties of LTCC at T-tubule of MI RV myocytes back to control level. A) Open probability of LTCC measured at -6.7 mV in T-tubule of control RV, post-MI RV and post-MI RV myocytes in presence of H89, PKA antagonist (n of channels control- 17, MI – 12, MI +H89 – 5, ***p<0.001, by Kruskal-Wallis test). B) Mean LTCC conductance at T-tubule of control, post-MI and post-MI treated with H89 RV myocytes. (n of channels control- 8, MI – 8, MI +H89 – 4, ***p<0.001, by Kruskal-Wallis test).

5.3.7 Molecular analysis of $Ca_v1.2$ expression and level or kinases activity in control and MI myocytes

Western blot analysis was performed to check the relative expression of $Ca_v1.2$ and Cav3; also we wanted to understand the relative kinase activity in control and MI myocytes. Figure 5.18 and Figure 5.19 are presenting the blots of the proteins levels in control and MI RV and LV myocytes, respectively. Expression of $Ca_v1.2$ was similar in control and MI RVM (Figure 5.18B). According to (Bers, 2001), LTCC can be phosphorylated via PKA and CaMKII. In LV myocytes we observed high CaMKII activity with a reduced PKA phosphorylation (Figure 5.19), similar to observed before (Sanchez-Alonso et al., 2016). MI RV myocytes have similar levels of pPKA substrates expression and slightly higher pCaMKII level as compared to control RV myocytes (Figure 5.18B). As discussed before, Cav3 is important for caveolae, which houses LTCC in T-tubule and sarcolemma membrane (Balijepalli et al., 2006). Expression of Cav3 in MI RV myocytes was ~50 % lower than in control RV myocytes (not significant, Figure 5.18B).

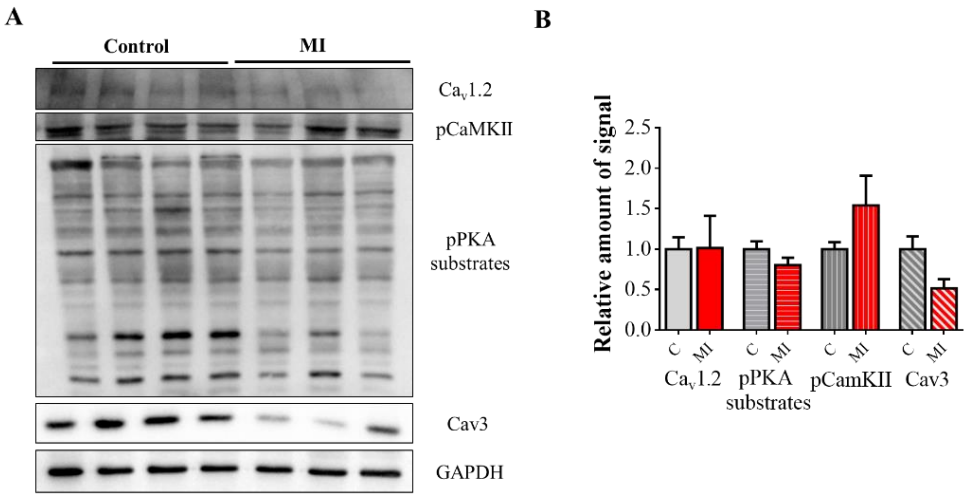

Figure 5.18. Western blot analysis of protein expression in control and MI RV myocytes. A) Representative blots of $Ca_v1.2$, pCaMKII, pPKA substrates, Cav3 and GAPDH protein levels in control and MI RV myocytes, B) Mean density of $Ca_v1.2$, pCaMKII, pPKA substrates, and cav3 normalized to GAPDH. (Control (C) n=4, MI n=3 hearts).

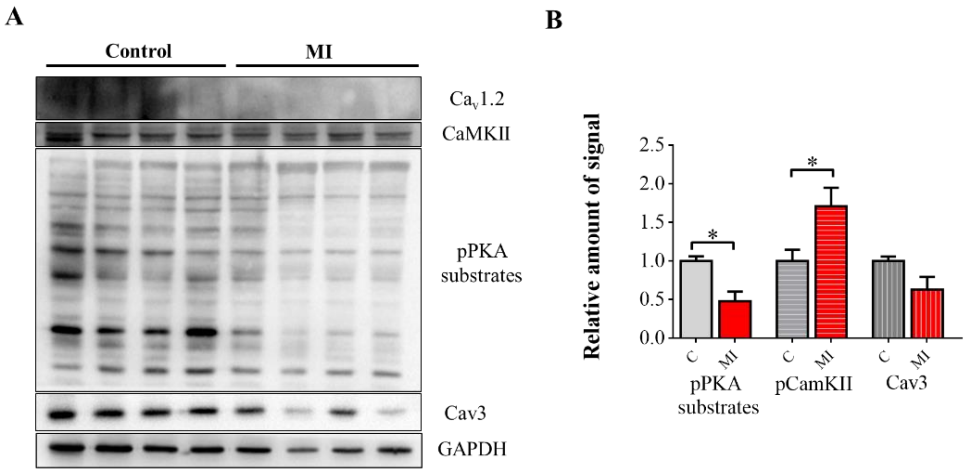

Figure 5.19 Western blot analysis of protein expression in control and MI LV myocytes. A) A representative blot showing $Ca_v1.2$, pCaMKII, pPKA substrate, Cav3 and GAPDH expression in the LV myocytes from control and MI rats. B) Relative average density of the pPKA band, pCaMKII and cav3 bands normalized to the GAPDH signal, (Control n=4 MI: n=4 rats). ($Ca_v1.2$ signal was almost undetectable).

5.4 Discussion

Here we observed alterations in the shape of CMC from both RV and LV myocytes in MI rats (Figure 5.1). Myocytes from both RV and LV became significantly longer and wider, but RV changed to a lesser extent. The LWR was reduced in LV and not altered in RV myocytes after MI (Figure 5.1C). The shape of myocytes plays important role in maintaining the passive conductance properties, as was shown before (Van Rijen et al., 2004). Moreover the alterations of cells shape in HF could be accompanied with changes in surface topography and disturbance of TAT structure (Schobesberger et al., 2017). We observed significant flattering of surface topography in RV myocytes after MI (Figure 4.2), similar to what was observed in failing LV myocytes (Lyon et al., 2009; Sanchez-Alonso et al., 2016). That was accompanied by the reduction of TAT density and regularity in RV myocytes (Figure 5.5). In HF many researchers observed the disturbance of TAT network of LV myocytes (Louch et al., 2004; Lyon et al., 2009; Sanchez-Alonso et al., 2016). Analysis of TAT skeleton in control and MI RV myocytes showed significant reduction of skeleton length per area with preserved levels of A-tubules and T-tubules in MI RV myocytes (Figure 5.6 and 5.7). This could be related to a late stages of disease, Schobesberger et al. observed that after the initial grow of axial tubules on the 4 and 8 weeks after MI, then A-tubules were lost at the 16 weeks of MI (Schobesberger et al., 2017). This overall reduction of TAT density in the late HF could be related to switch from adaptive to maladaptive remodelling in the heart and could be induced via increased wall stress observed in HF (Heinzel et al., 2008). Moreover, Stefanon and co-workers observed an increased deposition of collagen in extracellular matrix of RV and LV myocytes (Stefanon et al., 2013). This collagen deposition could promote tubular dilatation and loss (Crossman et al., 2017).

MI promoted also functional alterations of RV myocytes. We observed a significantly higher amplitude and longer decay of Ca^{2+} transients evoked by 1 Hz stimulation in MI RV myocytes as compared to control RV myocytes (Figure 5.8). There are some contradictions about the change of amplitude of Ca^{2+} transient in failing LV myocytes with some reports indicating smaller amplitude and longer

duration (Heinzel et al., 2008; Lyon et al., 2009), whereas other showed larger amplitude with a longer repolarization (Louch et al., 2006). In most of those studies the prolongation of the Ca^{2+} transient decay was promoted by down-regulation of SERCA2. Moreover, prolongation and desynchronization of Ca^{2+} transient activation was observed in LV myocytes and was addressed to disturbance of TAT network and formation of orphaned RyR2 (Heinzel et al., 2008; Louch et al., 2006). However this study showed that time to peak of Ca^{2+} transient, and "desynchrony index" were similar in control and MI RV myocytes (Figure 5.7 and 5.8).

High frequency of spontaneous Ca^{2+} waves and Ca^{2+} sparks was found in MI RV myocytes (Figure 5.10 and 5.11). LV myocytes from failing rats had a significantly higher frequency of Ca^{2+} sparks (Lyon et al., 2009). This high activity of RyR2 is usually linked with disturbance of surface membrane and TAT network (Mørk et al., 2009; Song et al., 2006).

Moreover, we cannot exclude the increased sensitivity of RyR2 to cytosolic or luminal Ca^{2+} due to increased phosphorylation of RyRs by PKA, or CaMKII, or redox modification of RyRs (Terentyev et al., 2008). Whether these effects are modulated by a spatial loss of local control mechanisms, remain uncertain. Recent studies of RyR2 cluster organisation showed a higher dispersion of RyR2 clusters with an increased Ca^{2+} sparks activity (Jones et al., 2018; Macquaide et al., 2015). Ca^{2+} sparks in MIRV myocytes have higher mass and spark mediated Ca^{2+} leak was significantly higher in MI RV myocytes (Figure 5.11). This higher leak could trigger the additional Ca^{2+} releases and increase the rate of Ca^{2+} activity.

TAT network disturbance could have a primary implications in LTCC localisation and function. After MI the occurence of LTCC in the patch was slightly less at both T-tubule and crest as compared with control RV myocytes (Figure 5.13). The single channel density of LTCC at T-tubule was preserved probably due to higher chance of multi-channel occurrence (Figure 5.13B and 5.13C).

LTCC located at T-tubule of MI RV myocytes have higher conductance and higher open probability, whereas crest-LTCC in MI RV myocytes were similar to control ones (Figure 5.14 and Figure 5.15). In failing LV myocytes local control of LTCC was also observed with a higher Po of crest LTCC subpopulation (Bryant et al.,

2015; Sanchez-Alonso et al., 2016). Moreover, local regulation was also observed in atrial MI cells, which have the preserved LTCC occurrence but the T-tubule LTCC conductance was reduced(Glukhov et al., 2015). This regulation could be an attempt of myocytes to maintain its loading condition under the increased stress induced by HF. TAT network disturbance and Cav3 down-regulation in MI RV myocytes could promote the loss of LTCC its native localization and hyperphosphorylation.

Our recent findings showed that phosphorylation of LTCC located in different microdomains is produced by different kinases. Higher activity of the crest LTCC in LV myocytes was found to be induced via CaMKII hyperphosphorylation (Sanchez-Alonso et al., 2016). However, our study in failing human myocytes showed that LTCC in T-tubule could be locally phosphorylated by PKA (Sanchez-Alonso et al., 2018). Phosphorylation of L-type Ca^{2+} channels by PKA increases the probability and duration of the open state of the channels (Neumann et al., 1991). We applied H89 the PKA antagonist on MI myocytes and found significant reduction of both open probability and mean conductance back to the control values (Figure 5.17). Moreover, the total level of pPKA substrates was similar in control and MI RV myocytes, suggesting a possible local activation of the kinase. Increased PKA stimulation could be due to intensive cAMP production and cAMP compartmentation (Ather et al., 2013; Nikolaev et al., 2010). Loss of local cAMP signals was observed in failing LV myocytes (Lyon et al., 2009). PKA could also phosphorylate the RyR2 and hyperphosphorylation of RyR2 in HF leads to a 'leaky' channel phenotype, causing increased Ca^{2+} sparks and Ca^{2+} waves activity (Ono et al., 2000; Reiken et al., 2003).

5.4.1 Conclusion

In conclusion for this chapter, we could mention a different degree of structural and functional changes between RV and LV myocytes observed after 16 weeks of MI. The MI –induced remodelling of TATS, flattening of z-grooves, and distribution of LTCC are less severe in the RV myocytes than in the LV myocytes probably due to the more distant location of the RV myocytes from the infarcted area. These structural changes in RV myocytes are strong enough to induce a significant increase in spontaneous Ca^{2+} spark rate and an elevated Po of the LTCC in T-

tubules, perhaps as a result of local PKA phosphorylation. In the LV myocytes, as we have discovered previously, functional LTCC redistribute from T-tubular to crest location, with activation of crest subpopulation of LTCC by local CaMKII-mediated phosphorylation (Sanchez-Alonso et al., 2016). Thus, MI induces remodelling of different molecular pathways in RV and LV myocytes; however, it still remains to be studied whether these differences in pathways RV and LV myocytes occur due to different severity of MI-induced changes or due to intrinsic properties of RV and LV myocytes.

6 General discussion, limitations and future work

6.1 General discussion

Current study provides an evidence of structure- function relationship for rat RV myocytes. We observed differences in membrane organisation in RV versus LV myocytes, which could be responsible for a cascade of functional alterations, for example, observed differences in $Ca_v1.2$ density. Structure of the cells greatly affects the functioning of these cells, and we found pronounced changes in functioning of RV and LV myocytes; such as: the rate of Ca^{2+} activity, synchronization of Ca^{2+} transient activation, spatial Ca^{2+} sparks distribution and LTCC localization and open probability. These results are clearly indicates the importance of structural-functional relationship for cardiac myocytes.

Our work using the model of PH allowed us to conclude that even at the early stages both the RV and LV function was already changed. The RV is more suffering in the disease as it is directly linked with pulmonary vein, but the alterations of the LV cannot be neglected. The summary for Ca^{2+} handling alterations in RV myocytes is presented in Figure 6.1. PH myocytes have different shape and this affects both impulse propagation and spontaneous Ca^{2+} activity. Internal membrane reorganisation and reduced surface folding produced slower Ca^{2+} transients, a higher rate of local Ca^{2+} activity and an altered LTCC membrane localization. Colocalization of LTCCs with RyR2s was not reduced in PH. LV myocytes were atrophied with an increased complexity of TAT network and exhibited a longer Ca^{2+} releases. The results of this study will provide an insight on the mechanism of pathological changes in RV and LV under PH.

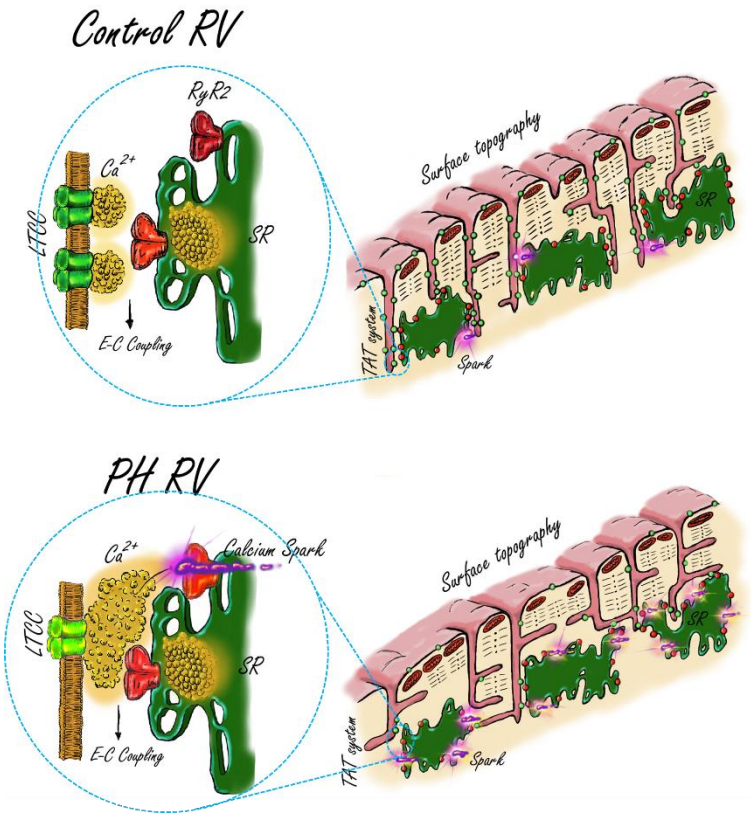

Figure 6.1. Schematic of PH-induced alterations in RV myocytes. Control RV myocytes have a highly organized surface membrane and TAT network that produce an efficient coupling between LTCC and RyR2. The Ca^{2+} efflux through LTCC is highly localized that can reach only closely located RyR2. In PH RV surface structure regularity and TAT structure deteriorates producing more spread Ca^{2+} influx from LTCC which could trigger more Ca^{2+} sparks from the RyR2.

The 5th chapter highlighted the RV -specific changes in microdomain organisation under the HF. The major discovery of this part is that a disruption in the membrane organisation after the failure of RV lead to hyperactivation of Ca^{2+} released channels in T-tubules, which can promote pathological changes in cellular physiology. Importantly, the changes on the cellular level were close to those occurred in LV myocytes, such as Z-groove reduction, TAT disturbance and Ca^{2+} transient prolongation. But on the microdomain level the reorganisation of RV myocytes was significantly different from the LV myocytes with preserving Ca^{2+} transient activation, reorganisation of LTCC located at T-tubule in clusters with a higher open probability and conductance. Long open states of LTCCs are particularly pro-arrhythmic in the setting of AP prolongation (Sanchez-Alonso et

al., 2016). Thus, our results indicated different mechanisms of microdomain regulation in RV and LV myocytes during HF and provide a new dimension in understanding of disease pathophysiology. But the understanding of the effect of these local alterations on cellular and organ behaviour will require the addition study.

6.2 Study Limitations

6.2.1 Differences between rat and human studies.

Animal models are usually good starting point for investigation of disease progression understanding of the underlying mechanisms but it has to be mentioned that not all of the observed findings can be directly implemented in humans. There are some strong differences in the physiology of humans and rodents. These alterations were discussed in details in Chapter 1. The human heart is beating at a slower rate and produces significantly longer action potentials (Wagner et al., 2009). On the cellular level, Ca^{2+} transients were significantly different in rats, whereas in large mammalian they showed just a different notch phase (Di Diego et al., 1996; Volders et al., 1999). The TAT membrane of human myocytes is far less organized than in the rat myocytes producing lower Ca^{2+} signal compartmentation in human cells (Schobesberger et al., 2017; Song et al., 2005). Therefore, the observed findings need to be proved directly in the human studies.

6.2.2 Limitations of cellular studies for the structural analysis of cell morphology and TAT structure

Isolated cardiomyocytes provide a great platform for investigation of cellular and sub-cellular physiology such as visualizing the cellular structure and precise localization of intracellular molecules. However, this model has several weak points such as loss of tissue integrity, including connections between neighbouring cardiac cells and the extracellular matrix and potential damage of the cells (Louch et al., 2011). Also, isolation has a potential risk of selecting the strongest cells from the heterogeneous population. Multicellular preparations, including isolated whole hearts and intact tissue samples (isolated trabeculae/ perfused tissue wedges), would be useful to avoid the issues associated with cell isolation (Watson et al., 2019). However, the work with these preparations requires a certain level of tissue

transparency or producing thin slices. Our preliminary experiments including visualisation of TAT in fixed RV and LV tissue using wheat germ agglutinin were not successful.

6.2.3 Limitations of cellular studies for the functional analysis

Work with isolated cells allowed to investigate local alterations in microdomain organized Ca^{2+} signalling in ventricular myocytes. However, a direct implication of these findings into the functioning of the whole ventricle is complicated. The RV and LV are working under a certain pressure and loading conditions, removal of this load will drastically alter the behaviour of the ventricles (Müller-Strahl et al., 2003). In PH patients multiple clinical and experimental studies showed that pressure overload in RV lead to impaired LV stroke volume and systolic pressure (Markus et al., 2001). However, when the pressure overload was removed in *ex vivo* and *in vitro* experiments, the LV was shown to develop the normal pressures (Han et al., 2018). Thus the ventricular loading conditions should be taken in account when the conclusions are drawing.

6.2.4 Early and delayed Ca^{2+} sparks analysis.

We performed the analysis of Ca^{2+} sparks localization based on assumption that TTF50 of Ca^{2+} transient is correlated with the distance to the nearest membrane. We used the methodology of Heinzel et al. to analysed the properties of early and delayed Ca^{2+} sparks (Heinzel et al., 2002). For a certain proof of the relation between Ca^{2+} transient TTF50 measured in this thesis and distance to the tubules a double staining protocol is needed, like was done in (Dries et al., 2013). They revealed a direct correlation between the two parameters in pig myocytes and divided the sparks in coupled, located < 0.5 µm to T-tubule from uncoupled, located > 2 µm from the membrane (Dries et al., 2013). Unfortunately, technical complications did not allow us to perform similar experimental setup. Thus we called sparks early and delayed assuming that separation was performed in accordance only with Ca^{2+} transient.

6.2.5 H89 is not a specific PKA blocker

In chapter 5 H89 was used as PKA antagonist to reveal the role of PKA phosphorylation in regulation of T-tubule LTCC in RV myocytes. There are many

evidences identified that H89 is not a specific PKA blocker, it can block another 8 protein kinases (Davies et al., 2000; Lochner and Moolman, 2006). Most of these kinases do not target LTCC, but at concentration of 10 μM H89 was shown to affect the sarcoplasmic reticulum Ca^{2+}-uptake (Lahouratate et al., 1997) , K^{+} channels (Sun Park et al., 2006), and phosphatidylcholine biosynthesis (Wieprecht et al., 1994). Some of these factors could indirectly affect the LTCC behaviour, so the data should be interpreted with care.

6.3 Prospective

In order to have the translational data we wish to make the model of RV myocytes and implement our findings of LTCC and Ca^{2+} sparks behaviour in control and PH RV myocytes and translate observed results in arrhythmogenesis in the whole heart. Similar approach was made previously with the use of a model of single myocytes (Grandi et al., 2010; Shannon and Bers, 2004) modified according to the observed relocation and hyperphosphorylation of LTCC in failing LV myocytes (Sanchez-Alonso et al., 2016). They implemented single cell model into three dimensional model of left ventricle (Moreno et al., 2011). Using this modelling process it was possible to link the changes of TAT network and LTCC localization with EADs observed on cellular level and that EADs could produce the formation of re-entrant arrhythmias on the whole heart level (Sanchez-Alonso et al., 2016).

As was said in section 6.1.2, lack of mechanical load in isolated myocytes reduced the significance of the obtained results. In chapter 4 we tried to link the alterations on the cellular level in RV and LV myocytes with the electrophysiological data obtained *in vivo*. Some of the single cell data could affect the conduction velocity in the ventricles, such as, for example, alterations in sell shape and dimensions (see paragraph 4.3.2). Unfortunately, other properties of the RV and LV *in vivo* are load-dependent and for this reason no clear correlation with single cell data can be provided. One of the approached to overcome these differences is to study tissue slices that can be cultivates and kept at certain loading conditions, mimicking the loading conditions *in vivo* (Watson et al., 2019).

Observed TAT network organisation and LTCC spatial localization of RV myocytes were close to partially unloaded LV. One of the resent works of Ibrahim

et al. showed that unloaded failing hearts have myocytes with partial restored structural organisation and Ca^{2+} handling (Ibrahim et al., 2012). These observations drive us to hypothesize that loading conditions have the leading role in membrane organisation of myocytes.

6.4 Clinical implications

PH and HF could led to pathological increase in RV load and promote the maladaptive remodelling of RV leading to RV hypertension and failure (Handoko et al., 2010). The progress in treatment allowed reducing the mortality rate in PH patients, but there is still no treatments directed to RV (Thenappan et al., 2018). The results of RV studies in both PH and MI showed the importance of LTCC in disease progression. Ca^{2+} channel blockers are among the commonly used therapies for HF and could be used for some patients with PH (Thenappan et al., 2018). The applicability of Ca^{2+} channel blockers is determined by the vasodilatation test (Sitbon et al., 2010). These patients who treated with these drugs have a high five years survival rate ~90% (Rich et al., 1992). But these drugs are nonspecific blockers, the results of this thesis could give the possibility to treat the LTCC located at T-tubule as a target of the therapy. This work could provide the theoretical basement of further studies of the RV progression in disease development and could help to find the new treatment approaches.

6.5 Conclusions

Microdomain organisation of cardiac myocytes plays an important role in maintain ECC in health and under pathophysiological changes. More and more studies confirmed that in disease the disorganisation alterations of a small microdomain organisation such as TAT network disruption (Lyon et al., 2009; Schobesberger et al., 2017), dispersion of RyR2 clusters (Kolstad et al., 2018) and LTCC localization (Sanchez-Alonso et al., 2016) are responsible for the impaired contractility and could provoke arrhythmogenic activity. As compared to LV myocytes the organisation of RV myocytes are far less studied and understood. In this thesis we demonstrated that RV myocytes have a distinct membrane organisation and altered Ca^{2+} handling as compared to LV myocytes. PH and MI both promote a pronounced remodelling of TAT network and LTCC spatial localization, promoting higher

spontaneous Ca^{2+} activity and more desynchronous activation of Ca^{2+} transients and producing the pro-arrhythmogenic substrate in RV. Thus, our multilevel investigation showed the complex nature of the RV remodelling in disease. Moreover, in both PH and MI models we observed alterations of structure and function of both RV and LV myocytes, suggesting the importance of investigation all of the chambers in disease.

7 References

Abdul-Salam, V.B., Russomanno, G., Chien-Nien, C., Mahomed, A.S., Yates, L.A., Wilkins, M.R., Zhao, L., Gierula, M., Dubois, O., Schaeper, U., Endruschat, J., Wojciak-Stothard, B., 2019. CLIC4/Arf6 Pathway. Circ. Res. 124, 52–65.

Adamcová, M., Pelouch, V., 1999. Isoforms of troponin in normal and diseased myocardium. Physiol. Res. 48, 235–47.

Allessie, M.A., Bonke, F.I.M., Schopman, F.J.G., 1976. Circus movement in rabbit atrial muscle as a mechanism of tachycardia. II. The role of nonuniform recovery of excitability in the occurrence of unidirectional block, as studied with multiple microelectrodes. Circ. Res. 39, 168–177.

Allessie, M.A., Bonke, F.I.M., Schopman, F.J.G., 1977. Circus movement in rabbit atrial muscle as a mechanism of tachycardia. III. The "leading circle" concept: a new model of circus movement in cardiac tissue without the involvement of an anatomical obstacle. Circ. Res. 41, 9–18.

Alpert, N.R., Gordon, M.S., 1962. Myofibrillar adenosine triphosphatase activity in congestive heart failure. Am. J. Physiol. 202, 940–946.

Anavekar, N.S., Skali, H., Bourgoun, M., Ghali, J.K., Kober, L., Maggioni, A.P., McMurray, J.J.V., Velazquez, E., Califf, R., Pfeffer, M.A., Solomon, S.D., 2008. Usefulness of Right Ventricular Fractional Area Change to Predict Death, Heart Failure, and Stroke Following Myocardial Infarction (from the VALIANT ECHO Study). Am. J. Cardiol. 101, 607–612.

Anthony Lai, F., Erickson, H.P., Rousseau, E., Liu, Q.Y., Meissner, G., 1988. Purification and reconstitution of the calcium release channel from skeletal muscle. Nature 331, 315–319.

Antzelevitch, C., Jalife, J., Moe, G.K., 1980. Characteristics of reflection as a mechanism of reentrant arrhythmias and its relationship to parasystole. Circulation 61, 182–191.

Anumonwo, J.M., Pandit, S. V., 2015. Ionic mechanisms of arrhythmogenesis, Trends in Cardiovascular Medicine. Elsevier Inc.

Asghari, P., Schulson, M., Scriven, D.R.L., Martens, G., Moore, E.D.W., 2009. Axial tubules of rat ventricular myocytes form multiple junctions with the sarcoplasmic reticulum. Biophys. J. 96, 4651–4660.

Ather, S., Respress, J.L., Li, N., Wehrens, X.H.T., 2013. Alterations in ryanodine receptors and related proteins in heart failure. Biochim. Biophys. Acta - Mol. Basis Dis. 1832, 2425–2431.

Balijepalli, R.C., Foell, J.D., Hall, D.D., Hell, J.W., Kamp, T.J., 2006. Localization of cardiac L-type Ca 2+ channels to a caveolar macromolecular signaling complex is required for β 2 -adrenergic regulation. Proc. Natl. Acad. Sci. U. S. A. 103, 7500–7505.

Balijepalli, R.C., Lokuta, A.J., Maertz, N.A., Buck, J.M., Haworth, R.A., Valdivia, H.H., Kamp, T.J., 2003. Depletion of T-tubules and specific subcellular changes in sarcolemmal proteins in tachycardia-induced heart failure. Cardiovasc. Res. 59, 67–77.

Balshaw, D.M., Xu, L., Yamaguchi, N., Pasek, D.A., Meissner, G., 2001. Calmodulin binding and inhibition of cardiac muscle calcium release channel (ryanodine receptor). J. Biol. Chem. 276, 20144–53.

Bannister, M.L., Alvarez-Laviada, A., Thomas, N.L., Mason, S.A., Coleman, S., du Plessis, C.L., Moran, A.T., Neill-Hall, D., Osman, H., Bagley, M.C., MacLeod, K.T., George, C.H., Williams, A.J., 2016. Effect of flecainide derivatives on sarcoplasmic reticulum calcium release suggests a lack of direct action on the cardiac ryanodine receptor. Br. J. Pharmacol. 2446–2459.

Barman, S.A., Zhu, S., White, R.E., 2009. RhoA/Rho-kinase signaling: A therapeutic target in pulmonary hypertension. Vasc. Health Risk Manag. 5, 663–671.

Bayer, J.D., Narayan, S.M., Lalani, G.G., Trayanova, N.A., 2010. Rate-dependent action potential alternans in human heart failure implicates abnormal intracellular calcium handling. Hear. Rhythm 7, 1093–1101.

Beard, N.A., Wei, L., Dulhunty, A.F., 2009. Ca(2+) signaling in striated muscle: the elusive roles of triadin, junctin, and calsequestrin. Eur. Biophys. J. 39, 27–36.

Bennett, H.J., Davenport, J.B., Kitmitto, A., Webb, K., 2015. 172 Junctophilin-2 interacts with the cardiac L-Type voltage-gated calcium channel. Heart 101, A98.1-A98.

Benoist, D., Stones, R., Benson, A.P., Fowler, E.D., Drinkhill, M.J., Hardy, M.E.L., Saint, D.A., Cazorla, O., Bernus, O., White, E., 2014. Systems approach to the study of stretch and arrhythmias in right ventricular failure induced in rats by monocrotaline.

Prog. Biophys. Mol. Biol. 115, 162–172.

Benoist, D., Stones, R., Drinkhill, M., Bernus, O., White, E., 2011. Arrhythmogenic substrate in hearts of rats with monocrotaline-induced pulmonary hypertension and right ventricular hypertrophy. Am. J. Physiol. Heart Circ. Physiol. 300, H2230-7.

Benoist, D., Stones, R., Drinkhill, M.J., Benson, A.P., Yang, Z., Cassan, C., Gilbert, S.H., Saint, D.A., Cazorla, O., Steele, D.S., Bernus, O., White, E., 2012. Cardiac arrhythmia mechanisms in rats with heart failure induced by pulmonary hypertension. Am J Physiol Hear. Circ Physiol 302, 2381–2395.

Bers, D.M., 2000. Calcium fluxes involved in control of cardiac myocyte contraction. Circ. Res.

Bers, D.M., 2001. Excitation-Contraction Coupling and Cardiac Contractile Force, Developments in Cardiovascular Medicine. Springer Netherlands, Dordrecht.

Bers, D.M., 2004. Macromolecular complexes regulating cardiac ryanodine receptor function. J. Mol. Cell. Cardiol.

Bers, D.M., 2008. Calcium Cycling and Signaling in Cardiac Myocytes. Annu. Rev. Physiol. 70, 23–49.

Bers, D.M., Bassani, J.W.M., Bassani, R.A., 1996. Na-Ca exchange and Ca fluxes during contraction and relaxation in mammalian ventricular muscle. In: Annals of the New York Academy of Sciences. Blackwell Publishing Inc., pp. 430–442.

Bers, D.M., Bridge, J.H., MacLeod, K.T., 1987. The mechanism of ryanodine action in rabbit ventricular muscle evaluated with Ca-selective microelectrodes and rapid cooling contractures. Can. J. Physiol. Pharmacol. 65, 610–8.

Bers, D.M., Perez-Reyes, E., 1999. Ca channels in cardiac myocytes: structure and function in Ca influx and intracellular Ca release. Cardiovasc. Res. 42, 339–360.

Bers, Despa, S., 2013. Cardiac Excitation-Contraction Coupling. Encycl. Biol. Chem. Second Ed. 415, 379–383.

Best, J.M., Kamp, T.J., 2012. Different subcellular populations of L-type Ca 2+ channels exhibit unique regulation and functional roles in cardiomyocytes. J. Mol. Cell. Cardiol. 52, 376–387.

Bettex, D.A., Prêtre, R., Chassot, P.G., 2014. Is our heart a well-designed pump? the heart

along animal evolution. Eur. Heart J. 35, 2322–2332.

Bhargava, A., Lin, X., Novak, P., Mehta, K., Korchev, Y., Delmar, M., Gorelik, J., Charney, L.H., Bhargava, A., Lin, X., Novak, P., Mehta, K., Korchev, Y., Gorelik, J., 2013. Super-resolution scanning patch clamp reveals clustering of functional ion channels in adult ventricular myocyte. Circ. Res. 112, 1112–1120.

Biesmans, L., Macquaide, N., Heinzel, F.R., Bito, V., Smith, G.L., Sipido, K.R., 2011. Subcellular heterogeneity of ryanodine receptor properties in ventricular myocytes with low T-tubule density. PLoS One 6.

Birnbaumer, L., Qin, N., Olcese, R., Tareilus, E., Platano, D., Costantin, J., Stefani, E., 1998. Structures and functions of calcium channel β subunits. J. Bioenerg. Biomembr. 30, 357–375.

Bogaard, H.J., Abe, K., Noordegmaf, A.V., Voelkel, N.F., 2009. The right ventricle under pressure. Chest 135, 794–804.

Bolte, S., Martin, C.F.P., Cordelières, F.P., 2006. A guided tour into subcellular colocalization analysis in light microscopy. J. Microsc. 224, 213–232.

Boraso, A., Williams, A.J., 1994. Modification of the gating of the cardiac sarcoplasmic reticulum Ca2+- release channel by H2O2 and dithiothreitol. Am. J. Physiol. - Hear. Circ. Physiol. 267.

Borgatta, L., Watras, J., Katz, A.M., Ehrlich, B.E., 1991. Regional differences in calcium-release channels from heart. Proc. Natl. Acad. Sci. U. S. A. 88, 2486–9.

Bossuyt, J., Taylor, B.E., James-Kracke, M., Hale, C.C., 2006. The Cardiac Sodium-Calcium Exchanger Associates with Caveolin-3. Ann. N. Y. Acad. Sci. 976, 197–204.

Bouchard, R.A., Clark, R.B., Giles, W.R., 1995. Effects of action potential duration on excitation-contraction coupling in rat ventricular myocytes: Action potential voltage-clamp measurements. Circ. Res. 76, 790–801.

Bovo, E., De Tombe, P.P., Zima, A. V., 2014. The role of dyadic organization in regulation of sarcoplasmic reticulum Ca2+ handling during rest in rabbit ventricular myocytes. Biophys. J. 106, 1902–1909.

Brandenburg, S., Lederer, W.J., Stephan, E., Brandenburg, S., Kohl, T., Williams, G.S.B., Gusev, K., Wagner, E., Rog-zielinska, E.A., Hebisch, E., Dura, M., Didié, M.,

Gotthardt, M., Nikolaev, V.O., Hasenfuss, G., 2016. Axial tubule junctions control rapid calcium signaling in atria Find the latest version : Axial tubule junctions control rapid calcium signaling in atria 126, 3999–4015.

Brette, F., Despa, S., Bers, D.M., Orchard, C.H., 2005. Spatiotemporal characteristics of SR Ca2+ uptake and release in detubulated rat ventricular myocytes. J. Mol. Cell. Cardiol. 39, 804–812.

Brette, F., Orchard, C., 2003. T-tubule function in mammalian cardiac myocytes, Circulation Research.

Brillantes, A.M.B., Ondrias, K., Scott, A., Kobrinsky, E., Ondriašová, E., Moschella, M.C., Jayaraman, T., Landers, M., Ehrlich, B.E., Marks, A.R., 1994. Stabilization of calcium release channel (ryanodine receptor) function by FK506-binding protein. Cell 77, 513–523.

Brown, A.M., Kunze, D.L., Yatani, A., 1984. The agonist effect of dihydropyridines on Ca channels. Nature 311, 570–572.

Brown, G.C., Borutaite, V., 2007. Nitric oxide and mitochondrial respiration in the heart. Cardiovasc. Res. 75, 283–290.

Brunner, F., WöLkart, G., Haleen, S., 2002. Defective intracellular calcium handling in monocrotaline-induced right ventricular hypertrophy: Protective effect of long-term endothelin-A receptor blockade with 2-benzo[1,3]dioxol-5-yl-3-benzyl-4-(4-methoxy-phenyl-)-4-oxobut-2-enoate- sodium (PD 155080). J. Pharmacol. Exp. Ther. 300, 442–449.

Bryant, S., Kimura, T.E., Kong, C.H.T., Watson, J.J., Chase, A., Suleiman, M.S., James, A.F., Orchard, C.H., 2014. Stimulation of I Ca by basal PKA activity is facilitated by caveolin-3 in cardiac ventricular myocytes. J. Mol. Cell. Cardiol. 68, 47–55.

Bryant, S.M., Kong, C.H.T., Watson, J., Cannell, M.B., James, A.F., Orchard, C.H., 2015. Altered distribution of ICa impairs Ca release at the t-tubules of ventricular myocytes from failing hearts. J. Mol. Cell. Cardiol. 86, 23–31.

Bu, G., Adams, H., Berbari, E.J., Rubart, M., 2009. Uniform action potential repolarization within the sarcolemma of in situ ventricular cardiomyocytes. Biophys. J. 96, 2532–2546.

Bünemann, M., Gerhardstein, B.L., Gao, T., Hosey, M.M., 1999. Functional regulation of

L-type calcium channels via protein kinase A- mediated phosphorylation of the β2 subunit. J. Biol. Chem. 274, 33851–33854.

Buraei, Z., Yang, J., 2010. The β subunit of voltage-gated Ca2+ channels. Physiol. Rev. 90, 1461–1506.

Burashnikov, A., Antzelevitch, C., 2006. Late-phase 3 EAD. A unique mechanism contributing to initiation of atrial fibrillation. PACE - Pacing Clin. Electrophysiol.

Cabo, C., Pertsov, A.M., Baxter, W.T., Davidenko, J.M., Gray, R.A., Jalife, J., 1994. Wave-front curvature as a cause of slow conduction and block in isolated cardiac muscle. Circ. Res. 75, 1014–1028.

Cachelin, A.B., De Peyer, J.E., Kokubun, S., Reuter, H., 1983. Ca2+ channel modulation by 8-bromocyclic AMP in cultured heart cells. Nature 304, 462–464.

Calaghan, S., White, E., 2006. Caveolae modulate excitation-contraction coupling and β2-adrenergic signalling in adult rat ventricular myocytes. Cardiovasc. Res. 69, 816–824.

Caldwell, J.L., Smith, C.E.R.R., Taylor, R.F., Kitmitto, A., Eisner, D.A., Dibb, K.M., Trafford, A.W., 2014. Dependence of cardiac transverse tubules on the BAR domain protein amphiphysin II (BIN-1). Circ. Res. 115, 986–996.

Campian, M.E., Verberne, H.J., Hardziyenka, M., De Bruin, K., Selwaness, M., Van Den Hoff, M.J.B., Ruijter, J.M., Van Eck-Smit, B.L.F., De Bakker, J.M.T., Tan, H.L., 2009. Serial noninvasive assessment of apoptosis during right ventricular disease progression in rats. J. Nucl. Med. 50, 1371–1377.

Cannell, M.B., Cheng, H., Lederer, W.J., 1995. The control of calcium release in heart muscle. Science 268, 1045–9.

Carafoli, E., Santella, L., Branca, D., Brini, M., Inesi, G., 2001. Generation, Control, and Processing of Cellular Calcium Signals. Crit. Rev. Biochem. Mol. Biol. 36, 107–260.

Carmeliet, E., Vereecke, J., 2002. General description of electrical activity. pp. 1–6.

Carnevali, L., Trombini, M., Rossi, S., Graiani, G., Manghi, M., Koolhaas, J.M., Quaini, F., MacChi, E., Nalivaiko, E., Sgoifo, A., 2013. Structural and electrical myocardial remodeling in a rodent model of depression. Psychosom. Med. 75, 42–51.

Catterall, W.A., 2000. Structure and regulation of voltage-gated Ca2+ channels. Annu. Rev. Immunol. 16, 521–55.

Catterall, W.A., Perez-Reyes, E., Snutch, T.P., Striessnig, J., 2005. International Union of Pharmacology. L. Nomenclature and structure-function relationships of Voltage-Gated Calcium Channels. Pharmacol. Rev. 57, 451–454.

Cavalié, A., Pelzer, D., Trautwein, W., 1986. Fast and slow gating behaviour of single calcium channels in cardiac cells - Relation to activation and inactivation of calcium-channel current. Pflügers Arch. Eur. J. Physiol. 406, 241–258.

Cavalli, A., Eghbali, M., Minosyan, T.Y., Stefani, E., Philipson, K.D., 2007. Localization of sarcolemmal proteins to lipid rafts in the myocardium. Cell Calcium 42, 313–22.

Chase, A., Orchard, C.H., 2011. Ca efflux via the sarcolemmal Ca ATPase occurs only in the t-tubules of rat ventricular myocytes. J. Mol. Cell. Cardiol. 50, 187–193.

Chelu, M.G., Sarma, S., Sood, S., Wang, S., Van Oort, R.J., Skapura, D.G., Li, N., Santonastasi, M., Müller, F.U., Schmitz, W., Schotten, U., Anderson, M.E., Valderrábano, M., Dobrev, D., Wehrens, X.H.T., 2009. Calmodulin kinase II-mediated sarcoplasmic reticulum Ca2+ leak promotes atrial fibrillation in mice. J. Clin. Invest. 119, 1940–1951.

Chen-Izu, Y., McCulle, S.L., Ward, C.W., Soeller, C., Allen, B.M., Rabang, C., Cannell, M.B., Balke, C.W., Izu, L.T., 2006. Three-dimensional distribution of ryanodine receptor clusters in cardiac myocytes. Biophys. J. 91, 1–13.

Chen, B., Guo, A., Zhang, C., Chen, R., Zhu, Y., Hong, J., Kutschke, W., Zimmerman, K., Weiss, R.M., Zingman, L., Anderson, M.E., Wehrens, X.H.H.T., Song, L.S., 2013. Critical roles of junctophilin-2 in T-tubule and excitation-contraction coupling maturation during postnatal development. Cardiovasc. Res. 100, 54–62.

Cheng, H., Lederer, M.R., Lederer, W.J., Cannell, M.B., 1996. Calcium sparks and [Ca2+]i waves in cardiac myocytes. Am. J. Physiol. - Cell Physiol. 270, 148–59.

Cheng, H., Lederer, W., Cannell, M., 1993. Calcium sparks: elementary events underlying excitation-contraction coupling in heart muscle. Science (80-.). 262, 740–744.

Chesler, N.C., Roldan, A., Vanderpool, R.R., Naeije, R., 2009. How to measure pulmonary vascular and right ventricular function. Conf. Proc. ... Annu. Int. Conf. IEEE Eng. Med. Biol. Soc. IEEE Eng. Med. Biol. Soc. Annu. Conf. 2009, 177–80.

Chien, K.R., 1999. Stress pathways and heart failure. Cell 98, 555–558.

Cingolani, O.H., Yang, X.P., Liu, Y.H., Villanueva, M., Rhaleb, N.E., Carretero, O.A.,

2004. Reduction of Cardiac Fibrosis Decreases Systolic Performance Without Affecting Diastolic Function in Hypertensive Rats. Hypertension 43, 1067–1073.

Clark, R.B., Bouchard, R.A., Salinas-Stefanon, E., Sanchez-Chapula, J., Giles, W.R., 1993. Heterogeneity of action potential waveforms and potassium currents in rat ventricle. Cardiovasc. Res. 27, 1795–1799.

Cleland, J.G.F., Krikler, D.M., 1992. Torsade de pointes: Chaos, sixteen years on? Br. Heart J. 67, 1–3.

Colecraft, H.M., Alseikhan, B., Takahashi, S.X., Chaudhuri, D., Mittman, S., Yegnasubramanian, V., Alvania, R.S., Johns, D.C., Marbán, E., Yue, D.T., 2002. Novel functional properties of Ca(2+) channel beta subunits revealed by their expression in adult rat heart cells. J. Physiol. 541, 435–52.

Cooke, R., 1997. Actomyosin interaction in striated muscle. Physiol. Rev.

Copple, B.L., Ganey, P.E., Roth, R.A., 2003. Liver inflammation during monocrotaline hepatotoxicity. Toxicology 190, 155–169.

Correia-Pinto, J., Henriques-Coelho, T., Roncon-Albuquerque, R., Lourenço, A.P., Melo-Rocha, G., Vasques-Nóvoa, F., Gillebert, T.C., Leite-Moreira, A.F., 2009. Time course and mechanisms of left ventricular systolic and diastolic dysfunction in monocrotaline-induced pulmonary hypertension. Basic Res. Cardiol. 104, 535–545.

Cranefield, P.F., Aronson, R.S., 1989. Cardiac Arrhythmias: the Role of Triggered Activ- Drug Therapy in Dilated Cardiomyopathy and ity and Other Mechanisms Myocarditis, International Journal of Cardiology.

Crossman, D.J., Shen, X., Jüllig, M., Munro, M., Hou, Y., Middleditch, M., Shrestha, D., Li, A., Lal, S., Dos Remedios, C.G., Baddeley, D., Ruygrok, P.N., Soeller, C., 2017. Increased collagen within the transverse tubules in human heart failure. Cardiovasc. Res. 113, 879–891.

Crump, S.M., Andres, D.A., Sievert, G., Satin, J., 2013. The cardiac L-type calcium channel distal carboxy terminus autoinhibition is regulated by calcium. Am. J. Physiol. - Hear. Circ. Physiol. 304, 455–464.

Curran, J., Brown, K.H., Santiago, D.J., Pogwizd, S., Bers, D.M., Shannon, T.R., 2010. Spontaneous Ca waves in ventricular myocytes from failing hearts depend on Ca2+-calmodulin-dependent protein kinase II. J. Mol. Cell. Cardiol. 49, 25–32.

D'Alonzo, G.E., Barst, R.J., Ayres, S.M., Bergofsky, E.H., Brundage, B.H., Detre, K.M., Fishman, A.P., Goldring, R.M., Groves, B.M., Kernis, J.T., Levy, P.S., Pietra, G.G., Reid, L.M., Reeves, J.T., Rich, S., Vreim, C.E., Williams, G.W., Wu, M., 1991. Survival in patients with primary pulmonary hypertension: Results from a national prospective registry. Ann. Intern. Med. 115, 343–349.

Dahl, L.K., Heine, M., Tassinari, L., 1962. Effects of chronia excess salt ingestion. Evidence that genetic factors play an important role in susceptibility to experimental hypertension. J. Exp. Med. 115, 1173–1190.

Danton, M.H., Byrne, J.G., Flores, K.Q., Hsin, M., Martin, J.S., Laurence, R.G., Cohn, L.H., Aklog, L., Emery, R.W., 2001. Modified Glenn connection for acutely ischemic right ventricular failure reverses secondary left ventricular dysfunction. J. Thorac. Cardiovasc. Surg. 122, 80–91.

Das, M., Fessel, J., Tang, H., West, J., 2012. A process-based review of mouse models of pulmonary hypertension 2.

Davies, S.P., Reddy, H., Caivano, M., Cohen, P., 2000. Specificity and mechanism of action of some commonly used protein kinase inhibitors. Biochem. J. 351, 95–105.

De Azevedo, I.M., Watanabe, Y., Dreifus, L.S., 1973. Atrioventricular junctional rhythm: classification and clinical significance. Chest.

De Jongh, K.S., Murphy, B.J., Colvin, A.A., Hell, J.W., Takahashi, M., Catterall, W.A., 1996. Specific phosphorylation of a site in the full-length form of the α1 subunit of the cardiac L-type calcium channel by adenosine 3'-5'-cyclic monophosphate-dependent protein kinase. Biochemistry 35, 10392–10402.

De Jongh, K.S., Warner, C., Catterall, W.A., 1990. Subunits of purified calcium channels: a2 and hamma are encoded by the same gene. J. Biol. Chem. 265, 14738–14741.

De Man, F.S., Handoko, M.L., Van Ballegoij, J.J.M., Schalij, I., Bogaards, S.J.P., Postmus, P.E., Van Der Velden, J., Westerhof, N., Paulus, W.J., Vonk-Noordegraaf, A., 2012. Bisoprolol delays progression towards right heart failure in experimental pulmonary hypertension. Circ. Hear. Fail. 5, 97–105.

de Tombe, P., 1998. Altered contractile function in heart failure. Cardiovasc. Res. 37, 367–380.

De Vroomen, M., Lopes Cardozo, R.H., Steendijk, P., Van Bel, F., Baan, J., 2000.

Improved contractile performance of right ventricle in response to increased RV afterload in newborn lamb. Am. J. Physiol. - Hear. Circ. Physiol. 278–1, 100–5.

Delcroix, M., Naeije, R., 2010. Optimising the management of pulmonary arterial hypertension patients: emergency treatments. Eur. Respir. Rev. 19, 204–11.

Dell'Italia, L.J., Pearce, D.J., Blackwell, G.G., Singleton, H.R., Bishop, S.P., Pohost, G.M., 1995. Right and left ventricular volumes and function after acute pulmonary hypertension in intact dogs. J. Appl. Physiol. 78, 2320–2327.

Dessertenne, F., 1966. La tachycardie ventriculaire à deux foyers opposés variables. Arch. Mal. Coeur Vaiss. 59, 263–272.

Di Diego, J.M., Antzelevitch, C., 1993. Pinacidil-induced electrical heterogeneity and extrasystolic activity in canine ventricular tissues does activation of atp-regulated potassium current promote phase 2 reentry? Circulation 88, 1177–1189.

Di Diego, J.M., Sun, Z.Q., Antzelevitch, C., 1996. I(to) and action potential notch are smaller in left vs. right canine ventricular epicardium. Am. J. Physiol. - Hear. Circ. Physiol. 271, 548–61.

Di Salvo, T.G., Mathier, M., Semigran, M.J., Dec, G.W., 1995. Preserved right ventricular ejection fraction predicts exercise capacity and survival in advanced heart failure. J. Am. Coll. Cardiol. 25, 1143–1153.

Dias, C.A., Assad, R.S., Caneo, L.F., Abduch, M.C.D., Aiello, V.D., Dias, A.R., Marcial, M.B., Oliveira, S.A., 2002. Reversible pulmonary trunk banding. II. An experimental model for rapid pulmonary ventricular hypertrophy. J. Thorac. Cardiovasc. Surg. 124, 999–1006.

Dibb, K.M., Clarke, J.D., Horn, M.A., Richards, M.A., Graham, H.K., Eisner, D.A., Trafford, A.W., 2009. Characterization of an extensive transverse tubular network in sheep atrial myocytes and its depletion in heart failure. Circ. Hear. Fail. 2, 482–489.

Doi, M., Yano, M., Kobayashi, S., Kohno, Masateru, Tokuhisa, T., Okuda, S., Suetsugu, M., Hisamatsu, Y., Ohkusa, T., Kohno, Michihiro, Matsuzaki, M., 2002. Propranolol prevents the development of heart failure by restoring FKBP12.6-mediated stabilization of ryanodine receptor. Circulation 105, 1374–1379.

Dries, E., Bito, V., Lenaerts, I., Antoons, G., Sipido, K.R., Macquaide, N., 2013. Selective modulation of coupled ryanodine receptors during microdomain activation of

calcium/calmodulin-dependent kinase II in the dyadic cleft. Circ. Res. 113, 1242–1252.

Durell, S.R., Hao, Y., Guy, H.R., 1998. Structural models of the transmembrane region of voltage-gated and other K+ channels in open, closed, and inactivated conformations. J. Struct. Biol. 121, 263–284.

Egorov, Y. V., Lang, D., Tyan, L., Turner, D., Lim, E., Piro, Z.D., Hernandez, J.J., Lodin, R., Wang, R., Schmuck, E.G., Raval, A.N., Ralphe, C.J., Kamp, T.J., Rosenshtraukh, L. V., Glukhov, A. V, 2019. Caveolae-Mediated Activation of Mechanosensitive Chloride Channels in Pulmonary Veins Triggers Atrial Arrhythmogenesis. J. Am. Heart Assoc. 8, e012748.

Fabiato, A., Fabiato, F., 1978. Calcium-Induced Release of Calcium From the Sarcoplasmic Reticulum of Skinned Cells From Adult Human, Dog, Cat, Rabbit, Rat, and Frog Hearts and From Fetal and New-Born Rat Ventricles. Ann. N. Y. Acad. Sci. 307, 491–522.

Farraj, A.K., Hazari, M.S., Cascio, W.E., 2011. The Utility of the Small Rodent Electrocardiogram in Toxicology. Toxicol. Sci. 121, 11–30.

Fearnley, C.J., Roderick, H.L., Bootman, M.D., 2011. Calcium signaling in cardiac myocytes 3(11), a004242.

Felix, R., Gurnett, C.A., De Waard, M., Campbell, K.P., 1997. Dissection of functional domains of the voltage-dependent Ca2+ channel α2δ subunit. J. Neurosci. 17, 6884–6891.

Feng, J., 1998. Transmural heterogeneity of action potentials and I(to1) in myocytes isolated from the human right ventricle. Am. J. Physiol. - Hear. Circ. Physiol. 275.

Ferdinandy, P., Schulz, R., 2003. Nitric oxide, superoxide, and peroxynitrite in myocardial ischaemia-reperfusion injury and preconditioning. Br. J. Pharmacol. 138, 532–543.

Ferrantini, C., Coppini, R., Sacconi, L., Tosi, B., Zhang, M.L., Wang, G.L., Vries, E. De, Hoppenbrouwers, E., Pavone, F., Cerbai, E., Tesi, C., Poggesi, C., Ter Keurs, H.E.D.J., 2014. Impact of detubulation on force and kinetics of cardiac muscle contraction. J. Gen. Physiol. 143, 783–797.

Fink, M., Noble, D., 2010. Pharmacodynamic effects in the cardiovascular system: The modeller's view. In: Basic and Clinical Pharmacology and Toxicology. John Wiley

& Sons, Ltd, pp. 243–249.

Foell, J.D., Balijepalli, R.C., Delisle, B.P., Yunker, A.M.R., Robia, S.L., Walker, J.W., McEnery, M.W., January, C.T., Kamp, T.J., 2004. Molecular heterogeneity of calcium channel β-subunits in canine and human heart: Evidence for differential subcellular localization. Physiol. Genomics 17, 183–200.

Folino, A.F., Bobbo, F., Schiraldi, C., Tona, F., Romano, S., Buja, G., Bellotto, F., 2003. Ventricular Arrhythmias and Autonomic Profile in Patients with Primary Pulmonary Hypertension. Lung 181, 321–328.

Foschi, M., Di Mauro, M., Tancredi, F., Capparuccia, C., Petroni, R., Leonzio, L., Romano, S., Gallina, S., Penco, M., Cibelli, M., Calafiore, A., 2017. The Dark Side of the Moon: The Right Ventricle. J. Cardiovasc. Dev. Dis. 4, 18.

Fowler, E.D., Drinkhill, M.J., Stones, R., White, E., 2018. Diastolic dysfunction in pulmonary artery hypertension: Creatine kinase and the potential therapeutic benefit of beta-blockers. Clin. Exp. Pharmacol. Physiol. 45, 384–389.

Fraccarollo, D., Berger, S., Galuppo, P., Kneitz, S., Hein, L., Schütz, G., Frantz, S., Ertl, G., Bauersachs, J., 2011. Deletion of cardiomyocyte mineralocorticoid receptor ameliorates adverse remodeling after myocardial infarction. Circulation 123, 400–408.

Frisk, M., Koivumaki, J.T., Norseng, P.A., Maleckar, M.M., Sejersted, O.M., Louch, W.E., 2014. Variable t-tubule organization and Ca2+ homeostasis across the atria. AJP Hear. Circ. Physiol. 307, H609–H620.

Fujiwara, K., Tanaka, H., Mani, H., Nakagami, T., Takamatsu, T., 2008. Burst emergence of intracellular ca2+ waves evokes arrhythmogenic oscillatory depolarization via the Na+-Ca2+ exchanger: Simultaneous confocal recording of membrane potential and intracellular Ca2+ in the heart. Circ. Res. 103, 509–518.

Fuller-Bicer, G.A., Varadi, G., Koch, S.E., Ishii, M., Bodi, I., Kadeer, N., Muth, J.N., Mikala, G., Petrashevskaya, N.N., Jordan, M.A., Zhang, S.P., Qin, N., Flores, C.M., Isaacsohn, I., Varadi, M., Mori, Y., Jones, W.K., Schwartz, A., 2009. Targeted disruption of the voltage-dependent calcium channel α 2 /δ-1-subunit. Am. J. Physiol. - Hear. Circ. Physiol. 297, 117–124.

Fuller, M.D., Emrick, M.A., Sadilek, M., Scheuer, T., Catterall, W.A., 2010. Molecular

mechanism of calcium channel regulation in the fight-or-flight response. Sci. Signal. 3, 1–11.

Gao, L., Balshaw, D., Xu, L., Tripathy, A., Xin, C., Meissner, G., 2000. Evidence for a role of the lumenal M3-M4 loop in skeletal muscle Ca2+ release channel (ryanodine receptor) activity and conductance. Biophys. J. 79, 828–840.

Gao, T., Yatani, A., Dell'Acqua, M.L., Sako, H., Green, S.A., Dascal, N., Scott, J.D., Hosey, M.M., 1997. cAMP-dependent regulation of cardiac L-type Ca2+ channels requires membrane targeting of PKA and phosphorylation of channel subunits. Neuron 19, 185–196.

Gerdes, A.M., Capasso, J.M., 1995. Structural remodeling and mechanical dysfunction of cardiac myocytes in heart failure. J. Mol. Cell. Cardiol. 27, 849–856.

Gerhardstein, B.L., Puri, T.S., Chien, A.J., Hosey, M.M., 1999. Identification of the sites phosphorylated by cyclic AMP-dependent protein kinase on the β2 subunit of L-type voltage-dependent calcium channels. Biochemistry 38, 10361–10370.

Ghio, S., Tavazzi, L., 2005. Right ventricular dysfunction in advanced heart failure. Ital. Heart J. 6, 852–5.

Giles, W.R., Imaizumi, Y., 1988. Comparison of potassium currents in rabbit atrial and ventricular cells. J. Physiol. 405, 123–145.

Glukhov, A. V., Balycheva, M., Sanchez-Alonso, J.L., Ilkan, Z., Alvarez-Laviada, A., Bhogal, N., Diakonov, I., Schobesberger, S., Sikkel, M.B., Bhargava, A., Faggian, G., Punjabi, P.P., Houser, S.R., Gorelik, J., 2015. Direct evidence for microdomain-specific localization and remodeling of functional L-type calcium channels in rat and human atrial myocytes. Circulation 132, 2372–2384.

Goh, K.Y., Qu, J., Hong, H., Liu, T., Dell'italia, L.J., Wu, Y., O'rourke, B., Zhou, L., 2016. Impaired mitochondrial network excitability in failing Guinea-pig cardiomyocytes. Cardiovasc. Res. 109, 79–89.

Goldstein, J.A., 2002. Pathophysiology and management of right heart ischemia. J. Am. Coll. Cardiol. 40, 841–853.

Gonzalez-Gutierrez, G., Miranda-Laferte, E., Neely, A., Hidalgo, P., 2007. The Src homology 3 domain of the β-subunit of voltage-gated calcium channels promotes endocytosis via dynamin interaction. J. Biol. Chem. 282, 2156–2162.

Goodenough, D.A., Paul, D.L., 2009. Gap Junctions & Neurogenesis.pdf. Cold Spring Harb Perspect Biol 1, a002576.

Gorelik, J., Yang, L.Q., Zhang, Y., Lab, M., Korchev, Y., Harding, S.E., 2006. A novel Z-groove index characterizing myocardial surface structure. Cardiovasc. Res. 72, 422–429.

Grandi, E., Pasqualini, F.S., Bers, D.M., 2010. A novel computational model of the human ventricular action potential and Ca transient. J. Mol. Cell. Cardiol. 48, 112–121.

Greyson, C.R., 2008. Pathophysiology of right ventricular failure. Crit. Care Med. 36, S57–S65.

Greyson, C.R., 2010. The Right Ventricle and Pulmonary Circulation: Basic Concepts. Rev. Española Cardiol. (English Ed. 63, 81–95.

Grossman, W., Jones, D., McLaurin, L.P., 1975. Wall stress and patterns of hypertrophy in the human left ventricle. J. Clin. Invest. 56, 56–64.

Grund, A., Szaroszyk, M., Döppner, J.K., Malek Mohammadi, M., Kattih, B., Korf-Klingebiel, M., Gigina, A., Scherr, M., Kensah, G., Jara-Avaca, M., Gruh, I., Martin, U., Wollert, K.C., Gohla, A., Katus, H.A., Müller, O.J., Bauersachs, J., Heineke, J., 2019. A gene therapeutic approach to inhibit calcium and integrin binding protein 1 ameliorates maladaptive remodelling in pressure overload. Cardiovasc. Res. 115, 71–82.

Gu, Y., Gorelik, J., Spohr, H.A., Shevchuk, A., Lab, M.J., Harding, S.E., Vodyanoy, I., Klenerman, D., Korchev, Y.E., 2002. High-resolution scanning patch-clamp: new insights into cell function. FASEB J. 16, 748–750.

Guazzi, M., Borlaug, B.A., 2012. Contemporary Reviews in Cardiovascular Medicine Pulmonary Hypertension Due to Left Heart Disease. Circulation 126, 975–990.

Gupta, R.C., Shimoyama, H., Tanimura, M., Nair, R., Lesch, M., Sabbah, H.N., 1997. SR Ca2+-ATPase activity and expression in ventricular myocardium of dogs with heart failure. Am. J. Physiol. - Hear. Circ. Physiol. 273.

Gussak, I., Antzelevitch, C., 2003. Cardiac Repolarization: Bridging Basic and Clinical Science, Journal of Chemical Information and Modeling, Contemporary Cardiology. Humana Press, Totowa, NJ.

Guyton, A.C., Lindsey, A.W., Gillully, J.J., 1954. The limits of right ventricular

compensation following acute increase in pulmonary circulatory resistance. Circ. Res. 2, 326–332.

Györke, S., Stevens, S.C.W., Terentyev, D., 2009. Cardiac calsequestrin: quest inside the SR. J Physiol 587, 3091–3094.

Haddad, F., Hunt, S.A., Rosenthal, D.N., Murphy, D.J., 2008. Right ventricular function in cardiovascular disease, part I: Anatomy, physiology, aging, and functional assessment of the right ventricle. Circulation 117, 1436–48.

Hakamata, Y., Nakai, J., Takeshima, H., Imoto, K., 1992. Primary structure and distribution of a novel ryanodine receptor/calcium release channel from rabbit brain. FEBS Lett. 312, 229–235.

Hales, P.W., Schneider, J.E., Burton, R.A.B., Wright, B.J., Bollensdorff, C., Kohl, P., 2012. Histo-anatomical structure of the living isolated rat heart in two contraction states assessed by diffusion tensor MRI. Prog. Biophys. Mol. Biol. 110, 319–330.

Han, J.-C., Guild, S.-J., Pham, T., Nisbet, L., Tran, K., Taberner, A.J., Loiselle, D.S., 2018. Left-Ventricular Energetics in Pulmonary Arterial Hypertension-Induced Right-Ventricular Hypertrophic Failure. Front. Physiol. 8, 1–12.

Handoko, M.L., De Man, F.S., Allaart, C.P., Paulus, W.J., Westerhof, N., Vonk-Noordegraaf, A., 2010. Perspectives on novel therapeutic strategies for right heart failure in pulmonary arterial hypertension: Lessons from the left heart. Eur. Respir. Rev. 19, 72–82.

Hardziyenka, M., Surie, S., de Groot, J.R., de Bruin-Bon, H.A.C.M.R., Knops, R.E., Remmelink, M., Yong, Z.-Y., Baan, J., Bouma, B.J., Bresser, P., Tan, H.L., 2011. Right ventricular pacing improves haemodynamics in right ventricular failure from pressure overload: an open observational proof-of-principle study in patients with chronic thromboembolic pulmonary hypertension. Europace 13, 1753–9.

Hartzell, H.C., 1988. Regulation of cardiac ion channels by catecholamines, acetylcholine and second messenger systems. Prog. Biophys. Mol. Biol. 52, 165–247.

Harvey, R.D., Calaghan, S.C., 2012. Caveolae create local signalling domains through their distinct protein content, lipid profile and morphology. J. Mol. Cell. Cardiol. 52, 366–375.

Hatton, N., Ryan, J.J., 2014. Sex differences in response to pulmonary arterial hypertension

therapy: is what's good for the goose, good for the gander? Chest 145, 1184–1186.

Hayward, R., Hydock, D.S., 2007. Doxorubicin cardiotoxicity in the rat: An in vivo characterization. J. Am. Assoc. Lab. Anim. Sci. 46, 20–32.

He, J.Q., Conklin, M.W., Foell, J.D., Wolff, M.R., Haworth, R.A., Coronado, R., Kamp, T.J., 2001. Reduction in density of transverse tubules and L-type Ca2+ channels in canine tachycardia-induced heart failure. Cardiovasc. Res. 49, 298–307.

Hebisch, E., Ward, C.W., Brandenburg, S., Kohl, T., Williams, G.S.B., Gusev, K., Wagner, E., Rog-zielinska, E.A., 2016. Axial tubule junctions control rapid calcium signaling in atria Axial tubule junctions control rapid calcium signaling in atria 126, 3999–4015.

Hein, S., Kostin, S., Heling, A., Maeno, Y., Schaper, J., 2000. The role of the cytoskeleton in heart failure. Cardiovasc. Res. 45, 273–278.

Heinzel, F.R., Bito, V., Biesmans, L., Wu, M., Detre, E., Von Wegner, F., Claus, P., Dymarkowski, S., Maes, F., Bogaert, J., Rademakers, F., D'Hooge, J., Sipido, K., 2008. Remodeling of T-tubules and reduced synchrony of Ca2+ release in myocytes from chronically ischemic myocardium. Circ. Res. 102, 338–346.

Heinzel, F.R., Bito, V., Volders, P.G.A., Antoons, G., Mubagwa, K., Sipido, K.R., 2002. Spatial and temporal inhomogeneities during Ca2+ release from the sarcoplasmic reticulum in pig ventricular myocytes. Circ. Res. 91, 1023–30.

Hell, J.W., Westenbroek, R.E., Breeze, L.J., Wang, K.K.W., Chavkin, C., Catterall, W.A., 1996. N-methyl-D-aspartate receptor-induced proteolytic conversion of postsynaptic class C L-type calcium channels in hippocampal neurons. Proc. Natl. Acad. Sci. U. S. A. 93, 3362–3367.

Hess, P., Lansman, J.B., Tsien, R.W., 1984. Different modes of Ca channel gating behaviour favoured by dihidrohyridine Ca agonists and antagonists. Nature 311, 538–544.

Hiess, F., Vallmitjana, A., Wang, R., Cheng, H., Ter Keurs, H.E.D.J., Chen, J., Hove-Madsen, L., Benitez, R., Chen, S.R.W., D J ter Keurs, H.E., Chen, J., Hove-Madsen, L., Benitez, R., Wayne Chen, S.R., 2015. Distribution and function of cardiac ryanodine receptor clusters in live ventricular myocytes. J. Biol. Chem. 290, 20477–20487.

Hill, M.A., 2016. Cardiovascular System - Heart Histology. Embryology 1–6.

Hirsh, J., Hoak, J., 1996. Management of deep vein thrombosis and pulmonary embolism: A statement for healthcare professionals. Circulation 93, 2212–2245.

Hlaing, T., DiMino, T., Kowey, P.R., Yan, G.X., 2005. ECG repolarization waves: Their genesis and clinical implications. Ann. Noninvasive Electrocardiol. 10, 211–223.

Hoang-Trong, T.M., Ullah, A., Jafri, M.S., 2015. Calcium Sparks in the Heart: Dynamics and Regulation. Res. Rep. Biol. 6, 203–214.

Hoeper, M.M., Bogaard, H.J., Condliffe, R., Frantz, R., Khanna, D., Kurzyna, M., Langleben, D., Manes, A., Satoh, T., Torres, F., Wilkins, M.R., Badesch, D.B., 2013. DefHoeper, M. M., Bogaard, H. J., Condliffe, R., Frantz, R., Khanna, D., Kurzyna, M., … Badesch, D. B. (2013). Definitions and diagnosis of pulmonary hypertension. Journal of the American College of Cardiology, 62(25 Suppl), D42–50. doi:10.1016/j.jacc.201. J. Am. Coll. Cardiol. 62, D42-50.

Holubarsch, C., Ruf, T., Goldstein, D.J., Ashton, R.C., Nicki, W., Pieske, B., Pioch, K., Lüdemann, J., Wiesner, S., Hasenfuss, G., Posival, H., Just, H., Burkhoff, D., 1996. Existence of the Frank-Starling mechanism in the failing human heart: Investigations on the organ, tissue, and sarcomere levels. Circulation 94, 683–689.

Hon, J.K.F., Steendijk, P., Khan, H., Wong, K., Yacoub, M., 2001. Acute effects of pulmonary artery banding in sheep on right ventricle pressure-volume relations: Relevance to the arterial switch operation. Acta Physiol. Scand. 172, 97–106.

Hong, T., Yang, H., Zhang, S.-S., Cho, H.C., Kalashnikova, M., Sun, B., Zhang, H., Bhargava, A., Grabe, M., Olgin, J., Gorelik, J., Marbán, E., Jan, L.Y., Shaw, R.M., 2014. Cardiac BIN1 folds T-tubule membrane, controlling ion flux and limiting arrhythmia. Nat. Med. 20, 624–632.

Hopkins, P.M., 2006. Skeletal muscle physiology. Contin. Educ. Anaesthesia, Crit. Care Pain 6, 1–6.

Horsfield, K., 1978. Morphometry of the small pulmonary arteries in man. Circ. Res. 42, 593–597.

Hryshko, L. V., Bers, D.M., 1990. Ca current facilitation during postrest recovery depends on Ca entry. Am. J. Physiol. - Hear. Circ. Physiol. 259.

Huang, J., Wolk, J.H., Gewitz, M.H., Mathew, R., 2010. Progressive endothelial cell

damage in an inflammatory model of pulmonary hypertension. Exp. Lung Res. 36, 57–66.

Huke, S., Bers, D.M., 2007. Temporal dissociation of frequency-dependent acceleration of relaxation and protein phosphorylation by CaMKII. J. Mol. Cell. Cardiol. 42, 590–9.

Hund, T.J., Mohlerp, P.J., 2016. Atrial-specific pathways for control of intracellular signaling and myocyte function. J. Clin. Invest. 126, 3731–3734.

Ibrahim, M., Gorelik, J., Yacoub, M.H., Terracciano, C.M., 2011. The structure and function of cardiac t-tubules in health and disease. Proc. R. Soc. B Biol. Sci. 278, 2714–2723.

Ibrahim, M., Navaratnarajah, M., Siedlecka, U., Rao, C., Dias, P., Moshkov, A. V., Gorelik, J., Yacoub, M.H., Terracciano, C.M., 2012. Mechanical unloading reverses transverse tubule remodelling and normalizes local Ca 2+-induced Ca 2+release in a rodent model of heart failure. Eur. J. Heart Fail. 14, 571–580.

Ibrahim, M., Siedlecka, U., Buyandelger, B., Harada, M., Rao, C., Moshkov, A., Bhargava, A., Schneider, M., Yacoub, M.H., Gorelik, J., Knöll, R., Terracciano, C.M., 2013. A critical role for Telethonin in regulating t-tubule structure and function in the mammalian heart. Hum. Mol. Genet. 22, 372–383.

Ikeda, T., Uchida, T., Hough, D., Lee, J.J., Fishbein, M.C., Mandel, W.J., Chen, P.S., Karagueuzian, H.S., 1996. Mechanism of spontaneous termination of functional reentry in isolated canine right atrium: Evidence for the presence of an excitable but nonexcited core. Circulation 94, 1962–1973.

Inui, M., Saito, A., Fleischer, S., 1987. Purification of the ryanodine receptor and identity with feet structures of junctional terminal cisternae of sarcoplasmic reticulum from fast skeletal muscle. J. Biol. Chem. 262, 1740–1747.

Ion-conductance, T.S., Hansma, P.K., Drake, B., Marti, O., Gould, A.C., Prater, C.B., 1987. The Scanning Ion-Conductance. Source Sci. New Ser. Eds. (Ant. Museum-Ephe 3, 1–3.

Jacobs, W., van de Veerdonk, M.C., Trip, P., de Man, F., Heymans, M.W., Marcus, J.T., Kawut, S.M., Bogaard, H.-J., Boonstra, A., Vonk Noordegraaf, A., 2014. The right ventricle explains sex differences in survival in idiopathic pulmonary arterial hypertension. Chest 145, 1230–1236.

Janse, M.J., Wit, A.L., 1989. Electrophysiological mechanisms of ventricular arrhythmias resulting from myocardial ischemia and infarction. Physiol. Rev.

January, C.T., Riddle, J.M., 1989. Early afterdepolarizations: Mechanism of induction and block. A role for L-type Ca2+ current. Circ. Res. 64, 977–990.

Jayaraman, T., Brillantes, A.M., Timerman, A.P., Fleischer, S., Erdjument-Bromage, H., Tempst, P., Marks, A.R., 1992. FK506 binding protein associated with the calcium release channel (ryanodine receptor). J. Biol. Chem. 267, 9474–9477.

Jayasinghe, I.D., Cannell, M.B., Soeller, C., 2009. Organization of ryanodine receptors, transverse tubules, and sodium-calcium exchanger in rat myocytes. Biophys. J. 97, 2664–2673.

Jayasinghe, I.D., Crossman, D.J., Soeller, C., Cannell, M.B., 2010. A new twist in cardiac muscle: dislocated and helicoid arrangements of myofibrillar z-disks in mammalian ventricular myocytes. J. Mol. Cell. Cardiol. 48, 964–71.

Jiang, B.H., Tardif, J.C., Shi, Y., Dupuis, J., 2011. Bosentan does not improve pulmonary hypertension and lung remodeling in heart failure. Eur. Respir. J. 37, 578–586.

Jiang, D., Wang, R., Xiao, B., Kong, H., Hunt, D.J., Choi, P., Zhang, L., Chen, S.R.W., 2005. Enhanced store overload-induced Ca2+ release and channel sensitivity to luminal Ca2+ activation are common defects of RyR2 mutations linked to ventricular tachycardia and sudden death. Circ. Res. 97, 1173–1181.

Jones, P.P., MacQuaide, N., Louch, W.E., 2018. Dyadic Plasticity in Cardiomyocytes. Front. Physiol. 9, 1–14.

Joseph, J., Washington, A., Joseph, L., Koehler, L., Fink, L.M., Hauer-Jensen, M., Kennedy, R.H., 2002. Hyperhomocysteinemia leads to adverse cardiac remodeling in hypertensive rats. Am. J. Physiol. - Hear. Circ. Physiol. 283, H2567–H2574.

Josephson, I.R., Varadi, G., 1996. The β subunit increases Ca2+ currents and gating charge movements of human cardiac L-type Ca2+ channels. Biophys. J. 70, 1285–1293.

Jung, D.H., Mo, S.H., Kim, D.H., 2006. Calumenin, a multiple EF-hands Ca2+-binding protein, interacts with ryanodine receptor-1 in rabbit skeletal sarcoplasmic reticulum. Biochem. Biophys. Res. Commun. 343, 34–42.

Kääb, S., Nuss, H.B., Chiamvimonvat, N., O'Rourke, B., Pak, P.H., Kass, D.A., Marban, E., Tomaselli, G.F., 1996. Ionic Mechanism of Action Potential Prolongation in

Ventricular Myocytes From Dogs With Pacing-Induced Heart Failure. Circ. Res. 78, 262–273.

Kaftan, E., Marks, A.R., Ehrlich, B.E., 1996. Effects of Rapamycin on Ryanodine Receptor/Ca2+-Release Channels from Cardiac Muscle. Circ. Res. 78, 990–997.

Kalogeropoulos, A.P., Vega, J.D., Smith, A.L., Georgiopoulou, V. V., 2011. Pulmonary hypertension and right ventricular function in advanced heart failure. Congest. Hear. Fail. 17, 189–198.

Kamp, T.J., Hell, J.W., 2000. Regulation of cardiac L-type calcium channels by protein kinase A and protein kinase C. Circ. Res. 87, 1095–1102.

Kamp, T.J., Pérez-García, T.M., Marban, E., 1996. Enhancement of ionic current and charge movement by coexpression of calcium channel β1A subunit with α1C subunit in a human embryonic kidney cell line. J. Physiol. 492, 89–96.

Kapiloff, M.S., Jackson, N., Airhart, N., 2001. mAKAP and the ryanodine receptor are part of a multi-component signaling complex on the cardiomyocyte nuclear envelope. J. Cell Sci. 114, 3167–3176.

Karunanithi, M.K., Michniewicz, J., Copeland, S.E., Feneley, M.P., 1992. Right ventricular preload recruitable stroke work, end-systolic pressure- volume, and dP/dt(max)-end-diastolic volume relations compared as indexes of right ventricular contractile performance in conscious dogs. Circ. Res. 70, 1169–1179.

Kasahara, Y., Kiyatake, K., Tatsumi, K., Sugito, K., Kakusaka, I., Yamagata, S.I., Ohmori, S., Kitada, M., Kuriyama, T., 1997. Bioactivation of monocrotaline by P-450 3A in rat liver. J. Cardiovasc. Pharmacol. 30, 124–129.

Kaul, T., 2000. Postoperative acute refractory right ventricular failure: incidence, pathogenesis, management and prognosis. Cardiovasc. Surg. 8, 1–9.

Kawai, M., Hussain, M., Orchard, C.H., 1999. Excitation-contraction coupling in rat ventricular myocytes after formamide-induced detubulation. Am. J. Physiol. - Hear. Circ. Physiol. 277, H603–H609.

Kawakami, M., Okabe, E., 1998. Superoxide anion radical-triggered Ca2+ release from cardiac sarcoplasmic reticulum through ryanodine receptor Ca2+ channel. Mol. Pharmacol. 53, 497–503.

Kléber, A.G., Rudy, Y., 2004. Basic Mechanisms of Cardiac Impulse Propagation and

Associated Arrhythmias. Physiol. Rev. 84, 431–488.

Kleiman, R.B., Houser, S.R., 1988. Electrophysiologic and mechanical properties of single feline RV and LV myocytes. J. Mol. Cell. Cardiol. 20, 973–982.

Klugbauer, N., Marais, E., Hofmann, F., 2003. Calcium Channel α2δ Subunits: Differential Expression, Function, and Drug Binding. J. Bioenerg. Biomembr.

Knollmann, B.C., Katchman, A.N., Franz, M.R., 2001. Monophasic action potential recordings from intact mouse heart: Validation, regional heterogeneity, and relation to refractoriness. J. Cardiovasc. Electrophysiol. 12, 1286–1294.

Knollmann, B.C., Schober, T., Petersen, A.O., Sirenko, S.G., Franz, M.R., 2007. Action potential characterization in intact mouse heart: steady-state cycle length dependence and electrical restitution. Am. J. Physiol. Circ. Physiol. 292, H614–H621.

Kohlhaas, M., Zhang, T., Seidler, T., Zibrova, D., Dybkova, N., Steen, A., Wagner, S., Chen, L., Brown, J.H., Bers, D.M., Maier, L.S., 2006. Increased sarcoplasmic reticulum calcium leak but unaltered contractility by acute CaMKII overexpression in isolated rabbit cardiac myocytes. Circ. Res. 98, 235–244.

Kokubun, S., Reuter, H., 1984. Dihydropyridine derivatives prolong the open state of Ca channels in cultured cardiac cells. Proc. Natl. Acad. Sci. U. S. A. 81, 4824–4827.

Kolstad, T.R., van den Brink, J., Macquaide, N., Lunde, P.K., Frisk, M., Aronsen, J.M., Norden, E.S., Cataliotti, A., Sjaastad, I., Sejersted, O.M., Edwards, A.G., Lines, G.T., Louch, W.E., 2018. Ryanodine receptor dispersion disrupts Ca 2+ release in failing cardiac myocytes. Elife 7, 1–24.

Kondo, R.P., Dederko, D.A., Teutsch, C., Chrast, J., Catalucci, D., Chien, K.R., Giles, W.R., 2006. Comparison of contraction and calcium handling between right and left ventricular myocytes from adult mouse heart: a role for repolarization waveform. J. Physiol. 571, 131–146.

Konopelski, P., Ufnal, M., 2016. Electrocardiography in rats: a comparison to human. Physiol. Res. 65, 717–725.

Korchev, Y.E., Bashford, C.L., Milovanovic, M., Vodyanoy, I., Lab, M.J., 1997. Scanning ion conductance microscopy of living cells. Biophys. J. 73, 653–658.

Koschak, A., Obermair, G.J., Pivotto, F., Sinnegger-Brauns, M.J., Striessnig, J., Pietrobon, D., 2007. Molecular nature of anomalous L-type calcium channels in mouse

cerebellar granule cells. J. Neurosci. 27, 3855–3863.

Kuramochi, T., Honda, M., Tanaka, K., Enornoto, K. -i, Hashimoto, M., Morioka, S., 1994. Calcium Transients in Single Myocytes and Membranous Ultrastructures During the Development of Cardiac Hypertrophy and Heart Failure in Rats. Clin. Exp. Pharmacol. Physiol. 21, 1009–1018.

La Vecchia, L., Zanolla, L., Varotto, L., Bonanno, C., Spadaro, G.L., Ometto, R., Fontanelli, A., 2001. Reduced right ventricular ejection fraction as a marker for idiopathic dilated cardiomyopathy compared with ischemic left ventricular dysfunction. Am. Heart J. 142, 181–189.

Lacerda, A.E., Kim, H.S., Ruth, P., Perez-Reyes, E., Flockerzi, V., Hofmann, F., Birnbaumer, L., Brown, A.M., 1991. Normalization of current kinetics by interaction between the α1 and β subunits of the skeletal muscle dihydropyridine-sensitive Ca2+ channel. Nature 352, 527–530.

Lacinová, L., Ludwig, A., Bosse, E., Flockerzi, V., Hofmann, F., 1995. The block of the expressed L-type calcium channel is modulated by the β 3 subunit. FEBS Lett. 373, 103–107.

Lahouratate, P., Guibert, J., Camelin, J.C., Bertrand, I., 1997. Specific inhibition of cardiac and skeletal muscle sarcoplasmic reticulum Ca2+ pumps by H-89. Biochem. Pharmacol. 54, 991–8.

Lambermont, B., Ghuysen, A., Kolh, P., Tchana-Sato, V., Segers, P., Gérard, P., Morimont, P., Magis, D., Dogné, J.M., Masereel, B., D'Orio, V., 2003. Effects of endotoxic shock on right ventricular systolic function and mechanical efficiency. Cardiovasc. Res. 59, 412–418.

Lamberts, R.R., Vaessen, R.J., Westerhof, N., Stienen, G.J.M., 2007. Right ventricular hypertrophy causesimpairment of left ventricular diastolicfunction in the rat. Basic Res. Cardiol. 102, 19–27.

Lanner, J.T., Georgiou, D.K., Joshi, A.D., Hamilton, S.L., 2010. Ryanodine receptors: structure, expression, molecular details, and function in calcium release. Cold Spring Harb. Perspect. Biol. 2.

Larose, E., Ganz, P., Reynolds, H.G., Dorbala, S., Di Carli, M.F., Brown, K.A., Kwong, R.Y., 2007. Right Ventricular Dysfunction Assessed by Cardiovascular Magnetic

Resonance Imaging Predicts Poor Prognosis Late After Myocardial Infarction. J. Am. Coll. Cardiol. 49, 855–862.

Laver, D.R., Baynes, T.M., Dulhunty, A.F., 1997. Magnesium inhibition of ryanodine-receptor calcium channels: evidence for two independent mechanisms. J. Membr. Biol. 156, 213–29.

Lee, K.S., 1987. Potentiation of the calcium-channel currents of internally perfused mammalian heart cells by repetitive depolarization. Proc. Natl. Acad. Sci. U. S. A. 84, 3941–3945.

Lehnart, S.E., Wehrens, X.H.T., Reiken, S., Warrier, S., Belevych, A.E., Harvey, R.D., Richter, W., Jin, S.L.C., Conti, M., Marks, A.R., 2005. Phosphodiesterase 4D deficiency in the ryanodine-receptor complex promotes heart failure and arrhythmias. Cell 123, 25–35.

Lenaerts, I., Bito, V., Heinzel, F.R., Driesen, R.B., Holemans, P., D'Hooge, J., Heidbüchel, H., Sipido, K.R., Willems, R., 2009. Ultrastructural and functional remodeling of the coupling between Ca 2+ influx and sarcoplasmic reticulum Ca 2+ release in right atrial myocytes from experimental persistent atrial fibrillation. Circ. Res. 105, 876–885.

LeWinter, M.M., VanBuren, P., 2002. Myofilament remodeling during the progression of heart failure. In: Journal of Cardiac Failure. Churchill Livingstone Inc.

Lichter, J.G., Carruth, E., Mitchell, C., Barth, A.S., Aiba, T., Kass, D.A., Tomaselli, G.F., Bridge, J.H., Sachse, F.B., 2014. Remodeling of the sarcomeric cytoskeleton in cardiac ventricular myocytes during heart failure and after cardiac resynchronization therapy. J. Mol. Cell. Cardiol. 72, 186–95.

Lindsey, M.L., Bolli, R., Canty, J.M., Du, X.J., Frangogiannis, N.G., Frantz, S., Gourdie, R.G., Holmes, J.W., Jones, S.P., Kloner, R.A., Lefer, D.J., Liao, R., Murphy, E., Ping, P., Przyklenk, K., Recchia, F.A., Longacre, L.S., Ripplinger, C.M., Van Eyk, J.E., Heusch, G., 2018. Guidelines for experimental models of myocardial ischemia and infarction. Am. J. Physiol. - Hear. Circ. Physiol.

Linnenbank, A.C., de Bakker, J.M.T., Coronel, R., 2014. How to measure propagation velocity in cardiac tissue: a simulation study. Front. Physiol. 5, 267.

Liu, Z., Hilbelink, D.R., Crockett, W.B., Gerdes, A.M., 1991. Regional changes in

hemodynamics and cardiac myocyte size in rats with aortocaval fistulas: 1. Developing and established hypertrophy. Circ. Res. 69, 52–58.

Llach, A., Molina, C.E., Prat-Vidal, C., Fernandes, J., Casad, V., Ciruela, F., Llus, C., Franco, R., Cinca, J., Hove-Madsen, L., 2011. Abnormal calcium handling in atrial fibrillation is linked to up-regulation of adenosine A 2A receptors. Eur. Heart J. 32, 721–729.

Lochner, A., Moolman, J.A., 2006. The Many Faces of H89. Cardiovasc. Drug Rev. 24, 261–274.

Long, C.S., Ordahi, C.P., Simpson, P.C., 1989. α1-Adrenergic receptor stimulation of sarcomeric actin isogene transcription in hypertrophy of cultured rat heart muscle cells. J. Clin. Invest. 83, 1078–1082.

Louch, W.E., Bito, V., Heinzel, F.R., Macianskiene, R., Vanhaecke, J., Flameng, W., Mubagwa, K., Sipido, K.R., 2004. Reduced synchrony of Ca2+ release with loss of T-tubules - A comparison to Ca2+ release in human failing cardiomyocytes. Cardiovasc. Res. 62, 63–73.

Louch, W.E., Mørk, H.K., Sexton, J., Strømme, T.A., Laake, P., Sjaastad, I., Sejersted, O.M., 2006. T-tubule disorganization and reduced synchrony of Ca2+ release in murine cardiomyocytes following myocardial infarction. J. Physiol. 574, 519–533.

Louch, W.E., Sejersted, O.M., Swift, F., 2010. There goes the neighborhood: Pathological alterations in T-tubule morphology and consequences for cardiomyocyte Ca2+ handling. J. Biomed. Biotechnol. 503906.

Louch, W.E., Sheehan, K.A., Wolska, B.M., 2011. Methods in cardiomyocyte isolation, culture, and gene transfer. J. Mol. Cell. Cardiol.

Lowes, B.D., Minobe, W., Abraham, W.T., Rizeq, M.N., Bohlmeyer, T.J., Quaife, R.A., Roden, R.L., Dutcher, D.L., Robertson, A.O., Voelkel, N.F., Badesch, D.B., Groves, B.M., Gilbert, E.M., Bristow, M.R., 1997. Changes in gene expression in the intact human heart: Downregulation of α-myosin heavy chain in hypertrophied, failing ventricular myocardium. J. Clin. Invest. 100, 2315–2324.

Lu, X., Ginsburg, K.S., Kettlewell, S., Bossuyt, J., Smith, G.L., Bers, D.M., 2013. Online Supplement for Local Gradients of Intra-Mitochondrial [Ca] in Cardiac Myocytes during SR Ca Release Online Supplement for Local Gradients of Intra-Mitochondrial

[Ca] in Cardiac Myocytes during SR Ca Release. Circ. Res. 112, 424–431.

Lue, W.M., Boyden, P.A., 1992. Abnormal electrical properties of myocytes from chronically infarcted canine heart: Alterations in V̇max and the transient outward current. Circulation 85, 1175–1188.

Lukas, A., Antzelevitch, C., 1989. Reflected reentry, delayed conduction, and electrotonic inhibition in segmentally depressed atrial tissues. Can. J. Physiol. Pharmacol. 67, 757–764.

Lukas, A., Antzelevitch, C., 1996. Phase 2 reentry as a mechanism of initiation of circus movement reentry in canine epicardium exposed to simulated ischemia. Cardiovasc. Res. 32, 593–603.

Lukyanenko, V., Ziman, A., Lukyanenko, A., Salnikov, V., Lederer, W.J., 2007. Functional groups of ryanodine receptors in rat ventricular cells. J. Physiol. 583, 251–269.

Luss, I., Boknik, P., Jones, L.R., Kirchhefer, U., Knapp, J., Linck, B., Lüss, H., Meissner, A., Müller, F.U., Schmitz, W., Vahlensieck, U., Neumann, J., 1999. Expression of cardiac calcium regulatory proteins in atrium v ventricle in different species. J. Mol. Cell. Cardiol. 31, 1299–1314.

Luttrell, L.M., Lefkowitz, R.J., 2002. The role of β-arrestins in the termination and transduction of G-protein-coupled receptor signals. J. Cell Sci. 115, 455–465.

Lyon, A.R., MacLeod, K.T., Zhang, Y., Garcia, E., Kanda, G.K., Lab, M.J., Korchev, Y.E., Harding, S.E., Gorelik, J., 2009. Loss of T-tubules and other changes to surface topography in ventricular myocytes from failing human and rat heart. Proc. Natl. Acad. Sci. 106, 6854–6859.

Machackova, J., Barta, J., Dhalla, N.S., 2006. Myofibrillar remodelling in cardiac hypertrophy, heart failure and cardiomyopathies. Can. J. Cardiol.

Mackenzie, L., Roderick, H.L., Berridge, M.J., Conway, S.J., Bootman, M.D., 2004. The spatial pattern of atrial cardiomyocyte calcium signalling modulates contraction. J. Cell Sci. 117, 6327–6337.

Macquaide, N., Tuan, H.T.M., Hotta, J.I., Sempels, W., Lenaerts, I., Holemans, P., Hofkens, J., Jafri, M.S., Willems, R., Sipido, K.R., 2015. Ryanodine receptor cluster fragmentation and redistribution in persistent atrial fibrillation enhance calcium

release. Cardiovasc. Res. 108, 387–398.

Maier, L.S., Bers, D.M., 2002. Calcium, calmodulin, and calcium-calmodulin kinase II: Heartbeat to heartbeat and beyond. J. Mol. Cell. Cardiol. 34, 919–939.

Maier, L.S., Zhang, T., Chen, L., DeSantiago, J., Brown, J.H., Bers, D.M., 2003. Transgenic CaMKIIδc overexpression uniquely alters cardiac myocyte Ca2+ handling: Reduced SR Ca2+ load and activated SR Ca2+ release. Circ. Res. 92, 904–911.

Manders, E.M.M., Verbeek, F.J., Aten, J.A., 1993. Measurement of co-localization of objects in dual-colour confocal images. J. Microsc. 169, 375–382.

Marengo, J.J., Hidalgo, C., Bull, R., 1998. Sulfhydryl oxidation modifies the calcium dependence of ryanodine-sensitive calcium channels of excitable cells. Biophys. J. 74, 1263–77.

Martin, C.A., Siedlecka, U., Kemmerich, K., Lawrence, J., Cartledge, J., Guzadhur, L., Brice, N., Grace, A.A., Schwiening, C., Terracciano, C.M., Huang, C.L.H., 2012. Reduced Na+ and higher K+ channel expression and function contribute to right ventricular origin of arrhythmias in Scn5a+/2 mice. Open Biol. 2, A2–A3.

Mattocks, A.R., Legg, R.F., Jukes, R., 1990. Trapping of short-lived electrophilic metabolites of pyrrolizidine alkaloids escaping from perfused rat liver. Toxicol. Lett. 54, 93–99.

Maughan, W.L., Shoukas, A.A., Sagawa, K., Weisfeldt, M.L., 1979. Instantaneous pressure-volume relationship of the canine right ventricle. Circ. Res. 44, 309–315.

Mcdonald, T.F., Pelzer, S., Trautwein, W., Pelzer, D.J., 1994. Regulation and modulation of calcium channels in cardiac, skeletal, and smooth muscle cells. Physiol. Rev. 74, 365–507.

Mcintosh, M.A., Cobbe, S.M., Smith, G.L., 2000. Heterogeneous changes in action potential and intracellular Ca in left ventricular myocyte sub-types from rabbits with heart failure, Cardiovascular Research.

Mckee, P.A., Castelli, W.P., Mcnamara, P.M., Kannel, W.B., 1971. The Natural History of Congestive Heart Failure: The Framingham Study. N. Engl. J. Med. 285, 1441–1446.

Meissner, G., 1984. Adenine nucleotide stimulation of Ca2+-induced Ca2+ release in sarcoplasmic reticulum. J. Biol. Chem. 259, 2365–2374.

Meissner, G., 1986. Ryanodine activation and inhibition of the Ca2+ release channel of sarcoplasmic reticulum. J. Biol. Chem. 261, 6300–6306.

Meissner, G., Henderson, J.S., 1987. Rapid calcium release from cardiac sarcoplasmic reticulum vesicles is dependent on Ca2+ and is modulated by Mg2+, adenine nucleotide, and calmodulin. J. Biol. Chem. 262, 3065–3073.

Michael, G., Xiao, L., Qi, X.Y., Dobrev, D., Nattel, S., 2009. Remodelling of cardiac repolarization: How homeostatic responses can lead to arrhythmogenesis. Cardiovasc. Res. 81, 491–499.

Mines, G.R., 1913. On dynamic equilibrium in the heart. J. Physiol. 46, 349–383.

Mitra, R., Morad, M., 1986. Two types of calcium channels in guinea pig ventricular myocytes. Proc. Natl. Acad. Sci. U. S. A. 83, 5340–5344.

Mitterdorfer, J., Grabner, M., Kraus, R.L., Bering, S., Prinz, H., Glossmann, H., Striessnig, J., 1998. Molecular Basis of Drug Interaction with L-Ttype Ca 2+ Channels 319–335.

Miyauchi, T., Yorikane, R., Sakai, S., Sakurai, T., Okada, M., Nishikibe, M., Yano, M., Yamaguchi, I., Sugishita, Y., Goto, K., 1993. Contribution of endogenous endothelin-1 to the progression of cardiopulmonary alterations in rats with monocrotaline-induced pulmonary hypertension. Circ. Res. 73, 887–897.

Moe, G.K., 1975. Evidence for reentry as a mechanism of cardiac arrhythmias. Rev. Physiol. Biochem. Pharmacol.

Molina, C.E., Heijman, J., Dobrev, D., 2016. Differences in Left Versus Right Ventricular Electrophysiological Properties in Cardiac Dysfunction and Arrhythmogenesis. Arrhythmia Electrophysiol. Rev. 5, 14–9.

Molina, C.E., Johnson, D.M., Mehel, H., Spätjens, R.L.H.M.G., Mika, D., Algalarrondo, V., Slimane, Z.H., Lechêne, P., Abi-Gerges, N., van der Linde, H.J., Leroy, J., Volders, P.G.A., Fischmeister, R., Vandecasteele, G., 2014. Interventricular differences in β-adrenergic responses in the canine heart: Role of phosphodiesterases. J. Am. Heart Assoc. 3, 10–12.

Morano, I., Hädicke, K., Haase, H., Böhm, M., Erdmann, E., Schaub, M.C., 1997. Changes in essential myosin light chain isoform expression provide a molecular basis for isometric force regulation in the failing human heart. J. Mol. Cell. Cardiol. 29, 1177–1187.

Morano, M., Zacharzowski, U., Maier, M., Lange, P.E., Alexi-Meskishvili, V., Haase, H., Morano, I., 1996. Regulation of human heart contractility by essential myosin light chain isoforms. J. Clin. Invest. 98, 467–473.

Mørk, H.K., Sjaastad, I., Sejersted, O.M., Louch, W.E., 2009. Slowing of cardiomyocyte Ca 2+ release and contraction during heart failure progression in postinfarction mice. Am. J. Physiol. - Hear. Circ. Physiol. 296, H1069-79.

Müller-Strahl, G., Hemker, J., Zimmer, H.G., 2003. Afterload- and preload-dependent interactions in the isolated biventricular working rat heart. Exp. Clin. Cardiol. 7, 180–187.

Munro, M.L., Soeller, C., 2016. Early transverse tubule development begins in utero in the sheep heart. J. Muscle Res. Cell Motil. 37, 195–202.

Murphy, R.M., Mollica, J.P., Beard, N.A., Knollmann, B.C., Lamb, G.D., 2011. Quantification of calsequestrin 2 (CSQ2) in sheep cardiac muscle and Ca2+-binding protein changes in CSQ2 knockout mice. Am. J. Physiol. Heart Circ. Physiol. 300, H595-604.

Näbauer, M., Callewaert, G., Cleemann, L., Morad, M., 1989. Regulation of calcium release is gated by calcium current, not gating charge, in cardiac myocytes. Science 244, 800–3.

Naeije, R., 2005. Pulmonary hypertension and right heart failure in chronic obstructive pulmonary disease. Proc. Am. Thorac. Soc. 2, 20–22.

Naeije, R., Manes, A., 2014. The right ventricle in pulmonary arterial hypertension. Eur. Respir. Rev. 23, 476–487.

Nakai, J., Imagawa, T., Hakamat, Y., Shigekawa, M., Takeshima, H., Numa, S., 1990. Primary structure and functional expression from cDNA of the cardiac ryanodine receptor/calcium release channel. FEBS Lett. 271, 169–77.

Nerbonne, J.M., Kass, R.S., 2005. Molecular physiology of cardiac repolarization. Physiol. Rev. 85, 1205–1253.

Nikolaev, V.O., Moshkov, A., Lyon, A.R., Miragoli, M., Novak, P., Paur, H., Lohse, M.J., Korchev, Y.E., Harding, S.E., Gorelik, J., 2010. β2-adrenergic receptor redistribution in heart failure changes cAMP compartmentation. Science (80-.). 327, 1653–1657.

Nixon, G.F., Mignery, G.A., Somlyo, A. V, 1994. Immunogold localization of inositol

1,4,5-trisphosphate receptors and characterization of ultrastructural features of the sarcoplasmic reticulum in phasic and tonic smooth muscle. J. Muscle Res. Cell Motil. 15, 682–700.

Nogueira-Ferreira, R., Faria-Costa, G., Ferreira, R., Henriques-Coelho, T., Author, C., 2017. Animal Models for the Study of Pulmonary Hypertension: Potential and Limitations. Cardiol. Cardiovasc. Med. 01, 01–22.

Novak, P., Gorelik, J., Vivekananda, U., Shevchuk, A.I., Ermolyuk, Y.S., Bailey, R.J., Bushby, A.J., Moss, G.W.J., Rusakov, D.A., Klenerman, D., Kullmann, D.M., Volynski, K.E., Korchev, Y.E., 2013. Nanoscale-Targeted Patch-Clamp Recordings of Functional Presynaptic Ion Channels. Neuron 79, 1067–1077.

Novak, P., Li, C., Shevchuk, A.I., Stepanyan, R., Caldwell, M., Hughes, S., Smart, T.G., Gorelik, J., Ostanin, V.P., Lab, M.J., Moss, G.W.J., Frolenkov, G.I., Klenerman, D., Korchev, Y.E., 2009. Nanoscale live-cell imaging using hopping probe ion conductance microscopy. Nat. Methods 6, 279–281.

Nuss, H.B., Houser, S.R., 1993. T-type Ca2+ current is expressed in hypertrophied adult feline left ventricular myocytes. Circ. Res. 73, 777–782.

O'Rourke, B., 2008. The ins and outs of calcium in heart failure. Circ. Res. 102, 1301–1303.

Oakley, C., 1988. Importance of right ventricular function in congestive heart failure. Am. J. Cardiol. 62, 14A-19A.

Okamoto, K., Aoki, K., 1963. Development of a strain of spontaneously hypertensive rats. Jpn. Circ. J. 27, 282–293.

Ono, K., Yano, M., Ohkusa, T., Kohno, Masateru, Hisaoka, T., Tanigawa, T., Kobayashi, S., Kohno, Michihuro, Matsuzaki, M., 2000. Altered interaction of FKBP12.6 with ryanodine receptor as a cause of abnormal Ca2+ release in heart failure. Cardiovasc. Res. 48, 323–331.

Otsu, K., Willard, H.F., Khanna, V.K., Zorzato, F., Green, N.M., MacLennan, D.H., 1990. Molecular cloning of cDNA encoding the Ca2+ release channel (Ryanodine receptor) of rabbit cardiac muscle sarcoplasmic reticulum. J. Biol. Chem. 265, 13472–13483.

Pan, L.C., Wilson, D.W., Lame, M.W., Jones, A.D., Segall, H.J., 1993. Cor pulmonale is caused by monocrotaline and dehydromonocrotaline, but not by glutathione or

cysteine conjugates of dihydropyrrolizine. Toxicol. Appl. Pharmacol. 118, 87–97.

Pandit, S. V., Clark, R.B., Giles, W.R., Demir, S.S., 2001. A mathematical model of action potential heterogeneity in adult rat left ventricular myocytes. Biophys. J. 81, 3029–3051.

Pandit, S. V., Jalife, J., 2013. Rotors and the dynamics of cardiac fibrillation. Circ. Res. 112, 849–862.

Patterson, E., Lazzara, R., Szabo, B., Liu, H., Tang, D., Li, Y.H., Scherlag, B.J., Po, S.S., 2006. Sodium-calcium exchange initiated by the Ca2+ transient: An arrhythmia trigger within pulmonary veins. J. Am. Coll. Cardiol. 47, 1196–1206.

Pawlush, D.G., Musch, T.I., Moore, R.L., 1989. Ca2+-dependent heterometric and homeometric autoregulation in hypertrophied rat heart. Am. J. Physiol. - Hear. Circ. Physiol. 256, H1139-47.

Petroff, M.G.V., Kim, S.H., Pepe, S., Dessy, C., Marbán, E., Balligand, J.L., Sollott, S.J., 2001. Endogenous nitric oxide mechanisms mediate the stretch dependence of Ca2+ release in cardiomyocytes. Nat. Cell Biol. 3, 867–873.

Pfeffer, M.A., Pfeffer, J.M., Fishbein, M.C., Fletcher, P.J., Spadaro, J., Kloner, R.A., Braunwald, E., 1979. Myocardial infarct size and ventricular function in rats. Circ. Res. 44, 503–512.

Phillips, D., Aponte, A.M., Covian, R., Neufeld, E., Yu, Z.-X., Balaban, R.S., 2011. Homogenous protein programming in the mammalian left and right ventricle free walls. Physiol. Genomics 43, 1198–206.

Piao, L., Marsboom, G., Archer, S.L., 2010. Mitochondrial metabolic adaptation in right ventricular hypertrophy and failure. J. Mol. Med. 88, 1011–1020.

Picht, E., Zima, A. V., Blatter, L.A., Bers, D.M., 2007. SparkMaster: automated calcium spark analysis with ImageJ. AJP Cell Physiol. 293, C1073–C1081.

Pinali, C., Bennett, H., Davenport, J.B., Trafford, A.W., Kitmitto, A., 2013. Three-dimensional reconstruction of cardiac sarcoplasmic reticulum reveals a continuous network linking transverse-tubules: This organization is perturbed in heart failure. Circ. Res. 113, 1219–1230.

Pitt, G.S., Zühlke, R.D., Hudmon, A., Schulman, H., Reuter, H., Tsien, R.W., 2001. Molecular Basis of Calmodulin Tethering and Ca2+-dependent Inactivation of L-type

Ca2+ Channels. J. Biol. Chem. 276, 30794–30802.

Pitts, B.J., 1979. Stoichiometry of sodium-calcium exchange in cardiac sarcolemmal vesicles. Coupling to the sodium pump. J. Biol. Chem. 254, 6232–5.

Pope, B., Hoh, J.F.Y., Weeds, A., 1980. The ATPase activities of rat cardiac myosin isoenzymes. FEBS Lett. 118, 205–208.

Portman, M.A., Bhat, A.M., Cohen, M.H., Jacobstein, M.D., 1987. Left ventricular systolic circular index: An echocardiographic measure of transseptal pressure ratio. Am. Heart J. 114, 1178–1182.

Postma, A. V., Denjoy, I., Hoorntje, T.M., Lupoglazoff, J.M., Da Costa, A., Sebillon, P., Mannens, M.M.A.M., Wilde, A.A.M., Guicheney, P., 2002. Absence of calsequestrin 2 causes severe forms of catecholaminergic polymorphic ventricular tachycardia. Circ. Res. 91.

Poulet, C., Sanchez-Alonso, J., Swiatlowska, P., Mouy, F., Lucarelli, C., Alvarez-Laviada, A., Gross, P., Terracciano, C., Houser, S., Gorelik, J., 2020. Junctophilin-2 tethers T-tubules and recruits functional L-type calcium channels to lipid rafts in adult cardiomyocytes. Cardiovasc. Res.

Pouleur, H., Lefevre, J., Van Mechelen, H., Charlier, A.A., 1980. Free-wall shortening and relaxation during ejection in the canine right ventricle. Am. J. Physiol. - Hear. Circ. Physiol. 8, H601-13.

Pragnell, M., De Waard, M., Mori, Y., Tanabe, T., Snutch, T.P., Campbell, K.P., 1994. Calcium channel β-subunit binds to a conserved motif in the I-II cytoplasmic linker of the α1-subunit. Nature 368, 67–70.

Price, K.M., Littler, W.A., Cummins, P., 1980. Human atrial and ventricular myosin light-chain subunits in the adult and during development. Biochem. J. 191, 571–580.

Prins, K.W., Tian, L., Wu, D., Thenappan, T., Metzger, J.M., Archer, S.L., 2017. Colchicine depolymerizes microtubules, increases junctophilin-2, and improves right ventricular function in experimental pulmonary arterial hypertension. J. Am. Heart Assoc. 6, e006195.

Puri, T.S., Gerhardstein, B.L., Zhao, X.L., Ladner, M.B., Hosey, M.M., 1997. Differential effects of subunit interactions on protein kinase A- and C- mediated phosphorylation of L-type calcium channels. Biochemistry 36, 9605–9615.

Quaife, R.A., Christian, P.E., Gilbert, E.M., Datz, F.L., Volkman, K., Bristow, M.R., 1998. Effects of carvedilol on right ventricular function in chronic heart failure. Am. J. Cardiol. 81, 247–250.

Ramakers, C., Stengl, M., Spätjens, R.L.H.M.G., Moorman, A.F.M., Vos, M.A., 2005. Molecular and electrical characterization of the canine cardiac ventricular septum. J. Mol. Cell. Cardiol. 38, 153–161.

Ramakers, C., Vos, M.A., Doevendans, P.A., Schoenmakers, M., Wu, Y.S., Scicchitano, S., Iodice, A., Thomas, G.P., Antzelevitch, C., Dumaine, R., 2003. Coordinated down-regulation of KCNQ1 and KCNE1 expression contributes to reduction of IKs in canine hypertrophied hearts. Cardiovasc. Res. 57, 486–496.

Ramos, M., Lamé, M.W., Segall, H.J., Wilson, D.W., 2007. Monocrotaline pyrrole induces Smad nuclear accumulation and altered signaling expression in human pulmonary arterial endothelial cells. Vascul. Pharmacol. 46, 439–448.

Reiken, S., Wehrens, X.H.T., Vest, J.A., Barbone, A., Klotz, S., Mancini, D., Burkhoff, D., Marks, A.R., 2003. B-Blockers Restore Calcium Release Channel Function and Improve Cardiac Muscle Performance in Human Heart Failure. Circulation 107, 2459–2466.

Reuter, H., 1967. The dependence of slow inward current in Purkinje fibres on the extracellular calcium-concentration. J. Physiol. 192, 479–492.

Reynolds, J.O., Quick, A.P., Wang, Q., Beavers, D.L., Philippen, L.E., Showell, J., Barreto-Torres, G., Thuerauf, D.J., Doroudgar, S., Glembotski, C.C., Wehrens, X.H.T., 2016. Junctophilin-2 gene therapy rescues heart failure by normalizing RyR2-mediated Ca2 + release. Int. J. Cardiol. 225, 371–380.

Rich, S., Kaufmann, E., Levy, P.S., 1992. The Effect of High Doses of Calcium-Channel Blockers on Survival in Primary Pulmonary Hypertension. N. Engl. J. Med. 327, 76–81.

Richards, M.A., Clarke, J.D., Saravanan, P., Voigt, N., Dobrev, D., Eisner, D.A., Trafford, A.W., Dibb, K.M., 2011. Transverse tubules are a common feature in large mammalian atrial myocytes including human. Am. J. Physiol. - Hear. Circ. Physiol. 301, 1996–2005.

Riehle, C., Bauersachs, J., 2019. Small animal models of heart failure. Cardiovasc. Res.

Riehle, C., Wende, A.R., Zaha, V.G., Pires, K.M., Wayment, B., Olsen, C., Bugger, H., Buchanan, J., Wang, X., Moreira, A.B., Doenst, T., Medina-Gomez, G., Litwin, S.E., Lelliott, C.J., Vidal-Puig, A., Abel, E.D., 2011. PGC-1β deficiency accelerates the transition to heart failure in pressure overload hypertrophy. Circ. Res. 109, 783–793.

Rocchetti, M., Sala, L., Rizzetto, R., Irene Staszewsky, L., Alemanni, M., Zambelli, V., Russo, I., Barile, L., Cornaghi, L., Altomare, C., Ronchi, C., Mostacciuolo, G., Lucchetti, J., Gobbi, M., Latini, R., Zaza, A., 2014. Ranolazine prevents INaL enhancement and blunts myocardial remodelling in a model of pulmonary hypertension. Cardiovasc. Res. 104, 37–48.

Rosen, M.R., Schwartz, P.J., 1991. The Sicilian Gambit: A New Approach to the Classification of Antiarrhythmic Drugs Based on Their Actions on Arrhythmogenic Mechanisms. Circulation 84, 1831–1851.

Rosenbaum, D.S., Jackson, L.E., Smith, J.M., Garan, H., Ruskin, J.N., Cohen, R.J., 1994. Electrical Alternans and Vulnerability to Ventricular Arrhythmias. N. Engl. J. Med. 330, 235–241.

Rosenberg, R.L., Hess, P., Tsien, R.W., 1988. Cardiac calcium channels in planar lipid bilayers: L-Type Channels and Calcium-permeable Channels Open at Negative Membrane Potentials. J. Gen. Physiol. 92, 27–54.

Rosenkranz, S., Gibbs, J.S.R., Wachter, R., De Marco, T., Vonk-Noordegraaf, A., Vachiéry, J.L., 2016. Left ventricular heart failure and pulmonary hypertension. Eur. Heart J. 37, 942–954.

Rossi, S., Baruffi, S., Bertuzzi, A., Miragoli, M., Corradi, D., Maestri, R., Alinovi, R., Mutti, A., Musso, E., Sgoifo, A., Brisinda, D., Fenici, R., Macchi, E., 2008. Ventricular activation is impaired in aged rat hearts. Am. J. Physiol. Circ. Physiol. 295, H2336–H2347.

Rougier, J.S., Abriel, H., 2016. Cardiac voltage-gated calcium channel macromolecular complexes. Biochim. Biophys. Acta - Mol. Cell Res. 1863, 1806–1812.

Rousseau, E., Smith, J.S., Meissner, G., 1987. Ryanodine modifies conductance and gating behavior of single Ca2+ release channel. Am. J. Physiol. 253, C364-8.

Rozanski, G.J., Jalife, J., Moe, G.K., 1984. Reflected reentry in nonhomogeneous ventricular muscle as a mechanism of cardiac arrhythmias. Circulation 69, 163–173.

Rubart, M., Zipes, D.P., 2005. Mechanisms of sudden cardiac death. J. Clin. Invest.

Ruiter, G., De Man, F.S., Schalij, I., Sairras, S., Grúnberg, K., Westerhof, N., Van Der Laarse, W.J., Vonk-Noordegraaf, A., 2013. Reversibility of the monocrotaline pulmonary hypertension rat model. Eur. Respir. J. 42, 553–556.

Ryan, J., Bloch, K., Archer, S.L., 2011. Rodent models of pulmonary hypertension: Harmonisation with the world health organisation's categorisation of human PH. Int. J. Clin. Pract.

Ryan, J.J., Marsboom, G., Archer, S.L., 2013. Rodent Models of Group 1 Pulmonary Hypertension. pp. 105–149.

Sabourin, J., Boet, A., Rucker-Martin, C., Lambert, M., Gomez, A.M., Benitah, J.P., Perros, F., Humbert, M., Antigny, F., 2018. Ca2+ handling remodeling and STIM1L/Orai1/TRPC1/TRPC4 upregulation in monocrotaline-induced right ventricular hypertrophy. J. Mol. Cell. Cardiol. 118, 208–224.

Sahara, M., Sata, M., Morita, T., Nakamura, K., Hirata, Y., Nagai, R., 2007. Diverse contribution of bone marrow-derived cells to vascular remodeling associated with pulmonary arterial hypertension and arterial neointimal formation. Circulation 115, 509–517.

Salamon, J.N., Kelesidis, I., Msaouel, P., Mazurek, J.A., Mannem, S., Adzic, A., Zolty, R., 2014. Outcomes in world health organization group II pulmonary hypertension: Mortality and readmission trends with systolic and preserved ejection fraction-induced pulmonary hypertension. J. Card. Fail. 20, 467–475.

Sambi, M.P., White, F.N., 1960. The electrocardiogram of the normal and hypertensive rat. Circ. Res. 8, 129–134.

Samsó, M., Feng, W., Pessah, I.N., Allen, P.D., 2009. Coordinated Movement of Cytoplasmic and Transmembrane Domains of RyR1 upon Gating. PLoS Biol. 7, e1000085.

Sanchez-Alonso, J.L., Bhargava, A., O'Hara, T., Glukhov, A. V., Schobesberger, S., Bhogal, N., Sikkel, M.B., Mansfield, C., Korchev, Y.E., Lyon, A.R., Punjabi, P.P., Nikolaev, V.O., Trayanova, N.A., Gorelik, J., Hara, T.O., Glukhov, A. V., Bhogal, N., Sikkel, M.B., Mansfield, C., Korchev, Y.E., Punjabi, P.P., Nikolaev, V.O., Trayanova, N.A., Gorelik, J., O'Hara, T., Glukhov, A. V., Schobesberger, S., Bhogal,

N., Sikkel, M.B., Mansfield, C., Korchev, Y.E., Lyon, A.R., Punjabi, P.P., Nikolaev, V.O., Trayanova, N.A., Gorelik, J., 2016. Microdomain-Specific Modulation of L-Type Calcium Channels Leads to Triggered Ventricular Arrhythmia in Heart Failure. Circ. Res. 119, 944–945.

Sanchez-Alonso, J.L., Schobesberger, S., Poulet, C.E., Bhogal, N., Chowdhury, R., Gorelik, J., 2018. Function of L-Type Calcium Channel Microdomain in Human Myocytes from Hearts with Ischemic versus Dilated Cardiomyopathies. Biophys. J. 114, 638a.

Sanchez-Quintana, D., Garcia-Martinez, V., Hurle, J.M., 1990. Myocardial fiber architecture in the human heart. Anatomical demonstration of modifications in the normal pattern of ventricular fiber architecture in a malformed adult specimen. Acta Anat. (Basel). 138, 352–8.

Sandoval, J., Bauerle, O., Palomar, A., Gómez, A., Martínez-Guerra, M.L., Beltrán, M., Guerrero, M.L., 1994. Survival in primary pulmonary hypertension. Validation of a prognostic equation. Circulation 89, 1733–44.

Sarnoff, S.J., Braunwald, E., Welch, G.H., Case, R.B., Stainsby, W.N., Macruz, R., 1958. Hemodynamic determinants of oxygen consumption of the heart with special reference to the tension-time index. Am. J. Physiol. 192, 148–156.

Sathish, V., Xu, A., Karmazyn, M., Sims, S.M., Narayanan, N., 2006. Mechanistic basis of differences in Ca2+ -handling properties of sarcoplasmic reticulum in right and left ventricles of normal rat myocardium. Am. J. Physiol. Heart Circ. Physiol. 291, H88-96.

Sato, P.Y., Chuprun, J.K., Schwartz, M., Koch, W.J., 2015. The evolving impact of g protein-coupled receptor kinases in cardiac health and disease. Physiol. Rev. 95, 377–404.

Saucerman, J.J., Bers, D.M., 2008. Calmodulin mediates differential sensitivity of CaMKII and calcineurin to local Ca2+ in cardiac myocytes. Biophys. J. 95, 4597–4612.

Savi, M., Bocchi, L., Rossi, S., Frati, C., Graiani, G., Lagrasta, C., Miragoli, M., Di Pasquale, E., Stirparo, G.G., Mastrototaro, G., Urbanek, K., De Angelis, A., Macchi, E., Stilli, D., Quaini, F., Musso, E., 2016. Antiarrhythmic effect of growth factor-supplemented cardiac progenitor cells in chronic infarcted heart. Am. J. Physiol. Circ. Physiol. 310, H1622–H1648.

Schaper, J., Kostin, S., Hein, S., Elsässer, A., Arnon, E., Zimmermann, R., 2002. Structural remodelling in heart failure. Exp. Clin. Cardiol. 7, 64–8.

Schaub, M.C., Hefti, M.A., Zuellig, R.A., Morano, I., 1998. Modulation of contractility in human cardiac hypertrophy by myosin essential light chain isoforms. Cardiovasc. Res.

Schindelin, J., Arganda-Carreras, I., Frise, E., Kaynig, V., Longair, M., Pietzsch, T., Preibisch, S., Rueden, C., Saalfeld, S., Schmid, B., Tinevez, J.Y., White, D.J., Hartenstein, V., Eliceiri, K., Tomancak, P., Cardona, A., 2012. Fiji: An open-source platform for biological-image analysis. Nat. Methods 9, 676–682.

Schobesberger, S., Wright, P., Tokar, S., Bhargava, A., Mansfield, C., Glukhov, A. V., Poulet, C., Buzuk, A., Monszpart, A., Sikkel, M., Harding, S.E., Nikolaev, V.O., Lyon, A.R., Gorelik, J., 2017. T-tubule remodelling disturbs localized β2-adrenergic signalling in rat ventricular myocytes during the progression of heart failure. Cardiovasc. Res. 113, 770–782.

Schunkert, H., Dzau, V.J., Tang, S.S., Hirsch, A.T., Apstein, C.S., Lorell, B.H., 1990. Increased rat cardiac angiotensin converting enzyme activity and mRNA expression in pressure overload left ventricular hypertrophy: Effects on coronary resistance, contractility, and relaxation. J. Clin. Invest. 86, 1913–1920.

Schwarzer, M., Osterholt, M., Lunkenbein, A., Schrepper, A., Amorim, P., Doenst, T., 2014. Mitochondrial reactive oxygen species production and respiratory complex activity in rats with pressure overload-induced heart failure. J. Physiol. 592, 3767–3782.

Scoote, M., Poole-Wilson, P.A., Williams, A.J., 2003. The therapeutic potential of new insights into myocardial excitation-contraction coupling. Heart 89, 371–376.

Scriven, D.R.L., Agnieszka, K., Lee, K., Moore, E., 2002. The molecular architecture of calcium microdomains in rat cardiomyocytes. Ann. New York Acad. Sci. 976, 488–499.

Scriven, D.R.L., Asghari, P., Schulson, M.N., Moore, E.D.W., 2010. Analysis of Cav1.2 and ryanodine receptor clusters in rat ventricular myocytes. Biophys. J. 99, 3923–3929.

Scriven, D.R.L., Dan, P., Moore, E.D.W., 2000. Distribution of proteins implicated in

excitation-contraction coupling in rat ventricular myocytes. Biophys. J. 79, 2682–2691.

Scriven, D.R.L., Klimek, A., Asghari, P., Bellve, K., Moore, E.D.W., 2005. Caveolin-3 is adjacent to a group of extradyadic ryanodine receptors. Biophys J 89, 1893–1901.

Seidel, T., Sankarankutty, A.C., Sachse, F.B., 2017. Remodeling of the transverse tubular system after myocardial infarction in rabbit correlates with local fibrosis: A potential role of biomechanics. Prog. Biophys. Mol. Biol. 130, 302–314.

Sengupta, P.P., Tajik, A.J., Chandrasekaran, K., Khandheria, B.K., 2008. Twist Mechanics of the Left Ventricle. Principles and Application. JACC Cardiovasc. Imaging 1, 366–376.

Serysheva, I.I., Ludtke, S.J., Baker, M.L., Cong, Y., Topf, M., Eramian, D., Sali, A., Hamilton, S.L., Chiu, W., 2008. Subnanometer-resolution electron cryomicroscopy-based domain models for the cytoplasmic region of skeletal muscle RyR channel. Proc. Natl. Acad. Sci. U. S. A. 105, 9610–5.

Shannon, T.R., Bers, D.M., 2004. Integrated Ca2+ management in cardiac myocytes. In: Annals of the New York Academy of Sciences. New York Academy of Sciences, pp. 28–38.

Shaver, J.A., Nadolny, R.A., O'Toole, J.D., Thompson, M.E., Reddy, P.S., Leon, D.F., Curtiss, E.I., 1974. Sound pressure correlates of the second heart sound. An intracardiac sound study. Circulation 49, 316–325.

Sheehan, K.A., Zima, A. V., Blatter, L.A., 2006. Regional differences in spontaneous Ca2+ sark activity and regulation in cat atrial myocytes. J. Physiol. 572, 799–809.

Shibata, E.F., Brown, T.L.Y., Washburn, Z.W., Bai, J., Revak, T.J., Butters, C.A., 2006. Autonomic regulation of voltage-gated cardiac ion channels. J. Cardiovasc. Electrophysiol. 17, 34–42.

Shistik, E., Ivanina, T., Puri, T., Hosey, M., Dascal, N., 1995. Ca2+ current enhancement by alpha 2/delta and beta subunits in Xenopus oocytes: contribution of changes in channel gating and alpha 1 protein level. J. Physiol. 489, 55–62.

Shou, W., Aghdasi, B., Armstrong, D.L., Guo, Q., Bao, S., Charng, M.J., Mathews, L.M., Schneider, M.D., Hamilton, S.L., Matzuk, M.M., 1998. Cardiac defects and altered ryanodine receptor function in mice lacking FKBP 12. Nature 391, 489–492.

Sicard, P., Jouitteau, T., Andrade-Martins, T., Massad, A., de Araujo, G.R., David, H., Miquerol, L., Colson, P., Richard, S., 2019. Right coronary artery ligation in mice: a novel method to investigate right ventricular dysfunction and biventricular interaction. Am. J. Physiol. - Hear. Circ. Physiol. 316, H684–H692.

Sikkel, M.B., Kumar, S., Maioli, V., Rowlands, C., Gordon, F., Harding, S.E., Lyon, A.R., Macleod, K.T., Dunsby, C., 2016. High speed sCMOS-based oblique plane microscopy applied to the study of calcium dynamics in cardiac myocytes. J. Biophotonics 9, 311–323.

Silverthorn, D.U., 2009. Human Physiology: An Integrated Approach (4 ed), Regulation. Pearson Education.

Simonneau, G., Robbins, I.M., Beghetti, M., Channick, R.N., Delcroix, M., Denton, C.P., Elliott, C.G., Gaine, S.P., Gladwin, M.T., Jing, Z.-C., Krowka, M.J., Langleben, D., Nakanishi, N., Souza, R., 2009. Pulmonary Hypertension Classification. J. Am. Coll. Cardiol. 54, S43-54.

Singer, D., Biel, M., Lotan, I., Flockerzi, V., Hofmann, F., Dascal, N., 1991. The roles of the subunits in the function of the calcium channel. Science (80-.). 253, 1553–1557.

Singh, J.K., Barsegyan, V., Bassi, N., Marszalec, W., Tai, S., Mothkur, S., Mulla, M., Nico, E., Shiferaw, Y., Aistrup, G.L., Wasserstrom, J.A., 2017. T-tubule remodeling and increased heterogeneity of calcium release during the progression to heart failure in intact rat ventricle. Physiol. Rep. 5.

Sitbon, O., Humbert, M., Jaïs, X., Ioos, V., Hamid, A.M., Provencher, S., Garcia, G., Parent, F., Hervé, P., Simonneau, G., 2010. Long-term response to calcium-channel blockers in non-idiopathic pulmonary arterial hypertension. Eur. Heart J. 31, 1898–1907.

Sitsapesan, R., Williams, A.J., 1995. The gating of the sheep skeletal sarcoplasmic reticulum Ca2+-release channel is regulated by luminal Ca2+. J. Membr. Biol. 146, 133–144.

Sjaastad, I., Wasserstrom, J.A., Sejersted, O.M., 2003. Heart failure - A challenge to our current concepts of excitation-contraction coupling. J. Physiol. 546, 33–48.

Slupsky, J.R., Ohnishi, M., Carpenter, M.R., Reithmeier, R.A.F., 1987. Characterization of Cardiac Calsequestrin. Biochemistry 26, 6539–6544.

Smith, J.S., Rousseau, E., Meissner, G., 1989. Calmodulin modulation of single sarcoplasmic reticulum Ca2+-release channels from cardiac and skeletal muscle. Circ. Res. 64, 352–9.

Smyrnias, I., Mair, W., Harzheim, D., Walker, S.A., Roderick, H.L., Bootman, M.D., 2010. Comparison of the T-tubule system in adult rat ventricular and atrial myocytes, and its role in excitation-contraction coupling and inotropic stimulation. Cell Calcium 47, 210–23.

Soeller, C., Cannell, M.B., 1999. Examination of the transverse tubular system in living cardiac rat myocytes by 2-photon microscopy and digital image-processing techniques. Circ. Res. 84, 266–275.

Soeller, C., Crossman, D., Gilbert, R., Cannell, M.B., 2007. Analysis of ryanodine receptor clusters in rat and human cardiac myocytes. Proc. Natl. Acad. Sci. U. S. A. 104, 14958–63.

Solaro, R.J., Stull, J.T., 2011. Thematic minireview series on signaling in cardiac sarcomeres in health and disease. J. Biol. Chem. 286, 9895.

Song, K.S., Scherer, P.E., Tang, Z., Okamoto, T., Li, S., Chafel, M., Chu, C., Kohtz, D.S., Lisanti, M.P., 1996. Expression of Caveolin-3 in Skeletal, Cardiac, and Smooth Muscle Cells. J. Biol. Chem. 271, 15160–15165.

Song, L.-S., Sobie, E.A., McCulle, S., Lederer, W.J., Balke, C.W., Cheng, H., 2006. Orphaned ryanodine receptors in the failing heart. Proc. Natl. Acad. Sci. 103, 4305–4310.

Song, L.S., Pi, Y.Q., Kim, S.J., Yatani, A., Guatimosim, S., Kudej, R.K., Zhang, Q., Cheng, H., Hittinger, L., Ghaleh, B., Vatner, D.E., Lederer, W.J., Vatner, S.F., 2005. Paradoxical cellular Ca2+ signaling in severe but compensated canine left ventricular hypertrophy. Circ. Res. 97, 457–464.

Sonnenblick, E.H., Ross, J., Covell, J.W., Spotnitz, H.M., Spiro, D., 1967. The ultrastructure of the heart in systole and diastole. Chantes in sarcomere length. Circ. Res. 21, 423–431.

Stefanon, I., Valero-Muñoz, M., Fernandes, A.A., Ribeiro, R.F., Rodríguez, C., Miana, M., Martínez-González, J., Spalenza, J.S., Lahera, V., Vassallo, P.F., Cachofeiro, V., 2013. Left and Right Ventricle Late Remodeling Following Myocardial Infarction in

Rats. PLoS One 8, e64986.

Stobierska-Dzierzek, B., Awad, H., Michler, R.E., 2001. The evolving management of acute right-sided heart failure in cardiac transplant recipients. J. Am. Coll. Cardiol. 38, 923–931.

Stølen, T.O., Høydal, M.A., Kemi, O.J., Catalucci, D., Ceci, M., Aasum, E., Larsen, T., Rolim, N., Condorelli, G., Smith, G.L., Wisløff, U., 2009. Interval training normalizes cardiomyocyte function, diastolic Ca 2+ control, and SR Ca2+ release synchronicity In a mouse model of diabetic cardiomyopathy. Circ. Res. 105, 527–536.

Stones, R., Benoist, D., Peckham, M., White, E., 2013. Microtubule proliferation in right ventricular myocytes of rats with monocrotaline-induced pulmonary hypertension. J. Mol. Cell. Cardiol. 56, 91–96.

Stoyanovsky, D., Murphy, T., Anno, P.R., Kim, Y.M., Salama, G., 1997. Nitric oxide activates skeletal and cardiac ryanodine receptors. Cell Calcium 21, 19–29.

Subias, P.E., Galiè, N., Subias, P.E., 2016. 015 ESC/ERS Guidelines for the Diagnosis and Treatment of Pulmonary Hypertension. Rev. Esp. Cardiol. 69, 102–108.

Subramanian, S., Viatchenko-Karpinski, S., Lukyanenko, V., Györke, S., Wiesner, T.F., 2001. Underlying mechanisms of symmetric calcium wave propagation in rat ventricular myocytes. Biophys. J. 80, 1–11.

Suematsu, N., Satoh, S., Kinugawa, S., Tsutsui, H., Hayashidani, S., Nakamura, R., Egashira, K., Makino, N., Takeshita, A., 2001. α1-adrenoceptor-Gq-RhoA signaling is upregulated to increase myofibrillar Ca2+ sensitivity in failing hearts. Am. J. Physiol. - Hear. Circ. Physiol. 281.

Suga, H., 2003. Cardiac Energetics : Sence And Nonsence. Clin. Exp. Pharmacol. Physiol. 30, 598–585.

Sun Park, W., Kyoung Son, Y., Kim, N., Boum Youm, J., Joo, H., Warda, M., Ko, J.H., Earm, Y.E., Han, J., 2006. The protein kinase A inhibitor, H-89, directly inhibits KATP and Kir channels in rabbit coronary arterial smooth muscle cells. Biochem. Biophys. Res. Commun. 340, 1104–1110.

Swift, F., Franzini-Armstrong, C., Oyehaug, L., Enger, U.H., Andersson, K.B., Christensen, G., Sejersted, O.M., Louch, W.E., 2012. Extreme sarcoplasmic

reticulum volume loss and compensatory T-tubule remodeling after Serca2 knockout. Proc. Natl. Acad. Sci. 109, 3997–4001.

Swynghedauw, B., 1986. Developmental and functional adaptation of contractile proteins in cardiac and skeletal muscles. Physiol. Rev. 66, 710–771.

Szwejkowski, B.R., Elder, D.H.J., Shearer, F., Jack, D., Choy, A.M.J., Pringle, S.D., Struthers, A.D., George, J., Lang, C.C., 2012. Pulmonary hypertension predicts all-cause mortality in patients with heart failure: a retrospective cohort study. Eur. J. Heart Fail. 14, 162–7.

Tamura, T., Onodera, T., Said, S., Gerdes, A.M., 1998. Correlation of myocyte lengthening to chamber dilation in the spontaneously hypertensive heart failure (SHHF) rat. J. Mol. Cell. Cardiol. 30, 2175–2181.

Terentyev, D., Kubalova, Z., Valle, G., Nori, A., Vedamoorthyrao, S., Terentyeva, R., Viatchenko-Karpinski, S., Bers, D.M., Williams, S.C., Volpe, P., Gyorke, S., 2008. Modulation of SR Ca Release by Luminal Ca and Calsequestrin in Cardiac Myocytes: Effects of CASQ2 Mutations Linked to Sudden Cardiac Death. Biophys. J. 95, 2037–2048.

Terentyev, D., Viatchenko-Karpinski, S., Valdivia, H.H., Escobar, A.L., Györke, S., 2002. Luminal Ca2+ controls termination and refractory behavior of Ca2+-induced Ca2+ release in cardiac myocytes. Circ. Res. 91, 414–20.

Thenappan, T., Ormiston, M.L., Ryan, J.J., Archer, S.L., 2018. Pulmonary arterial hypertension: Pathogenesis and clinical management. BMJ 360, 54–92.

Thenappan, T., Shah, S.J., Rich, S., Tian, L., Archer, S.L., Gomberg-Maitland, M., 2010. Survival in pulmonary arterial hypertension: a reappraisal of the NIH risk stratification equation. Eur. Respir. J. 35, 1079–87.

Thum, T., Gross, C., Fiedler, J., Fischer, T., Kissler, S., Bussen, M., Galuppo, P., Just, S., Rottbauer, W., Frantz, S., Castoldi, M., Soutschek, J., Koteliansky, V., Rosenwald, A., Basson, M.A., Licht, J.D., Pena, J.T.R., Rouhanifard, S.H., Muckenthaler, M.U., Tuschl, T., Martin, G.R., Bauersachs, J., Engelhardt, S., 2008. MicroRNA-21 contributes to myocardial disease by stimulating MAP kinase signalling in fibroblasts. Nature 456, 980–984.

Toischer, K., Rokita, A.G., Unsöld, B., Zhu, W., Kararigas, G., Sossalla, S., Reuter, S.P.,

Becker, A., Teucher, N., Seidler, T., Grebe, C., Preu, L., Gupta, S.N., Schmidt, K., Lehnart, S.E., Krüger, M., Linke, W.A., Backs, J., Regitz-Zagrosek, V., Schäfer, K., Field, L.J., Maier, L.S., Hasenfuss, G., 2010. Differential cardiac remodeling in preload versus afterload. Circulation 122, 993–1003.

Toldo, S., Bogaard, H.J., van Tassell, B.W., Mezzaroma, E., Seropian, I.M., Robati, R., Salloum, F.N., Voelkel, N.F., Abbate, A., 2011. Right ventricular dysfunction following acute myocardial infarction in the absence of pulmonary hypertension in the mouse. PLoS One 6.

Tse, G., 2016. Mechanisms of cardiac arrhythmias. J. Arrhythmia 32, 75–81.

Tsien, R.W., Bean, B.P., Hess, P., Lansman, J.B., Nilius, B., Nowycky, M.C., 1986. Mechanisms of calcium channel modulation by β-adrenergic agents and dihydropyridine calcium agonists. J. Mol. Cell. Cardiol. 18, 691–710.

Tsugorka, A., Ríos, E., Blatter, L.A., 1995. Imaging elementary events of calcium release in skeletal muscle cells. Science (80-.). 269, 1723–1726.

Tsuji, Y., Opthof, T., Kamiya, K., Yasui, K., Liu, W., Lu, Z., Kodama, I., 2000. Pacing-induced heart failure causes a reduction of delayed rectifier potassium currents along with decreases in calcium and transient outward currents in rabbit ventricle. Cardiovasc. Res. 48, 300–309.

Tung, L., 2011. Expanding on forty years of reflection. J. Physiol. 589, 2107–2108.

Umar, S., Lee, J.H., De Lange, E., Iorga, A., Partow-Navid, R., Bapat, A., Van Der Laarse, A., Saggar, R.R., Saggar, R.R., Ypey, D.L., Karagueuzian, H.S., Eghbali, M., 2012. Spontaneous ventricular fibrillation in right ventricular failure secondary to chronic pulmonary hypertension. Circ. Arrhythmia Electrophysiol. 5, 181–190.

Van Der Velden, J., Papp, Z., Boontje, N.M., Zaremba, R., De Jong, J.W., Janssen, P.M.L., Hasenfuss, G., Stienen, G.J.M., 2003. The effect of myosin light chain 2 dephosphorylation on Ca2+-sensitivity of force is enhanced in failing human hearts. Cardiovasc. Res. 57, 505–514.

van der Vijgh, W.J.F., van Velzen, D., van der Poort, J.S.E., Schlüper, H.M.M., Mross, K., Feijen, J., Pinedo, H.M., 1988. Morphometric study of myocardial changes during doxorubicin-induced cardiomyopathy in mice. Eur. J. Cancer Clin. Oncol. 24, 1603–1608.

Van Rijen, H.V.M., Eckardt, D., Degen, J., Theis, M., Ott, T., Willecke, K., Jongsma, H.J., Opthof, T., De Bakker, J.M.T., 2004. Slow Conduction and Enhanced Anisotropy Increase the Propensity for Ventricular Tachyarrhythmias in Adult Mice with Induced Deletion of Connexin43. Circulation 109, 1048–1055.

Van Wolferen, S.A., Marcus, J.T., Westerhof, N., Spreeuwenberg, M.D., Marques, K.M.J., Bronzwaer, J.G.F., Henkens, I.R., Gan, C.T.J., Boonstra, A., Postmus, P.E., Vonk-Noordegraaf, A., 2008. Right coronary artery flow impairment in patients with pulmonary hypertension. Eur. Heart J. 29, 120–127.

VanBuren, P., Harris, D.E., Alpert, N.R., Warshaw, D.M., 1995. Cardiac V_1 And V_3 Myosins Differ in Their Hydrolytic and Mechanical Activities In Vitro. Circ. Res. 77, 439–444.

Varro', A., Lathrop, D.A., Hester, S.B., Nfingtsi, P.P., Papp, J.G.Y.Y., Varró, A., Lathrop, D.A., Hester, S.B., Nánási, P.P., Papp, J.G.Y.Y., 1993. Ionic currents and action potentials in rabbit, rat, and guinea pig ventricular myocytes. Basic Res. Cardiol. 88, 93–102.

Vaughan Williams, E.M., 1982. QT and action potential duration. Br. Heart J. 47, 513–514.

Vescovo, G., Jones, S.M., Harding, S.E., Poole-Wilson, P.A., 1989. Isoproterenol sensitivity of isolated cardiac myocytes from rats with monocrotaline-induced right-sided hypertrophy and heart failure. J. Mol. Cell. Cardiol. 21, 1047–1061.

Voelkel, N.F., Quaife, R.A., Leinwand, L.A., Barst, R.J., McGoon, M.D., Meldrum, D.R., Dupuis, J., Long, C.S., Rubin, L.J., Smart, F.W., Suzuki, Y.J., Gladwin, M., Denholm, E.M., Gail, D.B., 2006. Right ventricular function and failure: Report of a National Heart, Lung, and Blood Institute working group on cellular and molecular mechanisms of right heart failure. Circulation 114, 1883–1891.

Voelkel, N.F., Tuder, R.M., 2000. Hypoxia-induced pulmonary vascular remodeling: A model for what human disease? J. Clin. Invest. 106, 733–738.

Volders, P.G.A., Sipido, K.R., Carmeliet, E., Wellens, H.J.J., Vos, M.A., 1999. Repolarizing K Currents I(TO1) and I(Ks) Are Larger in Right Than Left Canine Ventricular Midmyocardium. Circulation 99, 206–211.

Vonk Noordegraaf, A., Galiè, N., 2011. The role of the right ventricle in pulmonary arterial

hypertension. Eur. Respir. Rev.

Vonk Noordegraaf, A., Westerhof, B.E., Westerhof, N., 2017. The Relationship Between the Right Ventricle and its Load in Pulmonary Hypertension. J. Am. Coll. Cardiol. 69, 236–243.

Wagenknecht, T., Grassucci, R., Berkowitz, J., Wiederrecht, G.J., Xin, H.B., Fleischer, S., 1996. Cryoelectron microscopy resolves FK506-binding protein sites on the skeletal muscle ryanodine receptor. Biophys. J. 70, 1709–15.

Wagenknecht, T., Grassucci, R., Frank, J., Saito, A., Inui, M., Fleischer, S., 1989. Three-dimensional architecture of the calcium channel/foot structure of sarcoplasmic reticulum. Nature 338, 167–70.

Wagner, E., 2012. Cardiac T-Tubule Membranes Nanostructure and Remodeling Mechanisms in Disease Dissertation. Dissertation.

Wagner, E., Brandenburg, S., Kohl, T., Lehnart, S.E., 2014. Analysis of Tubular Membrane Networks in Cardiac Myocytes from Atria and Ventricles. J. Vis. Exp. e51823.

Wagner, E., Lauterbach, M.A., Kohl, T., Westphal, V., Williams, G.S.S.B., Steinbrecher, J.H., Streich, J.-H.H., Korff, B., Tuan, H.-T.M.T.M., Hagen, B., Luther, S., Hasenfuss, G., Parlitz, U., Saleet Jafri, M., Hell, S.W., Jonathan Lederer, W., Lehnart, S.E., Goettingen, C.E., Jafri, M.S., Hell, S.W., Lederer, W.J., Lehnart, S.E., 2012. Stimulated Emission Depletion Live-Cell Super-Resolution Imaging Shows Proliferative Remodeling of T-Tubule Membrane Structures After Myocardial Infarction. New Methods Cardiovasc. Biol. Stimul. 111, 402–14.

Wagner, G.S., Macfarlane, P., Wellens, H., Josephson, M., Gorgels, A., Mirvis, D.M., Pahlm, O., Surawicz, B., Kligfield, P., Childers, R., Gettes, L.S., 2009. AHA/ACCF/HRS Recommendations for the Standardization and Interpretation of the Electrocardiogram. Part VI: Acute Ischemia/Infarction A Scientific Statement From the American Heart Association Electrocardiography and Arrhythmias Committee, Council on Clinical Cardiology; the American College of Cardiology Foundation. J. Am. Coll. Cardiol.

Ward, M.-L., Crossman, D.J., 2014. Mechanisms underlying the impaired contractility of diabetic cardiomyopathy. World J. Cardiol. 6, 577–584.

Warren, M., Guha, P.K., Berenfeld, O., Zaitsev, A., Anumonwo, J.M.B., Dhamoon, A.S.,

Bagwe, S., Taffet, S.M., Jalife, J., 2003. Blockade of the inward rectifying potassium current terminates ventricular fibrillation in the guinea pig heart. J. Cardiovasc. Electrophysiol. 14, 621–631.

Watanabe, T., Delbridge, L.M., Bustamante, J.O., McDonald, T.F., 1983. Heterogeneity of the action potential in isolated rat ventricular myocytes and tissue. Circ. Res. 52, 280–90.

Wehrens, X.H.T., Lehnart, S.E., Huang, F., Vest, J.A., Reiken, S.R., Mohler, P.J., Sun, J., Guatimosim, S., Song, L.S., Rosemblit, N., D'Armiento, J.M., Napolitano, C., Memmi, M., Priori, S.G., Lederer, W.J., Marks, A.R., 2003. FKBP12.6 deficiency and defective calcium release channel (ryanodine receptor) function linked to exercise-induced sudden cardiac death. Cell 113, 829–840.

Wehrens, X.H.T., Lehnart, S.E., Reiken, S.R., Deng, S.X., Vest, J.A., Cervantes, D., Coromlias, J., Landry, D.W., Marks, A.R., 2004. Protection from Cardiac Arrhythmia Through Ryanodine Receptor-Stabilizing Protein Calstabin2. Science (80-.). 304, 292–296.

Wei, S., Guo, A., Chen, B., Kutschke, W., Xie, Y.-P.P., Zimmerman, K., Weiss, R.M., Anderson, M.E., Cheng, H., Song, L.-S.S., 2010. T-tubule remodeling during transition from hypertrophy to heart failure. Circ. Res. 107, 520–531.

Weiss, J.N., Chen, P.S., Qu, Z., Karagueuzian, H.S., Garfinkel, A., 2000. Ventricular fibrillation: How do we stop the waves from breaking? Circ. Res.

West, J., Hemnes, A., 2011. Experimental and Transgenic Models of Pulmonary Hypertension. In: Comprehensive Physiology. John Wiley & Sons, Inc., Hoboken, NJ, USA, pp. 769–782.

Westerhof, B.E., Saouti, N., Van Der Laarse, W.J., Westerhof, N., Vonk Noordegraaf, A., 2017. Treatment strategies for the right heart in pulmonary hypertension. Cardiovasc. Res. 113, 1465–1473.

Wiener, N., Rosenblueth, A., 1946. The mathematical formulation of the problem of conduction of impulses in a network of connected excitable elements, specifically in cardiac muscle. Arch. Inst. Cardiol. Mex. 16, 205–265.

Wieprecht, M., Wieder, T., Geilen, C.C., 1994. N-[2-bromocinnamyl(amino)ethyl]-5-isoquinolinesulphonamide (H-89) inhibits incorporation of choline into

phosphatidylcholine via inhibition of choline kinase and has no effect on the phosphorylation of CTP:phosphocholine cytidylyltransferase. Biochem. J. 297, 241–247.

Wier, W.G., Ter Keurs, H.E.D.J., Marban, E., Gao, W.D., Balke, C.W., 1997. Ca2+ "sparks" and waves in intact ventricular muscle resolved by confocal imaging. Circ. Res. 81, 462–469.

Winfree, A.T., 1989. Electrical instability in cardiac muscle: Phase singularities and rotors. J. Theor. Biol. 138, 353–405.

Wit, A.L., Hoffman, B.F., Cranefield, P.F., 1972. Slow conduction and reentry in the ventricular conducting system. I. Return extrasystole in canine Purkinje fibers. Circ. Res. 30, 1–10.

Witcher, D.R., Kovacs, R.J., Schulman, H., Cefali, D.C., Jones, L.R., 1991. Unique phosphorylation site on the cardiac ryanodine receptor regulates calcium channel activity. J. Biol. Chem. 266, 11144–11152.

Wojciak-Stothard, B., Abdul-Salam, V.B., Lao, K.H., Tsang, H., Irwin, D.C., Lisk, C., Loomis, Z., Stenmark, K.R., Edwards, J.C., Yuspa, S.H., Howard, L.S., Edwards, R.J., Rhodes, C.J., Gibbs, J.S.R., Wharton, J., Zhao, L., Wilkins, M.R., 2014. Aberrant chloride intracellular channel 4 expression contributes to endothelial dysfunction in pulmonary arterial hypertension. Circulation 129, 1770–1780.

Wong, J., Baddeley, D., Bushong, E.A., Yu, Z., Ellisman, M.H., Hoshijima, M., Soeller, C., 2013. Nanoscale Distribution of Ryanodine Receptors and Caveolin-3 in Mouse Ventricular Myocytes: Dilation of T-Tubules near Junctions. Biophys. J. 104, L22–L24.

Wong, Y.Y., Ruiter, G., Lubberink, M., Raijmakers, P.G., Knaapen, P., Marcus, J.T., Boonstra, A., Lammertsma, A.A., Westerhof, N., Van Der Laarse, W.J., Vonk-Noordegraaf, A., 2011. Right ventricular failure in idiopathic pulmonary arterial hypertension is associated with inefficient myocardial oxygen utilization. Circ. Hear. Fail. 4, 700–706.

Woodcock, E.A., Matkovich, S.J., 2005. Cardiomyocytes structure, function and associated pathologies. Int. J. Biochem. Cell Biol.

Woodman, S.E., Park, D.S., Cohen, A.W., Cheung, M.W.C., Chandra, M., Shirani, J.,

Tang, B., Jelicks, L.A., Kitsis, R.N., Christ, G.J., Factor, S.M., Tanowitz, H.B., Lisanti, M.P., 2002. Caveolin-3 knock-out mice develop a progressive cardiomyopathy and show hyperactivation of the p42/44 MAPK cascade. J. Biol. Chem. 277, 38988–38997.

Wright, P.T., Nikolaev, V.O., O'Hara, T., Diakonov, I., Bhargava, A., Tokar, S., Schobesberger, S., Shevchuk, A.I., Sikkel, M.B., Wilkinson, R., Trayanova, N.A., Lyon, A.R., Harding, S.E., Gorelik, J., 2014. Caveolin-3 regulates compartmentation of cardiomyocyte beta2-adrenergic receptor-mediated cAMP signaling. J. Mol. Cell. Cardiol. 67, 38–48.

Wright, P.T., Sanchez-Alonso, J.L., Lucarelli, C., Alvarez-Laviada, A., Poulet, C.E., Bello, S.O., Faggian, G., Terracciano, C.M., Gorelik, J., 2018. Partial mechanical unloading of the heart disrupts L-type calcium channel and beta-adrenoceptor signaling microdomains. Front. Physiol. 9, 1–11.

Xie, Y.P., Chen, B., Sanders, P., Guo, A., Li, Y., Zimmerman, K., Wang, L.C., Weiss, R.M., Grumbach, I.M., Anderson, M.E., Song, L.S., 2012. Sildenafil prevents and reverses transverse-tubule remodeling and Ca 2+ handling dysfunction in right ventricle failure induced by pulmonary artery hypertension. Hypertension 59, 355–362.

Xu, L., Eu, J.P., Meissner, G., Stamler, J.S., 1998. Activation of the cardiac calcium release channel (Ryanodoine receptor) by poly-S-nitrosylation. Science (80-.). 279, 234–237.

Xu, L., Mann, G., Meissner, G., 1996. Regulation of cardiac Ca2+ release channel (ryanodine receptor) by Ca2+, H+, Mg2+, and adenine nucleotides under normal and simulated ischemic conditions. Circ. Res. 79, 1100–1109.

Xu, X., Yano, M., Uchinoumi, H., Hino, A., Suetomi, T., Ono, M., Tateishi, H., Oda, T., Okuda, S., Doi, M., Kobayashi, S., Yamamoto, T., Ikeda, Y., Ikemoto, N., Matsuzaki, M., 2010. Defective calmodulin binding to the cardiac ryanodine receptor plays a key role in CPVT-associated channel dysfunction. Biochem. Biophys. Res. Commun. 394, 660–666.

Yang, L., Katchman, A., Morrow, J.P., Doshi, D., Marx, S.O., 2011. Cardiac L-type calcium channel (Ca v 1.2) associates with γ subunits. FASEB J. 25, 928–936.

Yeang, C., Hasanally, D., Que, X., Hung, M.-Y., Stamenkovic, A., Chan, D., Chaudhary,

R., Margulets, V., Edel, A.L., Hoshijima, M., Gu, Y., Bradford, W., Dalton, N., Miu, P., Cheung, D.Y., Jassal, D.S., Pierce, G.N., Peterson, K.L., Kirshenbaum, L.A., Witztum, J.L., Tsimikas, S., Ravandi, A., 2019. Reduction of myocardial ischaemia-reperfusion injury by inactivating oxidized phospholipids. Cardiovasc. Res. 115, 179–189.

Yin, F.C., 1981. Ventricular wall stress. Circ. Res. 49, 829–842.

Yuan, W., Bers, D.M., 1994. Ca-dependent facilitation of cardiac Ca current is due to Ca-calmodulin-dependent protein kinase. J. Chem. Inf. Model. 267, 982–93.

Yue, D.T., Herzig, S., Marban, E., 1990. Beta-adrenergic stimulation of calcium channels occurs by potentiation of high-activity gating modes. Proc. Natl. Acad. Sci. U. S. A. 87, 753–7.

Zable, A.C., Favero, T.G., Abramson, J.J., 1997. Glutathione modulates ryanodine receptor from skeletal muscle sarcoplasmic reticulum. Evidence for redox regulation of the Ca2+ release mechanism. J. Biol. Chem. 272, 7069–77.

Zaffran, S., Kelly, R.G., Meilhac, S.M., Buckingham, M.E., Brown, N.A., 2004. Right ventricular myocardium derives from the anterior heart field. Circ. Res. 95, 261–268.

Zapol, W.M., Snider, M.T., 1977. Pulmonary Hypertension in Severe Acute Respiratory Failure. N. Engl. J. Med. 296, 476–480.

Zhao, L., 2010. Chronic hypoxia-induced pulmonary hypertension in rat: The best animal model for studying pulmonary vasoconstriction and vascular medial hypertrophy. Drug Discov. Today Dis. Model. 7, 83–88.

Ziman, A.P., Gómez-Viquez, N.L., Bloch, R.J., Lederer, W.J., 2010. Excitation-contraction coupling changes during postnatal cardiac development. J. Mol. Cell. Cardiol. 48, 379–386.

Zong, X., Schreieck, J., Mehrke, G., Welling, A., Schuster, A., Bosse, E., Flockerzi, V., Hofmann, F., 1995. On the regulation of the expressed L-type calcium channel by cAMP-dependent phosphorylation. Pflugers Arch. 430, 340–7.

Zubieta, G.-C., Paulev, P.-E., 2004. Physiology And Pathophysiology Essentials and clinical problems.

Zygmuntt, A.C., Maylie, J., 1990. Threshold Calcium Current in Guinea-Pig Ventricular. J. Physiol. 428, 653–671.